

Durham E-Theses

Volcanic ash in jet engines: bouncing, sticking, and splashing of molten glass droplets.

LARK, THOMAS,ANDREW

How to cite:

LARK, THOMAS,ANDREW (2024) *Volcanic ash in jet engines: bouncing, sticking, and splashing of molten glass droplets.*, Durham theses, Durham University. Available at Durham E-Theses Online: <http://etheses.dur.ac.uk/15742/>

Use policy

The full-text may be used and/or reproduced, and given to third parties in any format or medium, without prior permission or charge, for personal research or study, educational, or not-for-profit purposes provided that:

- a full bibliographic reference is made to the original source
- a [link](#) is made to the metadata record in Durham E-Theses
- the full-text is not changed in any way

The full-text must not be sold in any format or medium without the formal permission of the copyright holders.

Please consult the [full Durham E-Theses policy](#) for further details.

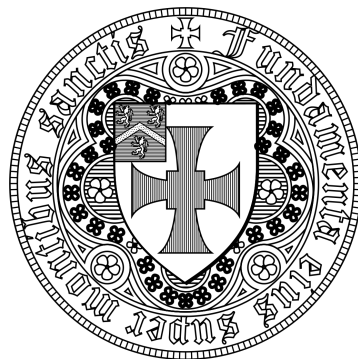
**Volcanic ash in jet engines: bouncing,
sticking, and splashing of molten glass
droplets.**

Thomas Andrew Lark

A thesis submitted in partial fulfilment of the requirements for
the degree of
Doctor of Philosophy.

**Department of Earth Sciences.
University of Durham.**

July 2024



Abstract

In the last thirty years there have been more than 250 incidents of aircraft encountering airborne volcanic ash. This volcanic ash can have a serious detrimental effect on the jet turbine engines of these aircraft, reducing the efficiency of the compressor and the airflow through the engine, making an engine surge more likely to occur. When volcanic ash enters an engine, it melts in the high temperatures and impacts the hot surfaces inside the engine. Upon impact these droplets can either bounce, stick, or splash. A quantitative understanding of molten ash droplet behaviour is needed, which can be used to determine the threshold ash concentration below which a jet aircraft can safely operate. To develop this understanding, I performed computational fluid dynamics (CFD) simulations of airflow laden with volcanic ash particles through High Pressure Nozzle Guide Vane (HP-NGV) arrays. The associated impact properties of the particles on the HP-NGVs were recorded. Using these impact properties and dimensionless numbers that I identified as important in controlling the droplet impact outcome, I designed scaled experiments using analogous materials that could capture the physics of the ash-droplet NGV interaction. The results of the first set of scaled experiments and further modelling presented here suggest that ash droplets do not splash on impact with the NGV. In the second set of experiments, soda-lime glass beads were heated in a flame and made to impact metal targets. An empirical critical viscosity model was adapted to incorporate a novel dependence on the impact angle, so that a particle is predicted to stick to the surface if its actual viscosity is lower than the corresponding critical viscosity (which is a function of the particle kinetic energy and impact angle). This model, which gave an adequate fit to the data, was then applied to the results of the CFD simulations of volcanic ash-laden airflow around the NGVs. Using the impact properties of the ash particles on the NGV and the new empirical critical viscosity model, the deposits of ash along the NGV surface were mapped for four different volcanic ash compositions. It was found that for less viscous ashes significantly larger amounts of ash stick to the NGV surface than do for more viscous ashes. It was also found that for the less viscous ashes, deposits were widely distributed on the NGV surfaces whereas for the more viscous ashes, deposits were clustered around the stagnation point and leading edge of the NGV. These results were found to have good qualitative agreement with evidence from investigations of engines.

Acknowledgements

Foremost I would like to thank my supervisory team: Professor Ed Llewellyn, Dr Fabian Wadsworth, and Dr Rory Clarkson. Their support and advice was invaluable to me during the course of this work, and it has been a privilege to work with them over the last 4 years.

I must thank Dr Richard Brooker of the University of Bristol who let me spend time in his laboratory, and went above and beyond in helping me complete my experiments. I must also thank Dr Lisong Yang who lent me so much of her time to help me conduct experiments in the laboratories of the Department of Chemistry in Durham. Thanks must also go to Professor Murray Lark for his assistance in teaching me how to use R, and for all his statistical advice.

I would also like to thank my friends from Durham University, whose kindness and good humour have been a constant source of joy and support during my time at Durham. I am grateful to my parents Andrea and Murray, and my sisters Catherine and Anna, for their support and encouragement during my studies. Finally I would like to thank Christina for her kind patience, encouragement and understanding over the course of my studies.

Declaration

I declare that this thesis, which I submit for the degree of Doctor of Philosophy at Durham University, is my own work, except where acknowledgement is made in the text, and not substantially the same as any work which has previously been submitted at this or any other university for any degree, diploma or other qualification.

©Copyright, Thomas Lark, July 2024. The copyright of this thesis rests with the author. No quotation from it should be published in any form without the author's prior written consent. All information derived from this thesis must be acknowledged appropriately.

Contents

Acknowledgements	1
Declaration	2
1 Introduction	8
1.1 Background	8
1.2 Previous Work	13
1.3 Aims and Objectives	16
1.3.1 What dimensionless numbers are important in controlling the stick/splash/bounce outcome of the ash droplet - NGV interaction?	16
1.3.2 What are the values of the dimensional impact properties and the dimensionless numbers associated with the ash droplet - NGV interaction?	17
1.3.3 Under what conditions do ash droplets stick, splash or bounce on impact with the NGV surfaces?	17
1.4 Summary of chapters presented	18
2 Understanding What Impact Properties Control Splashing.	19
2.1 Introduction.	19
2.1.1 Types of splashing behaviour.	20
2.1.2 Role of droplet properties.	21
2.1.3 Role of surface and ambient properties.	23
2.1.4 Dimensionless numbers.	26
2.2 Method.	30
2.2.1 Generalized Linear Models.	30
2.2.2 Analysis of droplet and surface properties.	32

2.2.3	Analysis of dimensionless numbers.	34
2.3	Results.	34
2.3.1	Results from analysis of droplet and surface properties.	34
2.3.2	Results of analysis of dimensionless numbers.	43
2.4	Discussion.	47
2.4.1	Dimensional properties.	47
2.4.2	Dimensionless properties.	48
2.4.3	Designing scaled experiments.	49
2.5	Conclusions	51
3	Understanding the Impact Properties of Ash Droplets on the NGVs.	53
3.1	Introduction	53
3.1.1	Background	56
3.2	Scaling Framework	59
3.3	Method	64
3.4	Results and Analysis	75
3.5	Discussion	83
3.6	Conclusions	94
4	Scaled Splashing experiments.	96
4.1	Introduction	96
4.2	Method	97
4.2.1	Identification of key dimensionless numbers.	97
4.2.2	Selection of analogous fluids.	98
4.2.3	Droplet production	102
4.2.4	Image capture and analysis	104
4.3	Results and Analysis	105
4.4	Discussion and Conclusions	115
5	Scaled Splashing Simulations.	118
5.1	Introduction	118
5.1.1	Motivation	118
5.1.2	Flow 3D Background	119
5.2	Modelling Methods	122

5.2.1	Model Physics and Set-up within Flow 3D.	122
5.3	Validation of model	124
5.3.1	Introduction	124
5.3.2	Selection of data	125
5.3.3	Results of the Validation Simulations	127
5.3.4	Analysis and Conclusions	130
5.4	Scaled modelling of droplets impacting the NGVs	130
5.4.1	Methods	130
5.4.2	Results	134
5.4.3	Discussion	138
5.4.4	Limitations and future work	140
5.5	Conclusions	141
6	Understanding What Controls Ash Bouncing off the NGV.	143
6.1	Introduction	143
6.1.1	Motivation.	143
6.1.2	Literature review.	144
6.1.3	The Weissenberg number	148
6.1.4	Purpose of this Chapter.	152
6.2	Method	152
6.2.1	Apparatus and materials.	152
6.2.2	Experimental Method	153
6.2.3	Calculating the temperature, velocity and size of the particles.	155
6.2.4	Calculation of particle impact properties	160
6.3	Results	161
6.4	Discussion	168
6.4.1	Limitations	172
6.5	Conclusions	173
7	Predicting Ash Deposition on the NGVs.	175
7.1	Introduction	175
7.2	Method	176
7.2.1	Computational Fluid Dynamics simulations.	176

7.2.2	Calculation of particle viscosities and critical particle viscosities. . .	178
7.2.3	Calculating the proportion of ash that sticks or bounces.	179
7.3	Results.	180
7.3.1	Overall levels of sticking.	180
7.3.2	Basalt	183
7.3.3	Andesite	187
7.3.4	Dacite	190
7.3.5	Rhyolite	194
7.4	Discussion	198
7.4.1	Basalt	202
7.4.2	Andesite	203
7.4.3	Dacite	205
7.4.4	Rhyolite	206
7.4.5	Comparison of Results with Engine Evidence.	207
7.4.6	Limitations	211
7.5	Conclusions	212
8	Conclusions	213
8.1	Summary	213
8.2	What dimensionless numbers are important in controlling the stick/splash/bounce outcome of the ash droplet - NGV interaction?	214
8.3	What are the values of the dimensional impact properties and the dimension- less numbers associated with the ash droplet - NGV interaction?	215
8.4	Under what conditions do ash droplets stick, splash or bounce on impact with the NGV surfaces?	216
8.4.1	The sticking/splashing threshold.	216
8.4.2	The sticking/bouncing threshold.	217
8.5	Synthesis and application of results.	217
8.6	Further Work	218
8.6.1	Further Droplet Impact Experiments, Better Scaled to the Weber Number.	218
8.6.2	Examine Behaviour of Deposition on ‘Dirty’ Surfaces.	219

8.6.3	Examine the Role of Other Properties Affecting Droplet Impact Outcomes.	219
9	Appendix	220
9.1	Chapter 2	220
9.2	Chapter 3	220
9.3	Chapter 4	222
9.4	Chapter 5	224
9.5	Chapter 6	248
9.6	Chapter 7	251
9.6.1	Basalt	251
9.6.2	Andesite	253
9.6.3	Dacite	255
9.6.4	Rhyolite	257

Chapter 1

Introduction

1.1 Background

The gas turbine engines currently used on aircraft are designed for use in clean air, free of any particulates or aerosols. However there are many contaminants suspended within the troposphere such as ice crystals, mineral dust, and volcanic ash that can cause significant damage to engine components when ingested by the engine. This ingestion can lead to degradation of engine performance, and in extreme circumstances can lead to in-flight engine failure [1].

The work of this Thesis focuses on the problems posed to gas turbine engines by the last of the particulate hazards mentioned, namely volcanic ash.

In 1982 British Airways Flight 009 encountered volcanic ash from the 9-month long eruption of Mount Galunggung in Java, Indonesia [2]. This led to the failure of all 4 engines on the aircraft. Fortunately, the pilots were able to re-start the engines and the aircraft landed safely. Since then, the hazard posed by volcanic ash to aircraft has been widely recognised by the aviation industry, with a global policy of aircraft avoiding any visible volcanic ash being implemented [1].

The consequences of encounters with volcanic ash for aircraft vary considerably. Some flights that encountered volcanic ash only experienced a smell of sulphur dioxide within the cockpit and cabin, or witnessed electrostatic discharge on the windscreen of the plane (also

known as St. Elmo's fire), or both. However some aircraft which encountered volcanic ash experienced in-flight degradation of engine performance, with nine aircraft that encountered volcanic ash between 1953 to 2009 facing temporary engine failure after exposure to ash that required an in-flight restart of the engine [1].

When volcanic ash enters the gas turbine engines, it can melt and soften in the high temperatures, as the melting temperature of magmatic silicate glass in volcanic ash is less than the operating temperatures of modern gas turbine engines [3]. The main damage mechanism by which volcanic ash can cause engine failure is the subsequent deposition (and in some circumstances re-solidification) of the molten volcanic ash on components inside the engine, in particular the Nozzle Guide Vanes (NGVs) [4, 5]. Below in Fig [1.1] is an image of a jet engine showing the location of the hot and cold components within the jet engine, and the location of the NGVs at the exit of the combustor and entrance of the turbine.

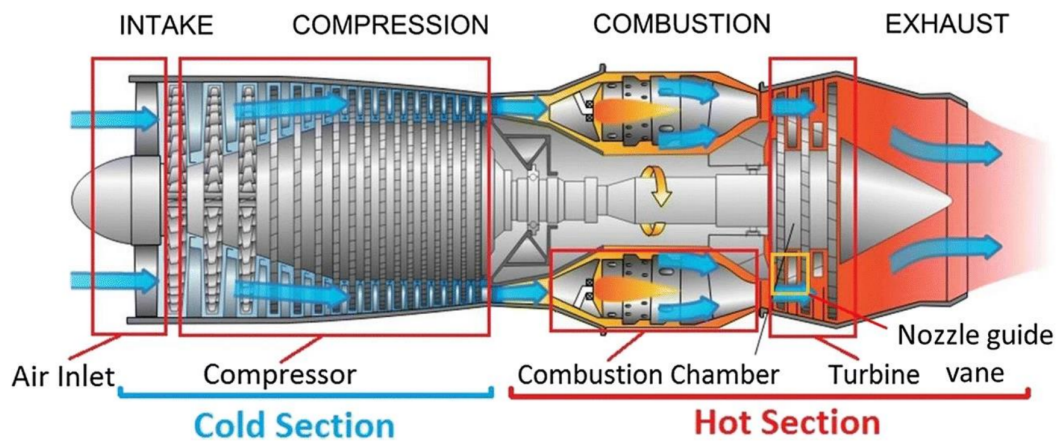


Figure 1.1: A cross-sectional diagram of a jet engine core, illustrating the key components including the Nozzle Guide Vanes (NGVs) located at the exit of the combustor and entrance to the turbine. The diagram highlights both the hot and cold sections of the engine. Taken from [6].

The volcanic ash remains molten as it exits the combustor and passes through the NGVs as molten droplets, where it can impact and deposit on the NGV surfaces. These ash deposits on the NGVs can restrict airflow through the engine, which can lead to subsequent engine failure. In Fig [1.2] is an image of some of the NGVs from BA Flight 009 from 1982 with ash deposits upon them.

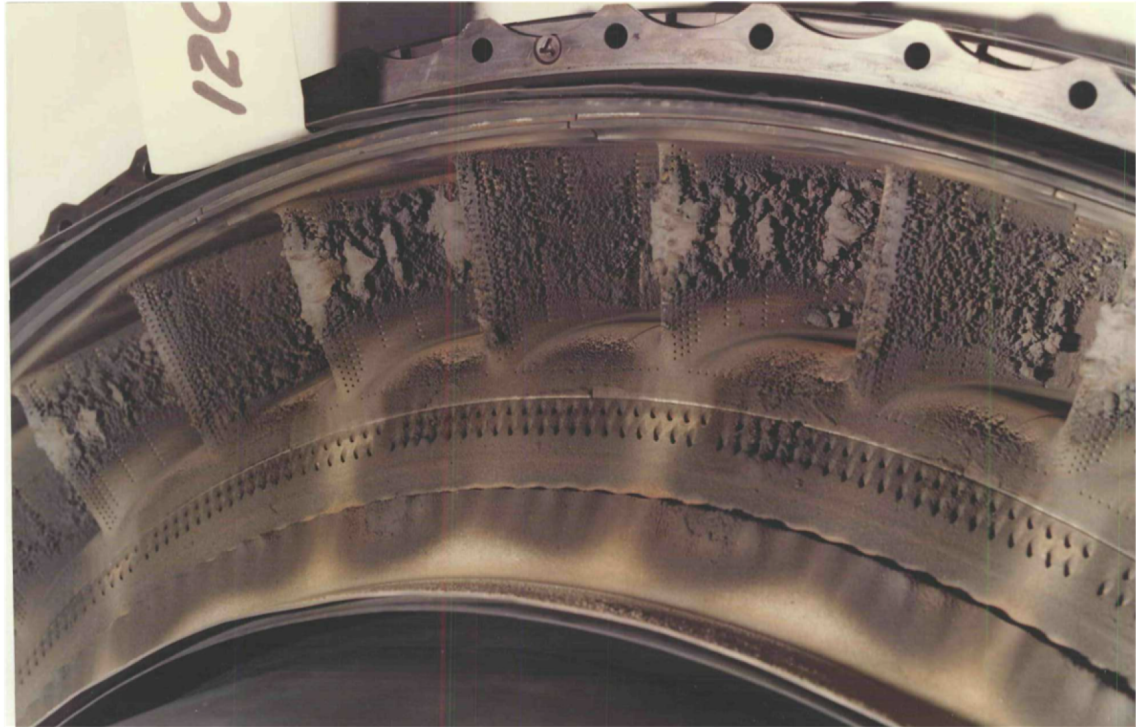


Figure 1.2: Image showing volcanic ash deposits on Nozzle Guide Vanes (NGVs) from the 1982 British Airways Flight 009 engine, illustrating the extent of ash buildup that can occur during volcanic ash encounters [7].

The serious potential risks posed to aircraft and potential tragic consequences have led (as previously mentioned) to a policy of total ash avoidance for aircraft by the aviation industry. This policy meant that when the Icelandic volcano Eyjafjallajökull erupted in 2010 the airspace over Northern Europe was shut for 13 days (resulting in the largest shut down of air traffic over Europe since the second world war) in response to concerns about the risks the ash posed to aircraft. This shutdown of airspace led to the cancellation of 10000 flights, leaving 10 million passengers stranded. It is estimated that the aviation industry lost 1.5 billion pounds as a result [8]. Flights only started again when new guidance was issued by the aviation industry allowing aircraft to fly through airspace where the concentration of volcanic ash was less than 2 mg m^{-3} [9].

The reader will have realised that this guidance provides no indication as to how long an aircraft could operate in such a volcanic ash concentration. This guidance would allow an aircraft to fly for an hour in an ash concentration of 2 mg m^{-3} , but would have forbidden a flight of half an hour through an ash concentration of 4 mg m^{-3} , even though the aircraft

would ingest the same bulk quantity of volcanic ash. To address this Clarkson et al. defined an ash ‘dose’ received by the engine, as the product of the ash concentration in which the engine operated and the duration of the engine exposure to the ash [9].

The principle of an ‘ash dose’ was then used by Clarkson et al. [9] to develop what they called a Duration of Exposure versus Ash Concentration (DEvAC) chart [9]. In this chart, events where aircraft have been exposed to volcanic ash are plotted according to the ash concentration (on the y-axis), and the duration of the event (on the x-axis). The events are plotted as bubbles, which accounts for the uncertainty in measurements of the duration of exposure and ash concentration for each event, with larger bubbles indicating greater uncertainty. In Fig [1.3] can be seen a DEvAC chart taken from [9].

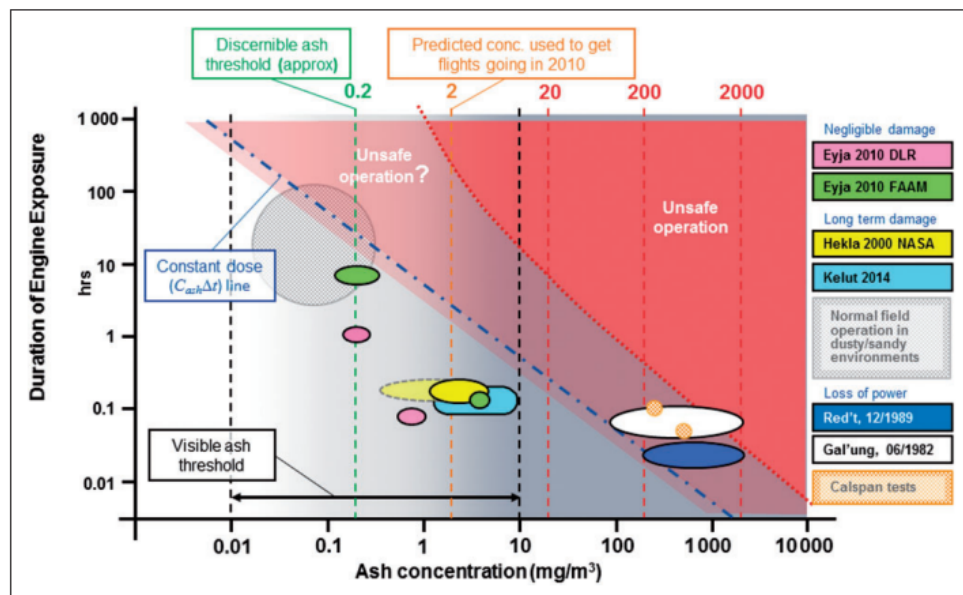


Figure 1.3: Duration of Exposure versus Ash Concentration (DEvAC) chart, adapted from [9], illustrating various aircraft encounters with volcanic ash. Each event is plotted as a bubble, where the size represents the uncertainty in the exposure duration and ash concentration measurements. Diagonal dashed lines represent constant ash dose levels, showing how an aircraft flying through a higher ash concentration for a shorter time can receive the same ash dose as one flying through a lower concentration for a longer duration.

Note in Fig [1.3] the diagonal dashed lines labelled ‘constant dose line’. These show how an aircraft flying through a given concentration of ash for a given length of time, will ingest the same ‘dose’ of ash as an aircraft flying through a higher concentration of ash but

for a shorter length of time. The authors of the DEvAC chart recommended that aircraft could operate on or below a constant dose line that is equivalent to an aircraft operating in a concentration of ash of 4 mg m^{-3} for one hour. Note that a flight in April 2010 that flew for more than 2 hours in the ‘safe’ concentration of ash (2 mg m^{-3}) recommended then to restart flights, would have exceeded the recommended safe dose from Clarkson et al.

In order to calculate this dose a simple model was derived by Clarkson et al. to describe the rate at which ash deposits build up on the NGV [10]. They considered two phenomena in defining their model, deposit accretion and deposit shedding. In seeking to represent the accretion effect they defined an accumulation factor, ζ , as being equal to the proportion of ash entering the engine core which will stick to the NGV surface. They apply this factor to calculate the mass of ash entering the core that will stick to the NGVs, by taking the product of the atmospheric ash concentration, the accumulation factor and the mass flow of air into the engine, and dividing through by the ambient air density. When they consider the shedding effect, they assume that the rate of deposit shedding is proportional to the mass of ash deposited, with the constant of proportionality being the shedding rate parameter λ . The difference between the accretion rate and the shedding rate is given as:

$$\frac{dm}{dt} = \dot{m}_{acc} - \dot{m}_{shed}. \quad (1.1)$$

Solving the above differential equation and using the mathematical definitions of the accretion and shedding rates, it is possible to derive the expression for the mass of deposited ash on the vane at any given moment. This is given below:

$$m(t) = m_0 e^{-\lambda t} + \frac{c_{ash} W \zeta}{\rho_{air} \lambda} \times (1 - e^{-\lambda t}). \quad (1.2)$$

Here λ [s^{-1}] and ζ [%] are the shedding and accumulation factors respectively, c_{ash} [mgm^{-3}] is the concentration of ash in the air, W [kgs^{-1}] the air mass flow through the engine core, ρ_{air} [kgm^{-3}] is the ambient air density, m_0 [kg] is the original amount of ash on the vane before the ash encounter, and t [s] is time. Note that the shedding factor is given as a rate, and the accumulation factor is given as a percentage.

Clarkson et al. derived the shedding and accumulation factors empirically from engine evidence, and then used them in conjunction with Eqn [1.2] to calculate a safe dose equivalent to an aircraft operating in a concentration of ash of 4 mg m^{-3} for one hour [10]. This estimation of the safe dose of airborne volcanic ash that an aircraft can withstand can be improved, by better refining the values of the accumulation and shedding factors. This can be achieved through an investigation and comprehensive understanding of the physics governing the behaviour of molten volcanic ash droplets upon impacting with NGV surfaces.

1.2 Previous Work

Work has been done using small-scale experiments to investigate the accumulation of volcanic ash on NGV surfaces. These experiments all used similar set-ups, where fine particles of volcanic ash are heated up to high temperatures $\approx 800 - 1000^\circ \text{C}$ and made to impact at speed, on a stationary metal target.

Taltavull et al. [11] collected volcanic ash from the Laki vent in Iceland, comprising particles with diameters ranging from 5 to 70 μm . These ash particles were introduced into the flame of a vacuum plasma spray system to heat and accelerate them. Subsequently, the particles impacted a metal coupon held at various angles (30° , 60° , 90°) relative to the horizontal. Taltavull et al. [11] found that if an ash particle was to stick it needed to have enough inertia to deviate from the flow lines around the coupon and reach a temperature above its glass transition temperature. They found these two important factors were strongly related to the particle size, with larger particles having a greater inertia but also taking longer to reach the glass transition temperature. The authors identified a ‘sweet spot’ of particle diameters ranging from 10 to 30 μm that are most likely to deposit on the NGVs, as they possess sufficient inertia to deviate from the flow lines and impact the NGV, while also reaching temperatures above the glass transition temperature. Furthermore, the authors observed that the probability of a particle adhering to the surface increased with the magnitude of the velocity component normal to the coupon surface, with particles experiencing more oblique impacts being less likely to stick to the coupon surface.

Dean et al. [12] used the same experimental set-up as Taltavull et al [11], but they used four different volcanic ash compositions with diameters from 5 to 50 μm . The authors

classified two of the ash compositions as having a low silica content (< 20 wt.%), while the other two compositions were classified as having a high silica content (> 20 wt.%). The findings of Dean et al. [12] were consistent with those of Taltavull et al. [11], indicating that ash particles are more likely to adhere to the surface at greater temperatures and impact angles closer to the normal with respect to the coupon surface. However, Dean et al. [12] also observed that the rate of ash adhesion to the coupon was less for the high silica ash, which they theorized was due to the greater viscosity. This suggests that viscosity plays an important role in controlling the adhesion of volcanic ash to the NGVs, with less viscous ash being more likely to stick. Note that the viscosity considered here is the dynamic viscosity, and the viscosity can be considered Newtonian for silicate melts[13] [14][15].

Giehl et al. [16] performed similar experiments to Taltavull et al. [11] and Dean et al. [12], where they dropped ash particles with diameters $5 - 500 \mu\text{m}$ into the flame of an oxy-acetylene torch where they were both heated and accelerated to impact a metal coupon held at 45° with respect to the horizontal. They used ash particles of 4 different compositional types: Basalt, Andesite, Dacite and Rhyolite. Their findings were consistent with respect to the role of particle size with those of Taltavull et al. [11] and Dean et al. [12]. They also found that the composition of the ash was important in controlling the resulting adhesion rate, more specifically the relative amounts of crystalline and amorphous phases within the ash. Giehl et al. [16] found that ash with more amorphous content was more likely to stick, as the ash would be less viscous on impact.

Pearson and Brooker [17] used a similar set up to Giehl et al. [16], dropping ash particles (with diameters of $4 - 125 \mu\text{m}$) from 7 different volcanoes into the flame of an oxy-acetylene torch, and making them impact a metal target. In contrast to Giehl et al. [16] they also performed experiments involving metal compounds that had a ceramic coating applied to them, the same as the thermal barrier coatings that are applied to NGVs in gas turbine engines. They found that the ash remained stuck to the ceramic coating more efficiently than the bare metal targets. They also found that low silica ash in their experiments was more likely to penetrate through the layers of the coating.

Song et al. [18] also performed experiments using a plasma spray system to heat and accelerate volcanic ash taken from Eyjafjallajökull, with diameters ranging from $5 - 70 \mu\text{m}$.

They impacted the ash particles onto coupons coated with thermal barrier coatings. They found that hotter lower viscosity droplets, impacting at angles closer to the coupon surface normal were more likely to adhere to the coupon surface- consistent with the other studies. They also found that droplets that impacted a rougher surface were more likely to stick.

The findings from these studies [11, 12, 16, 17, 18] are consistent with each other, and provide some useful insights into the dynamics of volcanic ash deposition on the NGV surfaces within the engine. However these studies have a series of drawbacks which mean further work is required.

The first of these shortcomings, as noted by Pearson and Brooker [17], is that the ash particles in the studies detailed previously generally impact the metal targets at lower velocities and temperatures than ash particles within the engine impact the NGV surfaces. It should also be noted that the range of particle diameters used in all these studies extend beyond the largest ash particle diameter ($\approx 25 \mu\text{m}$) found within the compressor of gas turbine engines that have been stripped down after exposure to volcanic ash [19]. This disparity in the impact conditions of the ash particles within the jet engine to those in the previous studies means that the studies may not be accurately capturing the same physics that governs the impact dynamics of volcanic ash impacting the NGVs. In other words, the experiments within [11, 12, 16, 17, 18] may not be well ‘scaled’ to the ash impacts on the NGVs. This means that the observations and conclusions reached by the authors of the previous studies may not apply to the case of ash impacting the NGVs.

The studies of [11, 12, 16, 17, 18] also only consider two outcomes for when a volcanic ash droplet impacts the NGV, does the droplet adhere to the surface or does it bounce off? It is well understood within the literature on droplet impact physics that there are many other potential outcomes from a droplet impacting a surface, such as prompt splash, corona splash, or partial rebound etc. These have not been considered in the work of [11, 12, 16, 17, 18], but if a significant proportion of the impacting ash droplets do splash on impact- this would have important ramifications for the accumulation rate of ash on the NGV. Therefore, to better refine values for the accumulation factor it is necessary to understand whether or not, and how much ash may splash on impact with the NGV.

The final major shortcoming of the studies conducted by [11, 12, 16, 17, 18] is that they

do not use their results to demonstrate how and where ash deposits would accumulate on the NGV. Previous research has characterized the ash impact properties on the NGV [20], revealing the distribution of impacting particle sizes, angles, and velocities along the NGV surface. This variation in ash impact properties along the NGV surface may result in different levels of ash deposition on various sections of the NGV. This, once again, could have significant implications for the accumulation factor and the safe threshold of volcanic ash exposure for gas turbine engines. A more comprehensive study would require applying an understanding of the physics governing ash impacts on the NGV to predict the ash deposition patterns on the NGV surfaces.

1.3 Aims and Objectives

The aim of this thesis is to develop an understanding of the physics that governs the impact dynamics of volcanic ash particles on the NGV surfaces by conducting scaled droplet impact experiments. The insights gained from these experiments will then be used to predict ash deposition patterns on the NGV surface.

In addressing these aims 3 questions were identified to be answered by this work.

1.3.1 What dimensionless numbers are important in controlling the stick/splash/bounce outcome of the ash droplet - NGV interaction?

One objective of this research is to design and conduct droplet impact experiments that accurately represent the impacts of ash on NGV surfaces. This will be achieved by calculating dimensionless numbers associated with the volcanic ash droplet impacts. Dimensionless numbers are combinations of droplet impact properties (such as velocity, density, surface tension, viscosity, and diameter) that represent ratios of forces experienced by the impacting droplets. In this study, the most critical dimensionless numbers controlling the droplet impact outcome will be identified, along with other properties (such as impact angle) that influence various droplet impact outcomes. This approach enables the design of experiments using analogous fluids that are well-scaled to the case of ash impacting on the NGV. By ensuring that the droplet impacts in the experiments occupy the same region of dimensionless

number space as the ash impacts on the NGV, the experiments can accurately simulate the ash impact conditions.

1.3.2 What are the values of the dimensional impact properties and the dimensionless numbers associated with the ash droplet - NGV interaction?

To comprehend the physics involved in the dynamics of ash impacting the NGV, understanding the impact conditions of the ash, such as impact velocities, angles, and temperatures, is crucial. This will be achieved through Computational Fluid Dynamics (CFD) modelling. Various engine designs will be modelled, each with different localized temperature fields around the NGVs. These temperature variations will result in differences in the impact temperatures of the volcanic ash particles. The impact properties obtained from the CFD modelling will then be used to calculate the dimensionless numbers associated with the impacting ash on the NGVs.

1.3.3 Under what conditions do ash droplets stick, splash or bounce on impact with the NGV surfaces?

This question will be addressed in this study through droplet impact experiments specifically designed to replicate the dimensionless numbers associated with ash impacts on NGV surfaces. By observing and filming the outcomes of these droplet impact experiments, insights can be gained into the behaviour of volcanic ash on NGV surfaces. Through variation of droplet properties such as diameter, viscosity, and impact velocity, different regions of dimensionless number space will be explored, aiming to identify which regions are associated with sticking, splashing, or bouncing phenomena. The results obtained from these experiments will be utilized to develop an empirical model capable of predicting the behaviour of volcanic ash particles upon impact with the NGV. This model will then be integrated with Computational Fluid Dynamics (CFD) simulations of volcanic ash particle impacts on the NGV to predict ash deposition patterns on the NGV surface for different compositions of volcanic ash.

1.4 Summary of chapters presented

The second chapter of this thesis will focus on identifying the dimensionless numbers and other dimensional properties that are crucial in determining whether a droplet splashes or adheres upon impact with a dry surface. It will describe how this was done by performing a combined statistical analysis of different published data sets.

In the third chapter, computational fluid dynamics modelling is employed to ascertain the impact properties of volcanic ash on the NGV and how these properties vary along the NGV surface. These impact properties will subsequently be used to compute the associated values of the dimensionless numbers identified in the second chapter.

Chapters 4 and 5 describe experiments and CFD simulations (respectively) of liquid droplet impacts onto dry surfaces scaled using the dimensionless numbers calculated in Chapter 3. These experiments and simulations investigate the conditions under which ash droplets might splash upon impact with the NGV surface.

Chapter 6 details the efforts made to identify dimensionless numbers capable of predicting the onset of an ash droplet bouncing off the NGV surface. The chapter further describes experimental work conducted to determine the conditions under which droplets of molten glass would bounce off a metal surface, and how the results from these experiments were used to construct an empirical model capable of predicting whether or not a molten glass droplet would bounce.

Finally, in Chapter 7, I apply the results from Chapters 4, 5, and 6 to the CFD modelling performed in Chapter 3, to predict ash deposition patterns on the NGV surface for four different ash compositions. This was carried out for four different engine designs with varying temperature fields around the NGVs. I will then conclude in Chapter 8 by evaluating the extent to which this thesis has addressed its stated aims and objectives, and discussing potential further work that could be undertaken based on this research.

Chapter 2

Understanding What Impact Properties Control Splashing.

2.1 Introduction.

One question this project seeks to answer is whether the droplets of volcanic ash splash when they impact on the Nozzle Guide Vanes (NGV) within the jet engine. In seeking to answer this question, I conducted experimental and modelling work which sought to capture the same physics that controls the dynamics of ash droplet impacts on the NGV. Before embarking on this work, it was necessary to understand what physical properties of the droplet impact are most likely to affect droplet splashing so that this behaviour could be studied. The challenge is that although droplet splashing was first studied by Professor Arthur Worthington in 1894 [21], the properties that control droplet splashing are still not fully understood.

In order to develop a more thorough understanding, I conducted a review of the literature on experiments investigating the onset of droplet splashing under various experimental conditions. Additionally, I performed a new combined statistical analysis of the data from these experiments to understand which properties, such as droplet velocity and viscosity, are most likely to affect droplet splashing.

I also used Buckingham-Pi theory to identify dimensionless numbers that are important in droplet impact dynamics. I then performed a statistical analysis of data from droplet impact experiments to determine which of the dimensionless numbers (the Reynolds, Weber, and Ohnesorge numbers which are defined later in this chapter), are most likely to affect droplet

splashing.

2.1.1 Types of splashing behaviour.

Broadly speaking the behaviour of droplet impacts can be split into two types: deposition and splashing. Deposition (as defined by Rioboo et al. [22] and consistent with the definitions of all other studies mentioned hereafter) is when a droplet on impact with a surface, remains completely in contact with the surface, and does not break up into secondary droplets but remains an intact single volume of fluid. Splashing can be broadly defined as the opposite of deposition– when a droplet on impact with a surface breaks up or doesn't remain in contact with the surface. Splashing behaviour has different types and each with different physical dynamics; they are defined as follows [22]:

1.) Prompt splashing: This is when the spreading edge of the droplet, the lamella, breaks up forming secondary droplets. This type of splashing is known to be sensitive to the surface topography.

2.) Corona splashing: This is when the lamella lifts off the surface and then breaks up into fine secondary droplets.

3.) Receding break up: This is one type of splashing that does not occur whilst the impacted droplet spreads on the surface. In a receding break up as the droplet retracts from its maximum spreading diameter, small secondary droplets are left behind. Rioboo et al. [22] found that this occurs due to the dynamic receding contact angle decreasing as the droplet retracts, and when this angle reaches 0° secondary droplets are left on the surface.

4.) Rebound and partial rebound: This is when after impact on the surface the droplet first spreads on the surface, and then recedes with enough energy for part if not all of the droplet to leave the surface.

In Fig [2.1] an image taken from Rioboo et al. [22] shows the different types of splashing behaviour.

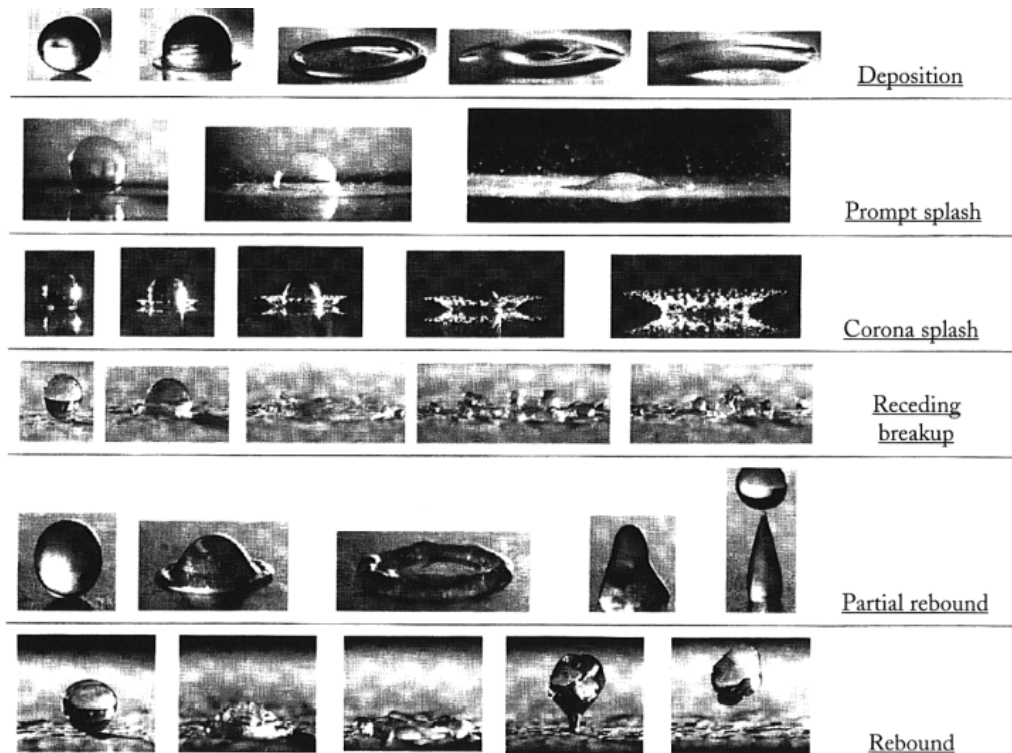


Figure 2.1: Image of various droplet impact behaviours from Rioboo et al. [22].

Many studies have looked at the effect of changing various experimental conditions on the deposition and splashing behaviour, and how changing these conditions can suppress or promote splashing behaviour. In the following I will present a review of these studies. I will discuss the observed effects of both the properties of the impacting droplet, and the properties of the surface and ambient atmosphere on the splashing behaviour.

2.1.2 Role of droplet properties.

Velocity.

In all the studies considered here increasing the velocity was found to increase the propensity for splashing behaviour. Rioboo et al. [22] found that an increase in the impact velocity of the droplet reduced the probability of a droplet just being deposited on the surface, and increased the propensity for all the other types of splashing behaviour. This is a trend consistent with all the other studies conducted in the literature. Many studies used their own data from droplet impact experiments to construct a deposition/splashing factor which took as arguments the droplet's impact conditions, if this factor was above a certain threshold then a splash was predicted to occur. The studies of Cossali et al.[23], Mundo et al. [24], Stow et al. [25],

Bai and Gosman [26], and Gavaises et al. [27] found their experimental data to be consistent with a deposition/splashing factor directly proportional to the square of the impact velocity, indicating that for a greater impact velocity a splash is a more likely outcome.

Viscosity.

The consensus of the majority of studies considered here was that increasing the viscosity of the droplet, decreases the propensity for splashing. Rioboo et al. [22] found that an increase in the viscosity reduced the probability of splashing and therefore increased the chances of deposition. The studies of Mundo et al. [24], Cossali et al. [23], and Stow et al. [25] found their experimental data to be consistent with a splashing factor inversely proportional to the droplet viscosity, indicating that for a greater droplet viscosity a splash is a less likely outcome. However, Vander val et al. [28] found that for a Reynold's number of over 2000, increasing viscosity encouraged splashing to occur. Almohammadi and Amirfazil [29] found that the deposition/splashing threshold had a non-monotonic relationship with the kinematic viscosity of the droplet, and that increasing the viscosity from $1 \times 10^{-6} \text{ m}^2\text{s}^{-1}$ - $5 \times 10^{-6} \text{ m}^2\text{s}^{-1}$ corresponded to an increase in splashing, but with an increase of viscosity above $5 \times 10^{-6} \text{ m}^2\text{s}^{-1}$ suppressing splashing. Most studies suggest that greater viscosity reduces splashing, although this isn't universally observed.

Surface Tension.

In all the studies considered, decreasing the surface tension was found to increase the propensity for prompt and corona splashing behaviour. Rioboo et al. [22] found that an increase in the surface tension suppresses the prompt and corona splash, but encourages the complete and partial rebound, and the receding breakup splash types. Cossali et al. [23], Mundo et al. [24], Stow et al. [25], Bai and Gosman [26], and Gavaises et al. [27] found their data to be consistent with splashing factors inversely proportional to the surface tension, with splashing more likely to occur with a decrease in the surface tension. This is consistent also with the studies of Range et al. [30] and Vander et al. [28] who hypothesised that a lower surface tension means that the lamella of the spreading droplet is more likely to disintegrate into secondary droplets.

Density and Diameter.

Rioboo et al. [22] found that an increase in the droplet size suppressed deposition and encouraged the prompt splash. This is also consistent with the results of Cossali et al. [23], Mundo et al. [24], Stow et al. [25], Bai and Gosman [26], and Gavaises et al. [27] whose splashing factors were proportional to the diameter of the droplet.

These studies also suggest that an increase in the density of the droplet also suppresses deposition and encourages the prompt splash, though the influence of the droplet density was not investigated by Rioboo et al. [22].

2.1.3 Role of surface and ambient properties.

Gas Pressure and Density.

In the studies considered here, it was generally found that increasing the gas pressure suppresses droplet splashing. Xu et al. [31] found that by reducing the surrounding air pressure while keeping all other parameters constant, they could suppress splashing. This result was also found by Hao et al. [32]. Burzynski and Bansmer [33] found that the density of the surrounding gas determines the dynamics of the spreading phase of the lamella, which is important in determining whether splashing occurs or not. Increasing the pressure of a gas leads to an increase in gas density, as described by the ideal gas law [34]:

$$\rho_g = \frac{PM}{RT}. \quad (2.1)$$

Here, ρ_g , M , P , and T represent gas density, gas molar mass, pressure, and temperature, respectively, and R is the gas constant. Eqn [2.1] demonstrates that gas pressure is directly proportional to gas density. The effect of lowering gas density (and subsequently pressure) was also found by Guo, Lian, and Sussman [35], who performed simulations looking at drop impingement and splashing on both dry and wet surfaces at impact velocities greater than 50 ms^{-1} . They found that by lowering the ambient gas density, they could suppress dry surface splashing. Additionally, they found that increasing gas density led to the production of more secondary droplets through the breakup of the lamella.

Surface Roughness.

The consensus in the literature is that increasing surface roughness decreases the likelihood of deposition and the corona splash and increases the likelihood of the prompt splash. Rio-boo et al. [22] found that an increase in surface roughness promotes prompt splashing and suppresses corona splashing, as surface roughness perturbs the spreading lamella, leading to its breakup. This finding is supported by studies like those of Zhang et al. [36] and de Goede et al. [37], who found that above a certain value of roughness, corona splashing could be suppressed, leading to the occurrence of prompt splashing. However, the perturbation of the lamella by surface roughness cannot fully explain prompt splashing, as prompt micro-splashing has been observed on a smooth glass surface by Thoroddsen et al. [38].

The roughness of a surface can be described in different ways, and it is important to understand the differences between them here, as different studies in the literature use different definitions and find relations between the deposition/splashing threshold and these measurements of surface roughness. The arithmetic average of the absolute deviations of all profile heights from the mean line of the surface is called R_a , or the roughness amplitude; R_{sm} is the mean width of a profile element - representing the average width of peaks along the surface profile, and R_{pk} is the average height of peaks above the roughness core profile.

Stow and Hadfield [25] found that their splashing threshold changes as a function of roughness amplitude, with an increase in roughness lowering the splashing threshold and, therefore, encouraging the prompt splash. However, they did not define the function by which the splashing threshold changes with R_a . Wu et al. [39] hypothesized that for small values of the Ohnesorge number, there exists a critical Weber number proportional to the logarithm of the inverse of R_a , above which splashing occurs. The experimental data of Range et al. [30] supported the hypothesis of Wu et al. [39], again supporting the observations that an increase in roughness promotes prompt splashing. Roisman et al. [40] conducted a large experiment involving droplets of three fluids on six different surfaces. They found that the characteristic slope of the substrate morphology, defined as $\frac{R_{pk}}{R_{sm}}$, was an important parameter in defining the deposition-to-prompt splash threshold, with an increase in magnitude of the slope causing an increase in the propensity for prompt splashing. They found the models of Stow et al. [25] to be inconsistent with their data and developed an average deposition/splashing threshold as a function of the characteristic slope. There seems to be a

broad consensus in the literature on the effect of surface roughness, but no universal model to describe the effect of surface roughness on the deposition/splashing threshold.

Impact Angle.

The effect of the angle at which the droplet hits the target (known as the impact angle) has been found to both promote and suppress splashing. Hao et al. [32] impacted droplets onto smooth surfaces for a range of impact angles and observed that droplet splashing can be entirely suppressed by making the droplet impacts more oblique. However, Bird et al. [41], performing experiments using droplets of ethanol over a range of impact angles, found that the tangential component of impact, which is greater for more oblique droplet impacts, can act to promote or suppress a splash. They observed three types of behaviour:

- 1.) The lamella would spread in all directions.
- 2.) Both sides of the droplet would splash.
- 3.) Asymmetric splashing would occur, with one side of the droplet splashing and the other not.

Surface Wettability.

The effect of the surface wettability on the splashing threshold is complex and previous studies have not shown a simple effect. Wettability refers to the ability of a liquid to spread or adhere to a solid surface. It is typically characterised by the contact angle formed between the liquid droplet and the surface. A contact angle of 0° indicates complete wetting (perfect adhesion), while a contact angle of 180° indicates complete non-wetting (no adhesion). Intermediate contact angles represent varying degrees of wettability. A hydrophobic surface is defined as when the contact angle is $> 90^\circ$, and a hydrophilic surface when the contact angle is $< 90^\circ$ [42].

The studies of Roisman et al. [40] and Latka et al. [43] which looked at surfaces with a range of contact angles, $19^\circ - 133^\circ$ and $0^\circ - 90^\circ$ found that the splashing threshold was independent of the surface wettability. However a range of studies have found that hydrophobic surfaces promote splashing, Aboud and Kietzig [44], and Zhang et al. [45] found that increasing the contact angle promoted the corona splash. Rioboo et al. [22] found also that increasing the value of the contact angle promotes the receding break-up and the partial and

complete rebound, but they did not find any effect of the contact angle on the prompt and corona splash.

2.1.4 Dimensionless numbers.

It is possible to combine these droplet impact properties into quantities known as dimensionless numbers. Dimensionless numbers represent combinations of dimensional properties, typically taking the form of ratios of forces. For example the Bond number is a dimensionless number of the form [46]:

$$Bo = \frac{\text{Gravitational force}}{\text{Surface tension force}} = \frac{\rho D^2 g}{\sigma}. \quad (2.2)$$

Here ρ [kg m^{-3}], σ [N m^{-1}] and D [m] are the droplet density, surface tension and diameter respectively, and g [ms^{-2}] is the acceleration due to gravity. The Bond number is often used to characterise the relative importance of gravitational to surface tension forces within a fluid system, such as a liquid droplet, or bubbles in a foam. Dimensionless numbers can also enable the design of ‘scaled’ experiments. In the context of this study, ash droplets impact surfaces within the jet engine at high velocities, viscosities, and temperatures. Replicating the exact jet engine environment in a laboratory setting is non-trivial. However, by calculating the dimensionless numbers associated with ash droplet impacts, we can design droplet impact experiments in the laboratory that are technically feasible. Ensuring these experiments share the same dimensionless numbers allows us to capture similar impact dynamics and physics as those observed in the jet engine. It is necessary to work out which dimensionless numbers need to be scaled for before embarking on any experiments.

In determining the dimensionless numbers to be considered the Buckingham-Pi theory was used. This theory was first proved by the mathematician Joseph Bertrand, though it was named after the physicist Edgar Buckingham. This theory states that for a set of m physical variables (such as velocity, pressure, or volume) a meaningful equation involving these can be written in terms of a group of $p = m - k$ unique dimensionless numbers made up of these physical variables [47]. Here k is the number of physical dimensions across the variables (such as length, mass or temperature). The theory provides a method for finding these dimensionless numbers, and it was this method that was used here to calculate the dimensionless groups of interest.

The first group of variables considered were: the velocity v , the droplet diameter D , the viscosity μ , the acceleration due to gravity g , the droplet density ρ , the surface tension of the droplet σ , the temperature of the droplet T_d , the bulk modulus G , and the temperature of the environment, T_∞ . The fundamental units of these variables are shown in Table 9.1 in the appendix to this thesis. Using these variables 7 Pi groups of interest were found ($\Pi_1 - \Pi_7$) and are displayed in the table below.

Table 2.1. The dimensionless groups ($\Pi_1 - \Pi_7$).

Π_i	Equation
Π_1	$\frac{\sigma}{GD}$
Π_2	$\frac{\mu^2 g}{\sigma G}$
Π_3	$\frac{Dg\rho}{G}$
Π_4	$\frac{T_d}{T_\infty}$
Π_5	$\frac{\mu v}{GD}$
Π_6	$\frac{\rho v^2 D}{\sigma}$
Π_7	$\frac{\rho v D}{\mu}$

From these Pi groups Π_7 was found to be equal to the Reynolds number, and Π_6 was equal to the Weber number. It was found that $\frac{\Pi_5}{\Pi_1}$ was equal to the Capillary number, and $(\frac{\Pi_2}{\Pi_3})^{\frac{1}{2}}$ is equal to the Ohnesorge number. The final dimensionless group was found to be a trivial ratio of the two temperatures. These four named dimensionless numbers: Ohnesorge, Weber, Capillary, and Reynolds number are found to be used in the literature to describe the different behaviours of droplets impacting solid substrates. These numbers are defined as: the Reynolds number

$$Re = \frac{\rho v_c D}{\mu}, \quad (2.3)$$

which is a ratio of inertial to viscous forces within the droplet, the Weber number,

$$We = \frac{\rho v^2 D}{\sigma}, \quad (2.4)$$

which is a ratio of inertial to surface tension forces within the droplet. Also, the Ohnesorge number, which is a ratio of the elastic to viscous forces in the droplet

$$Oh = \frac{\mu}{\sqrt{\rho\sigma D}}, \quad (2.5)$$

and finally the Capillary number, which is a ratio of surface tension to viscous forces,

$$Ca = \frac{\mu v_c}{\sigma}. \quad (2.6)$$

Here v_c is a characteristic spreading velocity of the droplet, and all other symbols retain their previously defined meaning.

Schiaffino and Sonin [48] studied deposition of molten metal droplets at low Weber numbers on a smooth flat surface. They found that the spreading of the droplets on impact is governed primarily by the Weber and Ohnesorge numbers. They found that the Weber number scales the driving force of the droplet's spreading on the surface, and the Ohnesorge number scales the force that resists the spreading. They found that within the Weber-Ohnesorge number plane there are 4 asymptotic regions where the droplet's spreading velocity and spreading time-scale have particular and distinct forms. These regions and the corresponding spreading velocities and timescales are shown in Fig [2.2] and Table 2.2.

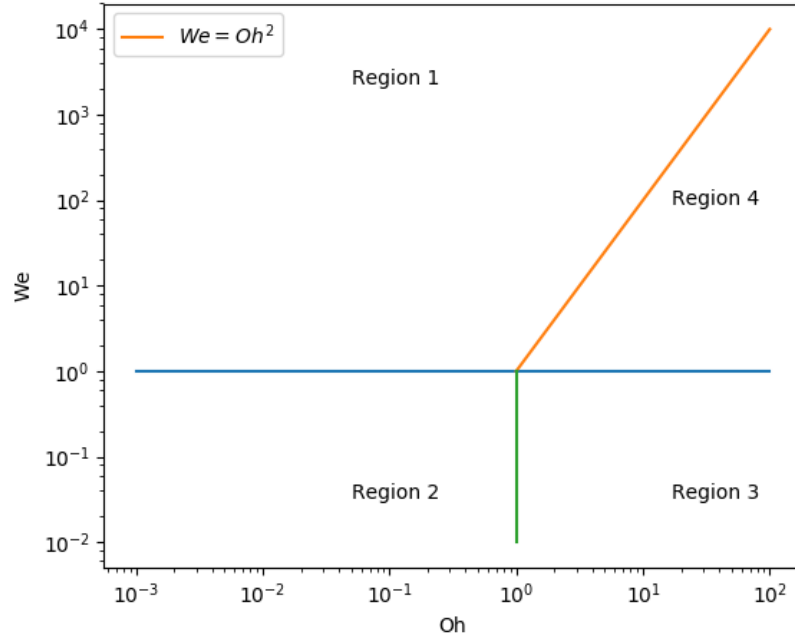


Figure 2.2: Reproduction of a figure from Schiaffino and Sonin [48] illustrating the four asymptotic regions in the Weber-Ohnesorge number plane. These regions define the dominant spreading behaviours of droplets upon impact, characterized by distinct combinations of impact pressure, capillarity, and viscous resistance. The diagram is used to identify the regimes where inertial, capillary, and viscous forces govern droplet dynamics.

Table 2.2. This is a reproduction of a table from Schiaffino and Sonin [48] detailing the four limits and their characteristics.

Region	Condition 1	Condition 2	Spreading Velocity	Driving force	Resistance
1	$We \gg 1$	$Oh \ll \sqrt{We}$	v	Impact pressure	Inertia
2	$We \ll 1$	$Oh \ll 1$	$\sqrt{\frac{\sigma}{D\rho}}$	Capillarity	Inertia
3	$We \ll 1$	$Oh \gg 1$	$\frac{\sigma}{\mu}$	Capillarity	Viscosity
4	$We \gg 1$	$Oh \gg \sqrt{We}$	$\frac{\rho v^2 D}{\mu}$	Impact pressure	Viscosity

In region 1 they find that the spreading is driven by the dynamic pressure of impact and

resisted by the droplet's inertia, in region 2 they find that the impact velocity is negligible on the droplet's spreading and that it is driven by the capillarity force imbalance at the contact line and is resisted again by the droplet's inertia. In region 3 the spreading is driven by the capillarity force and resisted by the viscosity of the droplet. In region 4 the spreading is driven by the dynamic pressure of the impact and resisted by the viscous shear.

It should be noted that some properties discussed here are not easy to scale for in experiments, as they cannot be combined into dimensionless numbers with the other properties. An example of this would be surface roughness. It is important to understand if these properties can be safely neglected in any scaled experiments or not. It is therefore necessary to understand which of the various droplet and surface properties are most likely to affect the splashing outcome.

It also is not possible to design experiments that can scale for all of the dimensionless numbers identified here, at the same time. It is therefore necessary again to understand which of the various dimensionless numbers are most likely to affect the splashing outcome. In the rest of this chapter, I will describe how I used Generalized Linear Models to analyse data from the literature to find which droplet and surface properties are most important in affecting the splashing outcome, and which dimensionless numbers are most influential in controlling the splashing outcome.

2.2 Method.

2.2.1 Generalized Linear Models.

In the general linear model some continuous response variable, y , is modelled as a linear combination of n explanatory variables or covariates as

$$\mathbf{y} = \mathbf{X}\beta + \mathbf{e}. \quad (2.7)$$

Here β is a set of parameters which are called linear prediction coefficients, \mathbf{X} are the explanatory variables and \mathbf{e} is a Gaussian random error [49].

A generalized linear model can not just model a continuous variable y with a Gaussian distribution, but also allows one to model non-normal random variables, including discrete variables (such as counts or 'yes/no' responses) by using what is known as a link function.

Overall, a generalized linear model has three components:

- 1.) Response variables, Y_1, \dots, Y_n , which are assumed to have the same distribution from the exponential family.
- 2.) A set of parameters β , and a set of explanatory variables:

$$\mathbf{X} = \begin{bmatrix} \mathbf{x}_1^T \\ \mathbf{x}_2^T \\ \vdots \\ \mathbf{x}_n^T \end{bmatrix} = \begin{bmatrix} x_{1,1} & \dots & x_{1,p} \\ \vdots & & \vdots \\ x_{n,1} & & x_{n,p} \end{bmatrix}. \quad (2.8)$$

In our case the explanatory variables are the droplet impact conditions such as velocity, droplet density and viscosity.

- 3.) A monotone link function which is defined as:

$$g(\mu_i) = \mathbf{x}_i^T \beta, \quad (2.9)$$

and which expresses a parameter of a non-normal distribution, e.g. the probability of a discrete event with a Binomial distribution, in terms of the covariates in \mathbf{X} and where

$$\mu_i = E(Y_i). \quad (2.10)$$

Here I am only concerned with one response variable (does an impacting droplet splash or not). The response variable was taken to be distributed as a binomial response variable with $y \in [0, 1]$. In my work the link function used was the logit of the probability of a splash occurring, where p is the probability and

$$g(p) = \text{logit}(p) = \log\left(\frac{p}{1-p}\right). \quad (2.11)$$

In the generalized linear model above the Gaussian error is a simple independent random variable. Where the observations to be modelled have some structure of dependency, such that certain subsets (in this case, groups of observations drawn from the same study) are likely to be correlated to some extent, this is handled by using a generalized linear mixed model (GLMM). Generalized linear mixed models allow us to model the correlation between observations within different data sets together as mixed models. This is done by including random effects in the linear predictor which allows for the possibility that there is some correlation between observations from the same study [49].

When the generalized linear model is built, the probability of a given droplet splashing can be found by inputting the corresponding values of the explanatory variables into the model as follows:

$$\text{logit}(p) = (\beta_1 \times \text{velocity}_{\text{droplet}}) + (\beta_2 \times \text{Diameter}_{\text{droplet}}) + \dots \quad (2.12)$$

Here the parameters $\beta_{1\dots p}$ are the set of parameters corresponding to the different explanatory variables in the model. The probability (p) of the given droplet splashing can be calculated by taking the inverse of the logit function, where if $y = \text{logit}(p)$:

$$p = \frac{1}{1 + e^{-y}}. \quad (2.13)$$

2.2.2 Analysis of droplet and surface properties.

Combining the data from Vander et al. [28], Palacios et al. [50], and Roisman et al. [40], linear mixed models were constructed with the impact velocity, droplet viscosity, droplet density, droplet surface tension and droplet diameter as explanatory variables. These data sets were chosen as it was possible to extract these specific droplet impact properties for each splashing/non-splashing observation. In order to rank the influence of the different variables in distinguishing between splashing and non-splashing events, the variables were added as sole explanatory variables in the GLMM and the corresponding reduction in deviance from the null model was recorded. An algorithm was used in **R** to calculate the set of parameters corresponding to the explanatory variables added to the GLMM, and the corresponding P -values for the respective explanatory variables and the deviance of the model. The deviance is a way of measuring the goodness of fit of a model to the data and is used for GLMs. It can be thought of as a way of quantifying how much variation in the data is accounted for in the model with a lower value of the deviance indicating a better fit of the model to the data. If a predictor variable is added to a GLMM or GLM then the deviance is expected to become smaller. The evidence that a predictor, x_i , improves the model is assessed by computing the probability of obtaining a deviance reduction as large as observed, or larger, under the null hypothesis that the corresponding predictor coefficient $\beta_i = 0$. This probability is called the P -value.

After the variables had been added one at a time, explanatory variables were sequentially added to the model, beginning with velocity, followed by velocity combined with viscosity,

and so on. The same algorithm was applied in R to compute the set of parameters corresponding to the added explanatory variables in the Generalized Linear Mixed Model (GLMM), along with their respective P -values and the deviance of the model. This analysis is important and separate to what is discussed previously. In a Generalized Linear Model (GLM), adding an explanatory variable—such as viscosity—individually to the model may lead to a reduction in deviance. However, when viscosity is added to a model that already includes another variable, such as velocity, and the associated P -value for viscosity is $P > 0.05$ it suggests that viscosity does not contribute significant additional information to the model beyond what is provided by the velocity.

When adding variables as predictors to a GLM or GLMM with different scales, it is necessary to standardize the variables so that they span similar ranges. To achieve this, each set of variables, such as velocity and viscosity, underwent standardization. Specifically, each value of the variable in the dataset used to construct the model was divided by the largest value of that variable in the dataset. For example, all values of the velocity in a dataset were divided by the largest value of velocity within that dataset. This was done for all variables considered.

One potential problem with calculating the P -value of successive explanatory variables added into the GLMs and comparing it to a threshold value of $P_{\text{threshold}} = 0.05$, is that this testing of multiple hypotheses can potentially lead to the false discovery of effects in the data which do not have the level of statistical evidence implied by $P < 0.05$. This is introduced and explained in greater detail by Lark [51]. A more robust approach to analyse the P -values is that proposed by Foster and Stine [52] which is called α investment. They show that this method allows for control of the false-discovery rate (FDR) in testing the various models sequentially, by comparing the P -values to a changing threshold α_i . For a given succession of P -values (like those calculated in Table 2.3 and Table 2.4) if $P_i < \alpha_i$, then $\alpha_{i+1} > \alpha_i$. However, if $P_i > \alpha_i$, then $\alpha_{i+1} < \alpha_i$. I used the expression for α_i as detailed by Lark [51] to control the FDR at 0.05. Any variable for which $P_i > \alpha_i$ was removed, rejected and not included as an explanatory variable in any subsequent models.

The data from Roisman et al. [40] contained many more variables than those found in Vander et al. [28], and Palacios et al. [50], including variables such as the surface roughness. I took the data set from Roisman et al [40] and applied the same methodology as described

in the above, however using this time a GLM not a GLMM, as I was considering data only from one set of experiments.

2.2.3 Analysis of dimensionless numbers.

So far I have discussed how changing the various parameters that describe the physical state of the droplet and the substrate, one can change the impact behaviour of the droplet. Many studies have used the dimensionless numbers described previously to try and discriminate between deposition and splashing behaviour. I took data for splashing and deposition and the respective dimensionless numbers from Mundo et al. [24], Stow et al. [25], Vander et al. [28], Roisman et al. [40], Palacios et al. [50], Yang et al. [53] and Pan et al. [54] and used the same methodology of building GLMMs as before.

In order to rank the influence of the different dimensionless numbers in distinguishing between splashing and non-splashing events in the data from Mundo et al. [24], Stow et al. [25], Vander et al. [28], Roisman et al. [40], Palacios et al. [50], Yang et al. [53] and Pan et al. [54], I added them as sole explanatory variables in the models and recorded the corresponding reduction in deviance from the null model.

In the final predictive model, the dimensionless numbers were added one-by-one, and the respective deviance and P -values were recorded.

2.3 Results.

2.3.1 Results from analysis of droplet and surface properties.

I will first present the results from the analysis using a mixed model of the data from Vander et al. [28], Palacios et al. [50], and Roisman et al. [40], looking at the influence of the impact velocity, droplet viscosity, droplet density, droplet surface tension and droplet diameter, on the splashing outcome.

In Fig [2.3] one can see the respective change in deviance from the null model, for the different variables, namely: impact velocity, droplet viscosity, droplet density, droplet surface tension and droplet diameter, as sole variables in the models.

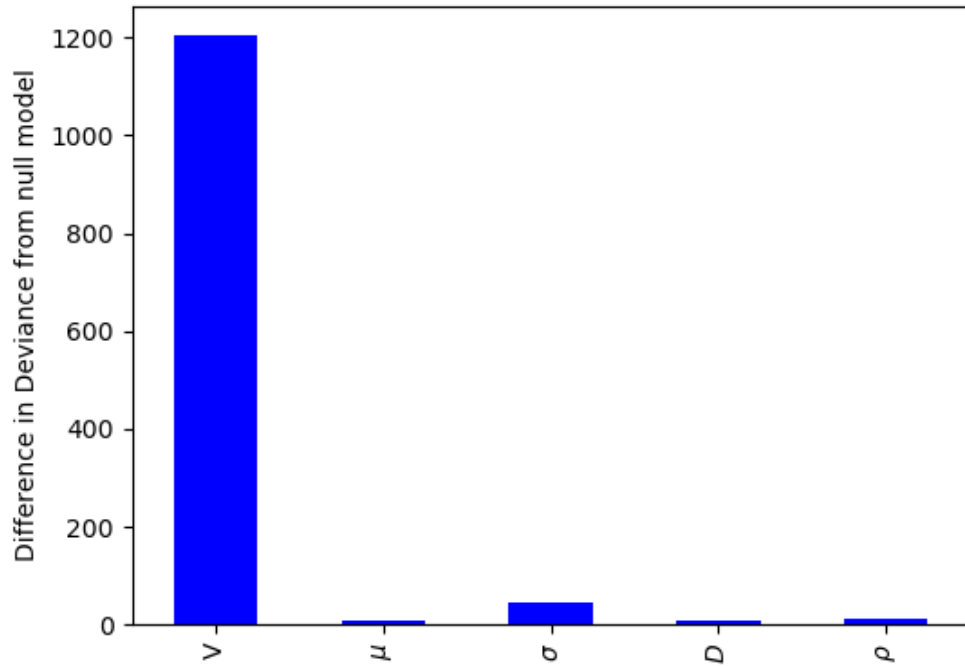


Figure 2.3: Plot illustrating the change in deviance from the Null model for various models with individual explanatory variables: impact velocity, droplet viscosity, droplet density, droplet surface tension, and droplet diameter.

As can be seen in Fig [2.3], a model with just velocity as a sole explanatory variable achieves the biggest reduction in deviance with respect to the Null model followed by the surface tension, the droplet density, the droplet diameter and the droplet viscosity. This would suggest that the velocity is by far the most influential parameter in whether or not a droplet will splash on impact, with the other variables having far less influence, and viscosity being the least influential parameter. This is an interesting result and could maybe explain the ambiguity found in the literature on the effect of viscosity on the deposition/splashing threshold, given that viscosity does not greatly influence the outcome for the data we have considered here.

The various droplet properties were then added in sequence, starting with the velocity, to the final GLMM. Other explanatory variables were added to the model one by one and the corresponding *P*-values and change in deviance was recorded.

Table 2.3. Mixed generalized linear models for data from Vander et al. [28], Roisman et al. [40] and Palacios et al. [50].

Variables in GLMM	Deviance	P -value for the newest variable
Null Model	4144.9	-
V	2939.7	$2e-16$
V+ μ	2939.7	0.279
V+ σ	2836.4	$2e-16$
V+ σ +D	2804.0	$1.38e-8$
V+ σ +D+ ρ	2798.4	$2.06e-2$

As described earlier, the false discovery rate was controlled with alpha investment. Below in Fig [2.4] can be seen a plot showing the P -values associated with each new variable added to the GLMM, alongside the corresponding α_i variables.

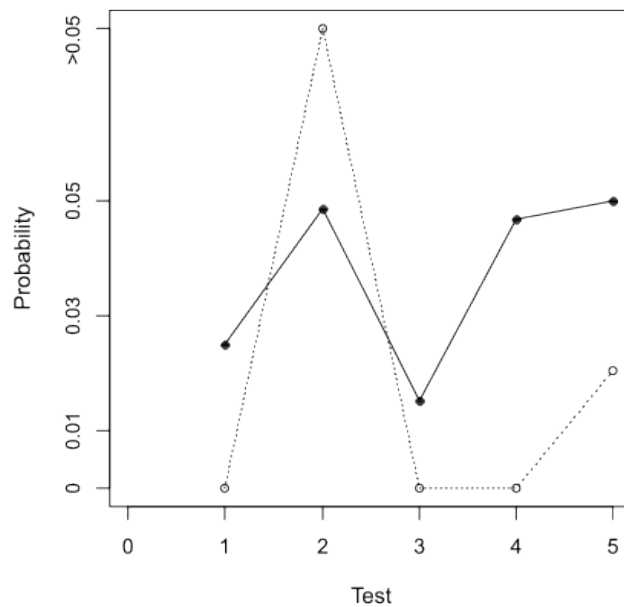


Figure 2.4: This figure shows the P -values from Table 2.3 (indicated by the open markers), and the corresponding α_i values (indicated by the filled markers).

As can be seen in Table 2.3, the viscosity has a P -value of $P = 0.279$ which is greater than the corresponding α_i value as seen in Fig [2.4]. This means that viscosity does not add any more information to the model in which the velocity is an explanatory variable. Below Fig [2.5] shows the changing deviance with the addition of new explanatory variables to the GLMM.

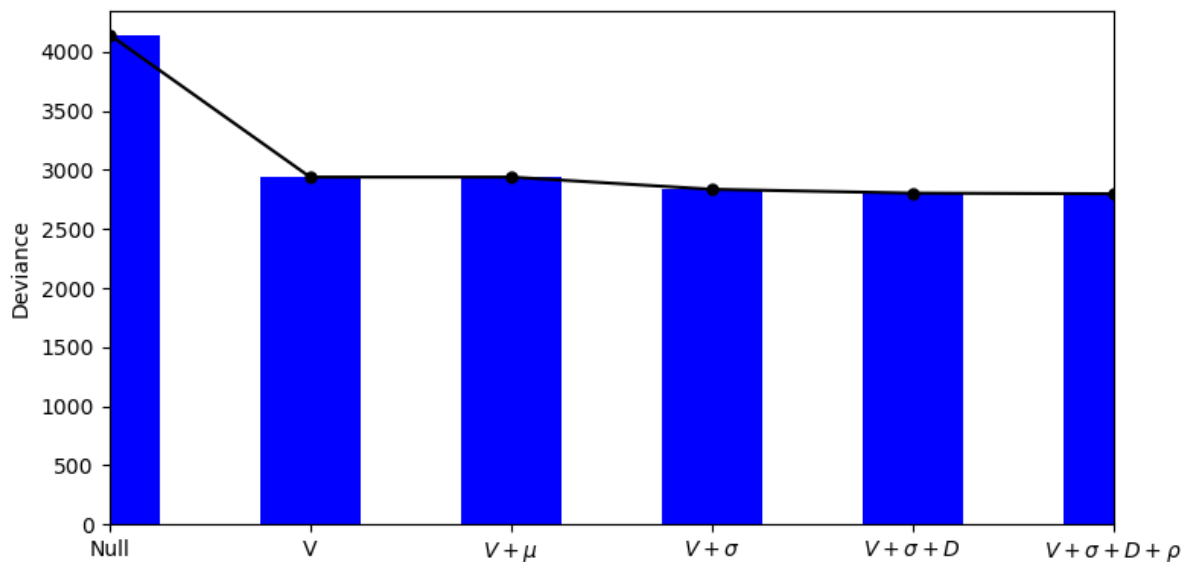


Figure 2.5: This figure shows the change in deviance with the addition of a new explanatory variables, added in sequence to the GLMM. It can be seen that with a model containing the velocity, subsequent explanatory variables do not lead to as a significant reduction to the deviance.

In Fig [2.6] below a histogram for the fitted probabilities for splashing is shown for the final GLMM model from Table 2.3. The data from Vander et al. [28], Palacios et al. [50], and Roisman et al. [40] was inputted into the model. It was found that the fitted probabilities from the final GLMM are distributed more towards 1 for splashing events, and more towards 0 for non-splashing events. However, it can be seen that the final GLMM is not perfectly distinguishing between splashing and non-splashing events as some non-splashing events have associated fitted probabilities of splashing greater than 0.8, and some fitted probabilities being less than 0.5 for splashing events.

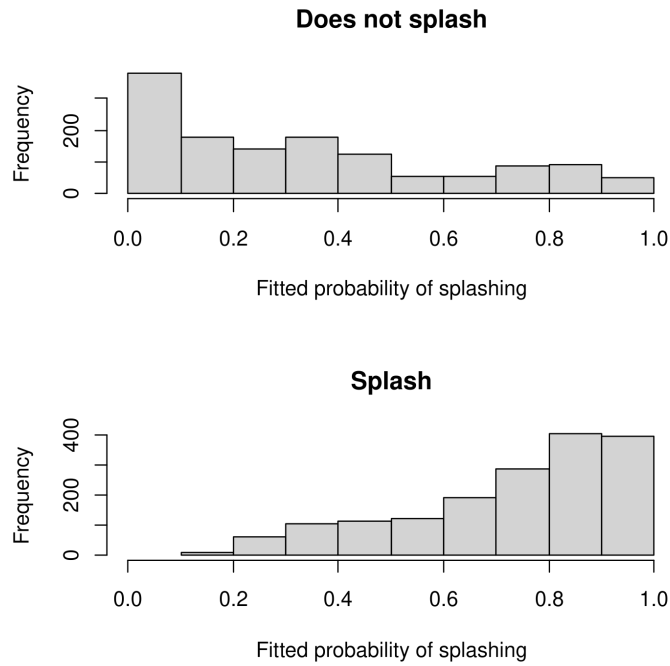


Figure 2.6: This figure shows the histograms for the fitted probabilities calculated from the final GLMM in Table 2.3 for splashing and non-splashing events.

I will now present the results of the analysis of just the Roisman 2015 [40] data using a GLM. In Fig [2.7] one can see the respective change in deviance from the null model, for the different variables, namely: impact velocity, droplet viscosity, droplet density, droplet surface tension, droplet diameter, the slope of the substrate morphology and the advancing contact angle added as sole variables in the models.

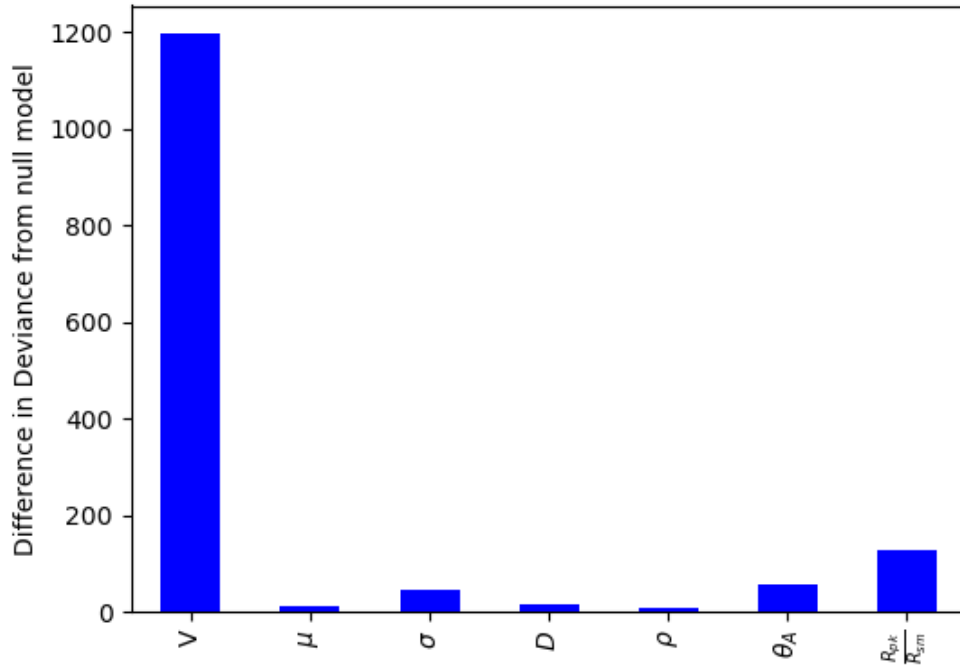


Figure 2.7: This figure shows the change in deviance with respect to the Null model for models with the explanatory variables (impact velocity, droplet viscosity, droplet density, droplet surface tension, droplet diameter, the slope of the substrate morphology and the advancing contact angle) as sole variables. It can be seen that the model containing the velocity causes the largest reduction in the deviance, with a model containing just the density-achieving the smallest reduction in the deviance.

As can be seen in Fig [2.7], a model with just velocity as a sole explanatory variable achieves the biggest reduction in deviance with respect to the Null model, followed by the slope of the substrate morphology, the advancing contact angle, the surface tension, the droplet diameter the droplet viscosity and then the droplet density. This is a very interesting result, as it suggests that after the droplet impact velocity the two next most influential parameters in affecting whether a droplet splashes or not are the properties of the substrate. However, it can be seen that overwhelmingly, velocity is the most influential parameter in distinguishing between splashing and non-splashing events.

To build a final predictive model the explanatory variables were added to a GLM one by one and the corresponding P -values and change in deviance was recorded.

Table 2.4. Generalized linear models for data from Roisman et al. (2015).

Variables in GLM	Deviance	<i>P</i> -value for the newest variable
Null Model	3997.8	-
V	2802.8	2e-16
V+ μ	2802.8	0.287
V+ σ	2707.4	2e-16
V+ σ +D	2674.8	8.79e-9
V+ σ +D+ ρ	2670.2	3.51e-2
V+ σ +D+ ρ + θ_A	2585.7	2e-16
V+ σ +D+ ρ + θ_A + $\frac{R_{pk}}{R_{sm}}$	2337.8	2e-16

As before the false discovery rate was controlled with alpha investment. Below, in Fig [2.8], a plot showing the *P*-values associated with each new variable added to the GLM can be seen, alongside the corresponding α_i variables.

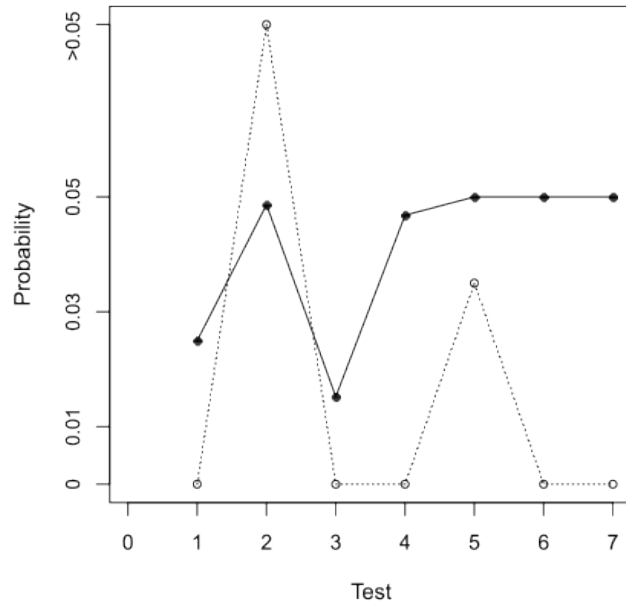


Figure 2.8: This figure shows the P -values from Table 2.4 (indicated by the open markers), and the corresponding α_i values (indicated by the filled markers).

The results in Table 2.4 show the viscosity has a P -value of $P = 0.278$ which is greater than the corresponding α_i value in Fig [2.8]. This again means that for the data available the viscosity does not add any further information to the model that already contains the velocity as an explanatory variable. Below Fig [2.9] shows the changing deviance with the addition of new explanatory variables to the GLM.

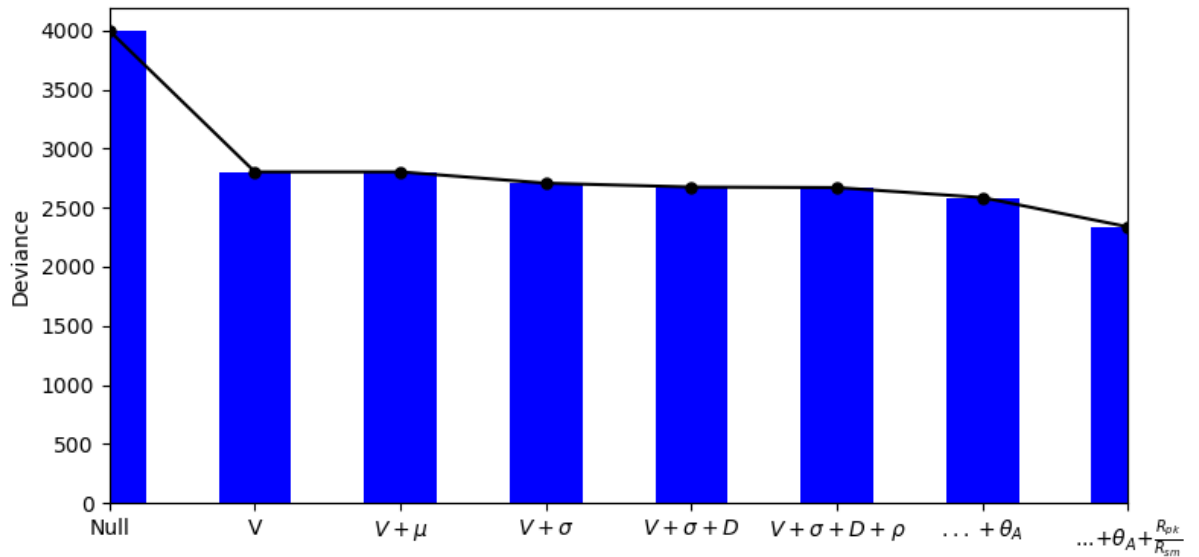


Figure 2.9: This figure shows the change in deviance with the addition of a new explanatory variables, added in sequence to the GLM. It can be seen that with a model containing the velocity, subsequent explanatory variables do not lead to as a significant reduction in the deviance, with the exception of the slope of the substrate morphology.

In Fig [2.10] histograms for the fitted probabilities for splashing are shown for the final GLM model from Table 2.4, with the data from Roisman et al [40] inputted into the model. It was found that the fitted probabilities from the final GLM are distributed more towards 1 for splashing events, and more towards 0 for non-splashing events. Again the final GLM is not perfectly distinguishing between splashing and non-splashing events as some non-splashing events have associated fitted probabilities of splashing greater than 0.8, but compared to the final model in Table 2.3 the splashing probabilities for splashing events are distributed closer to a probability of 1 and the splashing probabilities for non-splashing events are distributed closer to a probability of 0.

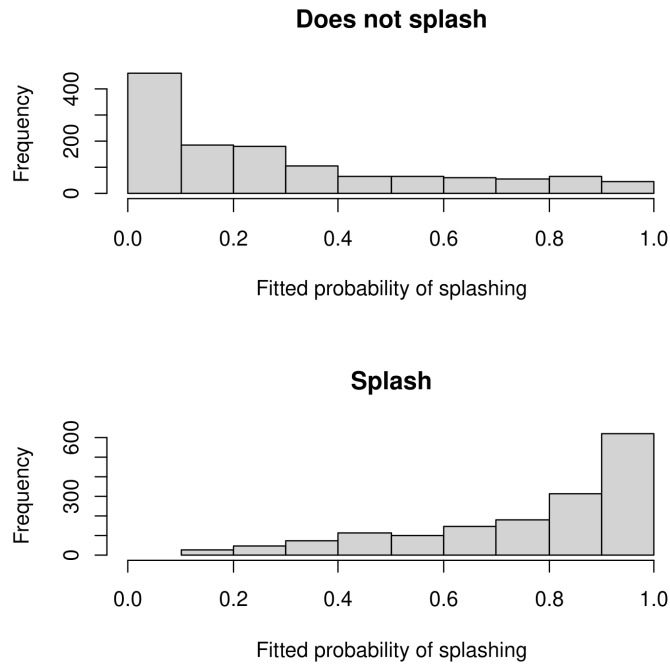


Figure 2.10: This figure shows the histograms for the fitted probabilities calculated from the final GLM in Table 2.4 for splashing and non-splashing events.

2.3.2 Results of analysis of dimensionless numbers.

I will now present the results of the analysis for the different dimensionless number in distinguishing between splashing and non-splashing events in the data from Mundo et al. [24], Stow et al. [25], Vander et al. [28], Roisman et al. [40], Palacios et al. [50], Yang et al. [53] and Pan et al. [54]. In Fig [2.11] one can see the respective change in deviance from the null model, for the different variables, namely: the Weber, Reynolds, Ohnesorge and Capillary numbers, as sole variables in the models.

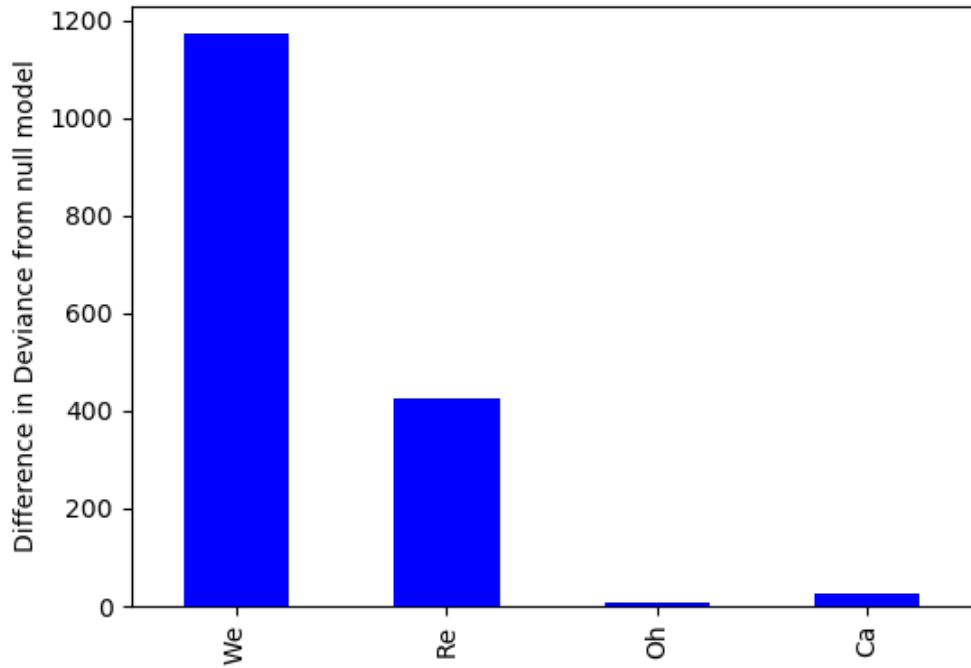


Figure 2.11: This figure shows the change in deviance with respect to the Null model for models with the explanatory variables (the Weber, Reynolds, Ohnesorge and Capillary numbers) as sole variables. It can be seen that the model containing the Weber number causes the largest reduction in the deviance, with a model containing just the Ohnesorge number-achieving the smallest reduction in the deviance.

As can be seen in Fig [2.11], adding the Weber number as a sole explanatory variable results in the largest reduction in deviance relative to the Null model, followed by the Reynolds number, the Capillary number and then finally the Ohnesorge number. This suggests that the Weber number is the most important dimensionless number in discriminating between splashing and non-splashing behaviour, with the Ohnesorge number being the least important.

To build a final predictive model the dimensionless numbers were added as explanatory variables one-by-one and the respective P -values and deviance were recorded.

Table 2.5. Generalized linear models for data from Mundo et al. [24], Stow et al. [25], Vander et al. [28], Roisman et al. [40], Palacios et al. [50], Yang et al. [53] and Pan et al. [54].

Variables in GLMM	Deviance	P -value for the newest variable
Null	4432.7	-
We	3260.7	2e-16
We+Re	3252.2	0.003
We+Re+Oh	3252.2	0.0538
We+Re+Ca	3246.1	0.016

As before the false discovery rate was controlled with alpha investment. Below, in Fig [2.12], a plot showing the P -values associated with each new variable added to the GLMM can be seen, alongside the corresponding α_i variables.

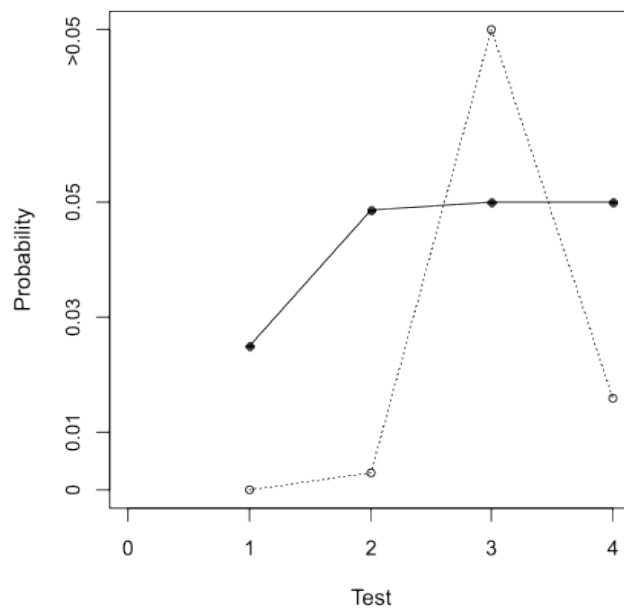


Figure 2.12: This figure shows the P -values from Table 2.3 (indicated by the open markers), and the corresponding α_i values (indicated by the filled markers).

As can be seen in Table 2.5 and Fig [2.12] by considering the P -values and the corresponding α_i values, the Ohnesorge number is found to have no statistically significant effect on whether or not a droplet splashes on impact when the Weber and Reynolds number are already considered within the model. Below Fig [2.13] shows the changing deviance with the addition of new explanatory variables to the GLMM. It can be seen in Fig [2.13] adding the Reynolds, Ohnesorge and Capillary number as explanatory variables to a model where the Weber number is already present as a variable, does not contribute significant additional information to the model beyond what is provided by the Weber number.

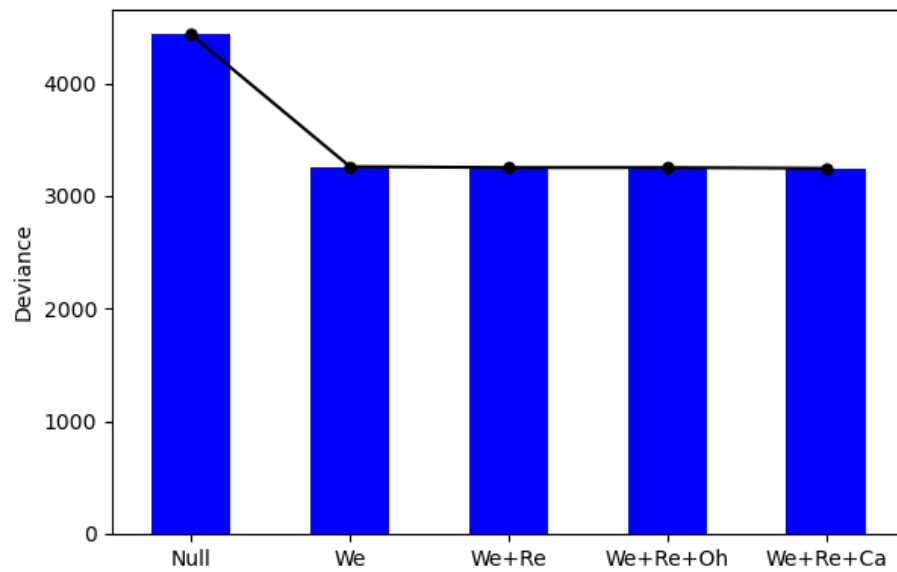


Figure 2.13: This figure shows the change in deviance with the addition of a new explanatory variable to the GLMM. It can be seen that with a model containing the Weber number, subsequent explanatory variables do not lead to a significant reduction in the deviance

In Fig [2.14] below histograms for the fitted probabilities for splashing are shown for the final GLMM model from Table 2.5, with the data from Mundo et al. [24], Stow et al. [25], Vander et al. [28], Roisman et al. [40], Palacios et al. [50], Yang et al. [53] and Pan et al. [54] inputted into the model. It was found that the fitted probabilities from the final GLMM are distributed more towards 1 for splashing events, and more towards 0 for non-splashing events. Again, as for the final models in Table 2.3 and Table 2.4 the final GLMM is not perfectly distinguishing between splashing and non-splashing events as some non-splashing events have associated fitted probabilities of splashing greater than 0.8. Compared to the final model in Table 2.4 the splashing probabilities for splashing events and non-splashing

events are more broadly distributed.

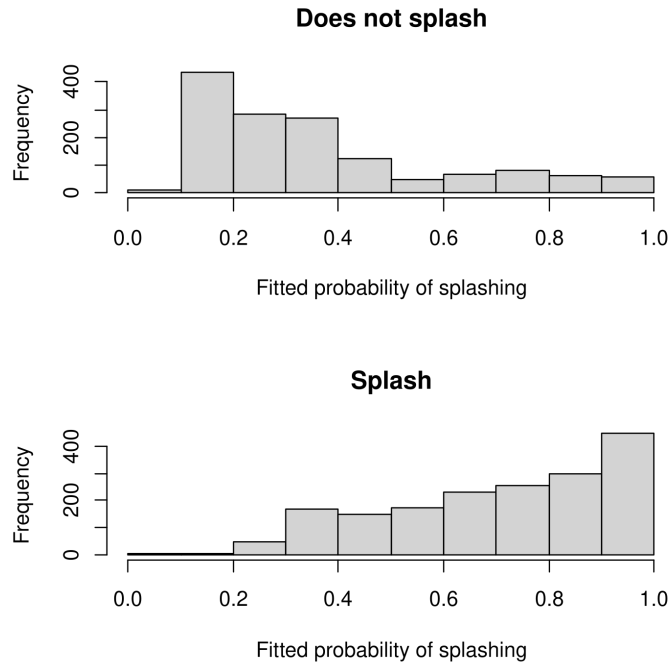


Figure 2.14: This figure shows the histograms for the fitted probabilities calculated from the final GLMM in Table 2.5 for splashing and non-splashing events.

2.4 Discussion.

2.4.1 Dimensional properties.

The results presented here indicate that the impact velocity is the most significant dimensional property, among those considered, in determining the splashing outcome of an impacting droplet. According to the analysis of the data from Vander et al. [28], Roisman et al. [40] and Palacios et al. [50], which solely focuses on droplet properties, surface tension ranks as the second most important dimensional property after velocity. However, it should be noted that the reduction in deviance associated with the null hypothesis, observed in a model containing only velocity as an explanatory variable, is far more significant than the reduction observed in a model containing only the surface tension.

According to the results found in the analysis of the data solely from Roisman et al. [40], the slope of the substrate morphology was the second most important property in determin-

ing a splashing outcome. However, again it should be noted that the reduction in deviance associated with the null hypothesis observed in a model containing only velocity as an explanatory variable, is far more significant than the reduction observed in a model containing only the slope of the substrate morphology as an explanatory variable.

The analysis of the combined data from Vander et al. [28], Roisman et al. [40] and Palacios et al. [50], and just the data from Roisman et al. [40], seems to indicate that the viscosity is the least important variable in determining the splashing outcome. For both sets of analysis, a model that already contained velocity as an explanatory variable was not ‘improved’ at all by the addition of viscosity as an additional explanatory variable.

The final predictive models, as presented in Table 2.3 and Table 2.4, demonstrate a relatively strong ability to forecast the splashing outcomes observed in the experimental data used for the model construction. Particularly, the model constructed solely from the dataset provided by Roisman et al. [40], outlined in Table 2.4, shows better predictive performance. This superiority is likely attributed to the inclusion of additional explanatory variables, such as surface properties, alongside liquid properties of the impacting droplet. Nevertheless, even this model occasionally misclassifies outcomes, assigning high probabilities of splashing to non-splashing events and vice versa. This suggests that while the variables recorded in Roisman et al. [40] contribute to droplet splashing, they may not fully explain the splashing/non-splash threshold.

2.4.2 Dimensionless properties.

In the analysis presented here, the Weber number is the most influential dimensionless number in determining the splashing outcome of an impacting droplet. The Reynolds number was identified as the second most significant dimensionless number. However, it is noteworthy that the decrease in deviance linked to the null hypothesis, observed in a model with only the Weber number as an explanatory variable, is more pronounced compared to the reduction observed in a model with only the Reynolds number. The Ohnesorge number was found to be the least influential dimensionless number. Indeed, a model which already contained the Weber number as an explanatory variable was not ‘improved’ by the addition of the Ohnesorge number as an explanatory variable.

The final predictive model, as presented in Table 2.5, which contained the Weber, Reynolds

and Capillary numbers as explanatory variables, again does a relatively good job in predicting splashing/non-splashing events observed in the experimental data used for building the model. This suggests that the dimensionless numbers identified here have significant control over the splashing outcome of an impacting droplet. However, this model still incorrectly predicts some outcomes, giving high probabilities of splashing for non-splashing events and vice versa, which suggests that the dimensionless numbers on their own cannot fully define the splashing/non-splashing threshold.

2.4.3 Designing scaled experiments.

It is clear from the results presented here that it is important for any experiments I perform to be scaled for the Weber number. However, I decided that it was also important to scale for the Ohnesorge number based on the following line of reasoning.

Recall the figure from Schiaffino and Sonin [48], reproduced in Fig [2.1], showing the four regions of the Weber and Ohnesorge number plane. Schiaffino and Sonin [48] define for each region a spreading velocity, which they use to calculate the Reynolds and Capillary numbers associated with droplet impacts. In region 1 the spreading velocity is equal to the impact velocity, whereas in region 4 the spreading velocity is equal to: $\rho v^2 D / \mu$.

The majority of the impacts in the data sets analysed previously occurred in region 1. To determine the area of the Weber-Ohnesorge number plane that is occupied by the impacts of volcanic ash droplets a back of the envelope calculation was performed, assuming a range of diameters of 5-30 μm , and a representative range of impact velocities of 40-420 ms^{-1} [20]. Using a temperature of 1700 K, the viscosity and densities of Basaltic, Andesitic, Dacitic and Rhyolitic ash were calculated using the models of [14] and [55] respectively. These quantities were used, alongside a surface tension of $\sigma = 0.25 \text{ Nm}^{-1}$ [56, 57], to calculate a range of Weber and Ohnesorge numbers. The extent of this range can be seen in Fig [2.15] below.

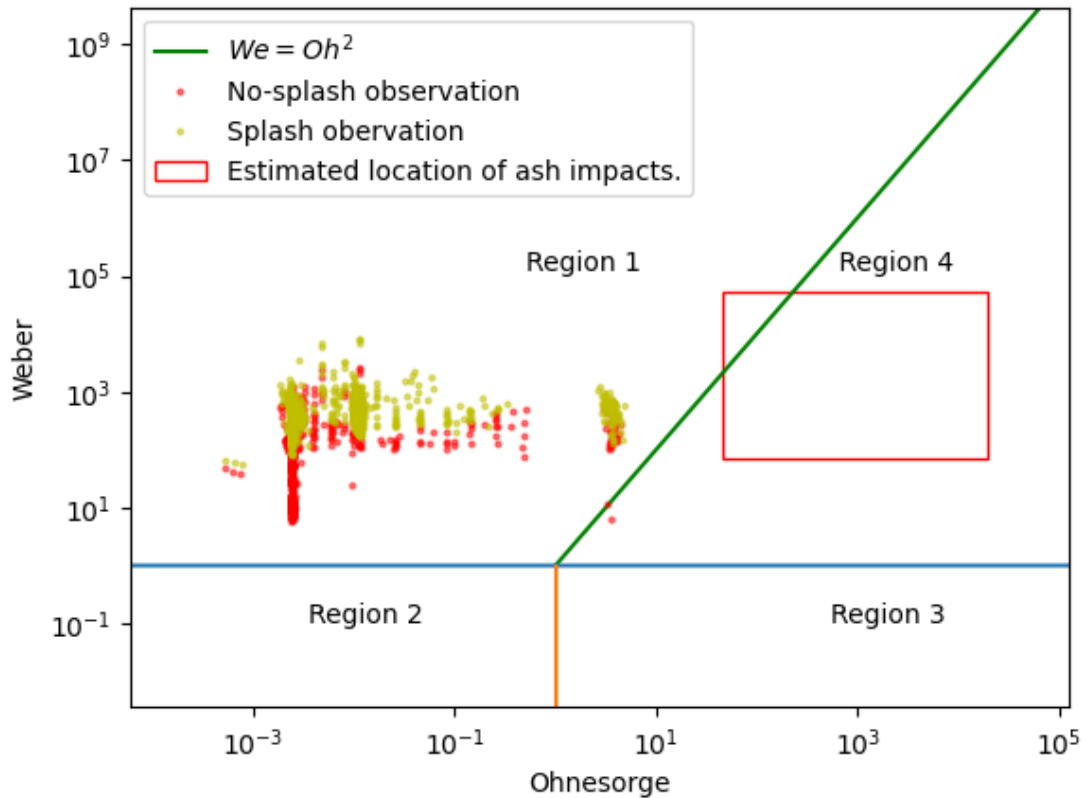


Figure 2.15: This figure shows the area of the Weber and Ohnesorge plane occupied by the data analysed in this chapter, alongside the estimated location of the ash impacts and the limits in the Weber–Ohnesorge plane as defined by Schiaffino and Sonin[48].

Although the analysis presented here found that the Ohnesorge number was not influential for droplet impacts within region 1, this may not be the case within region 4 where the majority of the ash droplet impacts are thought to occur. Given this, and considering that, according to Schiaffino and Sonin [48], the definitions of the Reynolds and Capillary numbers depend on the Weber and Ohnesorge numbers, it was deemed important to design experiments scaled for both the Ohnesorge and Weber numbers. It was also shown in Fig [2.13] that including the Reynolds, Ohnesorge, and Capillary numbers as explanatory variables in a model where the Weber number is already present does not add significant additional information beyond what the Weber number already provides. Therefore the Reynolds and Capillary numbers can be safely neglected in designing scaled experiments.

In the experiments I designed, I did not attempt to account for surface properties. This

decision was based on the difficulty of scaling for surface properties and the results of the analysis presented here, which indicate that, compared to impact velocity, surface properties were not nearly as influential in determining the splashing outcome.

2.5 Conclusions

In this chapter, I used Generalized Linear Models and Generalized Linear Mixed Models to analyse data from the literature, which recorded the outcomes of liquid droplets impacting onto surfaces, specifically whether the droplets splash or not. This analysis has revealed that velocity is the most important dimensional property in determining whether or not a droplet splashes on impact, while viscosity is the least determinant property. However, in models that included all recorded significant experimental conditions as explanatory variables, the model still could not accurately predict the splashing outcome for every experimental observation in the data. This suggests that there is not a complete understanding of the properties that control the splashing/non-splashing threshold.

The analysis presented here also showed that the Weber number was the most important dimensionless number in determining the splashing outcome, whereas the Ohnesorge number was the least determinative dimensionless number. A model with the Weber, Reynolds, and Capillary numbers as explanatory variables performed relatively well in predicting the outcomes of the experimental observations in the data, but it could not accurately predict the splashing outcome for every experimental observation. Therefore, the splashing behaviour of impacting droplets cannot be completely described with the dimensionless numbers considered here.

The conclusions drawn from this analysis, in the context of designing scaled experiments that can capture the same impact physics as occurs when ash droplets impact the NGV surface, emphasize the importance of scaling for the Weber number. Additionally, I decided to scale for the Ohnesorge number, as the location of droplet impacts within the different regions of the Weber-Ohnesorge number plane (as defined by Schiaffino and Sonin [48]) is crucial in defining the correct definition of the Reynolds and Capillary numbers to use. The vast majority of the data used in this analysis falls into a different region of the Weber-Ohnesorge number plane compared to the estimated majority of the ash impacts. Therefore, it is important to design new scaled experiments that can fit within the correct region of

Weber-Ohnesorge number space, regarding the impacts of volcanic ash within the jet engine, and are well-scaled to the Weber number, which is the most important dimensionless number for determining the splashing outcome.

Chapter 3

Understanding the Impact Properties of Ash Droplets on the NGVs.

This chapter has been prepared as a manuscript for submission for publication, hence some repetition of the introductory materials from Chapter 1. The chapter was derived from the manuscript version prior to the incorporation of any material contributed by co-authors; thus it solely reflects my own work. The work in this chapter sets out to answer the question of: What are the values of the dimensional impact properties and the dimensionless numbers associated with the ash droplet - NGV interaction?

3.1 Introduction

When volcanoes erupt explosively, they can deliver a large quantity of volcanic ash particles to altitudes up to 50 km [58]. This volcanic ash generally forms plumes and down-wind dispersal clouds in which the ash can remain suspended in the air for up to several weeks, with the very finest particles and aerosols remaining in the upper atmosphere for years [59]. Volcanic ash poses a significant hazard to aircraft especially when the ash is ingested by turbine engines [58]. There are multiple hazards posed by airborne volcanic ash to turbine engines, such as abrasive damage to the fan and compressor blades from low temperature solid ash particles. However, the main damage mechanism responsible for in-flight engine failure is the adherence of high temperature molten volcanic ash particles to the Nozzle Guide Vanes (NGVs) [10]. An example of this adherence of volcanic ash to the NGVs is shown in Fig [3.1].

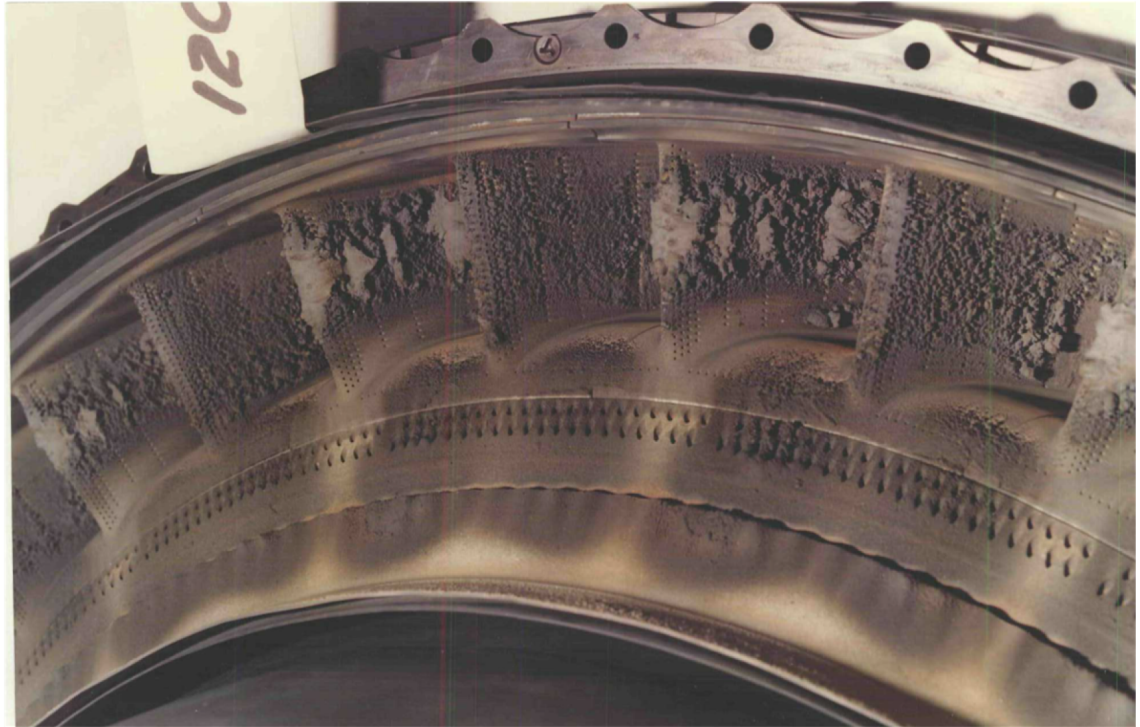


Figure 3.1: Volcanic ash deposition on the nozzle guide vanes of the turbine in a Rolls-Royce RB211-524C engine, resulting from an encounter with the volcanic ash plume during the 1982 eruption of Mount Galunggung in Indonesia [7]. This image was previously presented in Fig [1.2].

Since the 2010 eruption of the volcano Eyjafjallajökull in Iceland and the associated travel disruption, work has been focussed on the determination of a safe level of ash that an aircraft could fly through. Clarkson and Simpson [10] proposed an upper bound on the safe ‘dose’ of volcanic ash into the jet engine equivalent to operating in a concentration of ash of no more than 4 mg m^{-3} for an hour. This dose was calculated by considering two phenomena: deposit accretion and deposit shedding. In calculating the maximum safe dose Clarkson and Simpson [10] estimate the shedding and accumulation parameters using direct evidence from engine inspections following real-world engine-ash encounters (such as flight BA009 on 24/06/1982 and flight KLM867 on 15/12/1989) or from engine test data (such as the VIPRIII test [19]). However, these estimates are approximate and need to be refined using an understanding of the physics behind the accumulation and shedding of ash on the NGVs. The focus of this work is to develop a better understanding of the processes behind the accumulation of volcanic ash to the NGV surface. The rate of accumulation depends on the propensity for the volcanic ash to stick, bounce or splash on impact. This in turn depends

on: 1) Whether or not the ash particles hit the NGV ; 2) The ash temperature and resulting viscosity on impact; 3) The size and velocity of the impacting ash; and finally 4) The angle of impact.

In this work computational fluid dynamics (CFD) is used within the Ansys Fluent software to simulate the airflow around representative NGVs for a modern turbofan engine. Particles were then added to the simulation, with any particle impacts on the NGV surfaces recorded along with the associated particle impact velocity, diameter, and impact angles. Separate simulations were also conducted for different non-uniform inlet temperature fields.

Designing experiments to investigate the different impact behaviour of impacting volcanic ash is non-trivial as it is difficult to replicate jet engine conditions exactly in a laboratory environment. However by calculating dimensionless numbers, which scale the relevant forces involved in the deposition of volcanic ash on the NGV surface, an insight may be gained into the deposition of ash by performing scaled and accessible experiments using analogous fluids and materials based on the dimensionless numbers. Using the results from the simulations, relevant dimensionless numbers were then calculated for a variety of ash compositions. The variation of the impact conditions of the simulated particles along the NGV surface was studied, along with the variation of the dimensionless numbers which were considered to be relevant to impacts of molten volcanic ash droplets on the NGV surface.

Previous work performed by Ghenaïet et al [20] has looked at how the location of particle impacts on the NGV, in a PW-JT8- D17 engine, changes with particle diameter, and how this affects the resulting impact velocity and impact angle. However their data is not publicly available, they do not calculate any dimensionless numbers associated with volcanic ash impacts, and the range of particle diameters which they considered is not broadly representative of the size distribution of ash particles that are found in the combustor. By calculating the dimensionless numbers associated with volcanic ash impacts on an NGV in a modern gas turbine engine, my work will be able to help design experiments that can evaluate the propensity for volcanic ash to stick, bounce or splash on impact.

3.1.1 Background

During flight air is drawn into the engine through the engine fan which accelerates it, and a fraction of the air then passes into the compressor, with the remaining air ejected out the back of the engine. The air from the compressor passes into the combustor where it reaches temperatures of ≈ 2000 K. On exit from the combustor the hot gases pass through the Nozzle Guide Vanes. The NGVs are stationary in the engine and they are used to accelerate, deflect and distribute the hot gases that emerge from the combustion chamber. Fig [3.2a] shows the primary components of an aircraft turbine engine including an indication of where the temperatures are highest, and the location of the NGV array downstream of the combustor.

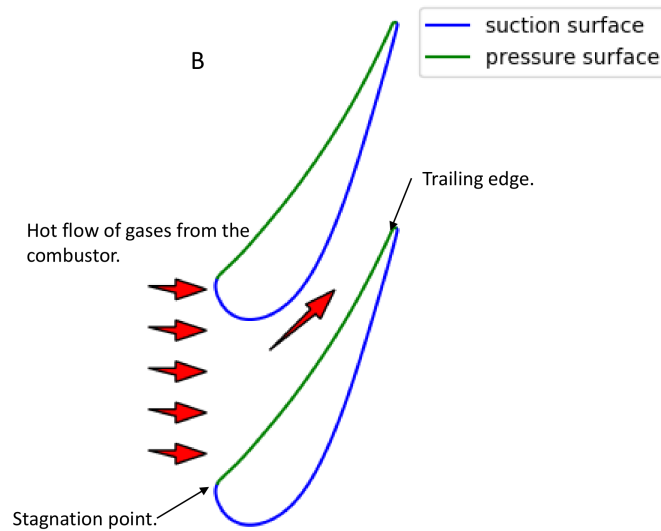
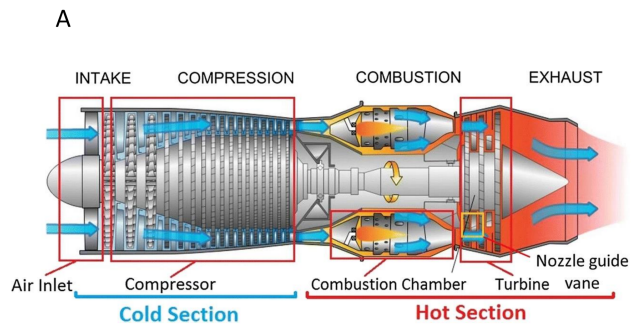


Figure 3.2: a: A cross section of a modern gas turbine engine [6]. Even though this is a turbojet engine, and almost all gas turbine engines operating today are turbofans, turboprops, or turboshafts all these engines have a core with the same layout and systems. b: Schematic of NGV array showing the general shape of an NGV, with the pressure surface and the suction surface indicated accordingly.

The minimum flow area in the passage formed between adjacent NGVs, as seen in Fig [3.2b], is called the throat gap. When volcanic ash is drawn into the engine, it typically melts in the high temperatures of the combustor and forms viscous liquid droplets. These droplets

remain molten as they pass through the NGV array and can therefore deposit on the NGV and cause the throat gap to narrow [7, 17]. Even if deposits form on the NGV upstream of the throat, the effective throat gap can narrow due to a thickened boundary layer, or a local separation bubble that reduces the flow through the throat. If this throat gap becomes narrowed the likelihood of an engine surge increases. An engine surge is when the flow through the engine reverses, which results in a major or total loss of controllable thrust and, possibly, damage to the compressor components. In severe exposure situations the reduction in flow through the NGV throat is so great that the engine runs down in power and stops.

The viscosity of volcanic ash is known to vary with both chemical composition and temperature. It is important to know the viscosity of the impacting volcanic ash as this could affect the behaviour of the ash droplets when they impact the NGV. In this work I calculate the viscosity of various compositions of volcanic ashes using the viscosity model from [14]. It was found that for all ash types at a temperature of 1000 K, which is cooler than the gases as they exit the combustor and flow over the NGVs, the viscosities are all smaller than $\mu < 10^{12}$ Pa s. One can therefore assume that all the ash impacts the NGV surface as a liquid. This is because the industrial definition of the glass transition temperature of a silicate melt is the temperature at which the viscosity of the melt is equal to 10^{12} Pa s [60]. The temperature has a significant impact on the viscosity of all the types of volcanic ash considered here, with the viscosity decreasing by up to 8 orders of magnitude going from a temperature of 1000 K to 2000 K. The densities of the volcanic ash compositions were calculated using the density model from [55]. The density of any ash composition here varied by less than 10% over the same temperature range.

The particle size of the ash is important, as the size of an ash particle will influence how well the particle is coupled to the air flow over the NGVs. This will influence if and where the ash particle impacts on the NGV. Within volcanic ash clouds, the distribution of ash particle diameters is non-uniform, with a notable skew towards smaller particles [61], and as ash particles make their way through the engine they undergo a ‘milling’ process. This means that the mean diameter of particles entering the engine is larger than that of the particles reaching the high pressure NGVs.

A relevant source of data indicating the ash particle size distribution (PSD) reaching

the NGVs is the NASA-USAF VIPR-III 2015 controlled volcanic ash exposure test [19]. During the post-test engine strip and inspection, the observations from which are reported in [19], the PSD of the ash deposits from the HPT 2nd stage rotor cavity in the engine were calculated. This PSD is shown in the figure below, alongside a PSD of a representative sample of volcanic ash.

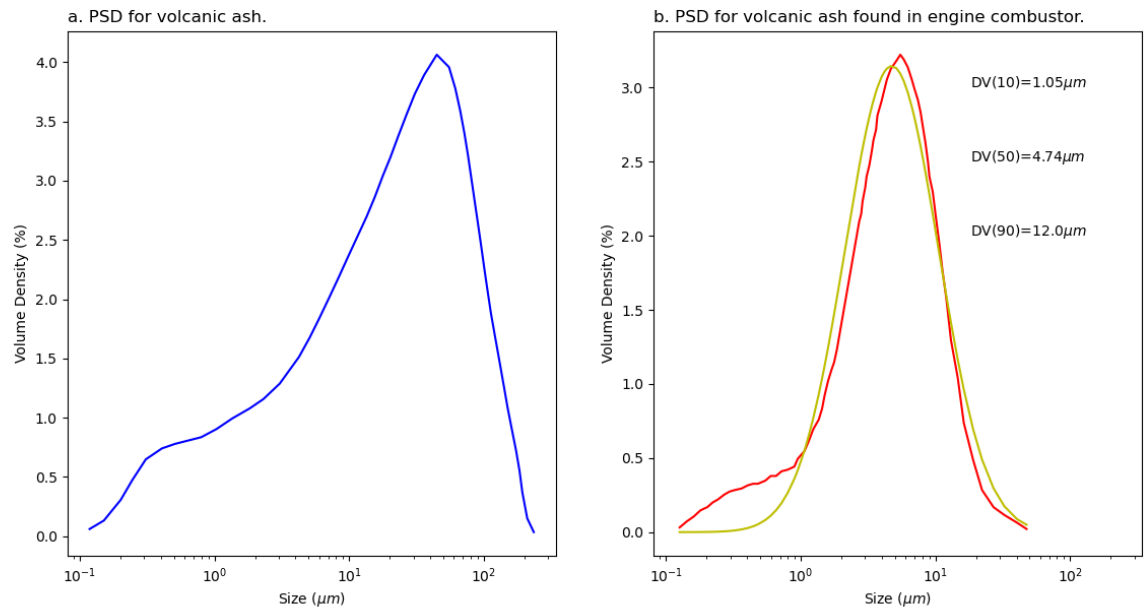


Figure 3.3: Fig 3a shows a reproduction of a particle size distribution of volcanic ash from [62]. Fig 3b shows a reproduction of a particle size distribution from NATO STO report [19], showing the particle size distribution of ash particles found inside the turbine of an engine that had been exposed to volcanic ash. $DV(90)$ is the particle size such that smaller particles comprise 90% of the total particle volume. The yellow curve in Fig 3b is the PSD I produced using the data from [19] and is described in more detail later.

3.2 Scaling Framework

Ash particles that are well coupled to the gas flowing through the turbine may bypass the NGV surfaces, whereas poorly coupled particles may hit the surfaces [11]. One can determine the degree of coupling between particles and the gas by considering the Stokes number. The Stokes number is a dimensionless number which can be used to capture the behaviour of a particle in a fluid flow around a larger object. It can be defined as the ratio of the char-

characteristic time for the velocity of the particle to change, to the time the fluid takes to pass the object. These two times are called the particle response time and the flow response time respectively. The Stokes number (Stk) is written below in Eqn [3.1] where t_0 [s] is the characteristic particle response time, u_0 [ms^{-1}] is the fluid velocity in the far-field away from the object, and l_0 [m] is a characteristic length of the object,

$$\text{Stk} = \frac{t_0 u_0}{l_0}. \quad (3.1)$$

For particles with $\text{Stk} \ll 1$ the particle remains coupled to the flow and follows the streamlines of the fluid around the object. For $\text{Stk} \gg 1$ the particle decouples from the flow and impacts on the object in the flow. Particles with a larger diameter have a greater momentum, and a greater drag force acting upon them from the flow. This means that the larger particles take longer to retard their acceleration with the fluid when the fluid begins to flow around the object and have a greater characteristic time t_0 , and therefore a larger Stokes number [11].

Bojdo et al [63] use the Stokes number to evaluate the probability of particles hitting the NGV. They first use the form of the Stokes number from Israel and Rosner [64]:

$$\text{Stk}_{\text{gen}} = \Psi \frac{\rho_p d_p^2 U}{18 \mu_f L}, \quad (3.2)$$

where ρ_p and d_p are the particle density and diameter, μ_f is the jet engine combustion gas viscosity and U and L are a characteristic velocity and length which were taken to be the inlet velocity to the NGVs, and the throat gap between the NGVs respectively. Ψ is a Stokes drag correction factor which is a function of the particle Reynolds number, Re_p :

$$\text{Re}_p = \frac{\rho_f |u - v| d_p}{\mu_f}, \quad (3.3)$$

where ρ_f is the density of the fluid the particle moves through, and $|u - v|$ is the magnitude of the difference in velocity between the particle and the fluid.

Using CFD simulations of a particle-laden flow around an NGV to predict the interaction rate of particles on the NGV surface, Bojdo et al [63] show that this generalised Stokes number can be used to predict the probability of a particle hitting the NGV surface, with the probability of impact increasing with the magnitude of the generalised Stokes number.

It is important to note that, unlike the general Stokes number in Eqn [3.1], Bojdo et al [63] do not conclude that for $\text{Stk}_{\text{gen}} \gg 1$ all particles will hit the vane and that for $\text{Stk}_{\text{gen}} \ll 1$

all particles will follow the streamlines around the vane. Instead, they define an expression for the interaction probability of ash hitting the NGV as a function of the generalised Stokes number. This expression is given below:

$$\eta_{\text{interaction}} = a \tanh(b \text{Stk}_{\text{gen}}^c) + d. \quad (3.4)$$

Here a , b , c , and d are constants that Bojdo et al [63] find empirically for different particle sphericities and flow response times, L/U . It is also important to note that these constants may change with different NGV designs.

By re-casting their particle impact data as a function of Stk_{gen} , Bojdo et al [63] have identified a powerful criterion variable to predict whether particles interact with the NGV surface. However, this does not provide any information as to whether the particle will stick to the NGV surface. For that Ellis et al [65] introduced a function that allows the probability of a droplet sticking to the NGV surface to be calculated as a function of the engine and particle properties through a dimensionless number they introduce as a thermal Stokes number. The thermal Stokes number can be used to predict whether a particle will reach the temperature of the gas in which it is suspended in the time it takes the particle to traverse the vane. They define the thermal Stokes number as:

$$\text{Stk}_{\text{th}} = \frac{\rho_p c_p d_p^2 U_{\text{in}}}{12 k_f L_{\text{th}}}, \quad (3.5)$$

where k_f is the thermal conductivity of air, L_{th} the throat gap, c_p the specific heat capacity of the particle, and U_{in} the inlet velocity to the NGV array. They recast this in terms of engine parameters:

$$\text{Stk}_{\text{th}} = \frac{c_p d_p^2 \rho_p}{12 k_f N h \rho_f} \frac{T_f}{T^*} \Psi. \quad (3.6)$$

The symbols in Eqn [3.6] have the same meaning as before, where ρ_f is the density of the combustion gas, T_f is the temperature of the combustion gas, N is the number of vanes, h is the height of the vanes and T^* is the softening temperature of the particle.

Ellis et al [65] use CFD simulations of a particle - laden airflow around an NGV. For the particles that hit the NGV they use the energy-based fouling particle fate model (EBFOG) of Casari et al [66] to evaluate whether or not the particle sticks to the vane. Using these results,

they work out the proportion of particles that will stick to the vane for a given thermal Stokes number. They call this the retention probability. Again it is important to note that unlike Eqn [3.1], Ellis and al [65] do not conclude that for $Stk_{th} \gg 1$ all particles will stick to the NGV surface; indeed their results show that the retention probability is still very low at $Stk_{th} = 1$. Instead, as in Bojdo et al [63], Ellis et al [65] define an expression for the retention probability as a function of their thermal Stokes number. This expression is given below:

$$\eta_{\text{retention}} = \frac{1}{A} \left[e + \frac{f - e}{\left[1 + \left(\frac{Stk_{th}}{g} \right)^h \right]^i} \right]. \quad (3.7)$$

Here A , e , f , g , h , and i are empirical constants.

The thermal Stokes number neglects the effect of particle viscosity on sticking, which has been shown to be important in the molten particle sticking/ bouncing threshold by Srinivasachar et al [67], Richter,[68] and Scharler et al [69]. The work of Ellis et al (2021) [65] also neglects the effect of the impact angle of the molten particles on whether or not they stick or bounce, this has been hypothesised in the literature to be an important variable [70]. Therefore, the thermal Stokes number cannot fully answer the question of how much of the ash sticks to the surface, as it neglects the effects of particle viscosity and impact angle.

A deeper understanding of the droplet -surface interaction physics would allow more accurate shedding and accumulation parameters to be calculated and allow more specific critical doses to be calculated for different engine types and different volcanic ash compositions. This can be achieved through experimental work, but any experiments need to be well scaled to the real system (viscous liquid droplets of volcanic ash impacting the NGV).

The interaction between a high temperature molten volcanic ash particle with the surface of an NGV is affected by many factors such as the droplet velocity, diameter, and rheology, etc [24]. These various physical parameters can be combined into dimensionless groups which capture ratios of forces and stresses involved in the interaction. Within the literature dimensionless numbers have been used to define the physics involved [48], and predict the behaviour associated with the droplet impacts [24, 25, 40, 50, 54], mainly in identifying under what conditions droplets splash on impact.

I now introduce the Weber number, We , which is a ratio of inertial to surface tension forces,

$$We = \frac{\rho v^2 D}{\sigma}, \quad (3.8)$$

and the Ohnesorge number, Oh , which is a ratio of the inertial to viscous forces in the droplet:

$$Oh = \frac{\mu}{\sqrt{\rho \sigma D}}. \quad (3.9)$$

Finally, I introduce the Weissenberg number which is a ratio of elastic forces to viscous forces:

$$Wi = \frac{v \lambda_s}{D}. \quad (3.10)$$

Here μ [Pa.s] is viscosity of the droplet, σ [N.m⁻¹] is surface tension, D [m] is the droplet diameter, ρ [kgm⁻³] is the droplet density, v [ms⁻¹] is velocity of the particle, and λ_s [s] is the relaxation time of the liquid droplet.

Investigating the deposition of molten metal droplets at low Weber numbers on a smooth flat surface, Schiaffino and Sonin [48] found that the spreading of the droplets on impact is governed primarily by the Weber and Ohnesorge numbers. They concluded that the Weber number scales the driving force of the droplet's spreading on the surface, and the Ohnesorge number scales the force that resists the spreading. Within the literature the Weber number has been used widely to predict the onset of droplets splashing on impact [24, 25, 40, 50, 54].

The Weissenberg number scales the shear strain rate to the relaxation time of a fluid. At $Wi \gg 1$ the material behaves in the non-Newtonian regime exhibiting solid or brittle-like behaviour as stress grows within the droplet faster than it can dissipate through viscous deformation. For $Wi \ll 1$ the stress within the droplet can dissipate easily through viscous deformation, and the material behaves as a Newtonian fluid. The onset of this brittle-like behaviour has been shown to occur for silicate melts at $Wi_c = 0.01$ by Dingwell & Webb [71] and Cordonnier et al [72]. Wadsworth et al [73] performed torsion experiments on various magmatic liquids and found the onset of this brittle behaviour to occur in the range $0.01 < Wi < 0.04$.

Based on this previous work it is hypothesised here that in the case of molten droplets of silicate melt impacting a solid surface, a high Weissenberg number may lead the droplet to bounce off the surface on impact- due to a solid like response from the particle.

The conclusion from Schiaffino and Sonin [48] is that the values of the Weber and Ohnesorge numbers of a liquid droplet impacting a surface are important in influencing the impact phenomena. I hypothesise that the Weissenberg number is also important in determining whether or not a droplet will bounce on impact. Therefore, calculating the dimensionless numbers associated with volcanic ash impacts can provide useful insight into the deposition behaviour of ash when it hits the NGV. Indeed, if there is a variation in the value of the dimensionless numbers at different points along the NGV, then the deposition behaviour of the ash could also vary along the NGV surface. In this work I calculate the values of the Weber, Ohnesorge and Weissenberg numbers associated with volcanic ash droplet impacts on the NGV surface. I present how the values of these numbers vary along the NGV surface. This will enable future experiments to be designed that can investigate the impact phenomena of ash droplet impacts on the NGV.

3.3 Method

Modelling the flow field.

The flow of hot gases from the combustor over the NGVs was modelled using Ansys Fluent. A domain was constructed using a 2D mid-span section of a representative NGV geometry generated from guidance provided by Rolls-Royce. The inlet and outlet were placed just over the length of one vane from the leading and trailing edges of the NGV. The domain was set up to depict a section of 36 NGVs in the engine core annulus, set at a distance of 276 mm from the engine centre line. Hence the vanes were spaced within the domain 48 mm from each other. Note that only a subset of these NGVs were included in the simulation domain, with periodic boundaries used to represent the effect of the presence of the remaining NGVs. The vane surface was treated as a smooth uniform wall with a no-slip boundary condition. The influence of the vane temperature was not considered or modelled in this work. The domain used is shown in Fig [3.4].

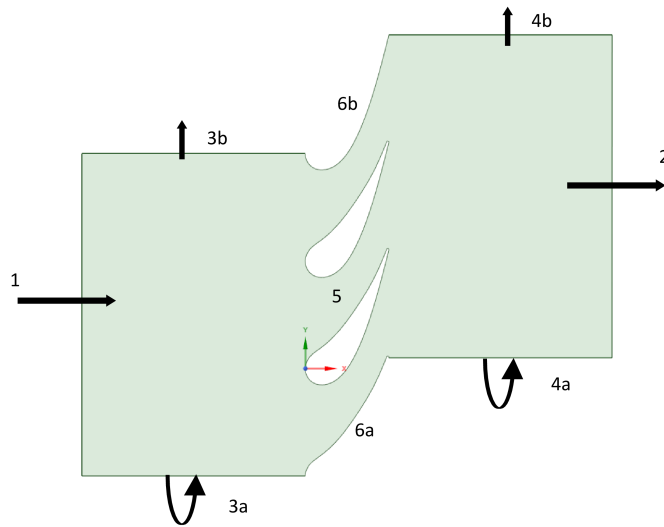


Figure 3.4: This figure shows a representative 2D domain of an NGV array over which the CFD simulation was conducted. The components of this domain are labelled as follows: 1- Inlet, 2- Outlet, 3a and 3b- these are periodic boundaries; anything that passes through boundary 3b appears through boundary 3a. 4a and 4b- these are also periodic boundaries as described previously. 5- These two aerofoil shapes are the Nozzle Guide Vanes (NGVs); these surfaces were set as walls with a no-slip condition imposed upon them. 6a and 6b- these correspond to the pressure and suction surfaces of the neighbouring NGVs in the domain; these surfaces were also set as walls with a no-slip condition.

The computational mesh was created using Ansys Meshing. The mesh in the far-field was unstructured, with the inflation tool used to create a layer of mesh around the vanes, surfaces 5, 6a, and 6b in the figure above, so as to resolve the boundary layer. Mesh dependency studies were conducted before the selection of the final mesh, to ensure that the mesh cell size did not affect the results of the calculations.

A non-dimensional wall distance for a wall bounded flow, commonly notated as y^+ , is used in boundary layer theory to determine how the boundary layer can be modelled [27]. The y^+ parameter is used to characterise the distance from a solid boundary to the point where the fluid flow is being analysed. It is defined as the dimensionless distance from the wall, normalised by the viscous length scale of the flow. In simpler terms, it represents how far away from the surface the turbulent effects become significant relative to the viscous effects. Within CFD code a finer mesh near the wall allows for better resolution of the near-wall flow, resulting in lower y^+ values. However, a coarser mesh may lead to higher y^+

values, implying a less resolved near-wall region.

In this work two approaches were used to model the boundary layer around the NGV walls in the domain. The log-law was used to model the boundary layer around the upper and lower walls (labelled 6a and 6b in Fig [3.4]), and an enhanced wall treatment was used to model the boundary layer around the two central NGVs, labelled surface 5 in Fig [3.4]. The log-law refers to a mathematical expression that describes the velocity profile in the turbulent boundary layer of a fluid flow near a solid surface. It is a fundamental component of the law of the wall, which characterises the velocity distribution in the near-wall region. An enhanced wall treatment is a numerical modelling approach used in CFD simulations, particularly in the context of simulating turbulent flows near solid boundaries. It is an improved treatment compared to standard wall functions and is designed to provide more accurate predictions of flow behaviour near walls. The wall treatment that Ansys Fluent uses to resolve the boundary layers around the walls in a simulation depends on the value of the y^+ around the respective walls.

The mesh was set so as to achieve a y^+ of $y^+ \approx 1$ and < 5 around the two central vanes in the domain. These values were selected so that an enhanced wall treatment could be used to fully resolve the boundary layer around the two central NGVs labelled surface 5 in Fig [3.4]. The mesh was set so as to achieve a $y^+ > 30$ for the upper and lowermost half-vane walls, labelled as surfaces 6a and 6b in Fig [3.4], employing a simpler log-law approach to model the boundary layer around them. This simpler approach was chosen to reduce the mesh structure's detail around those surfaces, saving computational time and facilitating the formation of periodic boundaries across surfaces 3a and 3b, and 4a and 4b, respectively. This approach resulted in a lower level of resolution in the velocity and pressure fields around surfaces 6a and 6b. Consequently, particle impacts on these surfaces were ignored, effectively treating them as 'scenery' boundaries.

Ansys Fluent was used to solve the Navier–Stokes equations for the velocity and pressure fields. The inlet and outlet conditions, provided by Rolls-Royce, are shown below. These conditions are representative of a modern turbofan engine on an aircraft during cruise, i.e., not during landing or take-off.

Table 3.1. Boundary conditions.

Conditions	Inlet	Outlet
Static Pressure(Pa)	1.79×10^5	1.1×10^5
Total Pressure(Pa)	1.91×10^5	NA
Temperature (K)	1728(Total)	1630(Static)

The turbulent variations were considered by using the realisable k-epsilon form of the Reynolds-averaged Navier-Stokes equations, which are shown in Eqns[9.1-9.5] in the Appendix. This form of the Navier-Stokes equations are suitable for dealing with compressible fluid flows, at velocities \approx Mach 1. Within this k-epsilon viscous model the options for enhanced wall treatment, and viscous heating were selected to fully resolve the boundary layer around the two vanes and model a compressible flow respectively. The density of the fluid was considered to be described by the ideal-gas equation, and the fluid viscosity, heat capacity and thermal conductivity were considered to be constant, with values of 5.35×10^{-5} Pa s, $1075 \text{ J kg}^{-1} \text{ K}^{-1}$, and $0.0955 \text{ Wm}^{-1}\text{K}^{-1}$ respectively. A turbulence intensity of 5% was chosen, to match values found experimentally [74] [65]. An initial solution was calculated using a first order least squares discretisation. After the solver had been initialised with this solution a calculation using a second-order discretisation was carried out. The solutions were taken to have converged when all the residuals calculated by the solver were of the order of magnitude 10^{-5} or less. The Fig [3.5a] shows the solved velocity field in terms of the Mach number.

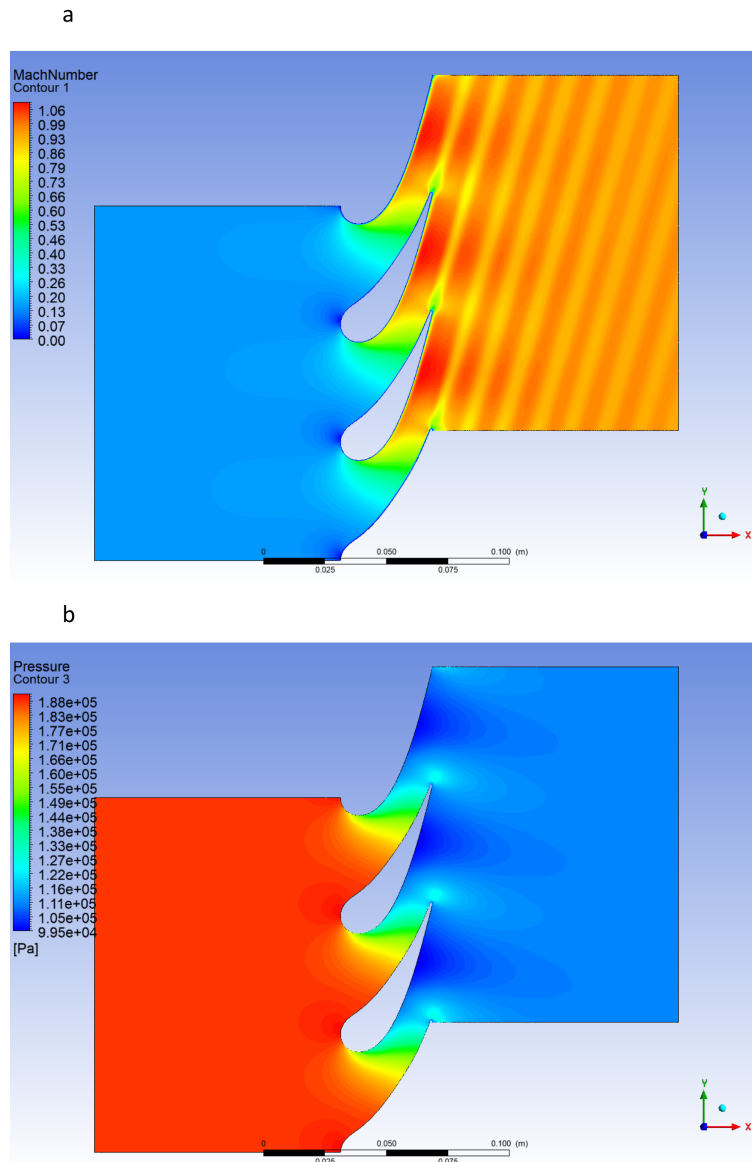


Figure 3.5: Fig 5a shows the velocity field in terms of the Mach number through the NGV array. It can be seen that the velocity through the throat gap is choked to approximately Mach 1. Fig 5b shows the static pressure field through the NGV array, where the static pressure drop across the NGV domain is approximately 1.7.

Verification of the CFD results was not simple due to the lack of any real relevant experimental data for the precise NGV geometry used here. However it is known that for a modern turbofan engine, the velocity of the air through the passage between two NGVs should be choked to a Mach number of ≈ 1 . As can be seen in Fig [3.5] this was the case for the simulation here. Rolls-Royce indicated a representative static pressure drop ratio across an NGV domain to be ≈ 1.7 [17]. The static pressure drop across the simulation domain was found to

be 1.706, and the static pressure field is shown in Fig [3.5b]. With the velocity and pressure fields in agreement with general data available on the flow field through a NGV domain, and with convergence achieved on the calculated values for the lift coefficient and drag force on the two central NGVs, one can be confident in the simulation for the study of trajectories of ash particles within an NGV flow field.

Modelling Particles.

After solving the flow field, particle trajectories were evaluated using the Lagrangian discrete phase in Ansys Fluent. Initially to investigate how changing the diameter changes the impact conditions of the particles and where they impact on the vane, 4 samples of 5000 particles were generated with different diameters of 2 μm , 5 μm , 10 μm and 25 μm respectively. These samples were injected individually into the CFD simulation using randomised injection points along the inlet. The particles were introduced with a velocity equal to the flow velocity at the inlet and with a representative density for volcanic ash of 2000 kgm^{-3} [16, 17]. The exchange of energy and momentum was assumed to be one way, from the fluid phase to the particles. After calculating the particle trajectories, the corresponding data was analysed in a piece of Python code that was written to calculate the impact velocity, position of impact on the vane, and impact angles of the particles that hit the NGV with respect to the surface normal to the NGV surface. This means very glancing impact angles were close to 90° , and more normal impacts had angles closer to 0° . These simulations allowed the effect of particle size on the impact angle and impact velocity to be investigated.

In Fig [3.6] a sample of particle trajectories, for a range of diameters, which impacted the NGV surface can be seen.

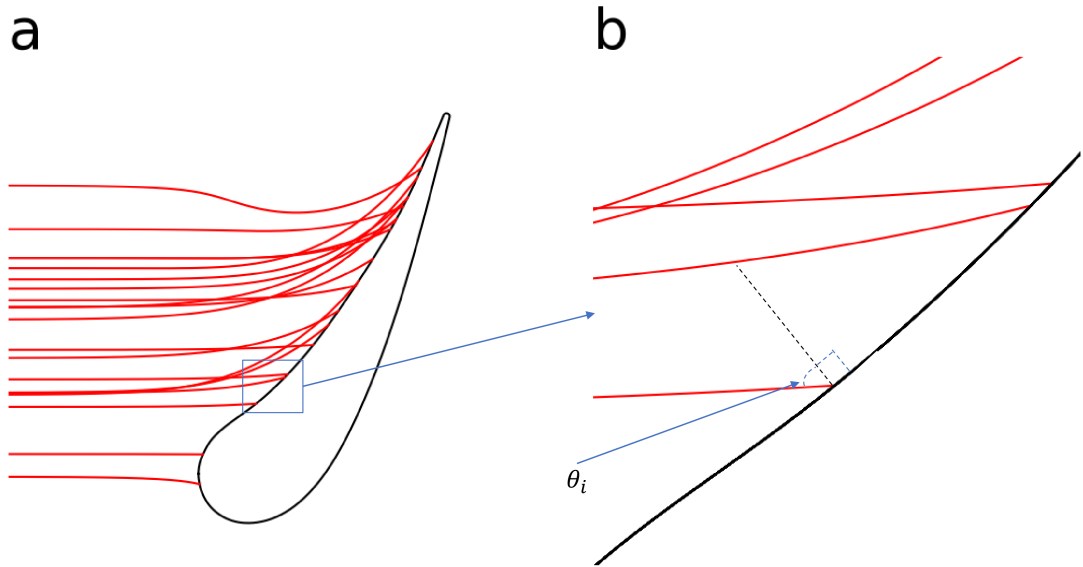


Figure 3.6: Fig 6a shows a sample of 20 particle trajectories that impacted the NGV. Note the particles here had a range of diameters 0 – 25 μm . Fig 6b -zoomed in, the angles were measured with respect to the surface normal to the NGV surface.

In order to accurately simulate an engine encounter with a volcanic ash cloud, it is necessary to know the distribution of particle sizes that leave the combustor and enter the turbine. This is important as due to Stoke’s law the size of a particle can have a dramatic effect on the particle’s trajectory through a flow field [75] [11]. A particle size distribution for volcanic ash found in an engine turbine was found in the VIPR report [19] and is shown in Fig [3.3b]. However, there being no way of accessing the data that the figure corresponds to, an open-source code in Python was used to generate a similar log-normal PSD [76]. The algorithm took arguments for $DV(50)$ and a spreading parameter s . The value of s was varied to achieve values of $DV(90) = 13.21$ and $DV(10) = 1.7$ which are within 1.2 μm and 0.65 μm respectively of those reported for the particle size distribution in the VIPR report. These were the closest values of $DV(90)$ and $DV(10)$ to those reported in [19] that could be achieved by varying s within the open-source code.

A uniform distribution of 5000 particles with diameters between 0 – 25 μm were created and injected into the CFD simulation from randomly selected positions along the inlet. A Gaussian kernel density estimation function [77] was used to process the particle impact data from the CFD simulation, and show how the impact velocity, impact angle and size of the impacting particles varied with respect to position on the NGV. Finally, the results for

the particle velocities at impact and their corresponding diameters were used to calculate the dimensionless numbers at impact for various compositions of volcanic ash. A Gaussian kernel density estimation function was used again to show how the values of the dimensionless numbers varied with respect to position on the NGV surface.

A Gaussian kernel density estimation function allows for an Estimation of the Probability Densities (EPD) for a random variable, generating a smooth curve from the original data set that approximates the underlying probability density. It can be used to find a 2D EPD for data points which have two variables associated with them. The resulting EPD can then be plotted as a 3D graph or a contour graph. Fig [3.7] shows the resulting 2D EPD for 1000 data points each of which have two variables (x and y) associated with them, which were drawn from a normal distribution with a mean of 1, and a standard deviation of 0.1.

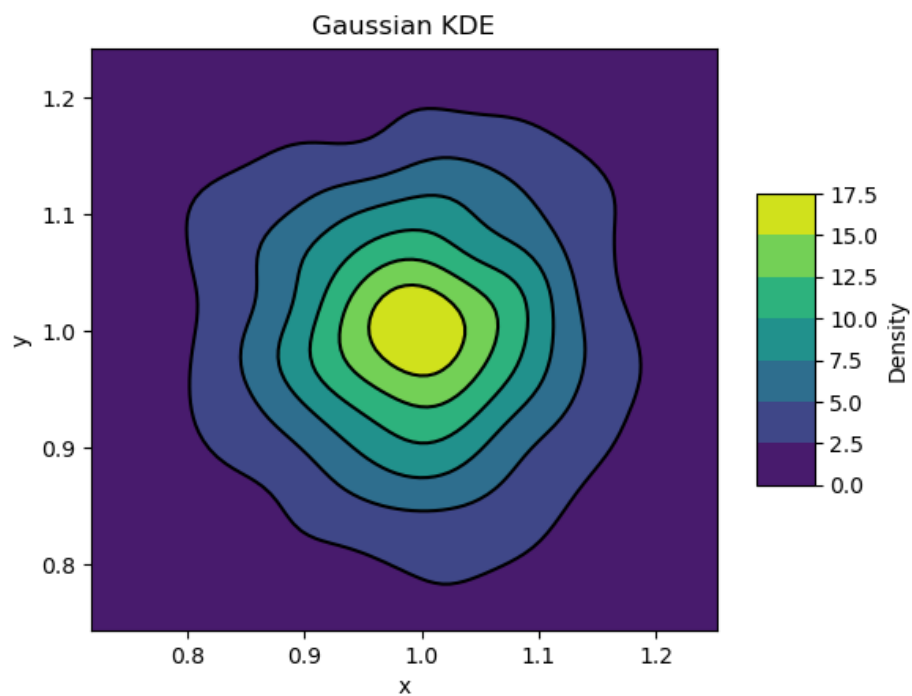


Figure 3.7: Gaussian kernel density plots of 1000 data points, with variables x and y drawn from the same normal distribution. The contour plot highlights the regions of highest data density, with brighter colours indicating areas where data points are more densely populated.

The brighter colours in the contour plot indicate the region most densely populated by the data points.

To account for the size distribution of particles that enter the turbine, each particle data point was weighted within the Gaussian kernel density estimation function, with a weight equal to the value of the particle size distribution function for a given particle's diameter. This allows for the effect of the distribution of particle sizes in the turbine to be captured in the distribution of the particles' impact velocities, angles and diameters associated with the particle impacts. When these Gaussian kernel density plots were used to demonstrate the distribution of particle impact properties, multiples of the same plots were produced with an increasing number of data points. This was done to ensure that the underlying distribution was robust and not overly sensitive to the selection of a particular sample size.

In order to make characterisations of the ash impact behaviour, as done here through the calculation of dimensionless numbers, specific attention needs to be paid to the behaviour of the bulk of the mass of the particles; as this is what ultimately determines the shedding and accumulation rates of ash on the NGV. As can be seen in Fig [3.3b], only 10% of the ash particles that reach the turbine have a diameter greater than 12 μm , but these larger particles will contain a proportion greater than 10% of the overall mass of ash entering the turbine, as particle mass is proportional to the cube of the particle diameter. To account for this, new weights need to be applied within the Gaussian kernel density function when calculating the distribution of particle impact velocities and angles, and the associated calculated dimensionless numbers. Expressions for the mass and the weights are shown below in Eqn [3.11] and Eqn [3.12], where m_i , d_i are the mass and diameter respectively of an individual particle, and $f_{\text{psd}}(d)$ is the particle size distribution function. The ash particles were all assumed to be perfect spheres,

$$m_i = \frac{4\pi}{3} \rho \left(\frac{d_i}{2} \right)^3, \quad (3.11)$$

$$w_i = \frac{m_i}{\sum_{j=1}^{5000} m_j} \times f_{\text{psd}}(d_i). \quad (3.12)$$

This allows the effect of the higher relative importance of the behaviour of the larger and heavier particles to be captured in the distribution of the calculated dimensionless numbers associated with the particle impacts.

Thermal modelling.

So far in this work only simulations with a uniform inlet temperature have been considered. Due to the position of the burners within the combustor the temperature field along the inlet is non-uniform. Though the temperature of the gases would not affect the impact velocity and angles of the volcanic ash on the NGV, or where the ash droplets impact on the NGV, the viscosity and density of the molten ash depend on temperature. Therefore, temperature is an important variable in calculating the associated dimensionless numbers. Here I describe how I repeated the particle simulations, of 5000 particles with diameters between 0 – 25 μm , for different inlet temperature fields.

After consultation with Rolls-Royce, the inlet temperature fields were approximated as a sinusoidal function with a mid-point temperature of 1700 K and a peak to trough temperature difference of between 200 – 300 K, and a wavelength equal to twice the distance between the stagnation points of two neighbouring NGVs. The general form of this temperature field along the inlet is shown in Eqn[9.6] in the Appendix. The ‘peaks’ in the inlet temperature field are known as hot-spots, and the location of these hot-spots with respect to the position of the NGVs varies for different engines. In consultation with Rolls-Royce two positions of the hot-spots were modelled. These two positions of the hot-spots were chosen, as they are most representative of the designs of gas-turbine engines in operation today. In what will be referred to here as Case A, the hot-spots were aligned with the stagnation point on alternate NGVs, whereas for Case B the hotspots were aligned with the centre of the flow passage between alternate pairs of NGVs. For both Case A and Case B two simulations were done, 4 simulations in total, with amplitudes in the inlet temperature field of 150 K and 100 K.

In order to allow the temperature field to match up across the periodic boundaries an extra NGV had to be added to the domain. The temperature fields for Case A and Case B with amplitudes of 150 K are shown in Fig [3.8].

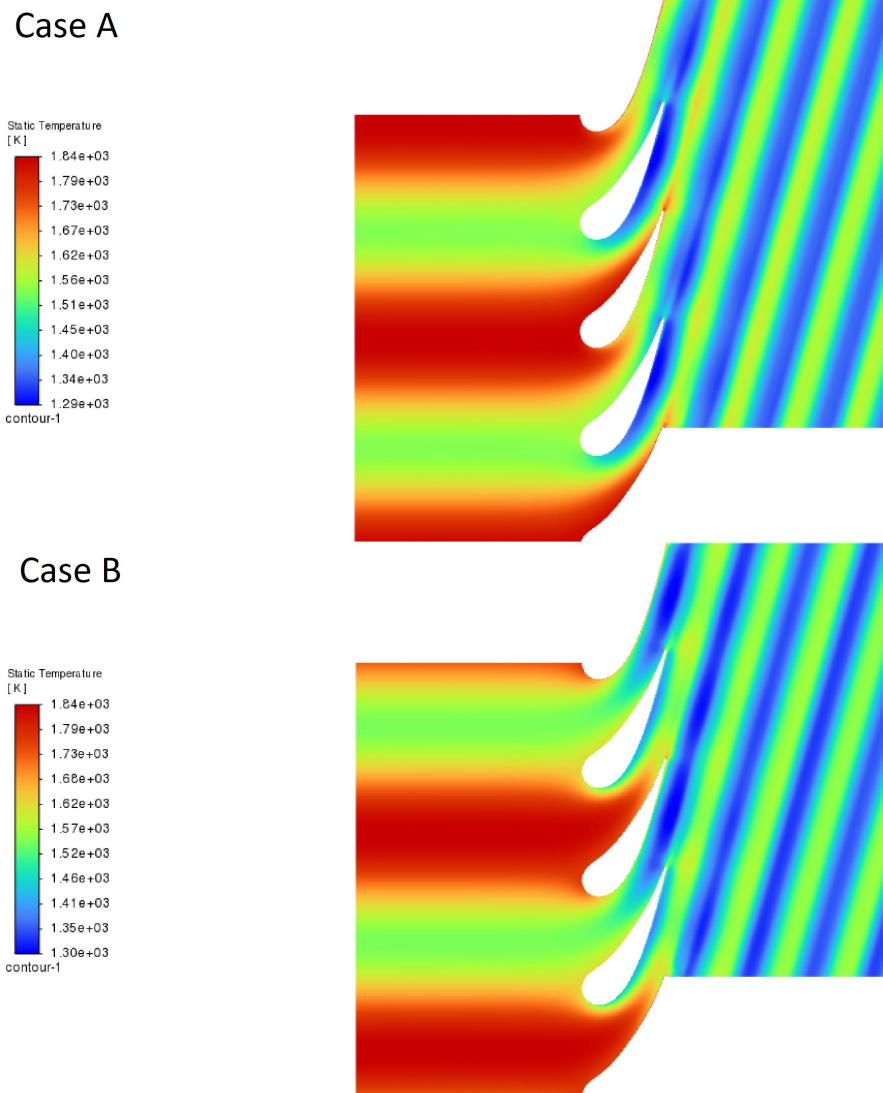


Figure 3.8: Visualisation of the inlet temperature fields for Case A and Case B, both with a temperature amplitude of 150 K. The plots demonstrate the spatial temperature distribution across the Nozzle Guide Vanes (NGVs), highlighting the variation in local temperatures experienced by each NGV.

A new mesh was created, and new simulations for the four different inlet temperature fields were completed using the same method as detailed earlier. The changing temperature fields did not change the results for the Mach number or Pressure contours. As can be seen in Fig [3.8], for either inlet temperature field (Case A and Case B) two neighbouring NGVs are exposed to different local temperatures, with one NGV exposed to hotter temperatures than the other. The particle impacts were modelled for both the ‘hot’ and ‘cold’ NGV for both sinusoidal temperature fields. The particles were assumed to be in thermal equilibrium with the gas at the inlet, and the in-built inert particle heating laws were used within Fluent to calculate the particle temperature [78]. The results of the particle impact velocity, impact

angle and impact position along the NGV were checked against the results for the isothermal temperature inlet simulation and were found to be the same. The temperatures of the different particles on impact were used within the density and viscosity models detailed previously to calculate the associated densities and viscosities for a variety of different ash compositions, and these were used to calculate the associated Weber, Ohnesorge and Weissenberg numbers.

3.4 Results and Analysis

Discrete Particle Diameters.

Below in Fig [3.9] the impact positions along the NGV surface for particles of diameter 2, 5, 10 and 25 microns can be seen, with the colours corresponding to the impact velocity in Fig [3.9a] and impact angle in Fig [3.9b].

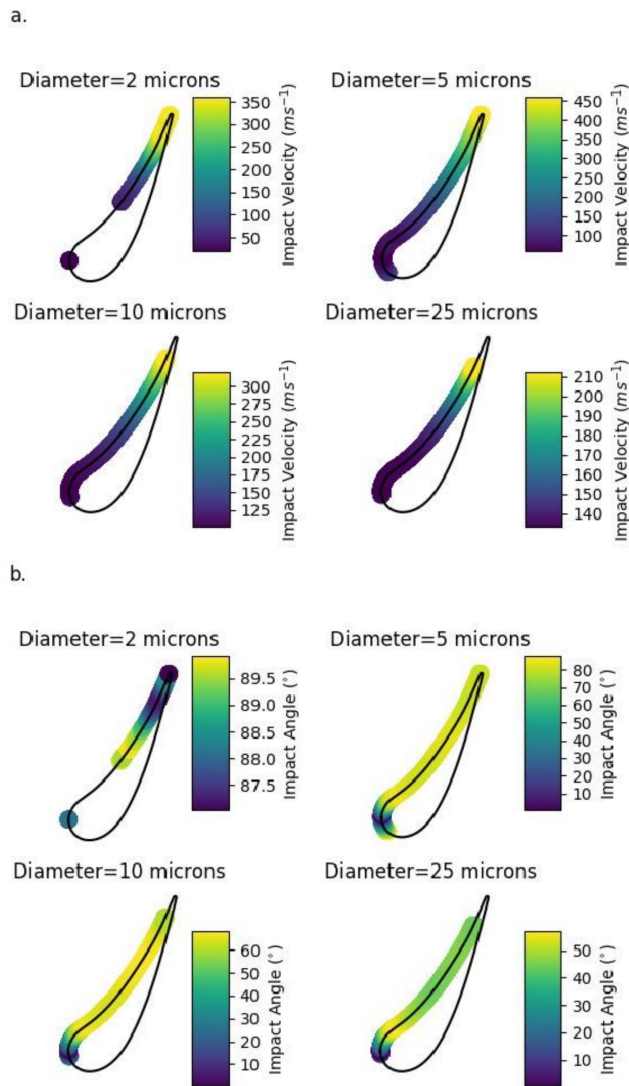


Figure 3.9: a: Shows the distribution of impact velocities along the NGV for different particle sizes. For certain parts of the NGV surface no impacts were recorded for the 2-micron particles. b: shows the distribution of impact angles along the NGV for different particle sizes. For certain parts of the NGV surface no impacts were recorded for the 2-micron particles.

To display the impact data for the 4 discrete particle sizes in a more quantitative way, the impact velocities and angles for each particle size were plotted against a non-dimensional ‘NGV distance’. This distance was defined with respect to the y-coordinates of the trailing edge and the stagnation point (i.e. in the circumferential direction in the engine). The upper-most point of the trailing edge corresponds to a distance of 1, with the stagnation point as the origin. Impacts that occurred on the suction surface correspond to a ‘negative’ distance with respect to the stagnation point. Fig [3.10] shows how the impact velocity and angle vary

with respect along the NGV surface for the 4 discrete particle sizes.

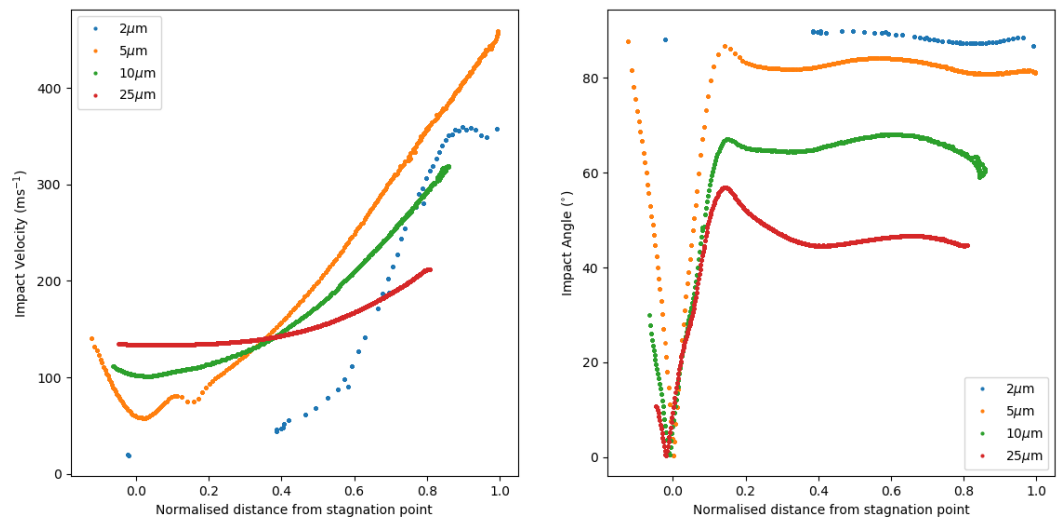


Figure 3.10: Plots of impact angle and velocity against a dimensionless distance along the NGV, for particles of diameters 2 μm, 5 μm, 10 μm and 25 μm. Impacts with a ‘negative’ distance are those that occurred on the suction surface of the NGV. The results highlight how particle size affects impact conditions, with smaller particles showing glancing impacts at a greater velocity near the trailing edge, and larger particles having more direct impacts at a lower velocity towards the stagnation point.

It can be seen in the above Fig [3.9-3.10] that changing the size of the particle can have a significant effect on the resulting impact conditions. It can be seen that for 2 μm particles the majority of the impacts occur towards the trailing edge of the pressure surface at very glancing angles close to 90°. As the particle diameter is increased from 5 μm to 10 μm and 25 μm, the impact angles decrease and become less glancing, and the particles impact the NGV surface lower down from the trailing edge of the NGV, i.e. towards the leading edge or stagnation point. However, for all the particle diameters considered here, it can be seen that for any particle diameter the impact velocity increases for impacts closer to the trailing edge and decreases for impacts closer to the stagnation point on the NGV. It can also be observed that for all diameters, particles that impact closer to the stagnation point generally have smaller impact angles, although the relationship is not strictly monotonically decreasing.

Continuous Particle Diameters.

The next set of results presented here looks at the impacts of a sample of particles drawn

from the uniform distribution of particle sizes, with each data point weighted with respect to the particle size distribution from [19]. In Fig [3.11] Gaussian kernel density plots can be seen for the impact velocity, angles, particle diameters and mass along the NGV surface. The mass was calculated using the particle diameters and assuming the particles could be treated as spheres, and then normalised by dividing through by the sum of the total mass that impacted on the NGV.

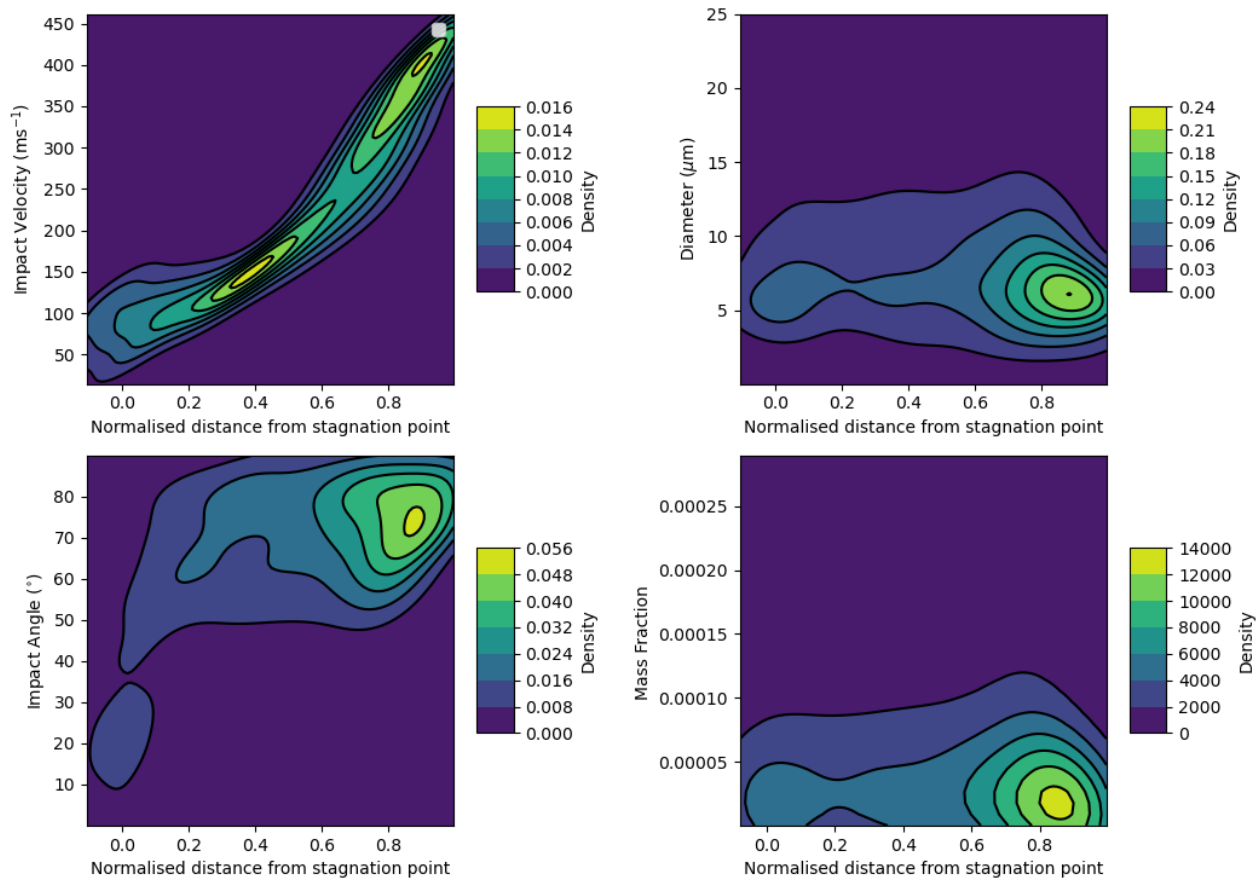


Figure 3.11: Gaussian kernel density plots of the impact velocities, impact angles, diameters and mass fraction of particles that impact the NGV against the dimensionless NGV distance. The plots highlight the regions of highest data density, with brighter colours indicating areas where data points are more densely populated.

It can be seen in Fig [3.11] that there is a variation in velocity along the surface of the NGV with impact velocities increasing further up towards the trailing edge of the pressure surface, and velocities decreasing closer to the stagnation point. It can also be seen that there is a relation with impact position on the NGV and the corresponding impact angle, with more glancing impacts occurring up towards the trailing edge of the pressure surface, with more

impacts closer to the normal to the surface of the NGV occurring on the suction surface. It can be seen that most of the particles that impact the NGV have diameters less than 15 μm , and that they impact the NGV closer to the trailing edge than the stagnation point. As mass was taken to be directly proportional to the cube of the diameter of the individual particles, the Gaussian density plot for mass along the NGV surface has a similar form to that of the particle diameter. It can be seen that the bulk of the particles impact the NGV towards the trailing edge.

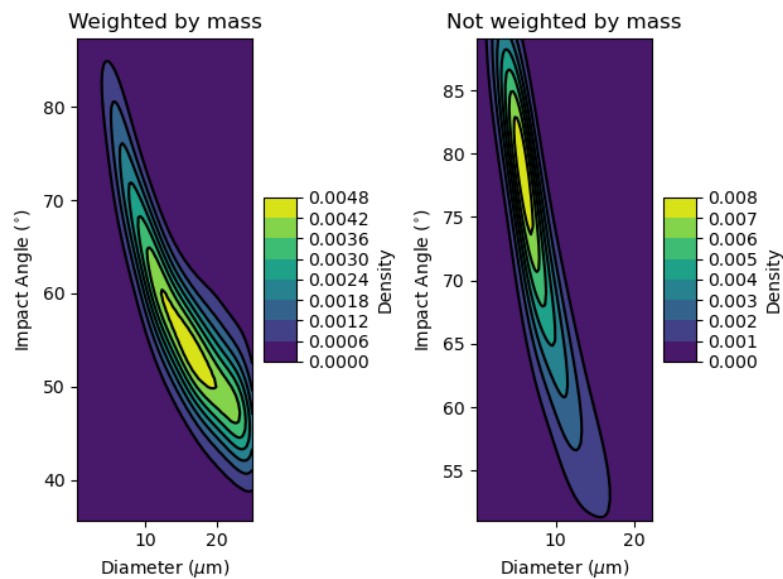


Figure 3.12: Gaussian kernel density plots for the impact angles of the particles against their diameter. The plot on the left-hand side is weighted for the mass and the PSD and shows the most likely diameters and impact angles for the bulk of the mass. The plot on the right-hand side is only weighted for the PSD, and so shows the most likely diameters and impact angles for all the impacting particles.

In Fig [3.12] Gaussian density plots can be seen for particle diameter against particle impact angle, with one plot having each data point weighted according to its non-dimensional mass. This shows that the majority of particles that impacted on the NGV with diameters in the range 4 μm -8 μm , had impact angles between 70°-80° respectively. It also shows that as the particle diameter was increased, the most likely corresponding impact angle decreased. It can also be seen that when mass weighting is applied, the range of impact angles of most interest is 50° -65° with diameters between 10 μm - 20 μm . This is to be expected when looking at the behaviour of the bulk of the mass of the particles entering the turbine, as the larger particles have more influence and generally impact with smaller angles with respect

to the surface normal.

Fig [3.13] shows Gaussian kernel density plots using the same data as in Fig [3.11], but with each data point now also weighted according to its corresponding dimensionless mass. This allows an examination of how the bulk mass of ash behaves as the particles impact the NGV.

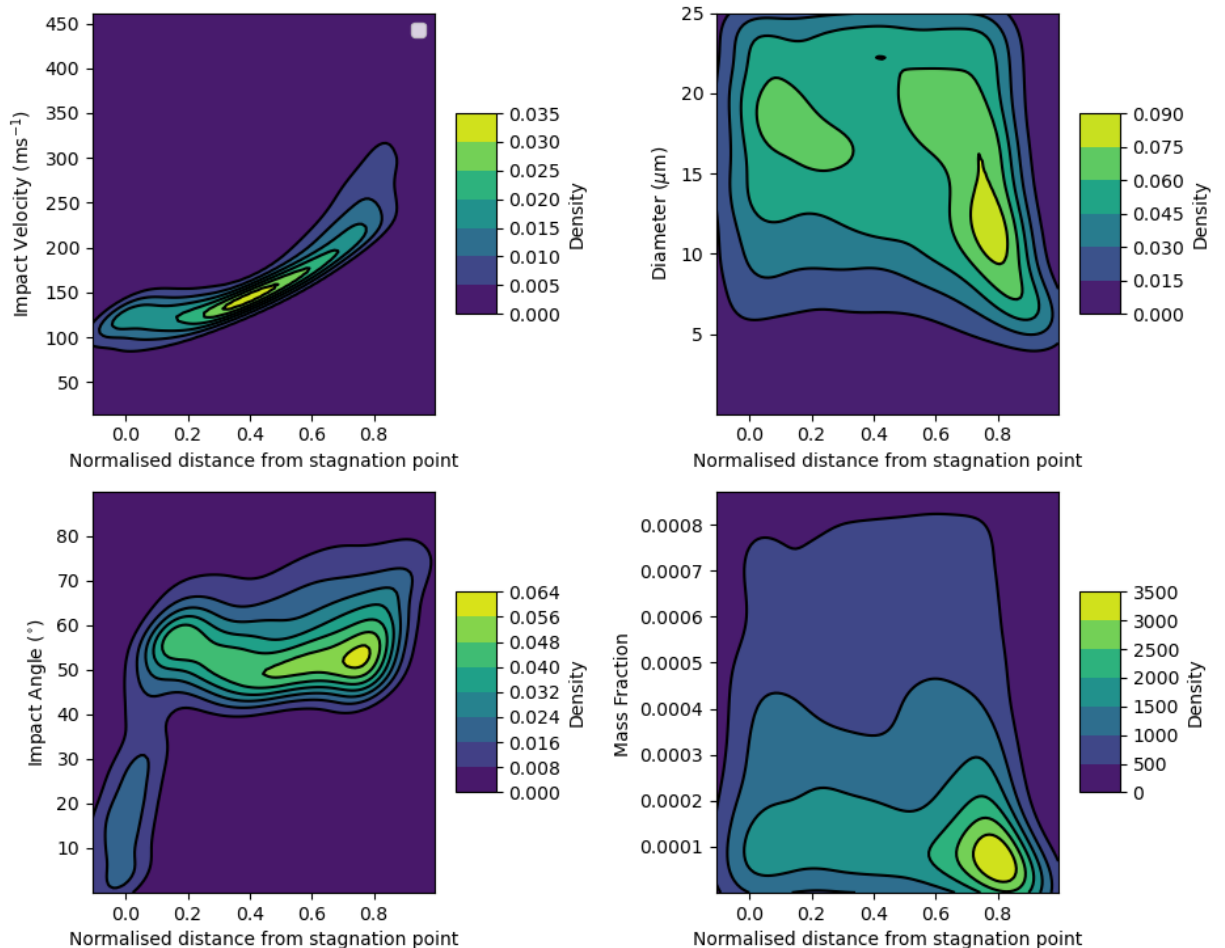


Figure 3.13: Gaussian kernel density plots of the impact velocities, impact angles, diameters and mass fraction of particles that impact the NGV against the dimensionless NGV distance, but with each data point weighted for the dimensionless mass of the particle.

When considering the bulk mass, Fig [3.13], the picture changes. Most of the mass is contained within the particles of diameter 10 μm -15 μm , which impact on the trailing edge of the NGV. However, a significant proportion of the total mass is in the larger particles 15 μm -20 μm which impact the NGV surface closer towards the stagnation point. The bulk of the mass is contained within the less ‘massive’ particles that impact towards the trailing edge

of the NGV. If this mass sticks and accumulates here on the NGV then this would lead to a narrowing of the throat gap and could lead to a surge event. Compared with Fig [3.11] it can be seen that the bulk of the mass has a lower impact velocity compared to the most likely impact velocity of any given particle, and that the range of velocities of interest is a lot smaller. This decrease in the range of impact velocities and angles of interest when weighting for the mass is considered, suggests that the bulk of the mass could behave in a less varied way than the behaviour of the majority of the individual particle impacts.

Thermal modelling results.

Here I present the results of the simulations of 5000 particles with diameters 0 – 25 μm , within the different inlet temperature fields. The impact positions along the NGV surface for particles drawn from a uniform distribution of particle diameters are shown in Fig [3.14] and Fig [3.15], with the colours corresponding to the temperature of the impacting particles. In Fig [3.14] and Fig [3.15] the impacting particles positions and temperatures can be seen for both the hot and cold NGV for the inlet temperature Case A and for the inlet temperature Case B. Both these sinusoidal inlet temperatures in Fig [3.14] have an amplitude of 150 K. In Fig [3.15] the sinusoidal inlet temperatures have an amplitude of 100 K.

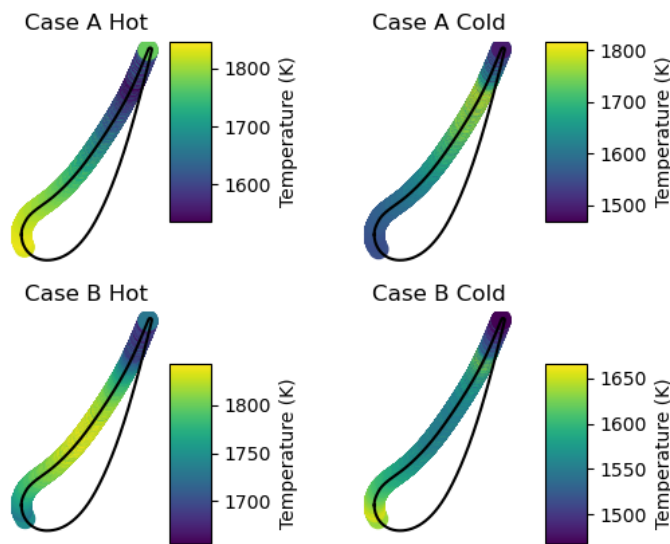


Figure 3.14: Distribution of particle impact temperatures along the NGV for particle diameters drawn from a uniform distribution with a range of 0 – 25 μm . The inlet temperature amplitude for all the NGVs shown here was 150 K.

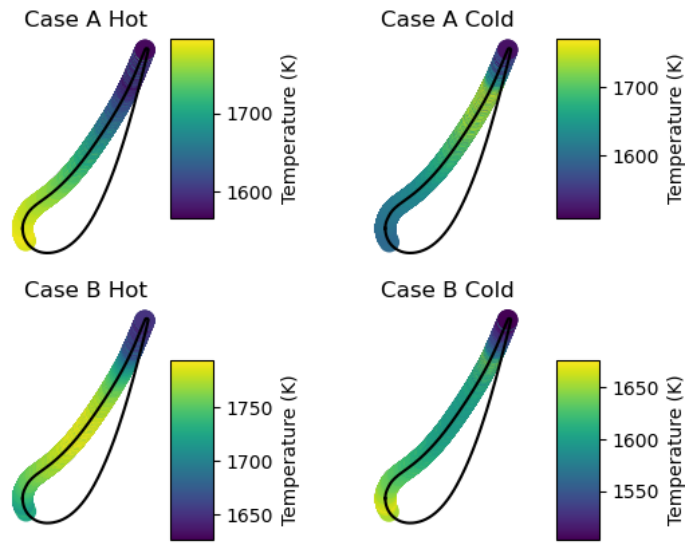


Figure 3.15: Distribution of particle impact temperatures along the NGV for particle diameters drawn from a uniform distribution with a range of 0 – 25 μm . The inlet temperature amplitude for all the NGVs shown here was 100 K.

Comparing Fig [3.14] for a sinusoidal inlet temperature amplitude of 150 K to Fig [3.15] for a sinusoidal inlet temperature amplitude of 100 K, it can be seen that for a lower temperature amplitude the particle impacts are cooler as would be expected. The greater inlet temperature amplitude in Fig [3.14] leads to a greater difference in impact temperature between the hot and cold NGV for Case B, than for the same case but with a temperature amplitude of 100 K in Fig [3.15].

For both temperature amplitudes the NGVs in the colder gases have lower particle impact temperatures than the NGVs in the hotter gases. For the ‘hot’ NGV in Case A, the hotter region is towards the stagnation point on the suction surface, whereas the hottest region on the ‘cold’ NGV is on the trailing edge of the NGV. The opposite is found for the inlet temperature field Case B. Here the hottest region on the ‘hot’ NGV is found on the trailing edge and the hottest region on the ‘cold’ NGV is found on the stagnation point. The results of the distribution of particle impact velocity, size and angle were the same as for the simulations with a uniform inlet temperature, so these results are not shown again here.

3.5 Discussion

Having found the dimensional quantities of particle impact velocity, angle, temperature and size and how they vary across the NGV surface, I can use these results to find the dimensionless numbers associated with these impacts. These dimensionless numbers can be used to design scaled droplet impact experiments that can capture the same droplet impact physics as the molten ash droplets impacting the NGV.

The first dimensionless number considered is the generalised Stokes number from [63], given in Eqn [3.3]. A sample of particles was taken from along the entrance to the NGV passage from the first CFD simulation and using Eqn [3.3] along with the drag correction factor $\psi(\text{Re}_p)$, the value of the generalised Stokes number for these particles was calculated individually. I plotted the Stokes number against the circumferential position in the engine (i.e. the y-axis in Fig [3.4]) for each particle. Comparing the results obtained in this study with those presented by Bojdo et al. [63] is difficult because different methodologies were used. Notably, Bojdo et al. conducted simulations using a different NGV geometry than the one used here. They also systematically manipulated the Reynolds numbers of the particles in the throat gap by injecting different samples of particles, with each sample containing particles with the same diameter. The current simulation did not include such variations. To facilitate a meaningful comparison and plot how the interaction rate varied with Stokes number, the computed Stokes numbers were ‘binned’ based on their order of magnitude, and the proportion of particles that hit the NGV were calculated for each bin. The bins were all of equal widths, apart from the first which included all Stokes numbers $\text{Stk}_{\text{gen}} \leq 10^{-3}$. This was done due to the sparsity of data for Stokes numbers of the order $\text{Stk}_{\text{gen}} < 10^{-3}$. The results of this can be seen in Fig [3.16].

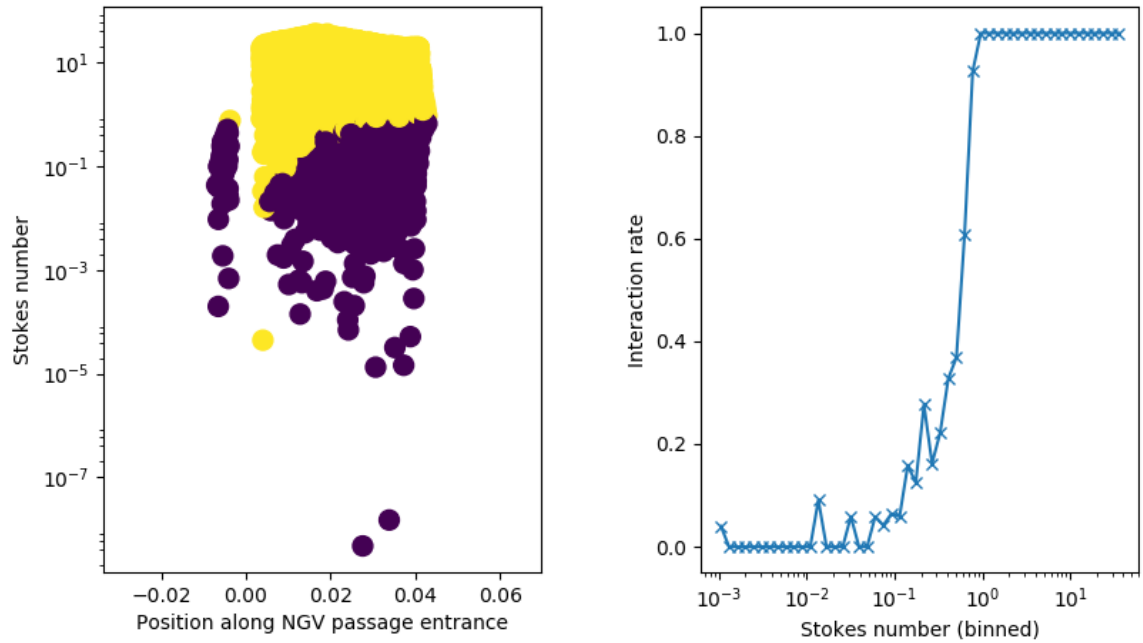


Figure 3.16: Figure illustrating the interaction outcomes of particles with the Nozzle Guide Vanes (NGV). The left plot displays particle impact results, with yellow points indicating impacts and purple points indicating misses. The right plot demonstrates the trend of interaction rates, showing that the probability of particles hitting the NGV increases with higher Stokes numbers.

It can be observed that at small Stokes numbers, there is a small probability of interaction, which steadily increases as the Stokes numbers increase. This trend continues until the interaction rate reaches unity above a critical Stokes number, approximately $Stk_{gen} \approx 1$. Comparing these results to those of Bojdo et al., the shape of the plot of the Stokes numbers against the interaction probability is visually consistent. Directly comparing these results with the expression for the interaction rate as a function of the Stokes number from [63], as shown in Eqn [3.5], is not feasible. This is because the values of the empirical constants in Eqn [3.5] were determined by [63] for a specific NGV design and setup, which differs from the design and setup used in this study. Nevertheless, the results are in agreement regarding the strong relationship between the Stokes number and the interaction rate of volcanic ash with the NGV surface.

Calculated dimensionless numbers.

The three main dimensionless numbers I consider in characterising the behaviour of a

droplet impact are the Weber, Ohnesorge and Weissenberg number. The first results for these numbers I will discuss are those from the CFD simulation with a uniform inlet temperature field. Composition data from several samples of volcanic ash, taken from a variety of volcanoes and rock types, were collected. The density and viscosity for each sample were initially calculated using the models in [55] and [14], respectively, for a temperature of 1728 K, typical of the cruise operating temperature for a modern turbofan engine. A value of $\sigma = 0.25 \text{ Nm}^{-1}$, which is typical for magmatic fluids [79, 80], was used for the surface tension. For the simulations with varying inlet temperature fields, the temperatures of the particles impacting along the NGV, calculated from Fluent, were used as the input temperature to the density and viscosity models. The same values as before for the physical properties of the ash were used. Along with the diameters of the impacting particles and their corresponding velocities, the Weber, Ohnesorge, and Weissenberg numbers were calculated for the various ash compositions. The results of these are shown in Fig [3.17] as Gaussian kernel density plots for the dimensionless numbers against the distance along the NGV. Each data point was weighted again for the particle's mass and the value of the particle size distribution for the particle's diameter.

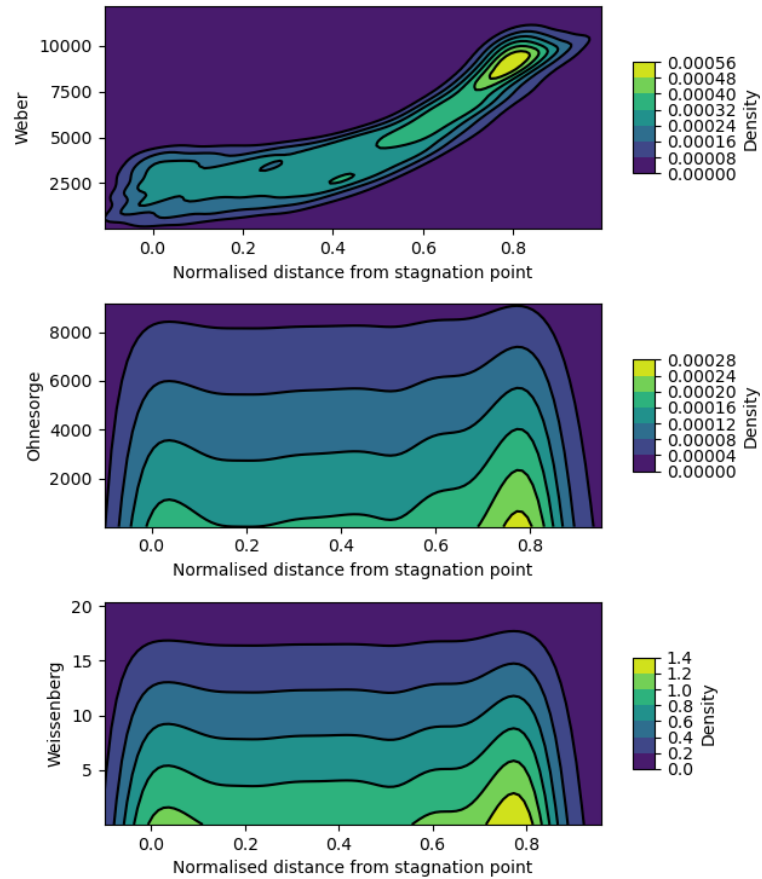


Figure 3.17: Gaussian kernel density plots for the Weber, Ohnesorge and Weissenberg numbers along the NGV surface from the first isothermal CFD simulation. Each data point was weighted with the PSD and the particle’s dimensionless mass.

Fig [3.17] shows that there is a variation of the Weber number with position on the vane, with a range of 2500-10000, with smaller Weber numbers closer to the stagnation point on the suction surface and larger Weber numbers towards the trailing edge of the pressure surface. The variation of the Weissenberg number and Ohnesorge number with position on the vane can also be seen. In these figures it is evident that the Ohnesorge and Weissenberg numbers do not vary greatly with respect to their position on the vane. Similar results were found for the simulations with the varying inlet temperature fields with respect to the variation of the Weber, Ohnesorge and Weissenberg numbers along the NGV surface, so these results are not shown in the main body of this work.

In order to get an insight into the behaviour of the bulk of the impacting mass on the NGV, a Gaussian kernel density plot of the impact Weber numbers against the impact Ohnesorge

numbers was produced, and the limits in the Weber Ohnesorge plane from Schiaffino and Sonin [48] were plotted on top. This can be seen in Fig [3.18], where each data point was weighted again for the particle’s mass and the value of the particle size distribution for the particle’s diameter.

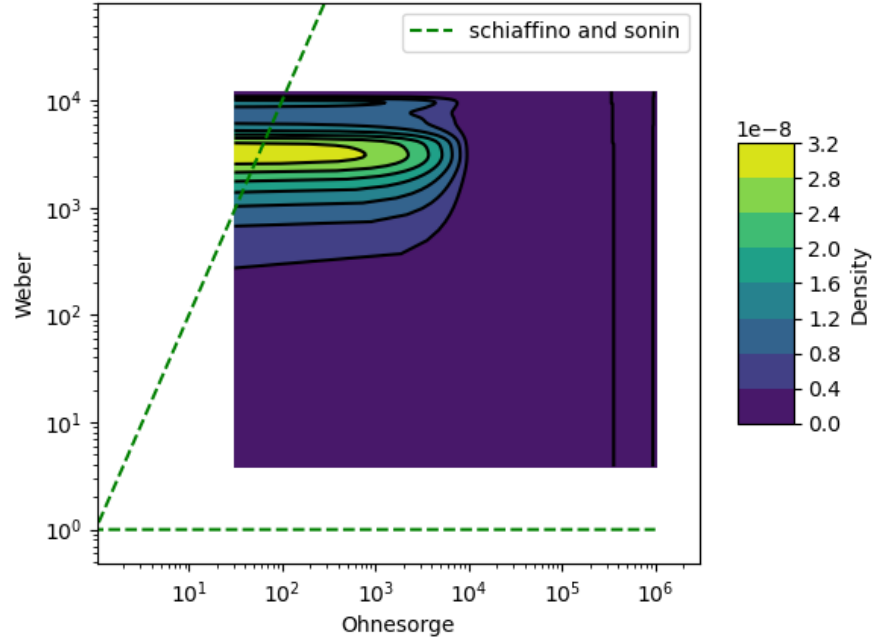


Figure 3.18: Gaussian kernel density plot of the Weber numbers against the Ohnesorge numbers. Each data point was weighted with the PSD and the particle’s dimensionless mass. The asymptotic limits in the Weber-Ohnesorge plane from Fig [2.2] are also shown.

Most of the impacts associated with the bulk of the mass occur in a narrow range of Weber and Ohnesorge numbers spanning approximately $10^2 < We < 10^4$ and $10^1 < Oh < 10^4$. It can be seen that most of the impacts occur in region 4 of the Schiaffino and Sonin Weber and Ohnesorge diagram, where the spreading of the droplets on the surface after impact is driven by the impact pressure and resisted by the viscous forces of the droplet. However, the most densely populated part of the Weber-Ohnesorge space crosses into region 1, where the spreading of the droplets is driven by impact pressure but resisted by inertial forces. This means according to Schiaffino and Sonin that two sets of different physics govern the impacts of ash particles on the vane, and different spreading dynamics can be expected.

A similar Gaussian density plot was also made but for the Weber and Weissenberg numbers, and the critical Weissenberg number of $Wi_c = 0.01$ was plotted. Above $Wi_c = 0.01$ it is thought elastic forces start to dominate over viscous forces, leading to the droplet po-

tentially bouncing off the surface instead of sticking. This can be seen in Fig [3.19], where each data point was weighted again for the particle’s mass and the value of the particle size distribution for the particle’s diameter.

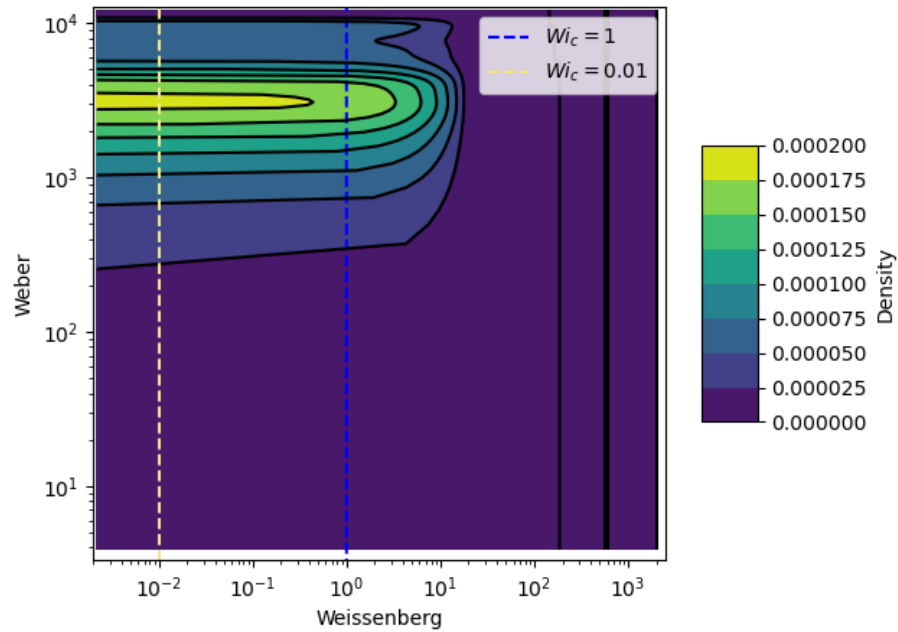


Figure 3.19: Gaussian kernel density plot of the Weber numbers against the Weissenberg numbers. Each data point was weighted with the PSD and the particle’s dimensionless mass. The limit of a hypothetical critical Weissenberg number of $Wi_c = 0.01$ and $Wi_c = 1$ are also shown.

The impacts associated with the bulk of the mass in Weber-Weissenberg number space are bisected by the Wi_c . This means that a significant proportion of the ash particles impacting the NGV could be expected to bounce off the surface. However, the exact value of Wi_c for molten silicate droplets is not known, and how the value of Wi_c changes with impact angle is also unknown. If $Wi_c = 0.01$ then most of the impacting volcanic ash droplets would bounce, however if $Wi_c = 1$ then most of the volcanic ash would be expected to stick on the surface.

I will now discuss the dimensionless numbers associated with the simulations involving the four different sinusoidal inlet temperature fields. The plots in Fig [3.18] and Fig [3.19] were reproduced for the simulations of the four different inlet temperature fields and both the resulting ‘hot’ and ‘cold’ NGV impacts where the impact particle temperatures were collected and used in the calculation of the associated dimensionless numbers. The subplots

are plotted on the same axis to enable comparison.

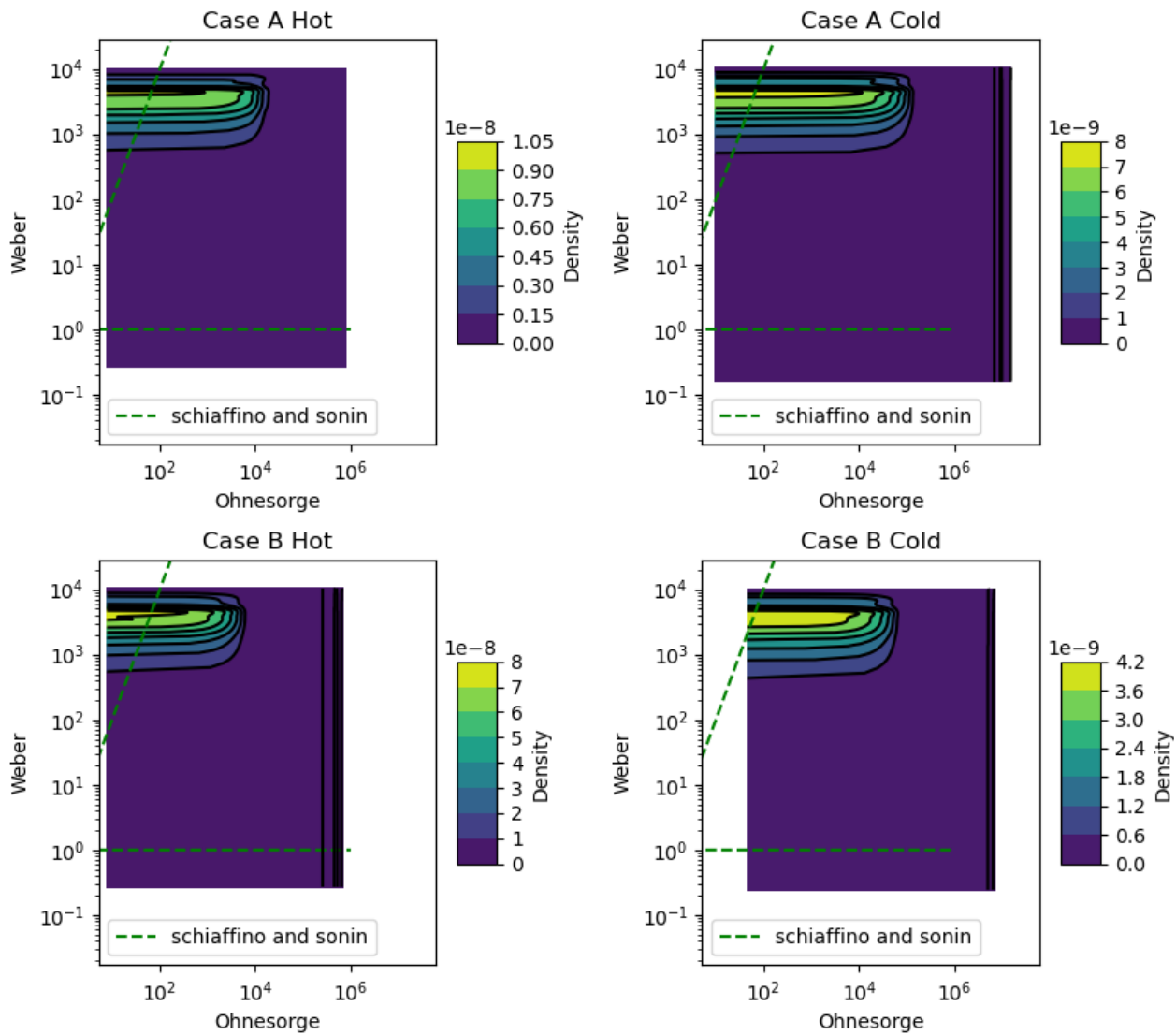


Figure 3.20: Gaussian kernel density plot of the Weber numbers against the Ohnesorge numbers. The asymptotic limits in the Weber-Ohnesorge plane from Fig [2.2] are also shown. The inlet temperature amplitude for all the NGVs shown here was 150 K.

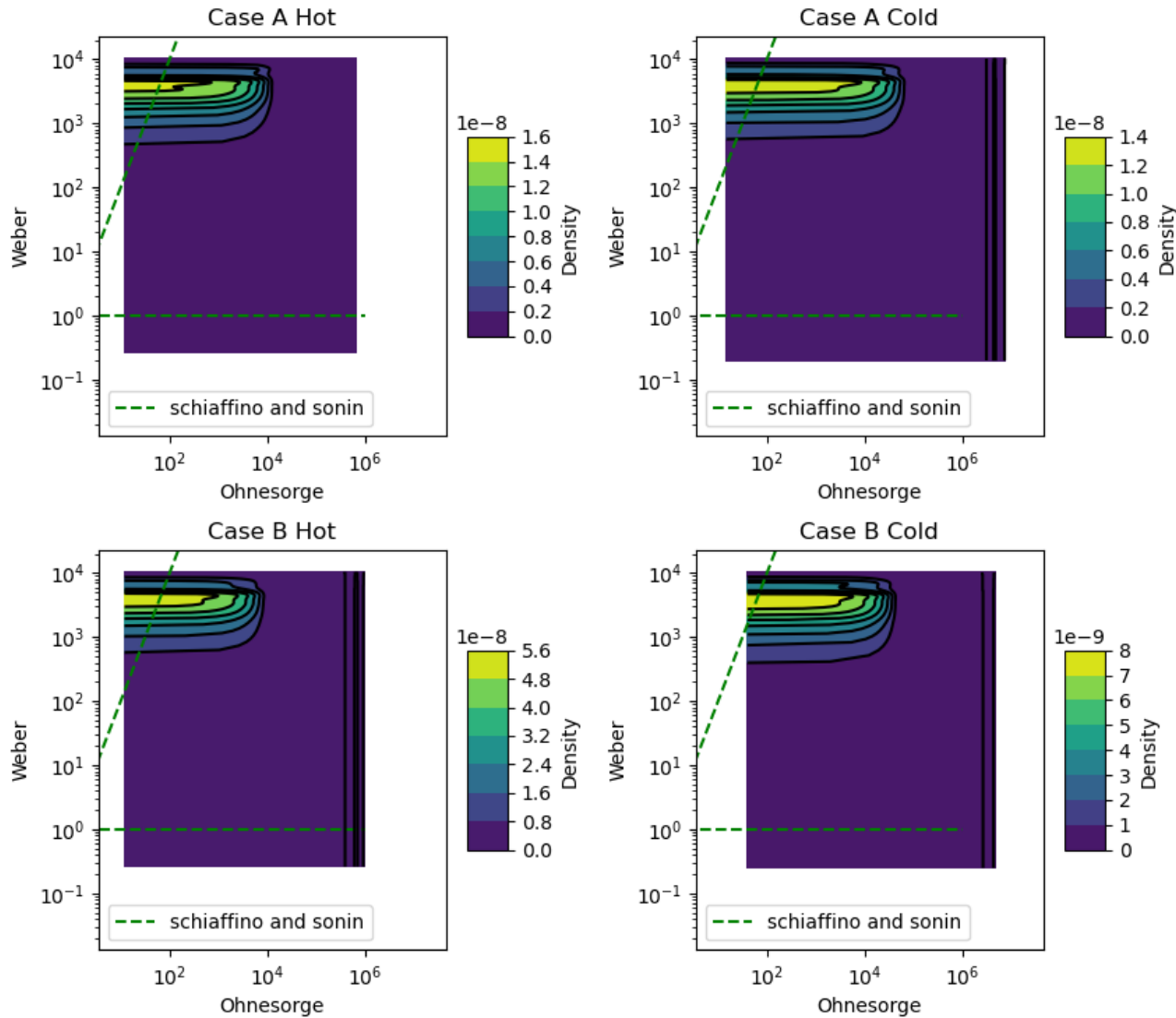


Figure 3.21: Gaussian kernel density plot of the Weber numbers against the Ohnesorge numbers. The asymptotic limits in the Weber-Ohnesorge plane from Fig [2.2] are also shown. The inlet temperature amplitude for all the NGVs shown here was 100 K.

In Fig [3.20] and Fig [3.21] can be seen kernel density plots of the Ohnesorge numbers against the Weber numbers. Comparing these figures to each other it can be seen that for all the inlet temperature fields and for both the case of the ‘hot’ and ‘cold’ NGVs the range of the Weber numbers is the same. This is thought to be because the only temperature sensitive quantity in the Weber number is the density of the molten volcanic ash, and at larger temperatures the density of the ash becomes less sensitive to changes in temperature. However, the effect of the changing impact temperatures can be seen more clearly in the variation of the Ohnesorge numbers, with the ‘cold’ NGV with temperature inlet field from

Case B with an amplitude of 100 K having the largest minimum Ohnesorge numbers. The variation in Ohnesorge numbers means that for different NGVs in different inlet temperature fields, there will be a significant variation in the proportion of impacts that fall into region 1 of the Schiaffino and Sonin Weber and Ohnesorge number diagram. This is particularly pronounced in the instance of the temperature inlet field of Case B for both amplitudes considered here. For engines of this type, the hotter NGV would have a greater proportion of the impacts upon it falling into region 1 of the Schiaffino and Sonin diagram whilst the neighbouring colder NGV would have a smaller proportion of the impact upon it falling into region 1 of the diagram.

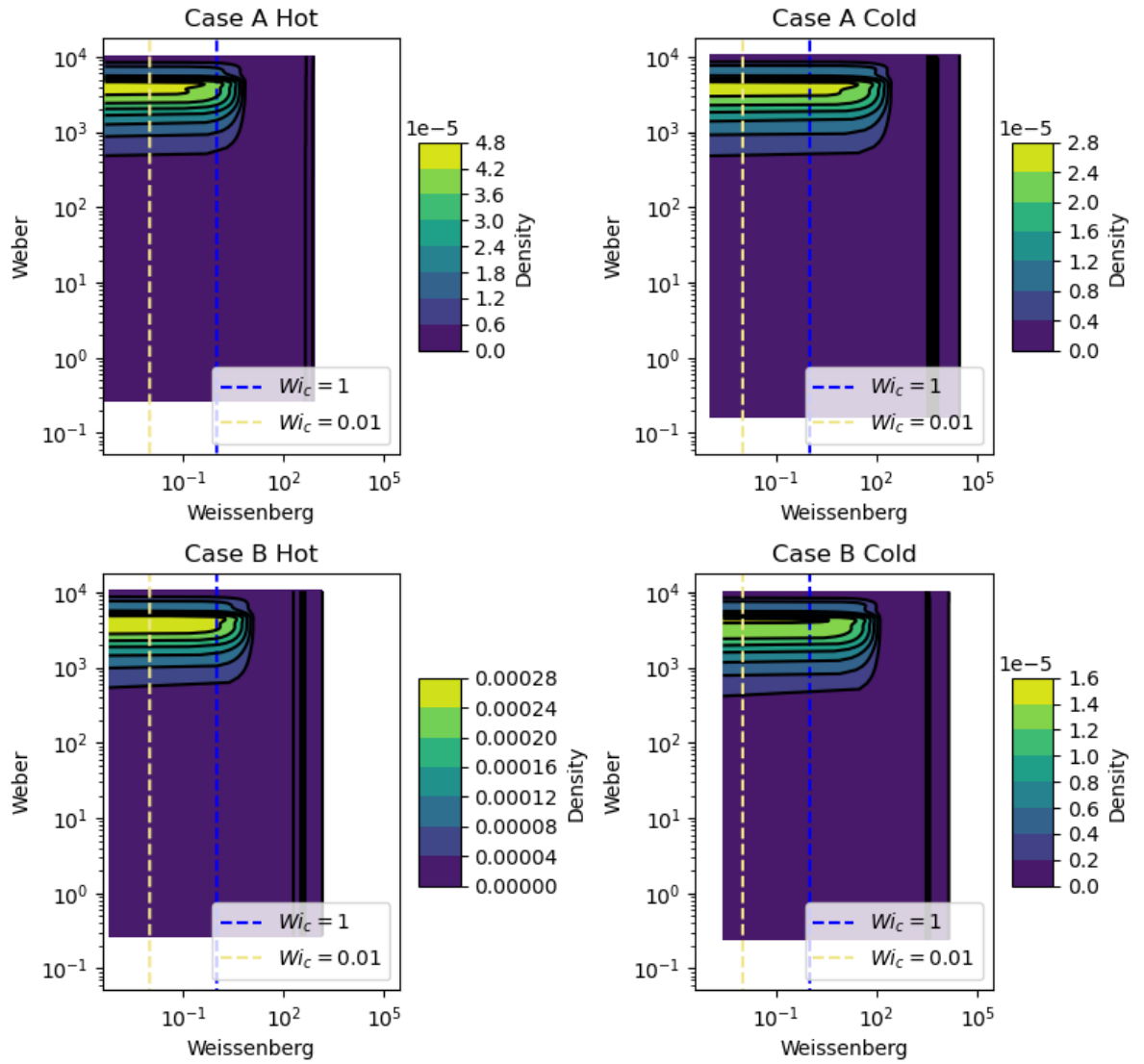


Figure 3.22: Gaussian kernel density plot of the Weber numbers against the Weissenberg numbers. The limit of a hypothetical critical Weissenberg number of $Wi_c = 0.01$ and $Wi_c = 1$ are also shown. The inlet temperature amplitude for all the NGVs shown here was 150 K.

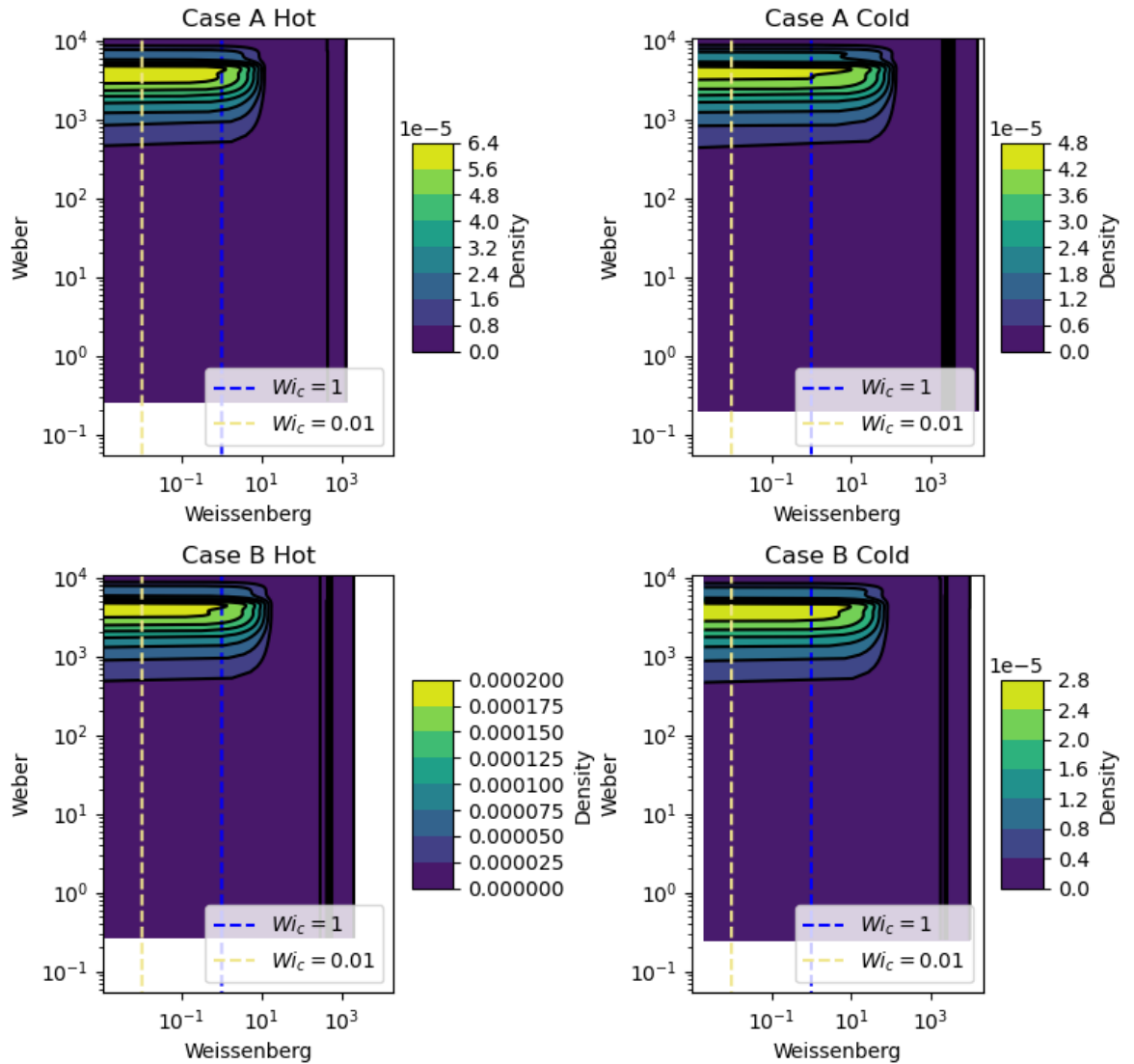


Figure 3.23: Gaussian kernel density plot of the Weber numbers against the Weissenberg numbers. The limit of a hypothetical critical Weissenberg number of $Wi_c = 0.01$ and $Wi_c = 1$ are also shown. The inlet temperature amplitude for all the NGVs shown here was 100 K.

Figures [3.22] and [3.23] display kernel density plots of the Weissenberg numbers against the Weber numbers. Across all the inlet temperature fields, the colder NGVs exhibit a higher minimum Weissenberg number compared to the neighbouring, hotter NGVs. This indicates that potentially, two neighbouring NGVs within a given engine could experience different proportions of impacts with a Weissenberg number $Wi < Wi_c$, resulting in different proportions of ash droplets impacting and bouncing off. For both the ‘hot’ and ‘cold’ NGVs with an inlet temperature field of Case B, the minimum Weissenberg numbers are greater than those for an inlet temperature of Case A. This suggests that a greater proportion of volcanic

ash droplets would likely bounce off NGVs in engines of Case B compared to Case A.

After identifying the values of the relevant dimensionless numbers associated with ash particles impacting on an NGV, the next necessary step in investigating the deposition and shedding of volcanic ash is to conduct scaled experiments of droplet impacts onto surfaces. I have reviewed previous droplet impact experiments in the broader literature and found that no experiments have been conducted previously within the same dimensionless number space. The aim of these scaled experiments would be to observe the behaviour of impacting droplets in the relevant dimensionless number space and to develop a better understanding of the physics that govern such impacts. Improved understanding of the physics behind the accumulation of ash droplets on NGV surfaces could lead to a better understanding of the tolerance of gas turbine engines when exposed to volcanic ash, as well as better estimations of the safe ‘doses’ of volcanic ash that aircraft engines can withstand in-flight.

3.6 Conclusions

In this work, computational fluid dynamics is undertaken in Ansys Fluent to simulate airflow laden with volcanic ash particles through a High-Pressure Nozzle Guide Vane (HP-NGV) array. Guided by variations in engine design and setup, I additionally vary the distribution of input temperature, mimicking variations in where the combustor burners aim their hot spots. The associated impact properties of the particles on the HP-NGVs are recorded, revealing significant variations in particle impact angle, velocity, diameter, and temperature with impact location on the Nozzle Guide Vane surface.

There was a strong variation in impact angle and velocity with position on the vane: more glancing impact angles were observed towards the trailing edge of the pressure surface, while more normal impacts occurred towards the stagnation point of the suction surface. Higher velocities were recorded towards the trailing edge, and lower velocities were noted towards the stagnation point.

The behaviour of the bulk of the mass was also studied, showing different impact conditions compared to the behaviour of the majority of the impacting particles. It was also demonstrated that most of the mass impacts on the pressure surface towards the trailing

edge, due to the impacts of many smaller particles on the same region of the NGV surface.

I then used the impact properties of the particles on the NGVs to compute the Weber number, Ohnesorge number, and Weissenberg number associated with each impact, and demonstrate how these dimensionless numbers change along the vane. To provide further insight into the sticking, splashing, and bouncing behaviour of volcanic ash particles on the NGV surface, it would be necessary to perform a set of experiments that are well scaled according to the dimensionless numbers and impact angles presented here. The efforts made by myself to perform these experiments are detailed in the following chapters of this thesis.

Chapter 4

Scaled Splashing experiments.

4.1 Introduction

In the previous chapters I identified the dimensionless numbers that are used in the literature to classify and describe droplet impacts on surfaces. I have also shown, through the analysis of combined datasets from the literature using generalised linear mixed models, that out of all the dimensional parameters, impact velocity is the most important factor in determining whether a droplet will splash on impact. This parameter is more significant than others, such as surface roughness and droplet viscosity. In terms of the dimensionless numbers, this new analysis has shown that the Weber number is the most important dimensionless number in determining whether a droplet splashes or not on impact, with the Ohnesorge number adding no additional information to a statistical model with the Weber and or Reynolds number already included.

I used computational fluid dynamics (CFD) modelling to find the regime space defined by the dimensionless numbers that the impacts of molten ash on the NGV occupy, and how they vary along the surface of the NGV. I found that the past experimental work does not represent this regime space well. I also found that very little work was done on the effect of the impact angle on the droplet splashing behaviour, and no work has been done on this angle effect in the regime space relevant to ash impacts in the jet engine.

This meant that new experiments needed to be designed that sit in the same regime space as the volcanic ash droplet impacts on the Nozzle Guide Vane (NGV) surface, in order to capture the behaviour of ash impacts and investigate whether or not ash splashes on impact

with the NGV in the engine. These experiments also needed to investigate the effect of impact angle in this regime. This is because it was found in Chapter 3 that the angle at which ash impacts on the NGV varies greatly, and the impact angle is known to affect the splashing behaviour [41].

This chapter describes how droplets of various fluids with different viscosities and other properties, were produced and made to impact on a smooth surface. It is described how the droplet properties were modified so as to produce impacts that were scaled to the jet engine case of ash droplet impacts on the NGV, and how the droplets were made to impact on surfaces with a range of inclination angles. Finally, it is described how the videos of the droplet impacts were analysed, and how the conclusions from this analysis informed the next stage of this investigation.

4.2 Method

4.2.1 Identification of key dimensionless numbers.

In order to produce scaled experiments, it was first necessary to decide which dimensionless numbers to use to determine the regime space. I chose the Weber number and the Ohnesorge number. The analysis of the past experimental data revealed that the Weber number was the most important dimensionless number in determining splashing, but it also showed that the Ohnesorge number had no real effect on the splashing/deposition outcome. I chose the Ohnesorge number despite this, as Schiaffino and Sonin [48] define their regime space in terms of both the Ohnesorge and Weber number. They also change the mathematical formulation of the other dimensionless numbers, like the Reynolds number, depending on the values of the Weber and Ohnesorge number. This means that according to Schiaffino and Sonin [48] the Weber and Ohnesorge numbers are the only dimensionless numbers whose definition is independent and unchanging. By presenting the experiments here in terms of the Weber and Ohnesorge number the results can be more easily compared with previous work, as the corresponding Reynolds number can be calculated using the definitions of [48] or the conventional definition. It was for these reasons, that the experiments were chosen to be scaled to the jet engine case by the Weber and Ohnesorge number.

4.2.2 Selection of analogous fluids.

The analogous fluids that were considered were glycerol and solutions of golden syrup in water varying in concentration from 69% – 95% golden syrup by mass. Solutions of water and golden syrup have long been used as analogous fluids in scaled experiments in volcanology. Due to this, and a large body of research into the properties of sugar solutions, the physical properties of golden syrup solutions and how these properties vary with temperature and sugar concentration are well known.

Pure silicate melts have a Newtonian rheology for strain rates much less than the inverse of their structural relaxation time, $\dot{\gamma} \ll 1/\lambda_r$ [13] [14][15]. A Newtonian fluid is one which deforms with a strain rate proportional to the applied stress, τ , where the constant of proportionality is the fluid's viscosity, μ :

$$\tau = \mu\dot{\gamma}. \quad (4.1)$$

Therefore, it is important that the analogous fluids that are used here also exhibit a Newtonian rheology.

Properties from the literature.

Jones et al [81] performed various rheological measurements of golden syrup, golden syrup solutions and glycerol. They used oscillatory rheometry to measure how the viscosity of these fluids varied with temperature. They found that both glycerol and the golden syrup solutions had a Newtonian rheology.

Using the data from their measurements, Jones et al [81] present an empirical equation for the viscosity of golden syrup solutions as a function of both temperature, T , and the proportion of water in the solution X_{water} , such that for a solution of 80% of golden syrup by mass, $X_{water} = 0.2$:

$$\mu = \mu_0(X_{water})\exp[-k(X_{water})T]. \quad (4.2)$$

Here μ_0 is the viscosity of a solution at a temperature of $T = 0^\circ\text{C}$ and varies with X_{water} as:

$$\mu_0 = 1641.7\exp[-40.752X_{water}], \quad (4.3)$$

and k is a constant with units $^\circ\text{C}^{-1}$ that varies with X_{water} as:

$$k(X_{water}) = 0.1609\exp[-3.679X_{water}]. \quad (4.4)$$

Jones et al [81] also found the rheology of glycerol to be Newtonian, and also highly dependent on temperature.

Equations [4.2-4.4] were used to identify the concentrations of golden syrup solutions needed to produce a selection of fluids with a range of desired viscosities.

In order to calculate the Weber and Ohnesorge numbers associated with the droplet impacts of the analogous fluids it is necessary to know both the surface tension and density of the fluids as well as the viscosity. Llewellyn et al [82] found a value for the surface tension of golden syrup $\sigma = 0.08\text{Nm}^{-1}$, but they did not perform the same measurements on solutions of golden syrup. However, Peacock [83] presents an empirical formula for how the surface tension of a sugar solution varies with temperature, T , and the Brix degree $^{\circ}B$ of the solution, where the Brix degree indicates the strength of a sugar solution as a percentage by mass:

$$\sigma = 0.07575 - 1.4518 \times 10^{-4}T - 2.3922 \times 10^{-7}T^2 + 1.10 \times 10^{-4} \times ^{\circ}B. \quad (4.5)$$

In Fig [4.1] it can be seen how the surface tension varies with the Brix degree at a temperature of $T = 21^{\circ}\text{C}$, according to Eqn [4.5].

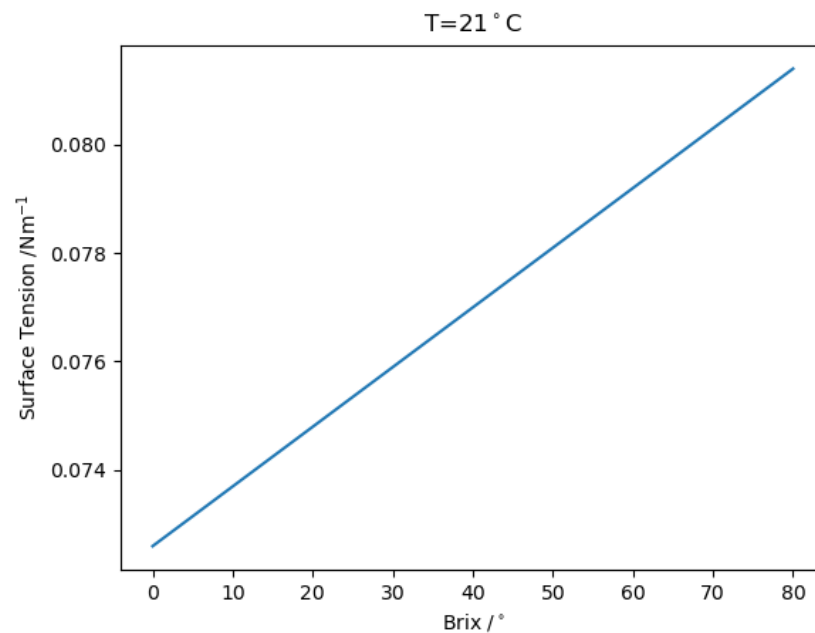


Figure 4.1: Variation of the surface tension of a sugar solution with the Brix degree at a constant temperature of 21°C .

It can be seen in Fig [4.1] that the surface tension increases linearly with an increase in the strength of the sugar solution. Given this linear relationship and that the difference between the surface tension of golden syrup and water is less than 10%, a constant value of $\sigma = 0.076 \pm 0.002 \text{ Nm}^{-1}$ was chosen to be used for all the golden syrup solutions used as analogous fluids in the experiments presented here.

The surface tension of glycerol has been well reported in the literature and is known to be $\sigma = 0.0634 \pm 0.0001 \text{ Nm}^{-1}$ at $T = 20^\circ\text{C}$ [84].

The remaining property of the analogous fluids required is the density. The density of glycerol at $T = 20^\circ\text{C}$ is known to be $\rho = 1264.02 \pm 0.01 \text{ kgm}^{-3}$ [85]. For the density of the golden syrup solutions, Jones et al [81] present an empirical equation for the density as a function of water concentration and temperature:

$$\rho = -0.58734T - 5.3542X_{water} + 1450.5. \quad (4.6)$$

Eqn [4.6] was used in the work reported below.

Analogous fluid production and measurements.

A mass of golden syrup was first measured on a balance, and then the mass of water needed to yield the desired concentration of golden syrup in the solution was found. The water was then added to the golden syrup and the two fluids were mixed together with an OHS 200 ADVANCE Overhead stirrer from VELP Scientific Srl (Via Stazione,16, 20865 , Usmate Velate (MB), Italy). The mixing was done slowly so as not to trap any air bubbles in the fluid which has been shown to alter the rheology [82].

The viscosities of all the fluids used were measured by rotational rheometry on a Thermo-Scientific (Waltham, Massachusetts, U.S.) HAAKE Viscotester iQ rheometer using a bob and cup geometry. The temperature of the sample fluid was controlled with a Peltier plate, and when the fluid was added it was left in the Peltier for 15 minutes each time to ensure that it reached the desired temperature. Before each measurement the rheometer was calibrated using its internal software to correct for inertia effects. During the rotational rheometry the strain rate was increased from 0.5 s^{-1} to 50 s^{-1} then decreased to 0.5 s^{-1} . Ten measurement

points were chosen, placed logarithmically equidistant from each other on this range. The applied stress and the viscosity were measured at each point.

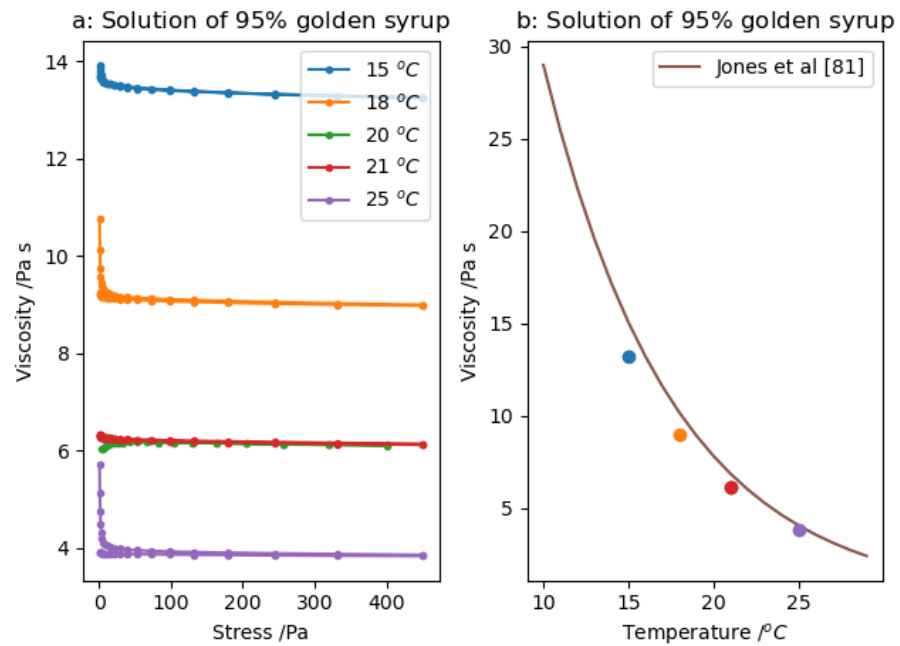


Figure 4.2: a: Changes in viscosity of a solution of 95% golden syrup when different stresses are applied at 5 different temperatures. b: Changes in viscosity of 95% golden syrup over 5 different temperatures. Note the error bars are smaller than the markers.

It can be seen in Fig [4.2] that, excluding low stresses where the measurements of viscosity are unreliable due to the rotational torque being too small [86], the viscosity of the solution is constant with increasing stress and hence the fluid shows a Newtonian rheology. It can also be seen that the viscosity increases significantly with a moderate decrease in temperature. For all the fluids that were used, the measured viscosity was taken to be when the viscosity became constant with increasing stress.

In Table 4.1 can be seen the fluids used and their viscosities at a temperature of $T = 21^{\circ}\text{C}$.

Table 4.1: The analogue fluids used and their viscosities at a temperature of $T = 21^{\circ}\text{C}$.

Fluid	Viscosity (Pa s)
69.0 % Golden syrup,	0.04 ± 0.01
70.0 % Golden syrup,	0.05 ± 0.01
75.0 % Golden syrup,	0.08 ± 0.01
80.0 % Golden syrup,	0.16 ± 0.01
85.0 % Golden syrup,	0.43 ± 0.01
87.5 % Golden syrup,	0.83 ± 0.01
89.8 % Golden syrup,	1.35 ± 0.01
90.8 % Golden syrup,	1.88 ± 0.01
92.0 % Golden syrup,	2.53 ± 0.01
95.0 % Golden syrup,	7.33 ± 0.02
Glycerol	1.41 ± 0.01

4.2.3 Droplet production

To create the droplets a Vermes 3020⁺ micro dispensing system (MDS) from Vermes (VERMES Microdispensing GmbH, Rudolf-Diesel-Ring 2 83607 Holzkirchen, Germany) was used. This system can handle fluids up to a viscosity of 8 Pa s. This system works by putting the fluid under constant pressure. A valve is then opened and closed to produce droplets of fluid, which are ejected at speed. By changing the time for which the valve is opened, how far the valve is opened, the speed of the valve being opened and closed, and the pressure the fluid is subject to, the droplet shape and velocity can be varied [87]. Below in Fig [4.3] and Fig [4.4] a diagram, taken from communication with Vermes, of the dispensing system can be seen.

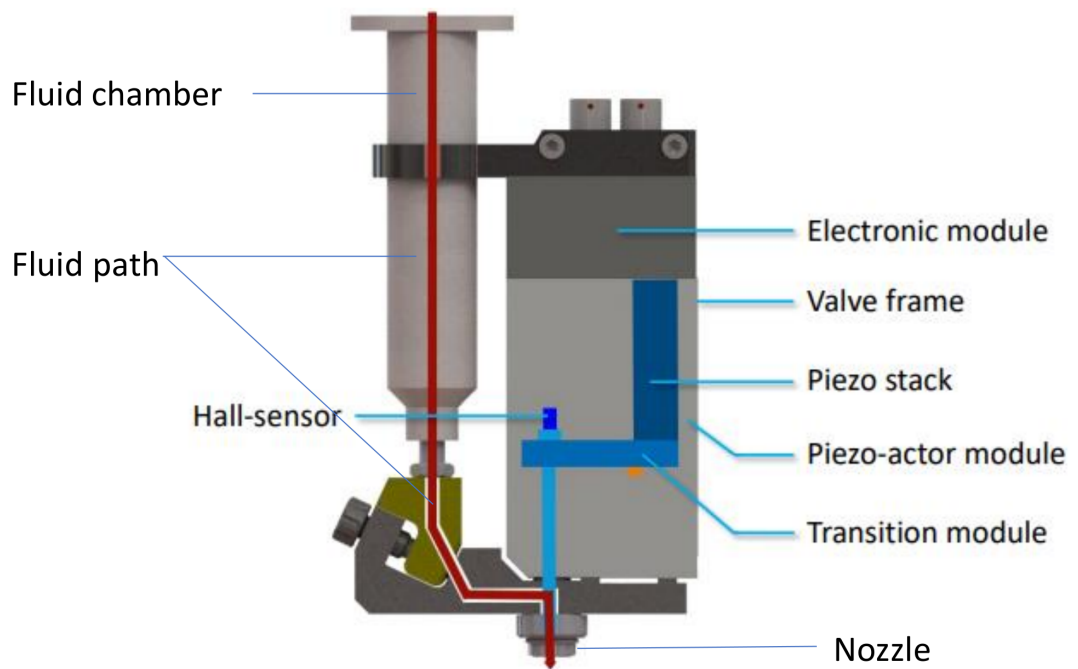


Figure 4.3: A diagram of the MDS 3020⁺ dispensing system that was used in this work, taken from communication with Vermes.

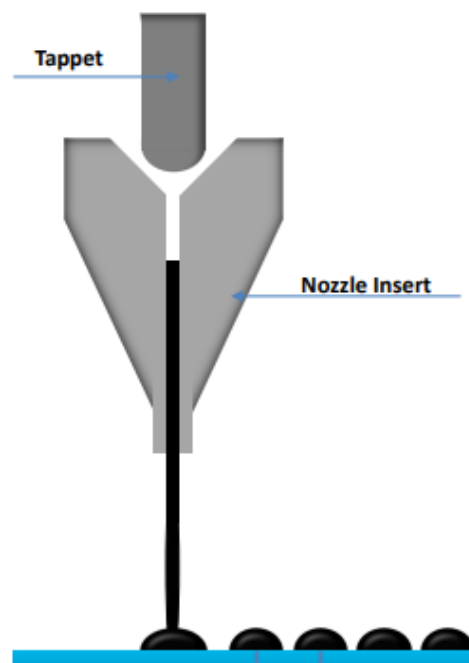


Figure 4.4: A diagram showing the position of the tappet with respect to the nozzle. When the tappet is open fluid flows through the nozzle to form droplets that then impact on the surface below.

In the first set of experiments for each analogue fluid in Table 4.1, the MDS was used

to dispense droplets onto a horizontal glass slide. The settings were varied for each fluid to produce droplets with increasing velocity whilst keeping the diameter as large as possible so as to achieve the largest Weber number possible. I stopped varying the system settings when the MDS could no longer produce droplets. Between each droplet ejection the nozzle was wiped with Isopropyl alcohol (IPA) to clean it, and at the end of each set of experiments the equipment was cleaned in a sonicator bath, rinsed with de-ionised water, and dried with compressed air. It was found that for droplets with a viscosity >1 Pa s, the maximum pressure that could be delivered to the fluid chamber (2 bar) was not enough to eject a droplet. Therefore, a system to supply a pressure of up to 6 bar to the fluid chamber was created that allowed more viscous droplets to be ejected, and the experiments were repeated.

The settings for a given droplet size and velocity were very sensitive to the fluid viscosity, with more viscous fluids needing a higher pressure to produce a droplet. Also, the dispensing settings did not allow the droplet size and velocity to be varied independently, for example to increase the velocity of an ejected droplet it was necessary to reduce the diameter of the droplet.

It was found to be very difficult to produce droplets of high viscosity $\mu \geq 2$ Pa s consistently. This is probably because residual fluid that had not been ejected as a droplet blocked further droplets from being ejected. For droplets of lower viscosity this problem could be solved by wiping the nozzle, and increasing the pressure but there was a pressure limit of 6 bar on the equipment used. For this reason, for further experiments involving angled impacts, only glycerol and golden syrup solutions of 89.8% and 87.5% were used. Less viscous fluids were not used as initial analysis from the impacts on a horizontal glass slide indicated they were not well scaled to the jet engine case.

To achieve non-normal droplet impact angles, a series of platforms that could hold a glass slide at an angle, were designed and then manufactured by 3D printing. The platforms were designed to allow impact angles of 60° , 50° , 40° , and 30° with respect to the surface normal.

4.2.4 Image capture and analysis

All the impacts were filmed with a Photron AX mini 200 camera manufactured by Phototron (Phototron, IMAGICA GROUP Inc., Tokyo, Japan). The videos of the impacts were then

analysed using a Python code written by myself, allowing the extraction of the velocity and diameter of the impacting drops. This allowed the Weber and Ohnesorge numbers to be calculated. Based on the pixel size of the camera and a frame rate of 10000 fps the relative error in the measurements of droplet diameter and velocity were taken to be 0.01 and 0.05 respectively. The evolution of the droplet shape on impact with the surface was also analysed using an open-source Python code [88]. This code works by fitting an ellipse to the edge of the droplet allowing the droplet contact angles, spreading diameter and height to be calculated and the evolution of these to be tracked during and after the initial impact. It should be noted that this code does not fit a full ellipse around the droplet, with some of the fitted ellipse extending below the surface on which the droplet rests. An example of an ellipse fitted to a frame of one video of a droplet spreading is shown in Fig [4.5].

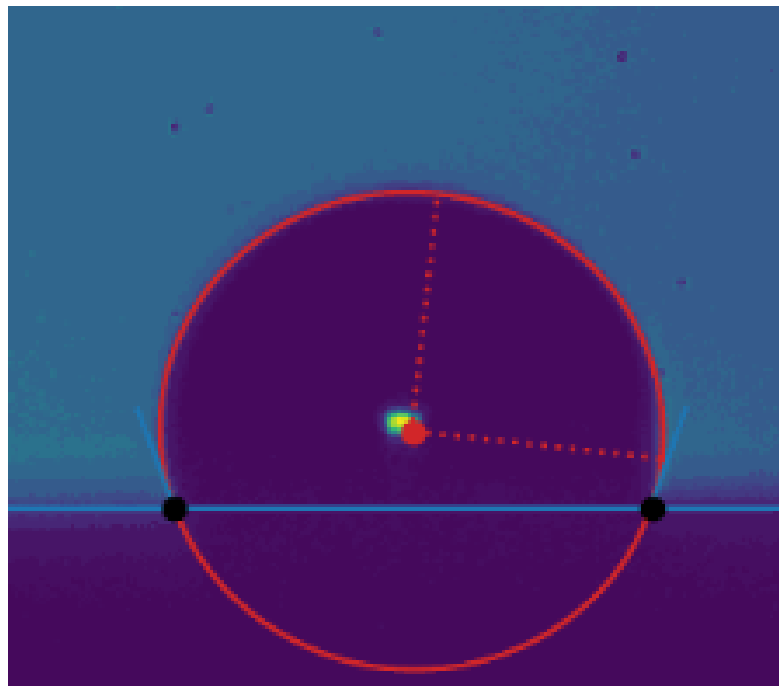


Figure 4.5: An ellipse fitted to an image of a droplet spreading on a surface using the code from [88]. Note the tangents fitted to the edges of the ellipse, the contact angles were measured with respect to them and the horizontal.

4.3 Results and Analysis

The droplet impact conditions recorded can be seen in Table 4.2.

Table 4.2: Droplet impact conditions from the scaled experiments.

Viscosity (Pa s)	ρ (kgm ⁻³)	Diameter (m)	σ (Nm ⁻¹)	Velocity (ms ⁻¹)	Angle (°)
1.41	1.26E+03	3.51E-04	6.34E-02	1.68	0
1.41	1.26E+03	3.86E-04	6.34E-02	0.40	0
1.41	1.26E+03	6.86E-04	6.34E-02	0.68	0
1.41	1.26E+03	6.10E-04	6.34E-02	0.61	0
1.41	1.26E+03	6.25E-04	6.34E-02	1.09	0
1.41	1.26E+03	5.99E-04	6.34E-02	1.17	0
1.41	1.26E+03	6.35E-04	6.34E-02	1.19	0
1.41	1.26E+03	5.74E-04	6.34E-02	1.35	0
1.41	1.26E+03	6.10E-04	6.34E-02	1.11	0
1.41	1.26E+03	2.95E-04	6.34E-02	8.13	0
1.41	1.26E+03	6.71E-04	6.34E-02	1.31	0
1.41	1.26E+03	7.32E-04	6.34E-02	1.39	0
1.41	1.26E+03	4.88E-04	6.34E-02	1.42	0
0.83	1.40E+03	3.73E-04	7.50E-02	5.10	0
0.83	1.40E+03	4.36E-04	7.50E-02	2.50	0
0.83	1.40E+03	2.75E-04	7.50E-02	3.82	0
0.83	1.40E+03	3.42E-04	7.50E-02	1.19	0
0.83	1.40E+03	3.37E-04	7.50E-02	1.22	0
0.83	1.40E+03	2.85E-04	7.50E-02	0.84	0
0.83	1.40E+03	6.28E-04	7.50E-02	0.80	0
0.83	1.40E+03	4.77E-04	7.50E-02	5.21	0
0.83	1.40E+03	3.27E-04	7.50E-02	0.45	0
0.83	1.40E+03	4.30E-04	7.50E-02	1.53	0
0.83	1.40E+03	3.16E-04	7.50E-02	2.67	0
1.41	1.26E+03	4.13E-04	6.34E-02	4.37	0
1.41	1.26E+03	3.82E-04	6.34E-02	4.02	0
1.41	1.26E+03	3.82E-04	6.34E-02	3.22	0
1.41	1.26E+03	5.52E-04	6.34E-02	2.06	0
1.41	1.26E+03	2.94E-04	6.34E-02	4.01	0

Table 4.2: Droplet impact conditions from the scaled experiments.

Viscosity (Pa s)	ρ (kgm ⁻³)	Diameter (m)	σ (Nm ⁻¹)	Velocity (ms ⁻¹)	Angle (°)
1.41	1.26E+03	3.51E-04	6.34E-02	4.68	0
1.41	1.26E+03	4.80E-04	6.34E-02	4.05	0
1.41	1.26E+03	3.15E-04	6.34E-02	2.44	0
1.41	1.26E+03	2.68E-04	6.34E-02	2.51	0
1.41	1.26E+03	2.68E-04	6.34E-02	2.51	0
1.41	1.26E+03	2.68E-04	6.34E-02	4.44	0
1.41	1.26E+03	2.48E-04	6.34E-02	0.66	0
1.41	1.26E+03	1.34E-04	6.34E-02	3.24	0
1.41	1.26E+03	3.51E-04	6.34E-02	3.83	0
1.41	1.26E+03	1.75E-04	6.34E-02	2.64	0
1.41	1.26E+03	2.84E-04	6.34E-02	1.61	0
1.41	1.26E+03	2.94E-04	6.34E-02	3.17	0
7.33	1.40E+03	5.81E-04	7.50E-02	0.83	0
7.33	1.40E+03	5.65E-04	7.50E-02	1.84	0
7.33	1.40E+03	2.80E-04	7.50E-02	3.07	0
7.33	1.40E+03	2.70E-04	7.50E-02	2.63	0
7.33	1.40E+03	4.56E-04	7.50E-02	2.78	0
7.33	1.40E+03	2.80E-04	7.50E-02	3.55	0
7.33	1.40E+03	2.07E-04	7.50E-02	2.71	0
0.04	1.30E+03	4.41E-04	7.50E-02	0.52	0
0.04	1.30E+03	8.46E-04	7.50E-02	1.31	0
0.04	1.30E+03	1.07E-03	7.50E-02	1.15	0
0.04	1.30E+03	8.15E-04	7.50E-02	1.16	0
0.04	1.30E+03	8.93E-04	7.50E-02	0.52	0
0.04	1.30E+03	9.45E-04	7.50E-02	1.23	0
0.04	1.30E+03	9.19E-04	7.50E-02	1.29	0
0.16	1.30E+03	5.03E-04	7.50E-02	2.06	0
0.16	1.30E+03	3.89E-04	7.50E-02	2.02	0
0.16	1.30E+03	2.70E-04	7.50E-02	2.00	0

Table 4.2: Droplet impact conditions from the scaled experiments.

Viscosity (Pa s)	ρ (kgm ⁻³)	Diameter (m)	σ (Nm ⁻¹)	Velocity (ms ⁻¹)	Angle (°)
0.16	1.30E+03	1.92E-04	7.50E-02	4.36	0
0.16	1.30E+03	1.40E-04	7.50E-02	1.69	0
0.16	1.30E+03	6.69E-04	7.50E-02	0.20	0
0.16	1.30E+03	3.06E-04	7.50E-02	3.50	0
1.41	1.26E+03	7.37E-04	6.34E-02	0.80	30
1.41	1.26E+03	7.32E-04	6.34E-02	0.77	30
1.41	1.26E+03	7.11E-04	6.34E-02	0.78	30
1.41	1.26E+03	7.72E-04	6.34E-02	1.21	30
1.41	1.26E+03	6.45E-04	6.34E-02	1.38	30
1.41	1.26E+03	7.55E-04	6.34E-02	0.83	40
1.41	1.26E+03	6.95E-04	6.34E-02	0.88	40
1.41	1.26E+03	7.15E-04	6.34E-02	0.92	40
1.41	1.26E+03	7.05E-04	6.34E-02	0.90	40
1.41	1.26E+03	7.15E-04	6.34E-02	0.89	50
1.41	1.26E+03	6.90E-04	6.34E-02	0.89	50
1.41	1.26E+03	7.05E-04	6.34E-02	0.92	50
1.41	1.26E+03	6.05E-04	6.34E-02	0.87	50
1.41	1.26E+03	5.35E-04	6.34E-02	0.88	50
1.41	1.26E+03	7.15E-04	6.34E-02	0.89	50
1.41	1.26E+03	6.90E-04	6.34E-02	0.89	50
1.41	1.26E+03	7.05E-04	6.34E-02	0.92	50
1.41	1.26E+03	6.05E-04	6.34E-02	0.87	50
1.41	1.26E+03	5.35E-04	6.34E-02	0.88	50
1.35	1.38E+03	5.89E-04	7.50E-02	1.57	30
1.35	1.38E+03	6.71E-04	7.50E-02	1.59	30
1.35	1.38E+03	6.71E-04	7.50E-02	1.58	30
1.35	1.38E+03	4.93E-04	7.50E-02	1.45	30
1.35	1.38E+03	5.84E-04	7.50E-02	1.59	30
1.35	1.38E+03	6.85E-04	7.50E-02	0.63	40

Table 4.2: Droplet impact conditions from the scaled experiments.

Viscosity (Pa s)	ρ (kgm ⁻³)	Diameter (m)	σ (Nm ⁻¹)	Velocity (ms ⁻¹)	Angle (°)
1.35	1.38E+03	5.25E-04	7.50E-02	0.69	40
1.35	1.38E+03	8.05E-04	7.50E-02	0.59	40
1.35	1.38E+03	6.90E-04	7.50E-02	0.57	40
1.35	1.38E+03	6.75E-04	7.50E-02	0.55	40
1.35	1.38E+03	8.75E-04	7.50E-02	0.74	50
1.35	1.38E+03	7.95E-04	7.50E-02	0.64	50
1.35	1.38E+03	9.00E-04	7.50E-02	0.79	50
1.35	1.38E+03	8.00E-04	7.50E-02	0.81	50
1.35	1.38E+03	8.30E-04	7.50E-02	0.63	50
1.35	1.38E+03	8.77E-04	7.50E-02	1.29	60
1.35	1.38E+03	8.82E-04	7.50E-02	1.20	60
1.35	1.38E+03	6.34E-04	7.50E-02	1.38	60
1.35	1.38E+03	8.15E-04	7.50E-02	0.95	60
1.35	1.38E+03	9.28E-04	7.50E-02	0.89	60
0.83	1.38E+03	7.32E-04	7.50E-02	1.08	30
0.83	1.38E+03	7.26E-04	7.50E-02	0.77	30
0.83	1.38E+03	7.72E-04	7.50E-02	1.06	30
0.83	1.38E+03	7.67E-04	7.50E-02	1.04	30
0.83	1.38E+03	2.00E-03	7.50E-02	1.02	30
0.83	1.38E+03	5.65E-04	7.50E-02	1.31	40
0.83	1.38E+03	6.05E-04	7.50E-02	1.34	40
0.83	1.38E+03	6.80E-04	7.50E-02	1.11	40
0.83	1.38E+03	7.60E-04	7.50E-02	0.47	40
0.83	1.38E+03	8.80E-04	7.50E-02	0.70	40
0.83	1.38E+03	9.05E-04	7.50E-02	0.59	50
0.83	1.38E+03	1.01E-03	7.50E-02	0.55	50
0.83	1.38E+03	1.03E-03	7.50E-02	0.69	50
0.83	1.38E+03	8.70E-04	7.50E-02	0.56	50
0.83	1.38E+03	9.30E-04	7.50E-02	0.48	50

Table 4.2: Droplet impact conditions from the scaled experiments.

Viscosity (Pa s)	ρ (kgm ⁻³)	Diameter (m)	σ (Nm ⁻¹)	Velocity (ms ⁻¹)	Angle (°)
0.83	1.38E+03	8.04E-04	7.50E-02	1.13	60
0.83	1.38E+03	7.32E-04	7.50E-02	1.05	60
0.83	1.38E+03	7.48E-04	7.50E-02	0.96	60
0.83	1.38E+03	7.48E-04	7.50E-02	0.91	60
0.83	1.38E+03	9.02E-04	7.50E-02	0.77	60

The main result from this work is that no splashing was observed. This was the case even at the highest Weber numbers recorded, which corresponded to Weber numbers where splashing had been observed in the literature [40], and for all of the impact angles for which experiments were run. Below in Fig [4.6] and Fig [4.7] video stills can be seen from droplets of an 87.5% golden syrup solution impacting at angles with respect to the normal of 0° and 60° respectively.

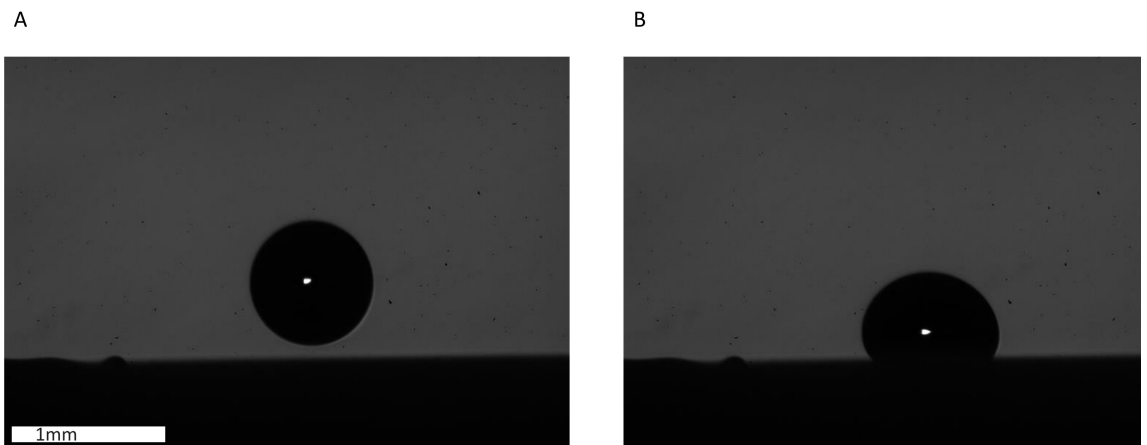


Figure 4.6: Video stills ≈ 0.002 seconds before and after impact of a droplet of 87.5% golden syrup solution impacting at a velocity of 1ms⁻¹ and angle of 0°. The scale bar indicates a length of 1mm.

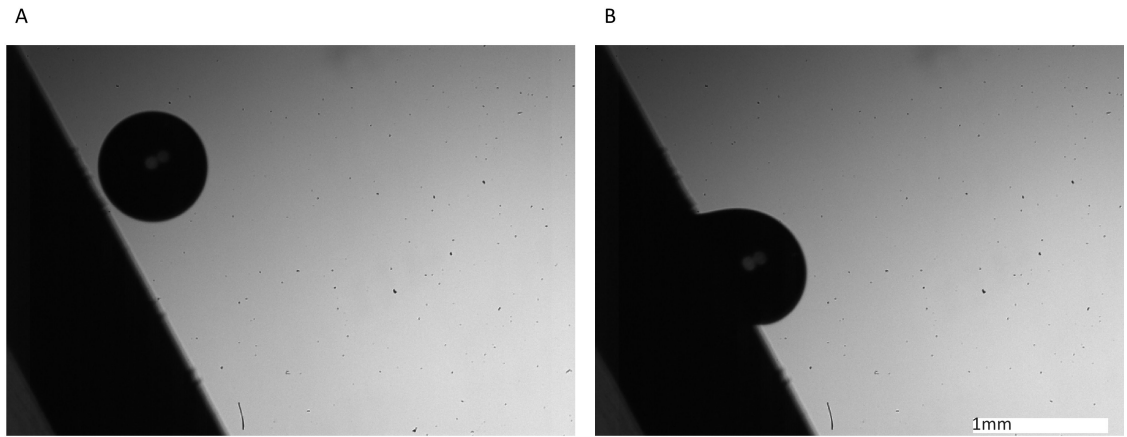


Figure 4.7: Video stills ≈ 0.002 seconds before and after impact of a droplet of 87.5% golden syrup solution impacting at a velocity of 0.4ms^{-1} and angle of 60° . The scale bar indicates a length of 1mm.

Having extracted velocities and diameters from the videography, and having measured and calculated the surface tensions, viscosities and densities of each of the analogous fluids used, the Weber and Ohnesorge numbers associated with each of the impacts were calculated. The Weber and Ohnesorge numbers associated with all impacts with impact angles of 0° , are plotted in Fig [4.8] below alongside the Gaussian kernel density estimation of the Weber and Ohnesorge numbers associated with ash droplet impacts on the NGVs inside the jet engine.

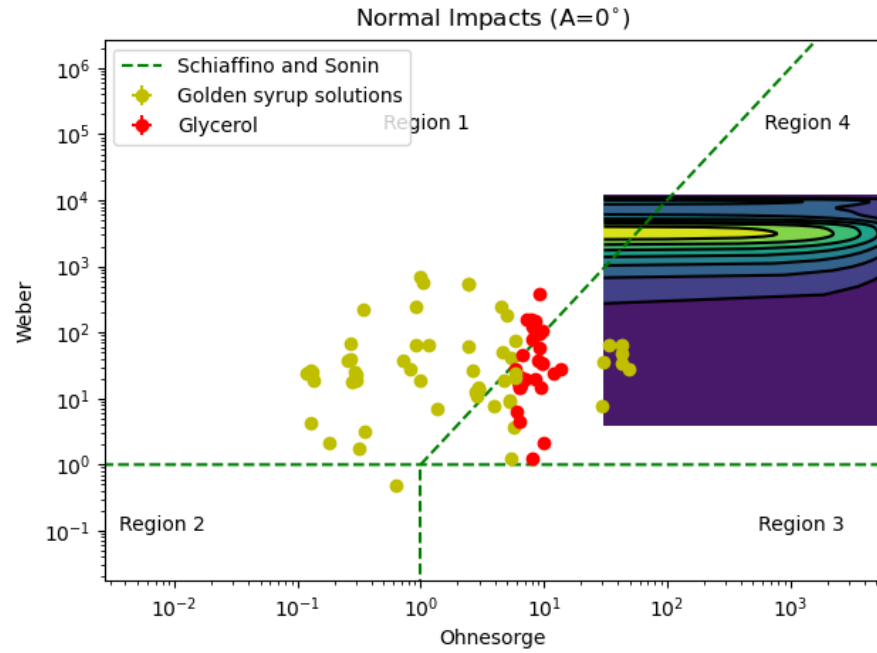


Figure 4.8: The Weber and Ohnesorge numbers of all impacts with impact angles of 0° plotted alongside a Gaussian kernel density estimation of the Weber and Ohnesorge numbers associated with ash droplet impacts on the NGVs, where each data point was weighted with the PSD and the particle's dimensionless mass. Note all error bars are smaller than the markers.

Fig [4.8] shows that most impacts fell into region 1 and region 4 of the Schiaffino and Sonin regime diagram [48], with one impact falling into region 2. It can also be seen that many impacts occurred close to the boundary between region 1 and region 4, and that only 8 impacts occurred in the same Weber and Ohnesorge space that is occupied by a small proportion of the impacts of ash droplets on the NGVs. Fig [4.9] contains similar plots to Fig [4.8], but for the 4 different impact angles.

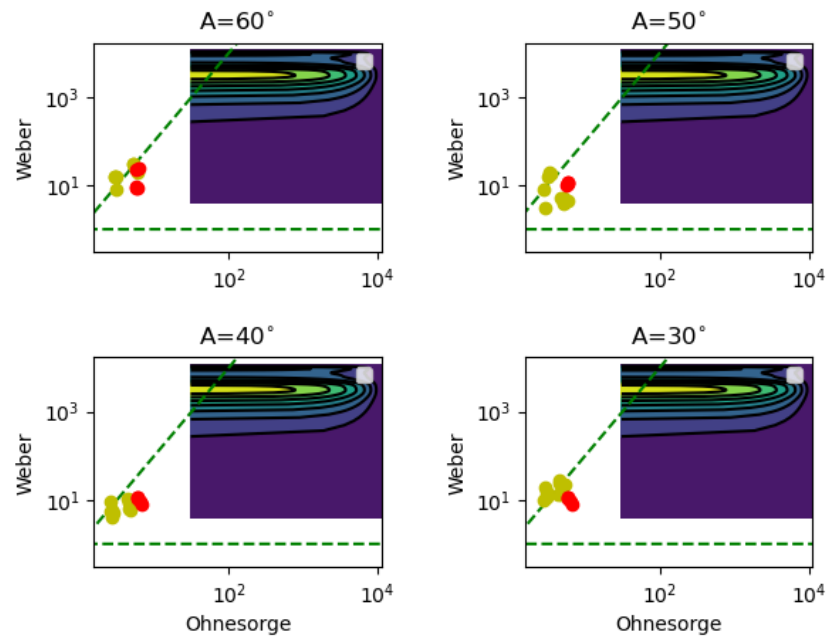


Figure 4.9: The Weber and Ohnesorge numbers of all impacts with impact angles of 60° , 50° , 40° , and 30° , respectively plotted alongside a Gaussian kernel density estimation of the Weber and Ohnesorge numbers associated with ash droplet impacts on the NGVs, where each data point was weighted with the PSD and the particle's dimensionless mass. Note all error bars are smaller than the markers.

It can be seen that no angled impacts occurred in the exact same Weber and Ohnesorge space as the impacts of ash droplets on the NGVs. It can also be seen that all the angled impacts straddled region 1 and region 4. Fig [4.10] below shows the results of the analysis of how the droplet radius, height, and contact angles evolved after impact for three droplets of the 87.5% golden syrup solution for an impact angle of 0° .

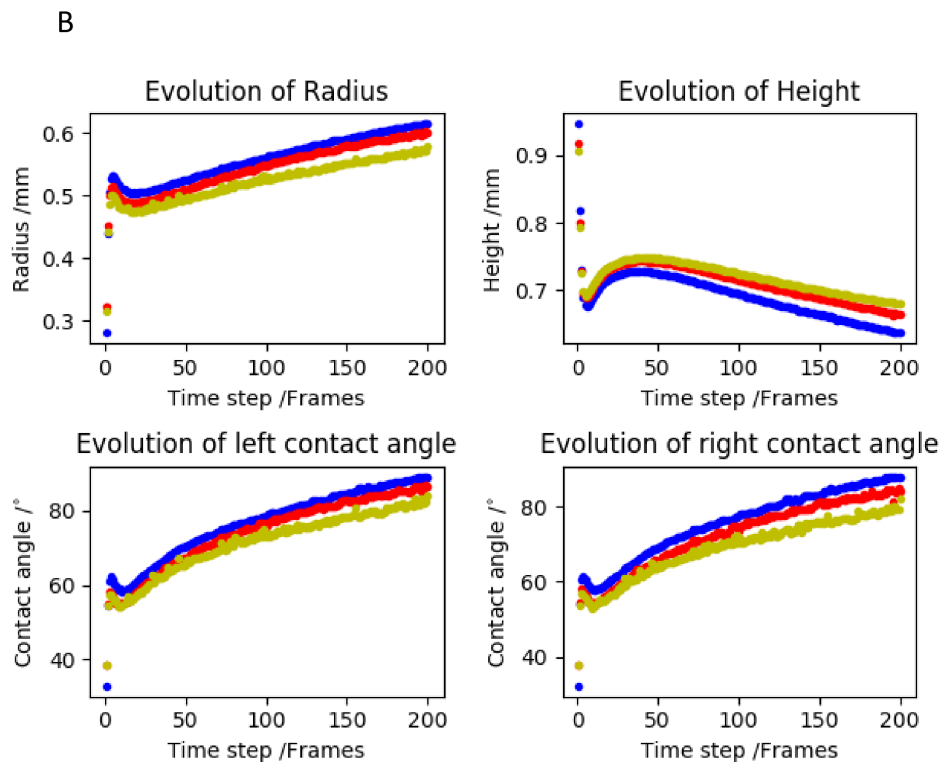
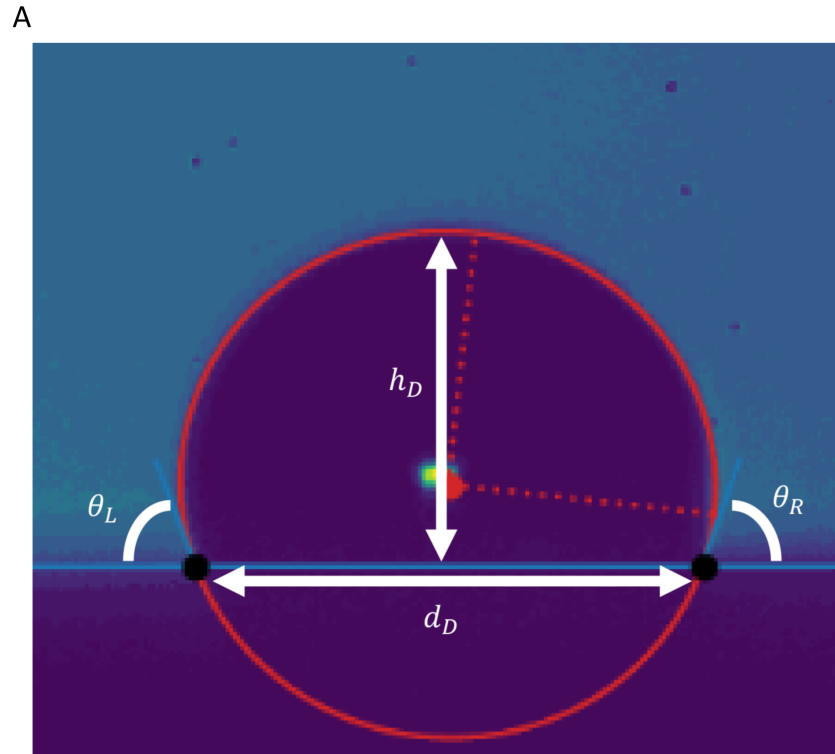


Figure 4.10: A: How the droplet height (h_D), diameter (d_D), and contact angles (θ_L and θ_R) were defined. B: The evolution of droplet radius, height, and contact angles after impact for three droplets of the 87.5% golden syrup solution for an impact angle of 0° . The frame rate here was 10000 frames per second.

The results in Fig [4.10] show that on impact the radius of a droplet rapidly increases as the droplet spreads on the surface, it then falls slightly before steadily increasing. A similar behaviour can be seen in the evolution of the contact angles. There is an initial sudden increase in the value of the contact angle, as the droplet spreads on impact. After this initial spreading, the droplet recedes and this can be seen in the slight reduction in the contact angle. After this receding the droplet starts to slowly spread under the influence of gravity, and this can be seen in the following steady increase in the contact angles. This behaviour is also captured in the droplet height, with the height decreasing when the droplet is spreading, and increasing when the droplet is receding.

This behaviour is consistent with the droplet initially spreading under a driving force, before these forces are overcome by the restoring forces, causing the droplet to stop spreading and start to recede. The droplet starts to spread again when gravitational forces start to dominate, causing the droplet to slowly spread on the surface. The driving forces are due to the impact pressure [48] and the resistance forces to the spreading are comprised of either inertial or viscous forces depending on whether the droplet is in region 1 or 4 of the Schiaffino and Sonin regime diagram [48].

4.4 Discussion and Conclusions

The main challenge in this work was the failure to observe any droplet splashing on impact. As mentioned previously, the velocity of the droplet could only be increased at the expense of decreasing the droplet diameter. This meant that there was a ‘ceiling’ in the Weber number for any given fluid. This challenge could not be solved simply by increasing the pressure either, as that caused non-spherical droplets to be produced with long tails. This Weber number ceiling decreased with increasing viscosity, as more viscous fluids were harder to dispense from the jetting system. This can be seen in Fig [4.8] as the maximum Weber numbers achieved in the droplet impacts decreases with increasing Ohnesorge number (which is directly proportional to the viscosity). These limitations meant I was not able to push to higher Weber numbers where one would expect to see the onset of splashing.

A further challenge in trying to investigate how the evolution of droplet shape on impact changed with impact conditions, was the difficulty had in fitting an ellipse to the droplets

that impacted on the angled surfaces. Below in Fig [4.11] can be seen an example of this problem.

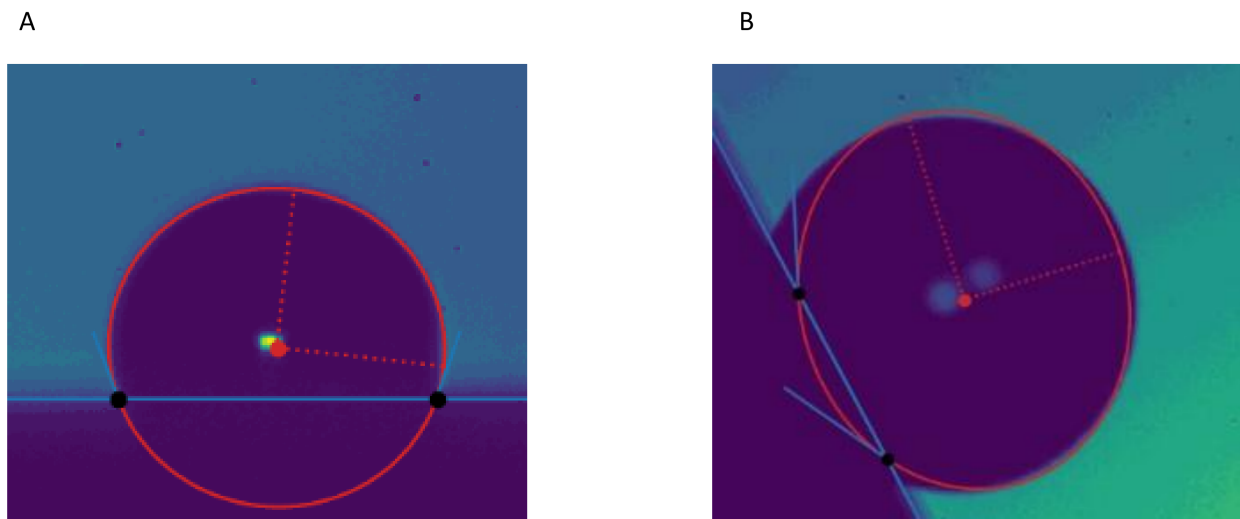


Figure 4.11: 4.11a shows an ellipse fitted to a droplet that impacted on a horizontal surface, note the tangents to the surface at the contact line from which the contact angles were measured. 4.11b shows an ellipse that was fitted to a droplet that impacted a surface at 60° .

It can be seen in Fig [4.11b] that a good fit around the droplet has not been achieved. This was the case for the majority of angled impacts, yielding inaccurate measurements of the contact angles, the spreading radius and the droplet height. For this reason, and that no splashing was observed in any of my experiments, I did not compare how the impact angle affected the evolution of the droplet shape after impact. From the analysis of the impacts at normal angle of incidence, no systematic dependence with the Weber and Ohnesorge numbers was found for the evolution of the droplet shape after impact.

As mentioned previously, some results from the experiments presented here were located in the same region of the Weber-Ohnesorge number space within which splashing had been observed in the literature [40], even though no splashing was observed in my experiments. In Fig [4.12a], it can be seen that there is some overlap between the non-splashing outcomes observed in my experiments and the splashing events in the literature. In Fig [4.12b], the same splashing events from the literature as in Fig [4.12a] are shown, but alongside deposition events from the literature in the same Weber-Ohnesorge number space. There is an overlap between the deposition and splashing events in the Weber-Ohnesorge number plane. This

would suggest that the data from the experiments reported here are not inconsistent with findings in the literature. However, it would also suggest, as was already known, that the Weber and Ohnesorge numbers cannot completely define, on their own, the splashing/non-splashing boundary.

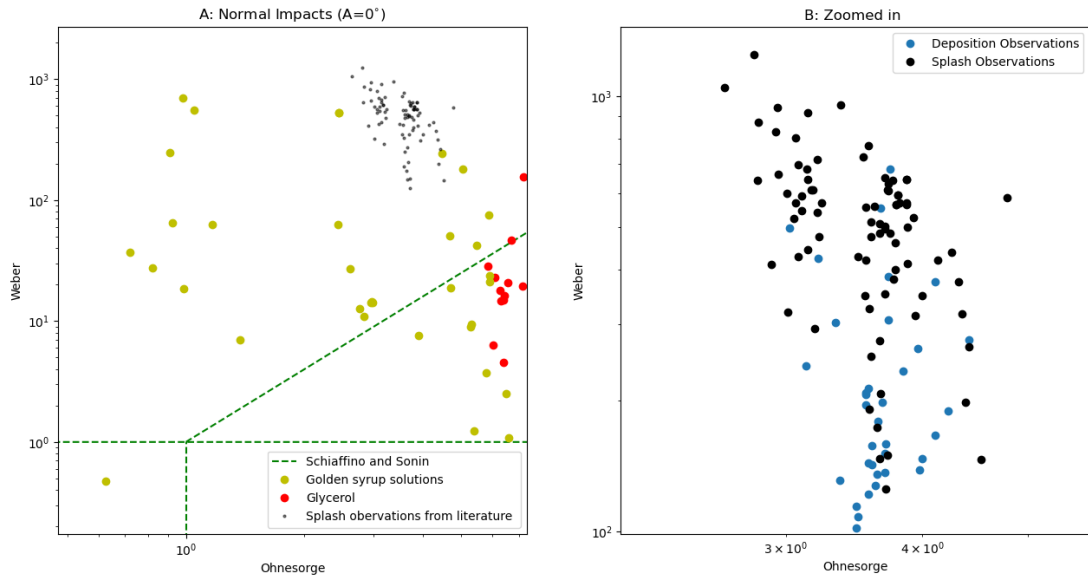


Figure 4.12: A: The locations of non-splashing impacts from the experiments reported here, and location of splashing impacts from the literature. B: Zoomed in on literature data from A, showing the overlap between deposition and splashing events found in the literature.

No final conclusions can be drawn from the data with regard to the question of whether ash droplets impacting on the NGVs splash, as I did not observe any splashing and was not able to achieve many droplet impacts in the exact same dimensionless number space as the ash droplet impacts. However, the results from the experiments presented here suggest that at least some of the ash impacts on the NGV surfaces do not lead to splashing. The challenge for any experiments investigating the onset of splashing of high viscosity droplets, is being able to achieve a high impact velocity. In order to achieve higher impact velocities other researchers have used moving platforms that they use to accelerate upwards towards the descending droplet, hence achieving a greater effective impact velocity [40]. Such an experimental set-up was considered, but due to time considerations it was decided instead to model droplet impacts using a CFD software called Flow 3D and use scaled simulations to investigate the splashing of volcanic ash on impact with the NGVs. This work is the subject of the next chapter.

Chapter 5

Scaled Splashing Simulations.

5.1 Introduction

5.1.1 Motivation

In Chapter 2 I identified the dimensionless numbers that are used in the literature to describe droplet impacts on surfaces and predict their splashing or non-splashing behaviour. In Chapter 3 I described how I used the computational fluid dynamics software Ansys-Fluent to simulate an ash droplet laden airflow around a Nozzle Guide Vane (NGV), and how I extracted the Weber and Ohnesorge numbers associated with the ash impacts on the NGV from these results. In Chapter 4 I described how I used these Weber and Ohnesorge numbers to design scaled experiments using analogous fluids, golden syrup solutions and glycerol, to capture the same physics as the ash droplet impacts and to observe at what point the onset of splashing occurs. These experiments were unsuccessful due to the limitations of the equipment available.

Despite the failure in Chapter 4, it is still important to understand the splashing behaviour of volcanic ash droplets when they impact the NGV surface and how this behaviour changes with variations in the Weber and Ohnesorge number, and the impact angle. To investigate this behaviour further, droplet impacts that were scaled to ash droplets hitting the NGVs (via the Weber and Ohnesorge numbers) were modelled using a Computational Fluid Dynamics Software called Flow 3D. This enabled the study of droplet impacts at Weber and Ohnesorge numbers that had been impossible to achieve experimentally.

This chapter will detail how a model was built in Flow 3D that could be used to model the impact of liquid droplets onto a smooth surface and determine the onset of droplet splashing under varying conditions. I will describe how the accuracy of the model within Flow 3D was determined via conducting simulations replicating droplet impacts taken from the literature and comparing the modelled and experimentally observed splashing outcomes. Finally, this chapter will describe how Flow 3D was used to simulate droplet impacts scaled to the same region of Weber and Ohnesorge space that is occupied by ash impacts on the NGV, and what the results from these suggest for the behaviour of volcanic ash inside the jet engine.

5.1.2 Flow 3D Background

Flow 3D is a CFD software which uses the volume of fluid method to simulate the dynamics of bodies of fluids. To model the unsteady flow associated with a droplet impacting a surface, any CFD software needs to be able to model the fluid interfaces of the droplet with the surrounding air accurately. A fluid interface is a type of free boundary, where free boundaries are surfaces which have discontinuities across them in one or more variables. In order to successfully simulate a free boundary any CFD code needs to be able to faithfully represent this surface, be able to define the evolution of the shape of the surface and be able to impose boundary conditions across the surface [89]. Flow 3D uses the volume of fluid method, which is an Eulerian CFD approach, to simulate fluid boundaries.

In a Lagrangian representation, the fluid is discretized into fluid elements or particles, and the mesh cells are associated with these specific fluid elements. This means that as the fluid moves, the mesh cells move with the fluid elements. Forces on individual mesh cells are easily defined, simplifying the computation of the physical response of the fluid elements [89]. On the other hand, in an Eulerian representation, the mesh cells are fixed in space and not permanently associated with individual fluid elements. The fluid within a mesh cell is considered as a continuum, and forces on this fluid within a given mesh cell can be calculated similarly to the Lagrangian approach. However, as the fluid moves, the individual fluid elements move through the fixed mesh cells. This necessitates the calculation of the flow of the fluid through the mesh, involving the averaging of properties of all fluid elements within a mesh cell at a given point in time [89]. The Lagrangian method is advantageous for tracking individual fluid particles, making it suitable for problems involving significant

deformation or fluid interfaces. However, it may face challenges in maintaining a regular grid structure. The Eulerian method, with its fixed mesh cells, is often more computationally efficient and better suited for problems with complex fluid flow patterns.

The Eulerian approach is generally used in CFD code due to it being more computationally efficient. However, the disadvantage in this approach with regard to simulating free surfaces, is the averaging process within the mesh cells. This averaging leads to a blurring or smearing of the discontinuous boundary of the free surface. Therefore, any CFD method needs to prevent this smearing, by preventing the averaging occurring over the boundary. This can be done by identifying regions that are occupied by fluid and not defining the free surface explicitly [89].

In the volume of fluid (VoF) method a function F is defined as $F = 1$ at a point in the simulation domain where fluid is present, and $F = 0$ at a point where fluid is not present. Within a mesh cell the average value of F then represents the volume of the cell that is occupied by fluid. For $F_{av} = 1$ the cell is completely full of fluid, for $F_{av} = 0$ the cell is completely void of fluid, and if $0 < F_{av} < 1$ then the cell contains a free surface. A diagram of this can be seen in Fig [5.1].

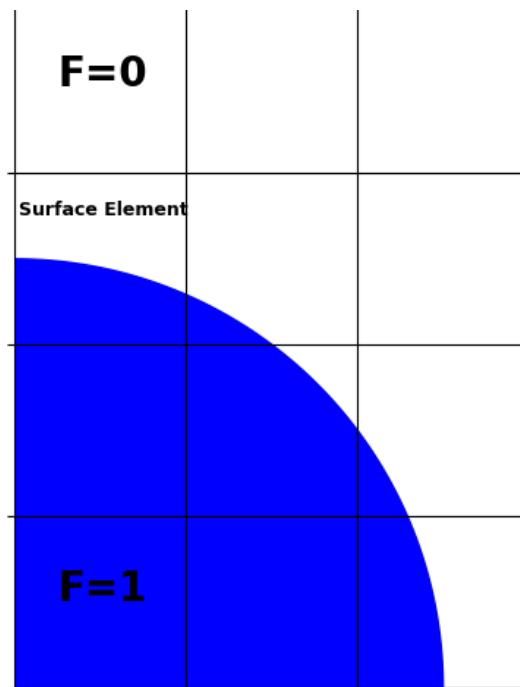


Figure 5.1: A mesh containing a fluid and a free surface. F represents the volume of the cell that is occupied by fluid.

Other methods also exist for modelling the free surface, such as using marker particles [90]. This method works by distributing marker particles over all fluid-occupied regions, and these particles move with the body of fluid. The location of the free surface is then defined as the boundary between regions with and without marker particles. A cell containing marker particles, but with a neighbouring cell that does not contain any marker particles, is defined as containing a free surface. However, the disadvantage of this method is the computational expense associated with the need for a large number of marker particles, each of which must be individually tracked.

The VoF method is less computationally intensive than the marker particle method and is the basis for Flow 3D. The fact that VoF defines the location of the bulk fluid as opposed to the location of the free surface makes it particularly good for simulating fluid break up. This makes Flow 3D a useful tool to model droplet splashing with.

Within an Eulerian CFD code the equations that need to be solved are the Navier Stokes equations. The incompressible form of the Navier-Stokes equations are shown in Eqn [5.1].

$$\frac{\partial \underline{u}}{\partial t} + \underline{u} \cdot \nabla \underline{u} = \frac{-\nabla P}{\rho} + \nu \nabla^2 \underline{u}. \quad (5.1)$$

Where \underline{u} is the velocity vector, P is the pressure, ρ is the fluid density and ν is the fluid kinematic viscosity. The dependent variables within these equations, such as velocity and fluid density, are defined at the centres of the mesh cells and at the centres of the boundaries between the mesh cells. Within each iteration of this CFD code, approximations of the Navier-Stokes equations are used to calculate initial estimates of the fluid velocities within the mesh cells, based on the initial conditions or previous values of pressure, acceleration, and density. To satisfy the conservation laws, adjustments to the pressures and velocities in the cells are made iteratively. Finally, the value of the fluid function F in each cell is updated to reflect the new fluid configuration.

The software Flow 3D and its previous versions have been used to perform simulations of impacting droplets in several instances in the literature including from: modelling different types of ink droplet impacts in the context of printing [91], to liquid droplet impingement in spraying processes [92], and modelling the behaviour of human blood droplets impacting surfaces [93]. Flow 3D has also been employed to investigate oblique droplet impacts [94], though due to the use of a coarse mesh by this study concerns have been raised on the

accuracy of their results [95]. Flow 3D has also been used by Sumner et al [96] to complement their analogue experiments investigating the onset of splashing when basaltic clasts produced from volcanic-fire fountains hit the ground. They modelled droplets with a diameter of $D_d = 0.1$ m, and viscosities ranging up to 3000 Pa s. These examples from the literature highlight the fact that Flow 3D is a useful tool to model oblique impacts of viscous droplets.

5.2 Modelling Methods

Flow 3D was used to simulate the impacts of liquid droplets onto smooth plane surfaces. The droplet diameter, impact velocity, and impact angle could be varied alongside the droplet velocity and surface tension. All droplets modelled were considered to be perfect spheres, and the simulations started with the droplet on the verge of impact with the surface. The simulations were run until a given amount of ‘time’ within the simulation had elapsed. This finish-time was varied with respect to the impact velocity. When setting up the simulations within Flow 3D different physics needed to be included within the model so the simulations of the impacting droplets would be accurate.

5.2.1 Model Physics and Set-up within Flow 3D.

The droplet impact velocities considered in this work were all $v_{\text{impact}} \ll \text{Mach } 1$. This means that the impacts can be modelled as incompressible flows. An incompressible flow is one in which the fluid density remains constant with respect to changes in pressure and temperature. It is important within CFD code to know if one should be modelling an incompressible or compressible flow, as this changes the form of the governing Navier Stokes equations.

When modelling the impact of a droplet on a surface it is important to consider the effects of surface tension. This is because the surface tension of a droplet influences the wetting behaviour on the surface, such as the contact angles and the subsequent spreading dynamics. It is also important to consider viscous effects, as viscous effects within the droplet can affect the droplet spreading behaviour on impact, with more viscous droplets resisting spreading on impact.

For the droplet simulations the free surface- one fluid TruVOF incompressible template was used. Within the software the following physics models were activated: gravity and non-inertial, surface tension, and viscosity and turbulence. Within the surface tension model the fluid surface tension could be varied, and the contact angle was set to 70° and kept constant for all the simulations that were performed. Within the viscosity and turbulence model, the viscous flow model was activated, and the laminar turbulence option was selected.

Before any simulations could be performed it was necessary to define a simulation domain and define a computational mesh. A thin rectangular surface was created by modifying the inbuilt rectangle geometry available within Flow 3D. The domain was defined over this surface to a height of $\approx 3\text{mm}$. Across this domain a mesh was created, consisting of square cells with a size of $2.6 \times 10^{-5}\text{m}$, resulting in a total of 21.8 million mesh cells. Mesh dependency studies were conducted, which led to the selection of the mesh cell size. In these studies the cell size was varied systematically for a simulation of a water droplet with a known splashing outcome from [40]. The cell size was decreased until the simulation outcomes remained constant, allowing confidence in the mesh's ability to yield accurate results. In Fig [5.2] can be seen a representative image of the simulation domain.

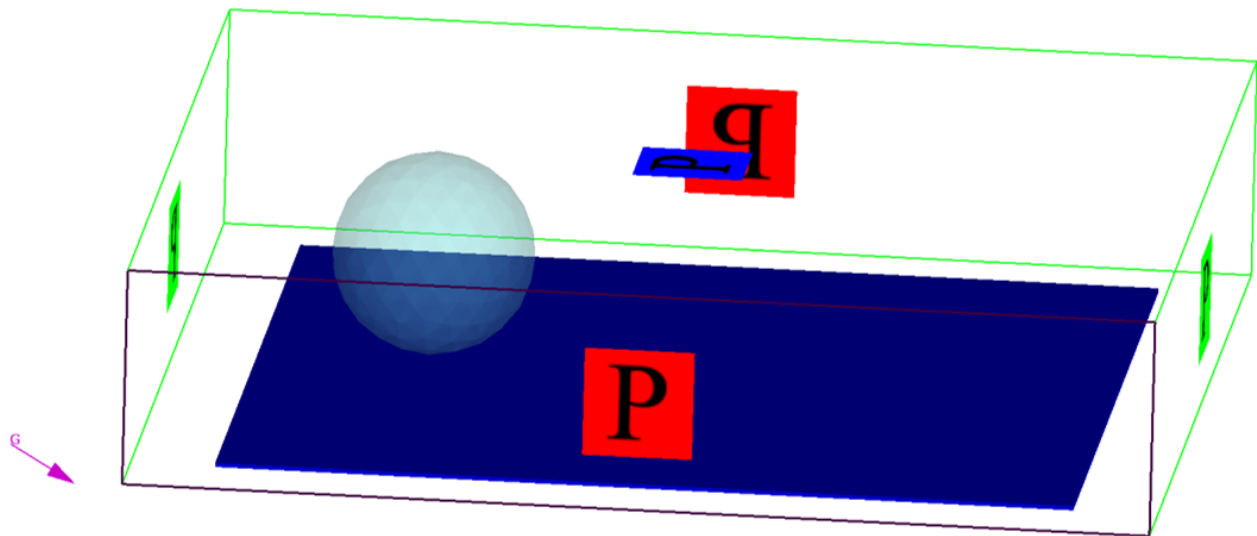


Figure 5.2: Showing the simulation domain. Note the pressure boundary labelled with the letter P. Note also the gravity vector set up for an oblique droplet impact.

The boundary conditions were set as pressure conditions with a void boundary. This

means that these boundaries in the simulation were treated as air at atmospheric pressure and 300 K. The numeric settings within Flow 3D were mostly left at the default settings for the simulations. However, the volume of fluid advection method was changed to the unsplit Lagrangian method, as recommended in the material from Flow 3D on droplet impact simulations, and for droplets with high viscosities the viscous stress solver was changed from explicit to successive under-relaxation. In the treatment of isolated fluid droplets, if a mesh cell was found with less than 1% of its volume occupied with fluid, this fluid was converted into particles and these particles were tracked using Lagrangian particle tracking. Droplets were created in the Sources tab within the Flow 3D software, where the droplet radius and initial impact velocity could be defined. The droplet viscosity, surface tension and density could also be varied separately.

In the simulation of oblique droplet impacts, the same domain and mesh were used. To model an oblique impact, the acceleration due to gravity felt by the droplet was split into ‘vertical’ and ‘horizontal’ components. The same approach was applied to the impact velocity. This allowed the simulation of droplet impacts at various impact angles, without having to change the orientation of the surface.

5.3 Validation of model

5.3.1 Introduction

Before simulating droplet impacts scaled to those of ash droplets on the NGV, it was necessary to assess the accuracy of the setup in Flow 3D for predicting droplet splashing upon impact. In order to do this, data from experiments investigating the onset of droplet splashing were extracted from the literature. Using the same experimental conditions as those for the droplet impacts performed in the literature, the same droplet impacts were simulated in Flow 3D. The results from these simulations were then compared to the corresponding experimental results. If the simulated and experimental results agreed on the splashing outcome of the droplet, the simulation was deemed accurate. By repeating this process for numerous experimental data points, the level of accuracy of the model within Flow 3D for predicting splashing could be determined.

5.3.2 Selection of data

In choosing the data with which to test the accuracy of the Flow 3D model, it was important to consider a wide range of Weber and Ohnesorge numbers, which spanned the area of Weber–Ohnesorge space occupied by ash impacts on the NGV. Many studies have investigated the onset of droplets splashing on impact with a surface, [24, 25, 40, 50, 54], but Roisman et al [40] published the largest database of the droplet characteristics and droplet impact conditions. They also included the surface properties of the surfaces that the droplets were impacting upon, including the porosity, and surface roughness measurements such as the mean height of the peaks above the core roughness profile (RPK), and the mean value of the width of a profile element (RSM), see Fig [5.3].

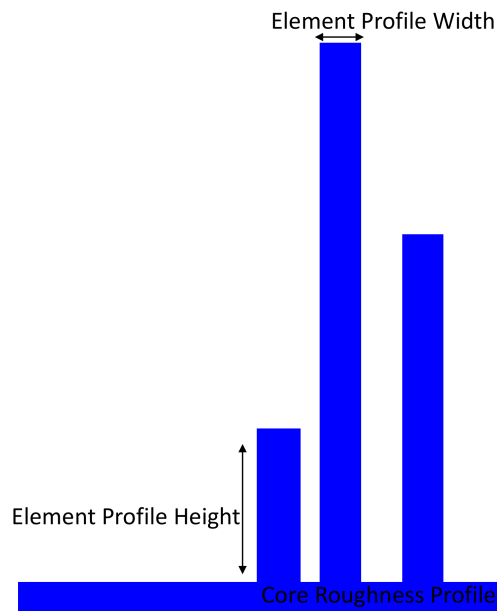


Figure 5.3: A depiction of the roughness profile of a surface, showing the protrusion of peaks above the core roughness profile.

A complication in faithfully replicating a drop impact in Flow 3D is including the surface properties in the simulation. Flow 3D does have options for varying the porosity of the surface, but it was not clear if how porosity was defined in Flow 3D was the same as [40], and it was also not possible to change the surface roughness within the software. In selecting the impacts from [40] to be simulated, only impacts of droplets onto non-porous surfaces were considered. The majority of the resulting impacts involved water droplets, with a minority involving droplets of isopropanol and glycerol. For the impacts involving water, a further

refinement was made with only impacts on the two smoothest surfaces used by [40] being simulated. However, due to the sparse nature of the data for impacts of isopropanol and glycerol (which correspond to the impacts with larger Ohnesorge numbers than those with water), all impacts on non-porous surfaces regardless of roughness were considered. This resulted in 146 experimental observations being simulated in Flow 3D.

If any fluid properties required by Flow 3D were unknown for glycerol and isopropanol (such as their compressibility) these were left the same as for water. Below in Fig [5.4] can be seen a plot of the 146 droplet impacts in the Weber-Ohnesorge number plane, which were simulated from [40].

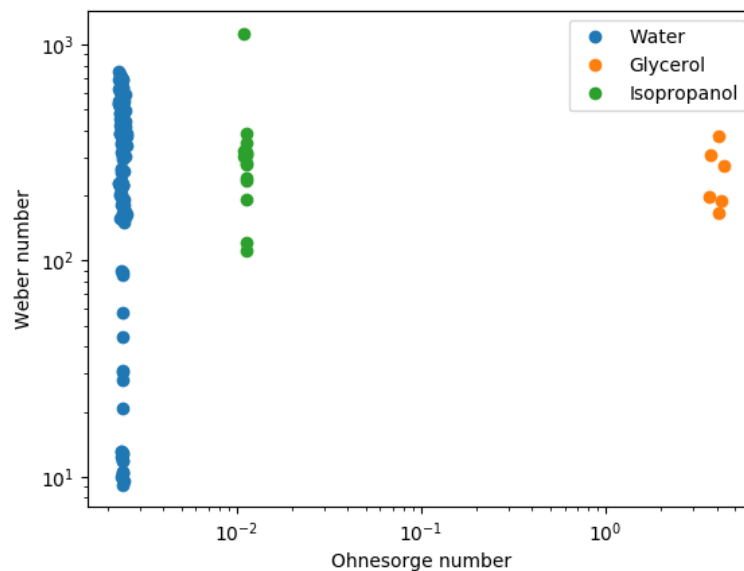


Figure 5.4: The 146 droplet impacts that were simulated in the Weber and Ohnesorge number plane. The fluids used were Water, Glycerol and Isopropanol.

It should be noted that for all the glycerol impacts that were considered here, no splashing was observed in the experiments [40]. The droplet physical properties and impact conditions, as well as the experimental and simulated outcomes are recorded and shown in Table 9.2 in the appendix for each of the simulated droplet impacts. In any given simulation result, a splash was said to occur if the simulation showed any or all of the three behaviours: The lamella breaking up and ‘fingers’ of fluid protruding from the main body of the spreading droplet; the production of secondary droplets; and the expulsion of Lagrangian fluid particles, from the droplet edge. If none of these behaviours were observed, then it was taken that

the simulated drop had not splashed.

5.3.3 Results of the Validation Simulations

Below in Table 5.1 can be seen the results from the verification simulations of 146 droplet impacts from [40].

Table 5.1: The results from the verification simulations showing the percentage of simulations that agreed with the experimental observations, and the percentage of simulated impacts that showed splashing or deposition that wasn't observed experimentally.

Result	% of impacts
Agreement	76.0%
False deposition	19.9%
False Splash	4.1%

It can be seen that 76% of the simulated drop impacts showed behaviour consistent with their respective experimental observations, and that there were almost 5 times as many incorrect deposition predictions than there were incorrect splashing predictions. In Fig [5.5] and Fig [5.6], can be seen examples of simulation results for a splash and a deposition that agreed with the experimental observations. Fig [5.7] and Fig [5.8] show examples of simulation results for a splash and a deposition that disagreed with the experimental observations.

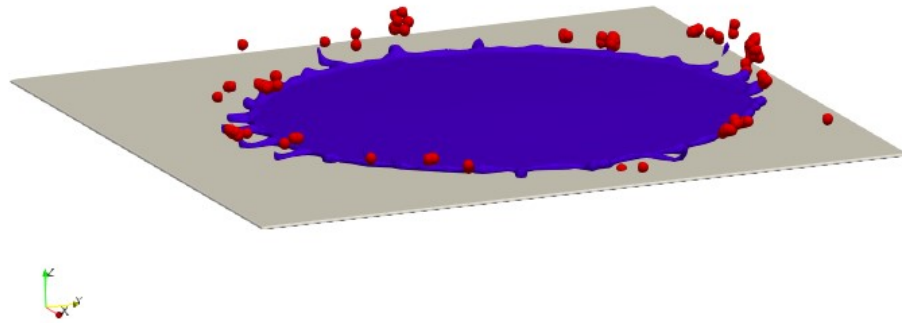


Figure 5.5: A simulated splash that agreed with the experimental observations, corresponding to simulation 82 in Table 9.2. The fluid is coloured blue, and any fluid particles are coloured red. Note that the Lagrangian fluid particles are not scaled according to the actual size of the fluid they represent.

In Fig [5.5] above can be seen a simulated splashing event that agreed with the corresponding experimental observation. It can be seen that there is fingering of the fluid, alongside the production of secondary droplets and fluid ‘particles’.

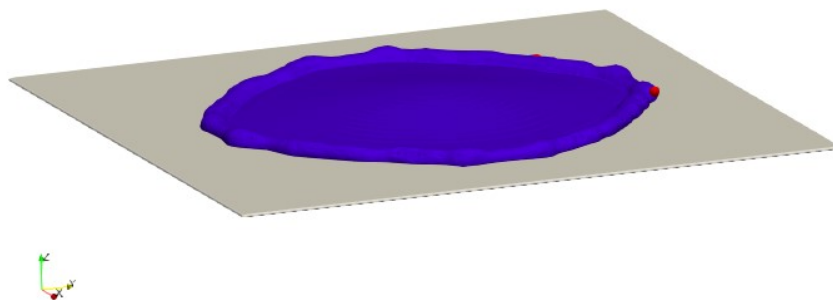


Figure 5.6: A simulated deposition that agreed with the experimental observations corresponding to simulation 15 in Table 9.2. The fluid is coloured blue, and any Lagrangian fluid particles are coloured red. Note that the fluid particles are not scaled according to the actual size of the fluid they represent.

In Fig [5.6] a simulated deposition than be seen which agreed with the experimental observation, there were no secondary droplets produced, and no fingering at the lamella

occurred. Only a single fluid particle can be seen, this remained attached to the lamella and so this simulation was recorded as a deposition.

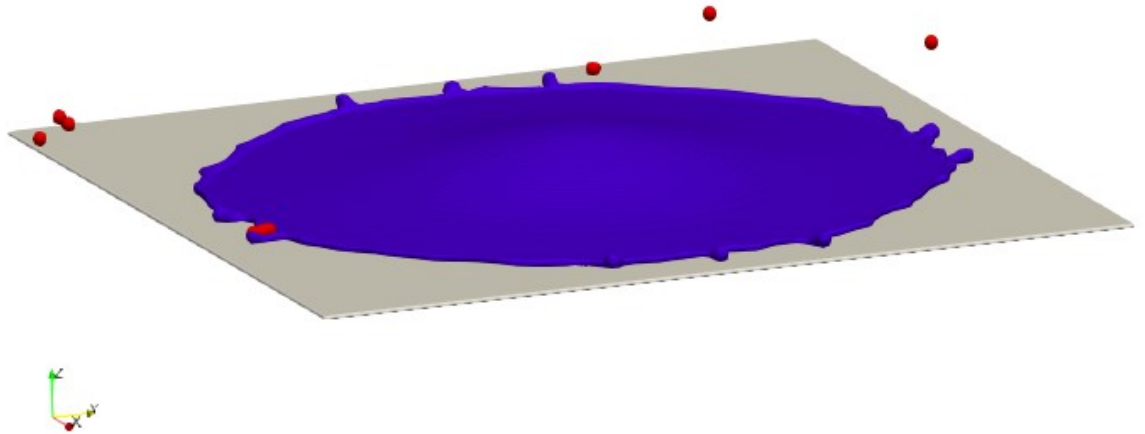


Figure 5.7: A simulated splash that disagreed with the experimental observations corresponding to simulation 2 in Table 9.2. The fluid is coloured blue, and any fluid particles are coloured red. Note that the fluid particles are not scaled according to the actual size of the fluid they represent.

In Fig [5.7] can be seen a simulation that was recorded as a splash, but the corresponding experimental observation recorded a deposition. There can be seen fingering at the lamella, and the production of fluid particles.

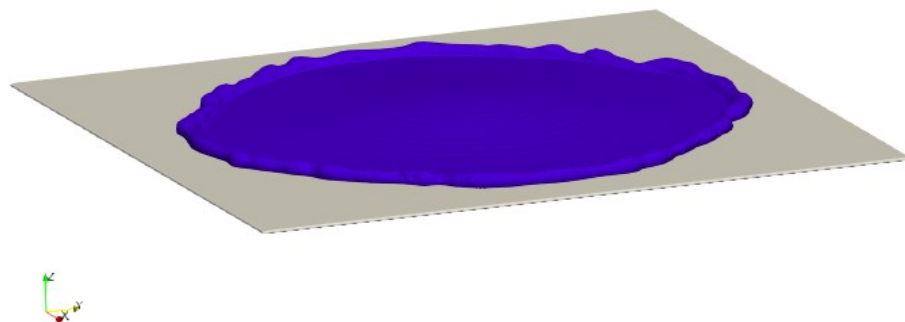


Figure 5.8: A simulated deposition that disagreed with the experimental observations corresponding to simulation 26 in Table 9.2. The fluid is coloured blue, and any fluid particles are coloured red. Note that the fluid particles are not scaled according to the actual size of the fluid they represent.

In Fig [5.8] can be seen a simulation that was recorded as a deposition, but the corresponding experimental observation recorded a splash. There can be seen no fingering at the

lamella, and there is no production of secondary droplets or fluid particles.

5.3.4 Analysis and Conclusions

The results of the verification simulations, as shown in Table 5.1, are encouraging with a majority of the simulated droplet impacts displaying the same splashing behaviour that was observed experimentally. The fact that the Flow 3D software tended to underpredict splashing far more than it failed to correctly predict deposition is perhaps not surprising. Though efforts were made to only simulate impacts that occurred on relatively smooth and non-porous surfaces from [40], it is safe to assume that the surface roughness associated with these impacts would still have had an effect on the experimentally observed droplet impact outcome. In Roisman et al [40] they define a generalised splashing/deposition threshold based on the Weber number and the surface roughness. With the critical Weber number, We_c , above which splashing occurs being a function of the surface roughness:

$$We_c = 10.2 \times \left(\frac{R_{pk}}{R_{sm}} \right)^{-0.83}. \quad (5.2)$$

The value of this critical Weber number decreases with increasing surface roughness, and so they find that a rougher surface promotes droplet splashing. Therefore, given the fact that in the simulations performed here surface roughness is neglected, it is not surprising that the majority (> 80%) of the incorrect predictions of drop impact behaviour from the simulations are failures to predict splashing.

It should be noted that in all these verification simulations, only 6 impacts considered from [40] occurred with an Ohnesorge number $Oh \gg 0.01$ and all these impacts were depositions in both the experiments and the simulations. Therefore, it is not possible to tell if Flow 3D over-predicts or under-predicts splashing at larger Ohnesorge numbers.

5.4 Scaled modelling of droplets impacting the NGVs

5.4.1 Methods

The simulation model shown and validated in the previous sections was used to investigate the splashing behaviour of molten ash particles impacting the NGVs. From work in Chapter 2 I have shown that in designing scaled experiments, the important dimensionless numbers

to consider are the Weber and Ohnesorge numbers. In Chapter 3 it was shown that the ash droplets impact the NGVs with a large range of impact angles, θ_i . The role of the impact angle on the splashing behaviour also needs to be investigated. I will now review the findings of Chapter 3 to constrain the appropriate Weber and Ohnesorge numbers, and impact angles to use in these simulations.

The range of these Weber and Ohnesorge numbers associated with the ash impacts on the NGVs is known from the computational fluid dynamics simulations performed in Chapter 3. The results of the calculations of these Weber and Ohnesorge numbers are shown in Fig [5.9] below.

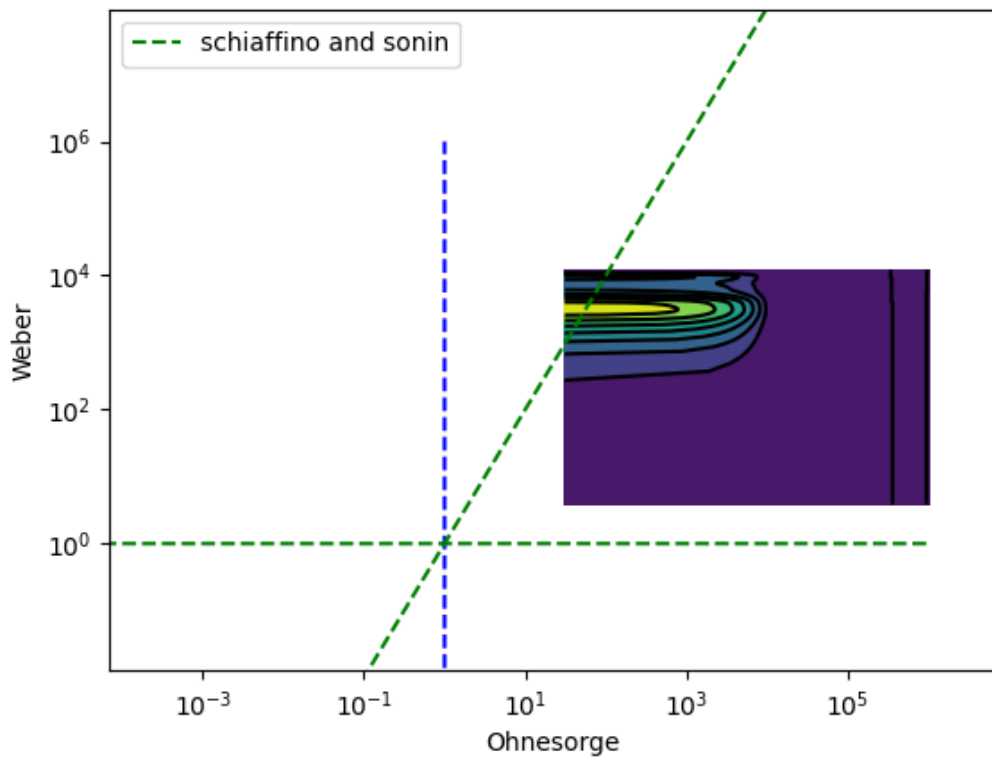


Figure 5.9: The Gaussian kernel density estimation for the Weber and Ohnesorge numbers associated with the bulk of the mass of volcanic ash that impacts the NGV. This figure is adapted from Chapter 3.

It can be seen that the range of Weber numbers associated with the ash impacting the NGV lies between $10^1 \leq We \leq 10^4$, with the bulk mass of the impacts falling in the range $10^3 \leq We \leq 10^4$. It can also be seen that the range of Ohnesorge numbers associated with the ash impacting the NGV lies between $10^1 \leq Oh \leq 10^6$, with the bulk mass of the impacts falling in the range $10^1 \leq Oh \leq 10^4$.

It is also found in the literature [41] that the value of the impact angle can influence the droplet impact outcome. Therefore, it is necessary to consider the effect impact angle may have on whether or not volcanic ash droplets splash on impact with the NGV. In Fig. [5.10] below the results from the previously discussed CFD simulations are shown, illustrating the impact angles of volcanic ash on the NGVs and how these angles vary with ash diameter. Note that the angles are measured with respect to the surface normal, so more oblique angles are closer to 90° .

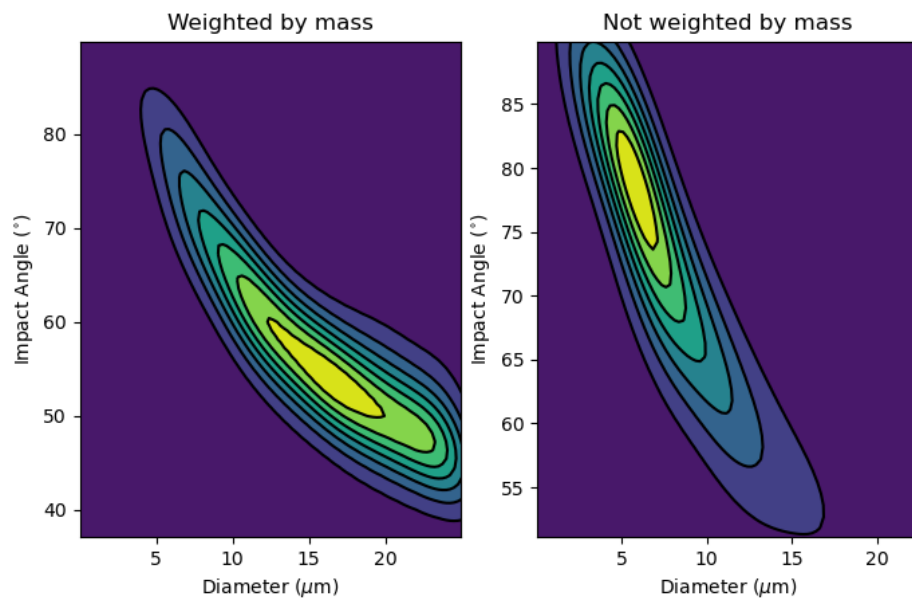


Figure 5.10: The Gaussian kernel density estimations for the ash droplet diameters and impact angles associated with the impacts of volcanic ash on the NGV, and the bulk of the mass of volcanic ash that impacts the NGV. This figure is reproduced from Chapter 3.

It can be seen in Fig [5.10] that most of the droplets impact the vane with angles between $65^\circ \leq \theta_i \leq 85^\circ$, with the bulk of the mass of the ash impacting at angles between $45^\circ \leq \theta_i \leq 70^\circ$.

Using these two results, simulations were designed that were scaled to the case of volcanic ash droplets. Previous analysis conducted, and which is discussed in Chapter 2, suggests that increasing the Ohnesorge number has no real effect on the droplet impact outcome. However high Ohnesorge $Oh \gg 1$ impacts are not well reported in the literature, and the impacts with $Oh > 1$ observed by Roisman et al [40] had many instances of both splashing and no splashing being observed under the same or similar experimental conditions. It being

clear that further investigation of the onset of splashing behaviour at higher Ohnesorge number is needed, simulations of impacts with $10^{-2} \leq Oh \leq 10^2$ were included, as I wanted to explore how the propensity for splashing changes when moving to higher Ohnesorge numbers.

For each simulation a virtual fluid was used. This had a density of $\rho = 100 \text{ kgm}^{-3}$, a surface tension of $\sigma = 0.0073 \text{ Nm}^{-1}$, and a contact angle on a smooth, non-porous surface of $\theta_c = 70^\circ$, these properties were kept constant across all simulations. The droplet diameter was set for all simulations as $D = 2.4 \text{ mm}$. The Ohnesorge number was varied systematically by increasing the droplet viscosity from 0.001 Pa s to 10 Pa s . For each droplet viscosity, the Weber number was varied by varying the droplet impact velocity from 1 ms^{-1} to 150 ms^{-1} . This led to for each impact angle, a total of 25 simulations. A range of impact angles were considered varying from $0^\circ - 70^\circ$ in 10° increments. Note these angles are with respect to the surface normal, so an impact angle of 0° indicates a ‘head-on’ impact between the droplet and surface. How these simulations are distributed in the Weber-Ohnesorge plane can be seen in Fig [5.11] below.

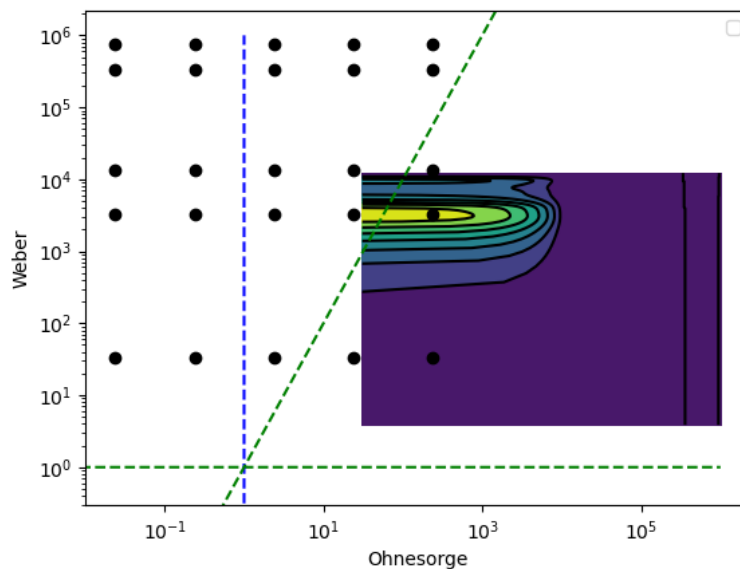


Figure 5.11: The Gaussian kernel density estimation for the Weber and Ohnesorge numbers associated with the bulk of the mass of volcanic ash that impacts the NGV, with the simulation points plotted in black.

It can be seen that the simulations span a range of Weber and Ohnesorge numbers, in-

cluding the area of Weber-Ohnesorge space most densely occupied by the bulk of the ash that impacts the NGV. However, most of the chosen simulation points do not lie within the specific region of Weber-Ohnesorge space directly affected by the ash impacts on the NGVs. This decision stemmed from the limited availability of experimental data to validate CFD simulations at larger Ohnesorge numbers, with the maximum Ohnesorge number included in the verification simulations being $Oh = 4$. It is impossible to know if simulations conducted at larger Ohnesorge numbers are accurate, as there is no experimental data with which to compare them against. By choosing simulation points to cover the Ohnesorge number space supported by experimental data and the Ohnesorge space relevant to ash impacts on NGVs, this approach allows for comparison between how the splashing threshold changes (within the simulations) within the Weber-Ohnesorge number space occupied by experimental data, and how the splashing threshold changes (again within the simulations) within the regime space occupied by volcanic ash impacts on NGVs, where experimental data is lacking.

These simulations were done initially for impact angles of 70° , 50° , 30° and 10° . Further simulations were performed at impact angles of 0° , 20° , 40° and 60° , though not all 25 simulation points were used for these angles due to time constraints. The simulation points for this second set of simulations were chosen from the first set of simulation points where the onset of splashing had been observed. For impact angles of 60° , 40° and 70° , impacts at higher Weber numbers were performed.

5.4.2 Results

Below in Fig [5.12] and Fig [5.13] can be seen the results of the simulations scaled to the same Weber-Ohnesorge space as the ash droplet impacts on the NGV. Note that the purple points indicate a deposition result, and the yellow points indicate a splashing result.

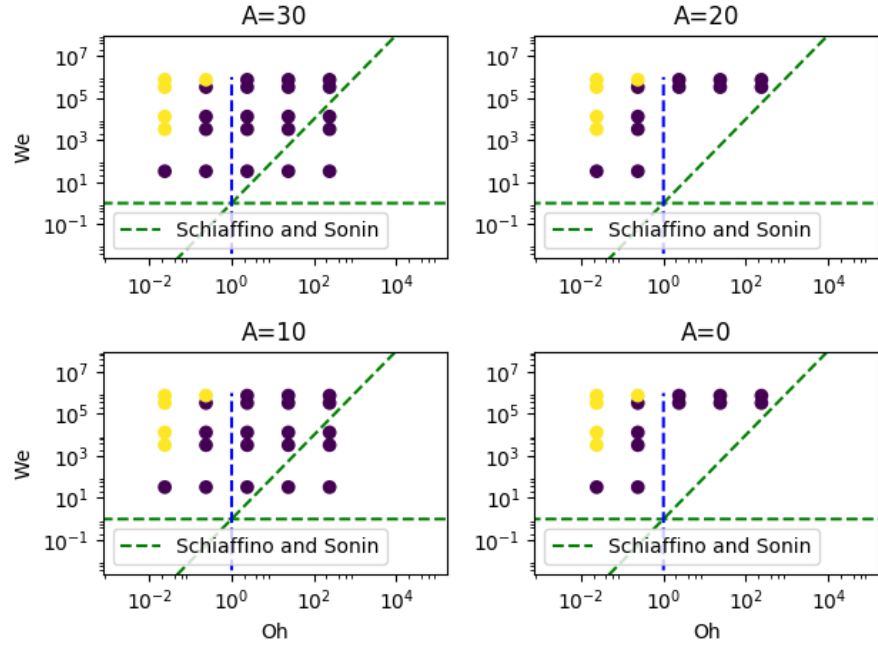


Figure 5.12: The results for the simulated droplet impacts for impact angles, with respect to the surface normal, of 0° , 10° , 20° and 30° . The purple points indicate deposition results, and the yellow points indicate splashing results. The boundaries in the Weber-Ohnesorge plane as defined by Schiaffino and Sonin [48] are shown in green.

In Fig [5.12] it can be seen (for all the impact angles considered here) that as the Ohnesorge number increases the Weber number at which splashing occurs also increases, with no splashing observed at Weber numbers up to $We \approx 10^6$ for Ohnesorge numbers $Oh > 1$. No effect due to impact angle is evident.

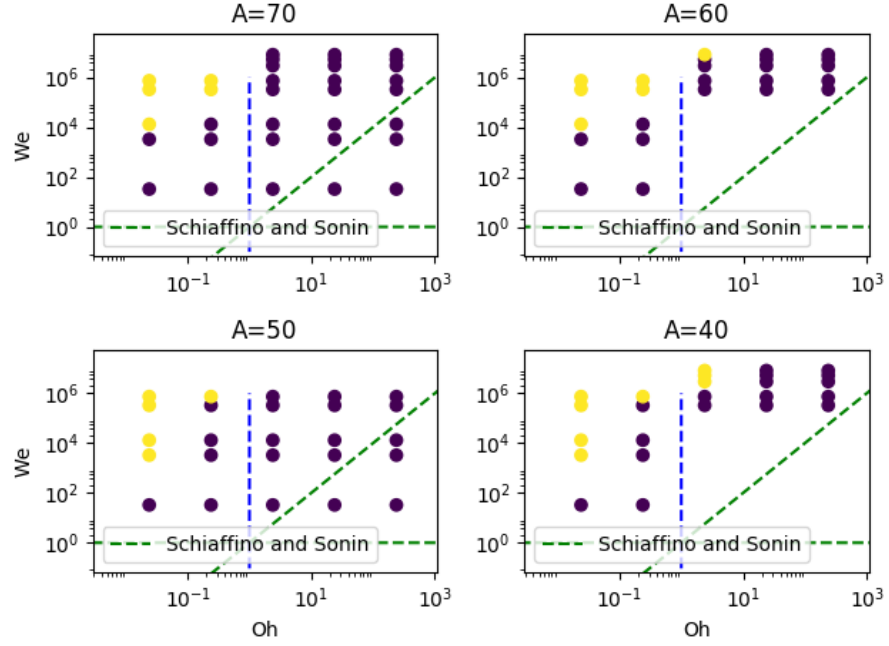


Figure 5.13: The results for the simulated droplet impacts for impact angles, with respect to the surface normal, of 40° , 50° , 60° and 70° . The purple points indicate deposition results, and the yellow points indicate splashing results. The boundaries in the Weber-Ohnesorge plane as defined by Schiaffino and Sonin [48] are shown in green.

Fig [5.13] shows, as in Fig [5.12], that for each impact angle the Weber number at which the onset of splashing occurs increases with increasing Ohnesorge number. However, for these more oblique impact angles, the value of the impact angle does seem to have an effect on the onset of splashing. From the transition from an impact angle of 50° to 60° , the Weber number at which splashing is observed for an Ohnesorge number of $Oh = 0.02$ increases. However, the Weber number at which splashing occurs for $Oh = 0.2$ decreases as the impact angle becomes more oblique. For an Ohnesorge number of $Oh = 2.39$, the onset of splashing for an impact angle of 40° occurs at a Weber number of $We = 2.9 \times 10^6$, however for an impact angle of 60° the onset of splashing for this Ohnesorge number increases to $We = 8.2 \times 10^6$.

Below in Fig [5.14] and Fig [5.15] can be seen simulation results for impacts at an Ohnesorge number of $Oh = 0.24$ and $Oh = 2.4$ respectively, both with a Weber number of $We = 7.4 \times 10^5$ at an impact angle of 60° .

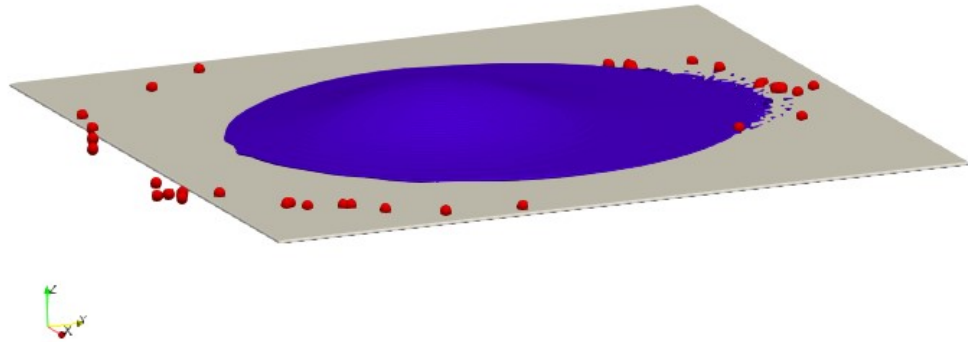


Figure 5.14: A simulated droplet impact at an impact angle of 60° , $Oh = 0.24$ and $We = 7.4 \times 10^5$. The fluid is coloured blue, and any fluid particles are coloured red. Note that the fluid particles are not scaled according to the actual size of the fluid they represent.

In Fig [5.14] it can be seen that a splash was simulated. Note that the far-right hand side of the surface is ‘upslope’ and the far-left hand side is ‘downslope’. It can be seen that upslope the lamella has broken into many secondary droplets whilst the droplet continues to spread downstream. In Fig [5.15] it can be seen that no splashing was observed, at an Ohnesorge number ten times greater.

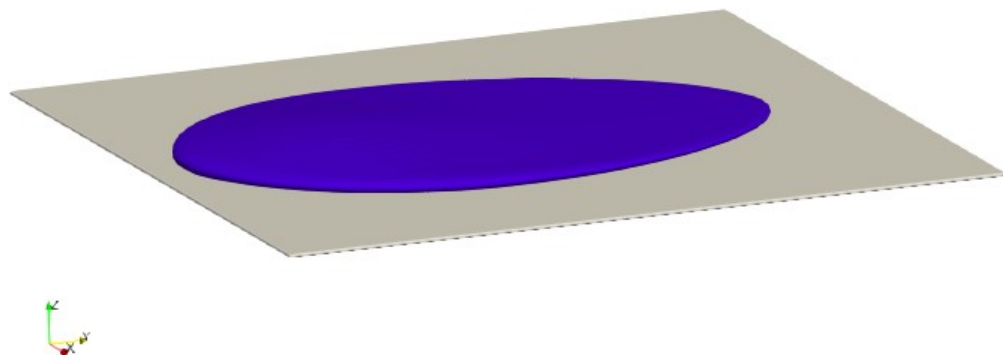


Figure 5.15: A simulated droplet impact at an impact angle of 60° , $Oh = 2.4$ and $We = 7.4 \times 10^5$. The fluid is coloured blue, and any fluid particles are coloured red. Note that the fluid particles are not scaled according to the actual size of the fluid they represent.

5.4.3 Discussion

In the results reported here there is some effect of varying the impact angle on the droplet impact outcome, with a variation in the impact angle being shown to both suppress and promote splashing depending on the Ohnesorge number. In Bird et al [41] they used droplets of ethanol to perform oblique droplet impacts. During these experiments they observed that under various conditions:

- 1.) The lamella would spread in all directions.
- 2.) Both sides of the droplet could splash.
- 3.) Asymmetric splashing could occur, with splashing observed at one side of the lamella but not the other.

These observations of [41] are consistent with the observations of the effect of impact angle in the results presented here, such as the example of asymmetric behaviour as seen in Fig [5.14].

The results presented here also show a clear influence of the Ohnesorge number on the onset of splashing, with an increase in the Ohnesorge number suppressing splashing. This is in stark contrast to the results from my analysis in Chapter 2, which showed that for droplet impact data in the literature there was no statistically relevant influence of the Ohnesorge number in determining whether or not the droplet splashed on impact. It is important to note that the majority of these impacts in the literature corresponded to an Ohnesorge number $Oh \ll 1$, and all occurred in region 1 of the Weber-Ohnesorge plane as defined by Schiaffino and Sonin [48] where the resistance to the droplet spreading is dominated by inertial forces.

It can be seen in Fig [5.12] and Fig [5.13], that the simulations that were performed fell into region 1 and 4 of the Schiaffino and Sonin diagram. In both region 1 and 4 the spreading of the droplet is driven by the impact pressure, however in region 1 inertial forces dominate the resistance to the droplet spreading and in region 4 the viscous forces dominate. Analysis in a previous chapter demonstrated that the Ohnesorge number had little effect on the splashing outcome of a droplet for impacts in region 1. However, in these results this is not the case, with the Ohnesorge number having a significant effect on suppressing splashing as the viscosity is increased within region 1 of the Schiaffino and Sonin diagram.

In order to see what these results mean for the impacts of volcanic ash, Fig [5.12] and Fig [5.13] are reproduced with the Gaussian kernel density estimation for the Weber and Ohnesorge numbers corresponding to the bulk of the mass of ash that impacts the NGV. These can be seen below in Fig [5.16] and Fig [5.17].

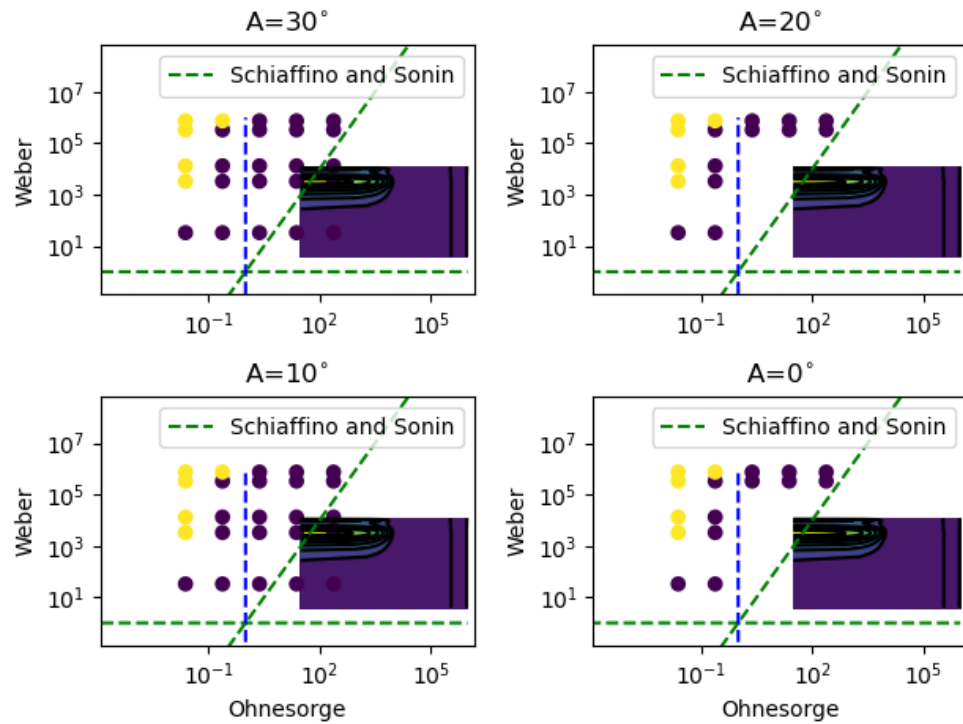


Figure 5.16: The Gaussian kernel density estimation for the Weber and Ohnesorge numbers associated with the bulk of the mass of volcanic ash that impacts the NGV, with the simulation points plotted for the different impact angles considered. Purple points correspond to deposition, and yellow points correspond to splashes.

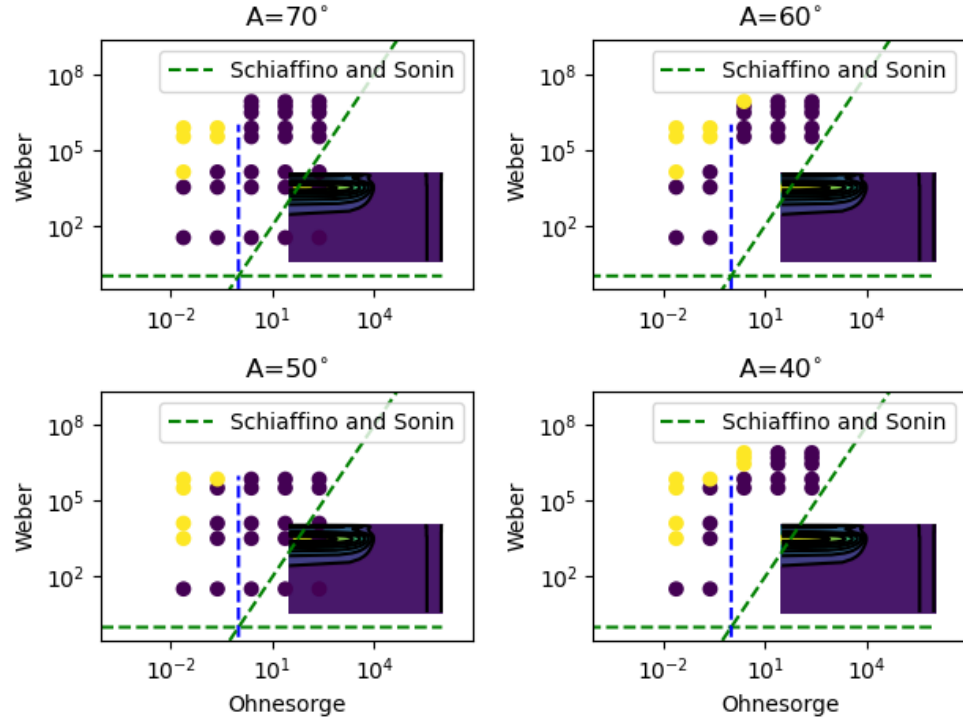


Figure 5.17: The Gaussian kernel density estimation for the Weber and Ohnesorge numbers associated with the bulk of the mass of volcanic ash that impacts the NGV, with the simulation points plotted for the different impact angles considered. Purple points correspond to deposition, and yellow points correspond to splashes.

It can be seen that for all the impact angles considered in these simulations, no splashing was observed in any simulations conducted within the same Weber-Ohnesorge number space as the impacts of volcanic ash droplets on the NGV surface. It can be seen that for the range of Ohnesorge numbers relevant to the ash droplet impacts, the Weber numbers needed for splashing to occur are much greater than the highest Weber numbers associated with the ash droplet impacts. These results would indicate that when molten volcanic ash droplets impact the NGV surface, no splashing occurs.

5.4.4 Limitations and future work

For all computational fluid dynamics simulations, the only true validation of the veracity of the simulation is in the direct comparison of the simulation to experimental results. Due to the lack of experiments performed at high Ohnesorge numbers, $Oh \gg 1$, there is not readily available data to perform verification simulations within the same Weber and Ohnesorge

space as ash droplet impacts. Therefore, even though successful verification simulations of many low Ohnesorge number impacts were performed, we cannot be entirely sure whether or not the simulations at high Ohnesorge numbers performed here in Flow 3D are accurate. I have found difficulty in producing high viscosity droplets at speeds that would yield the Weber numbers necessary for splashing. However, investigators at the King Abdullah University of Science and Technology have investigated the splashing of low Ohnesorge droplets at high velocities, 20 -1000 ms^{-1} [97]. This was done through the construction of a 26 m tube. This tube is positioned vertically, a vacuum is established within it and droplets are allowed to free fall the length of the tube and the impact is imaged using high speed cameras. Combining the viscous droplet creation performed and discussed in the previous chapter, alongside this experimental set up would allow us to explore impacts at high Weber and Ohnesorge numbers.

Within the simulations presented here the NGV surface roughness was neglected along with the surface contact angle and surrounding air pressure. All these variables have been shown in the literature to have an effect on the propensity for droplets to splash. These latter two variables would be trivial to explore within the Flow 3D software, however there is no easy way to change the surface roughness of the surface within Flow 3D. One potential option would be to define a surface within a computer aided design (CAD) editor with roughness elements, and upload that as the surface into the Flow 3D software. However a very fine mesh would be needed to resolve these roughness elements, and this could cause a significant increase in the computational times.

5.5 Conclusions

In this chapter, a model was developed within the CFD software Flow 3D to simulate liquid droplets impacting on a dry, smooth surface. The purpose of these simulations was to investigate the propensity for ash droplets to splash when they impact the Nozzle Guide Vane (NGV) surfaces within a jet engine, and to explore how the splashing threshold varies with Weber and Ohnesorge numbers, as well as impact angle.

The Flow 3D setup was validated against experimental observations of droplet impacts by simulating the same impacts in Flow 3D and comparing the simulated splashing outcomes

to the experimentally observed ones. Good agreement was found between the simulations and experiments, although limited experimental data was available for Ohnesorge numbers $Oh > 1$.

Simulations of droplet impacts were performed over a range of Weber and Ohnesorge numbers, including the regime space occupied by the impacts of ash on NGV surfaces. It was observed that as the Ohnesorge number increases, the Weber number required for splashing to occur also increases. These results suggest that ash droplets do not splash on NGV surfaces.

No significant effect of the impact angle on the splashing threshold was found. However, the asymmetric splashing of oblique impacts, and the ability of the impact angle to both promote and suppress splashing observed in these simulations, was consistent with experimental observations found in the literature for oblique droplet impacts.

Further work is needed to provide experimental observations against which the simulations performed here can be validated. Suggestions for how this can be achieved were described, along with how the CFD modelling could be adapted to include effects of surface roughness and ambient air pressure.

Chapter 6

Understanding What Controls Ash Bouncing off the NGV.

6.1 Introduction

6.1.1 Motivation.

In Chapter 3 of this thesis the physical conditions under which ash droplets impact the Nozzle Guide Vane (NGV) surfaces were constrained using Computational Fluid Dynamics (CFD) simulations. The results of these simulations were used to design scaled experiments and simulations aimed to capture the splashing behaviour of volcanic ash droplets on the NGV. This work was presented in Chapters 4 and 5. To determine the accumulation rate of volcanic ash on the Nozzle Guide Vanes (NGVs), it is necessary to understand the proportion of the molten ash droplets that adhere to the vane surface, rather than bouncing off, as well as the specific areas on the surface where most of the ash adheres. To achieve this understanding, it is imperative to comprehend the conditions under which molten ash droplets bounce upon impact with a surface and the conditions under which they adhere. To address this, I used the results from Chapter 3 to design scaled experiments that investigate the conditions governing the behaviour of molten volcanic ash droplets, particularly focusing on whether they bounce off or adhere to the NGV surfaces.

6.1.2 Literature review.

The conditions under which ash droplets bounce or stick have been investigated in the literature. Sirinivasachar et al [98] performed experiments to investigate ash deposition in coal fired boilers. They placed soda-lime glass beads with diameters 28 – 74 μm into a flow of hot gases, and impacted the glass beads onto a probe made of cylindrical mullite substrates with a diameter of 1.6 mm. For each particle temperature they recorded the proportion of glass beads that stuck to the probe. Srinivasachar et al [98] found that with increasing temperature more beads stuck to the probe. They also altered the impact velocity, and for a given bead kinetic energy recorded a corresponding critical viscosity below which the glass bead would stick and above which the bead would bounce off the probe.

Similar experiments have been reported in Scharler et al. and Richter et al. [99, 100]. Using the experimental data from [98, 99, 100], Kleinhans et al. [70] produced an expression for the critical viscosity as a function of the particle kinetic energy, $E_{p,\text{kin}}$:

$$\mu_{p,\text{crit}} = 5 \times 10^{-12} E_{p,\text{kin}}^{-1.78}. \quad (6.1)$$

The data from [98, 99, 100] are shown in Table 6.1, and Fig [6.1] shows the data for the critical viscosities from [98, 99, 100] along with the critical viscosity curve in Eqn [6.1].

Table 6.1. Reproduction of a table from [70] showing the data for the critical viscosities found for different particle sizes and velocities from [98, 99, 100].

Study	$D_p / \mu\text{m}$	$v_p / \text{m s}^{-1}$	$\log(\mu_{p,\text{crit}})$
Srinivasachar [98]	40.5	1	7.2
	40.5	2	6.3
	63.5	3	5.1
Richter [100]	43.5	0.33	8.3
	81.5	0.33	7.6
Schulze [99]	71	3.1	3.2
	105	3.1	3.1
	105	6.2	2.0

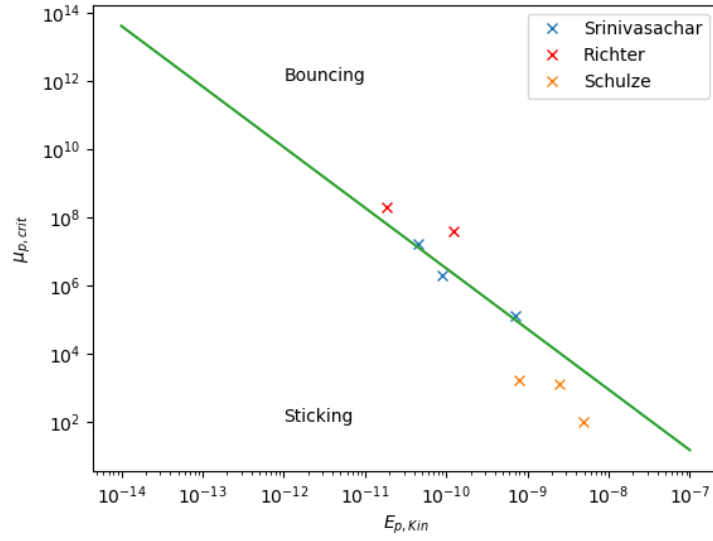


Figure 6.1: Plots of the critical viscosity against particle kinetic energy according to the model of [70]. The values of critical viscosity found for particles of given kinetic energies from [98, 99, 100] are also shown.

Kleinhans et al [70] performed their own experiments using soda-lime glass beads, and found that out of all the other sticking/bouncing models in the literature the model in Eqn [6.1] fitted their data best.

Kleinhans et al [70] adapted Eqn [6.1] to incorporate the effect of the impact angle on the tendency of molten glass beads to stick or bounce. Drawing on a mechanistic approach from Mao et al. [101], they segmented the impact process into five stages, and employed energy conservation principles to define an excess rebound energy E_{ERE} . If $E_{ERE} > 0$, then the impacting particle possesses sufficient energy to rebound off the surface. Conversely, if $E_{ERE} < 0$, there is insufficient energy available for the particle to rebound. The expression for the excess rebound energy is given as:

$$E_{ERE} = \frac{25}{172}\zeta^2(1 - \cos(\Theta_c)) + \frac{50}{129}\zeta^{-1} - \frac{3}{43}\zeta^{2.3}(1 - \cos(\Theta_c))^{0.63} - 1. \quad (6.2)$$

Here Θ_c is the contact angle between the liquid droplet, and the surface upon which it impacts. ζ is the maximum spreading diameter of the droplet, normalised by the droplet's initial diameter: $d_{p,max}/d_p$. An analytical expression for ζ is used by [70] to determine its value:

$$\left(\frac{1}{4}(1 - \cos \Theta_c) + 0.2\frac{We_p^{0.83}}{Re_p^{0.33}}\right)\zeta^3 - \left(\frac{We_p}{12} + 1\right)\zeta + \frac{2}{3} = 0. \quad (6.3)$$

Kleinhans et al [70] solve Eqn [6.2] and Eqn [6.3] for a critical viscosity. They did this for varying impact angles, defining the impact velocity as $v_p \times \sin(\theta)$ where v_p is the absolute velocity of the impacting particle and θ is the impact angle. Kleinhans et al [70] used this result to plot how the critical viscosity of a particle with a given kinetic energy changed with impact angle, to which they then fitted a tangent law. They then re-wrote Eqn [6.1] to include impact angle as a parameter:

$$\mu_{p,crit} = 5 \times 10^{-12} E_{p,kin}^{-1.78} \times 10^{-6.36/\tan(\theta)^{0.25}}. \quad (6.4)$$

Fig [6.2] reproduces a plot from [70] showing a plot of $\mu_{p,crit}$ against kinetic energy for different angles according to Eqn [6.4].

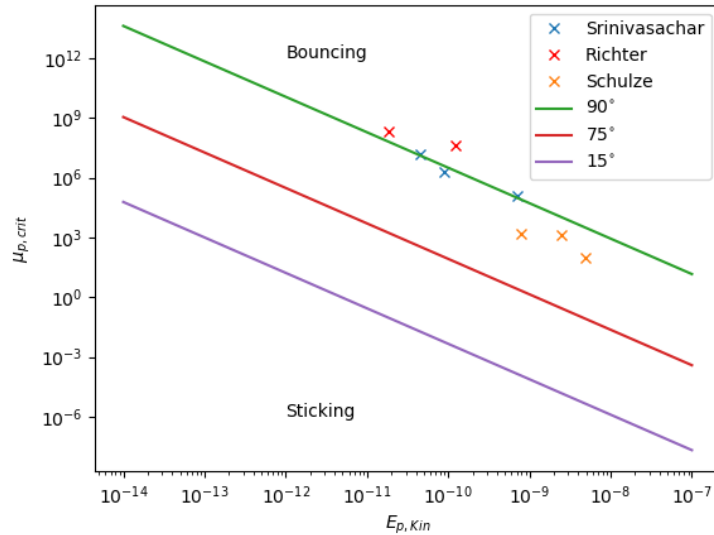


Figure 6.2: Plots of the critical viscosity against particle kinetic energy for different impact angles according to the model of [70]. The values of critical viscosity found for particles of given kinetic energies from [98, 99, 100] are also shown.

As was shown in Chapter 3 the impact angle of volcanic ash on the NGV is a significant variable. Therefore, when predicting the sticking and bouncing of volcanic ash, the effect of the impact angle needs to be considered. Although the model of Kleinhans et al [70] incorporates the impact angle, they have not compared the predictions of the model against any experimental data where the impact angle was a variable. No such experimental data has been found in the wider literature either. Consequently, the accuracy of predictions of this model for ash impacting at oblique angles is unknown.

When the model of Kleinhans et al. [70] was used in conjunction with the CFD results presented in Chapter 3, it was predicted that virtually none of the ash that impacted the NGV would stick, a result inconsistent with observations from stripped-down engines which had ingested volcanic ash in flight. It is clear therefore that more work is needed to define a threshold for the sticking/bouncing of volcanic ash impacting an NGV.

6.1.3 The Weissenberg number

It has been observed that under deformation magmatic fluids can stop behaving with a Newtonian rheology and instead exhibit a solid-like or brittle behaviour [72, 73, 102]. This is thought to depend on the ratio of the strain rate to the relaxation time scale of a magmatic fluid, with strain rates greater than the relaxation time scale leading to a solid-like response in the fluid, while strain rates smaller than the relaxation timescale lead to a liquid like response from the fluid [71, 102]. The simplest model of the structural relaxation timescale was proposed by Maxwell [103] as:

$$\tau = \frac{\mu}{G_{\infty}}, \quad (6.5)$$

where μ is the fluid viscosity and G_{∞} is the elastic shear modulus. For silicate melts and magmatic fluids the value of G_{∞} can be taken as $G_{\infty} = 10^{10}$ Pa, independent of temperature or chemical composition [104, 105].

Webb and Dingwell [102] first linked this relaxation timescale to the onset of brittle behaviour in silicate melts. They found that the onset of brittle behaviour occurred when the strain rate approached one hundredth of the relaxation timescale.

The ratio between the strain rate and the relaxation timescale can be written as a Weissenberg number:

$$Wi = \frac{\mu}{G_{\infty}} \dot{\gamma}, \quad (6.6)$$

where $\dot{\gamma}$ is the strain rate. The results of Webb and Dingwell [102] suggest the onset of brittle behaviour within a silicate melt occurs for $Wi \approx 0.01$. Cordonnier et al [72] performed 48 compression experiments on a molten liquid homogenous borosilicate glass, and found brittle behaviour dominated the melt when $Wi > 0.01$. Wadsworth et al [73] performed similar compression experiments on natural and synthetic volcanic glasses and found that $0.01 < Wi < 0.04$ represented a transitional window from viscous liquid behaviour to brittle behaviour.

Based on this previous work it is hypothesised here that the same physics applies for droplets of silicate melt impacting on a surface. When a droplet of diameter D and velocity v impacts a surface it undergoes a deformation, and the associated strain rate of the droplet can be written as v/D . This allows us to re-write the Weissenberg number for an impacting droplet as:

$$Wi_{\text{droplet}} = \frac{\mu}{G_{\infty}} \frac{v}{D}. \quad (6.7)$$

If $Wi_{\text{droplet}} > 0.01$ then one would expect brittle/solid-like behaviour to dominate the droplet and for it to bounce off the surface, and if $Wi_{\text{droplet}} < 0.01$ then fluid-like behaviour would dominate the droplet and it would stick to the surface. In Chapter 3 I calculated the Weissenberg and Weber numbers associated with the impacts of volcanic ash droplets on the NGV surface. In Fig [6.3] the results for the Weber and Weissenberg numbers are shown as a Gaussian density plot, with each point weighted to the associated particle's non-dimensional mass, the location of $Wi_c = 0.01$ is also shown.

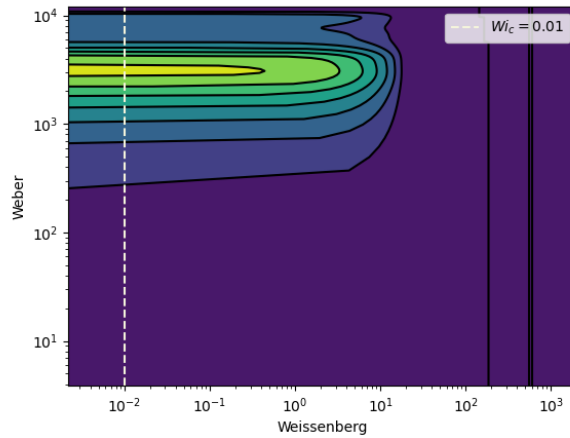


Figure 6.3: Gaussian kernel density plot of the Weber numbers against the Weissenberg numbers associated with the impacts of volcanic ash on the NGV surface, with each point weighted to the individual particle's non-dimensional mass. The limit of a hypothetical critical Weissenberg number of $Wi_c = 0.01$ is also shown. This Figure is reproduced from Chapter 3.

In Fig [6.3], it is apparent that a critical Weissenberg number, denoted as $Wi_c = 0.01$, delineates the primary area within the Weber-Weissenberg number space. Understanding if the critical Weissenberg number does control the bouncing of volcanic ash droplets off a surface, and if so how the value of the critical Weissenberg number may vary with impact

angle holds significant implications for understanding the accumulation of volcanic ash to the NGV surfaces.

Evidence for Wi_c from the literature.

Srinivasachar et al [98] impacted soda lime glass beads with diameters 53 – 74 μm with a velocity of 4 ms^{-1} onto a probe. They varied the bead temperatures and calculated the proportion of particles that stuck to the probe. They then plotted this ‘capture efficiency’ against the bead temperature. Using the bead temperatures from [98], I used a typical composition of soda lime glass [106], and a glass viscosity model [107] to calculate the corresponding glass bead viscosities. Using the calculated viscosities, the impact velocity of $v= 4 \text{ ms}^{-1}$, and a mean glass bead diameter of 63.5 μm , I calculated the Weissenberg numbers associated with the impacting glass beads. Fig [6.4] shows the original plot of the capture efficiency against the bead temperature from [98] alongside a plot of the Weissenberg numbers against the capture efficiency.

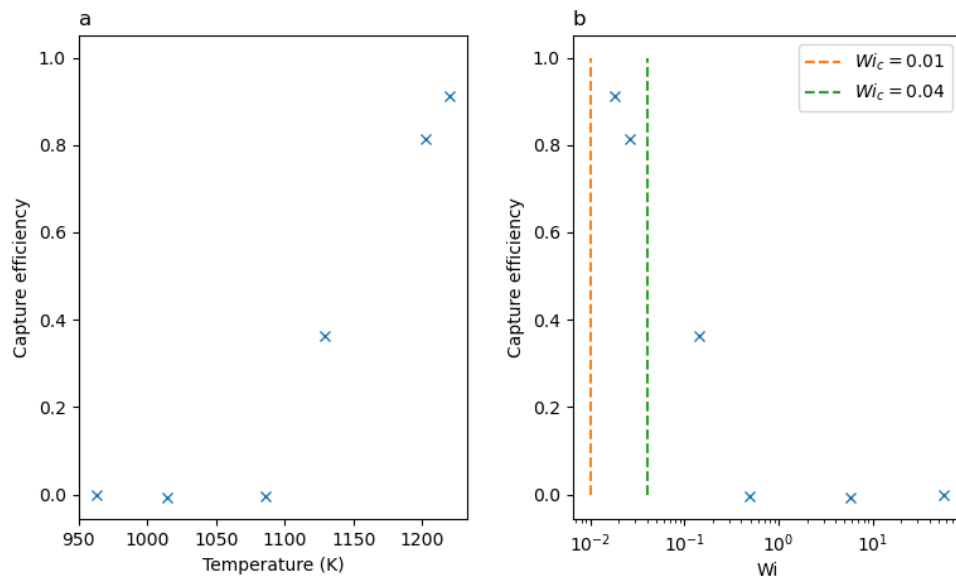


Figure 6.4: a: A reproduction of a plot from [98] showing how the capture efficiency of glass beads impacting a probe varies with particle temperature. b: Shows how the capture efficiency varies with the glass bead Weissenberg numbers.

Fig [6.4] shows that the Weissenberg numbers associated with the highest capture efficiencies from Srinivasachar et al [98], lie in the range identified by Wadsworth et al[73] $0.01 < Wi < 0.04$. This would seem to support the idea that the Weissenberg number can

be used to determine if a droplet of a silicate melt will bounce or stick on impact with a surface.

I used the critical viscosities from Table 6.1, and the associated particle diameters and velocities recorded by [98, 99, 100], along with an elastic modulus of $G = 10^{10}$ Pa to calculate the corresponding Weissenberg numbers shown in Table 6.2. If the data from [98, 99, 100] was consistent with the hypothesis of a critical Weissenberg number, then the Weissenberg numbers should fall in the range of $0.01 < Wi < 0.04$.

Table 6.2. Critical Weissenberg numbers calculated from critical viscosities found for different particle sizes and velocities from [98, 99, 100].

Study	Wi_{crit}
Srinivaachar [98]	39.1
	9.85
	0.793
Richter [100]	151
	16.1
Schulze [99]	6.1023×10^{-3}
	3.72×10^{-3}
	5.90×10^{-4}

It can be seen in Table 6.2 that the critical Weissenberg numbers calculated from the critical viscosities from [98, 99, 100] do not fall in the range $0.01 < Wi_c < 0.04$. This would seem to indicate that the Weissenberg number cannot be used to predict the bouncing/sticking behaviour of a silicate melt droplet.

6.1.4 Purpose of this Chapter.

The contradictory evidence presented here for a critical Weissenberg number that can describe the boundary between the sticking/bouncing behaviour of a droplet, suggests that more work is needed to investigate the role of the Weissenberg number in droplet impacts. It is also necessary to develop an understanding of how the effect of the impact angle would affect any critical Weissenberg number.

This chapter describes experiments to investigate the onset of sticking for molten soda lime glass beads. It details how the results from these experiments were used to evaluate the hypothesis of a critical Weissenberg number for droplet impacts, and how a new critical viscosity model was found that could predict the sticking/bouncing behaviour of impacting droplets.

6.2 Method

6.2.1 Apparatus and materials.

The experimental apparatus used was the same as described by [17]. An oxy-acetylene torch was mounted on a stand, and the flame was directed towards a metal target, the inclination angle of which could be set at specified values. The flow rate of acetylene and oxygen to the flame could be controlled, and this allowed a degree of control over the temperature of the flame and the velocity of the glass particles (indirectly via the gas velocity) that travelled through the flame. The target was made of Nimonic 75 material, a nickel-based superalloy, which is used to construct high temperature components for jet turbine engines.



Figure 6.5: Experimental set up, this comprises the ignited oxy-acetylene torch, the glass funnel through which glass particles were dropped, and the metal Nimonic 75 target plate.

Glass beads were made to pass through the funnel into the flame, upon which they would melt, and impact on the metal target. The glass beads were prepared a few days before in advance and sieved through a 64-micron sieve. However during storage, some particles clumped together into relatively large floccules of particles with diameters in the order of hundreds of microns across. To avoid delivering large clumps of glass particles into the flame, a 60 μm mesh was placed over the top of the funnel and the glass particles were put on top of the mesh. Then a fine-haired paint brush was used to brush gently over the glass beads causing particles to fall through the mesh into the flame.

Two types of glass particles were used, soda-lime glass and borosilicate glass. These were chosen for their different compositions and hence different viscosities when molten. The soda-lime glass beads were purchased from Potters Industries LLC (3222 Phoenixville Pike, Suite 103 Malvern, PA 19355, United States), and the borosilicate particles were prepared by crushing borosilicate rods provided by the National Glass Centre (University Of Sunderland, Sunderland, Tyne And Wear, SR1 3SD), and then grinding the shards to fine particles in a ball mill.

6.2.2 Experimental Method

The flame was turned on, and the flow-rates of oxygen and acetylene were varied until a steady blue flame was achieved. A thermocouple was used to measure the temperature

of the flame at the point where glass particles entered the flame. If this temperature was $T > 1500^{\circ}\text{C}$, then the flow rates of the gases were adjusted to reduce the temperature. Before particles were dropped into the flame, the flame temperature was measured at various distances from the nozzle of the oxy-acetylene torch to determine the temperature-distance profile of the flame. These measurements were taken 5 times, and the mean temperature was calculated for each distance. The error in each measurement of the temperature was taken to be $\pm 30^{\circ}\text{C}$. The Nimonic 75 plate was placed initially at a distance where the temperature of the flame was in the order of $300 - 400^{\circ}\text{C}$. For each flame setting tests were run for four different angles of inclination of the target plate ($30^{\circ}, 50^{\circ}, 70^{\circ}$, and 90° with respect to the horizontal). For each test a video recording was taken using a Phantom high-speed camera, with a frame rate of 1000 fps.

The camera was activated and then glass beads were encouraged into the flame by brushing the top of the mesh for approximately 4 seconds, at which point the camera would stop recording. After this time had elapsed, the target was examined to see whether any glass had stuck to the target surface, the target was then moved closer to the flame and the test was repeated. This whole process was done until glass was sticking firmly to the target surface and could not be detached by myself blowing gently across the surface of the target. Three ‘types’ of behaviour were observed: Firm bouncing, this was when no particles stuck to the surface of the target and the target was clean after the test; firm deposition, this was when particles stuck firmly to the target surface and could not be blown off; and finally uncertain deposition, this was where particles did stick to the surface but on blowing across the surface of the target they flew off leaving the target clean.

This was then repeated for different flames, with different temperature-distance profiles. When glass particles stuck to the target, the target was replaced before the next experiment. In delivering the borosilicate particles to the flame, it was observed that even with the particles being passed through the $60\ \mu\text{m}$ mesh, the particles would settle on the side of the funnel before falling into the flame as large floccules. The reason for this is unknown, but it could be that the particles were damp, and the moisture was causing them to stick together. For this reason, no further tests were done using the borosilicate particles, and all the results presented in this chapter are for the tests involving the soda-lime glass beads.

6.2.3 Calculating the temperature, velocity and size of the particles.

In order to calculate the kinetic energies, viscosities, Weissenberg and Weber numbers of the impacting glass particles, it was necessary to know the diameters of the impacting particles, their velocities, and their corresponding temperatures.

Particle Velocity

For each video from each test a selection of ten particles were manually tracked from frame to frame and the corresponding velocities of the particles were calculated. In the videos that were recorded the particles appeared as white streaks on a black background. Therefore, it was not possible to determine the size of any given particle, and therefore any correlation between the size of the particle and their impact velocity is unknown. The particle velocities were not found to change significantly with their passage through the flame. From the velocities of the ten particles, a mean velocity was calculated and this was used as the velocity for all the particles in the test in the subsequent calculations. These individual velocities are recorded in Table 9.4 in the appendix.

Particle size

To determine the particle size distribution of the soda lime glass beads, a sample of the beads was passed through a Camsizer X2 from Microtrac (Verder Scientific, Haan, Germany). The Camsizer has two modules, a Fall module and a Jet module. In the Fall module the particles fall under gravity past a camera which takes images of the particles from which diameters of the particles can be extracted. In the Jet module the particles are blown past the camera in a stream of air, this has the effect of breaking up any clumps of particles that may have formed. The resulting cumulative distribution functions found by both methods are shown in the figure below.

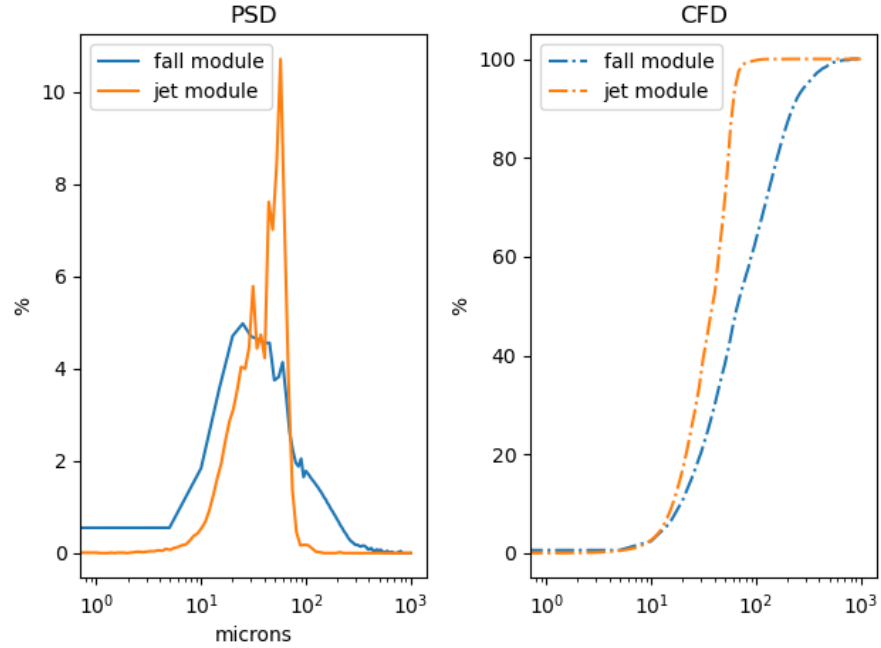


Figure 6.6: This figure depicts the CDFs and PSDs produced by the Camsizer for the soda lime glass samples of particles. It can be seen that there is a very fine tail in the distributions for the glass beads.

The Camsizer software only returns the data shown in Fig [6.6]. It does not return values for all the diameters of the particles that it measured. Therefore, the inversion method was used alongside the cumulative distribution function (CDF) measured with the fall module, to generate a sample of particle diameters representative of the soda lime glass beads.

The Inversion method works as follows. For a random variable, like a particle diameter d , the CDF $F(d)$ is a non-decreasing function with $0 \leq F(d) \leq 1$. This means that for a uniform distribution of random numbers r_n where $0 \leq r_n \leq 1$, by drawing a specific random number r a sample diameter can be found through:

$$d_s = F^{-1}(r). \tag{6.8}$$

An algorithm was written in Python to perform this method and generate a representative sample of 500 soda lime glass bead diameters. I chose to use the CDF measured via the Fall module as the particles were delivered into the flame in a way more consistent with the way the Fall module measures the particle diameters. The effect of the 60 μm mesh over the top of the funnel was accounted for, by rejecting any diameters generated from the Inversion method which were $>60 \mu\text{m}$.

Particle Temperature

First it was necessary to estimate the temperature-distance profile of each flame from point measurements of the temperature at different distances from the nozzle. This was done by linear regression. Two example flame profiles of different temperatures are shown in Fig [6.7]. Note that the particles in the cooler flame travelled at $5 \pm 0.1 \text{ ms}^{-1}$, and in the hotter flame at $15 \pm 0.2 \text{ ms}^{-1}$.

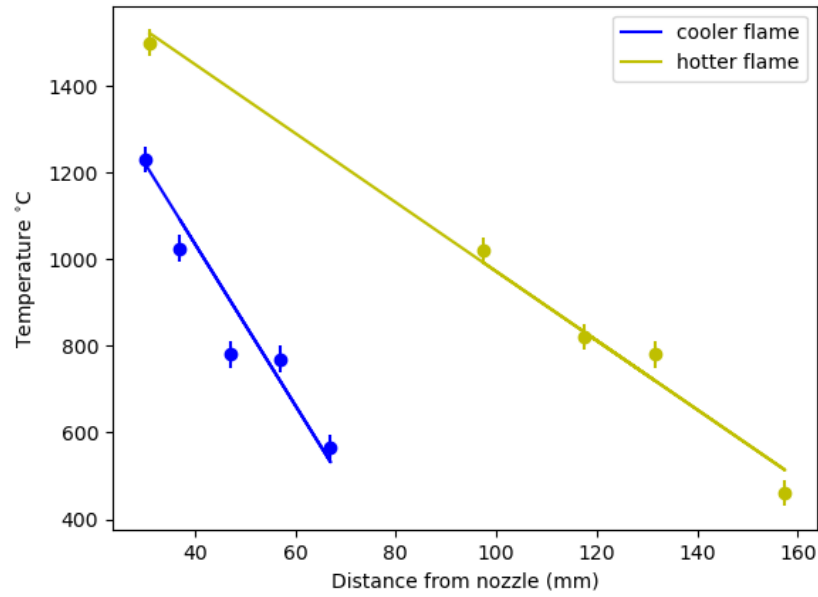


Figure 6.7: Profiles of the temperature fields for two distinct flame configurations with varying acetylene and oxygen flow rates.

To calculate the impact temperature of the particles the lumped capacity method was used. For a given body with mass m , specific heat capacity c , and surface area A , in a fluid at temperature of T_f , the variation in the temperature of the body, T (if the temperature of the body can be taken to be uniform at all times) is given by:

$$mc \frac{dT}{dt} = hA(T_f - T), \quad (6.9)$$

where h is the heat transfer coefficient. For a constant fluid temperature, where the body does not influence the temperature of the fluid, the temperature of the body after being immersed

in the fluid for a time t is given by:

$$T = T_f - (T_f - T_i)e^{-t(\frac{hA}{mc})}, \quad (6.10)$$

where T_i is the initial temperature of the body. The heat transfer coefficient was calculated from the Nusselt number:

$$Nu = \frac{hD}{k_f}, \quad (6.11)$$

where D is the diameter of the particle and k_f the thermal conductivity of the fluid. I assumed that the particles were coupled to the gas flow and therefore as they were travelling at the same velocity as the gas, the heat transfer was via natural convection rather than forced convection. The average Nusselt number of a sphere for natural convection, as defined by Incropera and DeWitt [108] is equal to:

$$Nu_{\text{average}} = 2 + \frac{0.589 \times Ra_D^{1/4}}{(1 + \frac{0.469}{Pr^{9/16}})^{4/9}}. \quad (6.12)$$

Here Pr is the Prandtl number, which for air and most gases has a value of $Pr = 0.71$, and Ra_D is the Rayleigh number of the particle, and is defined as:

$$Ra_D = \frac{g\beta|T - T_f|D^3}{v\alpha}. \quad (6.13)$$

Here g is the acceleration due to gravity, β the thermal expansion coefficient of air, v the kinematic viscosity of air, α the momentum diffusivity of air, and $|T - T_f|$ the difference in particle and flame temperature. The properties of air were determined for a temperature of 800°C. By setting the two expressions for the Nusselt number equal to each other the heat transfer coefficient can be calculated. In these calculations it was assumed that the particles could be treated as perfect spheres, and that the heat capacity of the glass and the thermal conductivity of the air were constant.

Before proceeding with the lumped capacity method, it is first necessary to examine the Biot number. For a small Biot number thermal equilibrium in a particle after a change in temperature of the surroundings is limited by convection at the surface as opposed to conduction within the particle. Therefore for a small Biot number, defined by [108] as $Bi \ll 0.1$, the temperature across the glass particles can be assumed to be uniform and the lumped capacity method can be used. The Biot number is defined by Incropera and DeWitt [108] as

:

$$Bi = \frac{h(D/6)}{k_{\text{glass}}}, \quad (6.14)$$

where k_{glass} is the thermal conductivity of glass. It is defined differently by [109]:

$$Bi_{\text{Wadsworth}} = \frac{h(D/2)}{\rho c D_{\text{th}}}, \quad (6.15)$$

where D_{th} is the thermal diffusivity of glass, taken to be $D_{\text{th}} = 10^{-6}$. For both these definitions of the Biot number in the range of diameters considered $D \leq 300 \mu\text{m}$, the calculated Biot numbers were $Bi \ll 0.1$ and so I could be confident in the use of the lumped capacity method.

For a given distance from the funnel, and for a given flame profile, the time of flight for a particle was calculated. This time was then divided into timesteps for each of which the particle distance from the flame was calculated, and then inputted into the linear models found for the flame temperature-distance profiles to find T_f at each given timestep. Assuming the glass particles started at room temperature (25°C), Eqn [6.10] was applied iteratively over all the timesteps for each of the distances, for particles of different sizes. The results of these calculations can be seen in Fig [6.8], which shows how the temperature of glass particles of different sizes vary as they travel through the flames corresponding to the flame profiles in Fig [6.7].

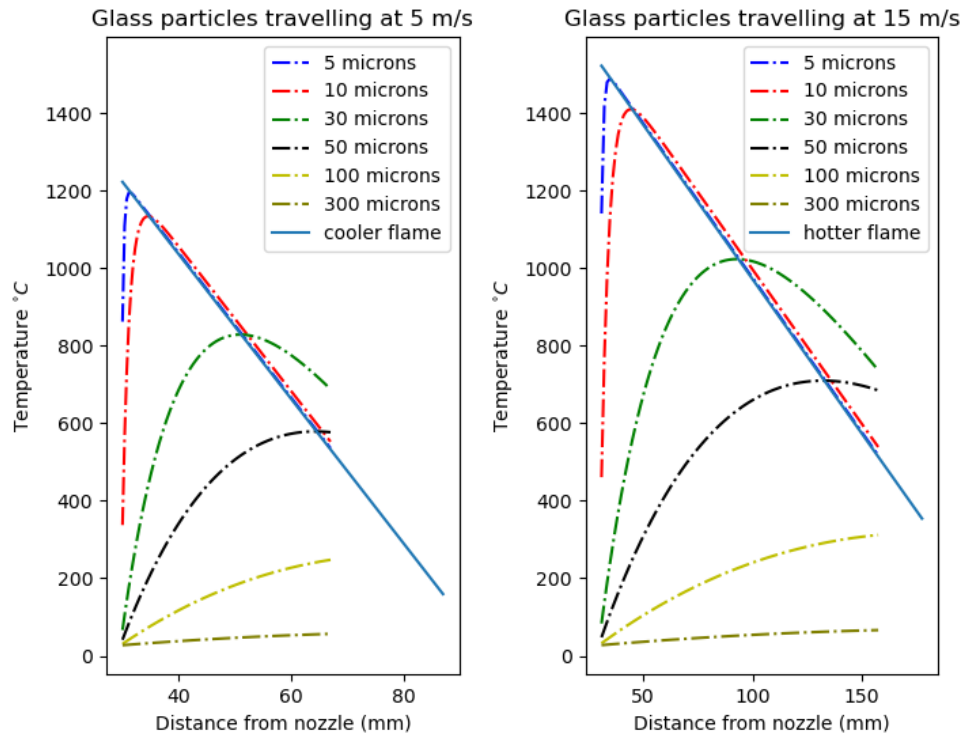


Figure 6.8: How the temperature of particles with diameters 5-300 μm would vary travelling through the flames associated with the two flame profiles in Fig [6.7].

It can be seen that the smaller particles are well thermally coupled to the flame, heating up quickly and cooling down at a similar rate to the flame as they travel further away from the nozzle. However larger particles take longer to heat up to the temperature of the flame, and also cool down at a slower rate than the flame.

6.2.4 Calculation of particle impact properties

Viscosity and kinetic energy

The glass viscosity model from [107] was used to calculate the viscosities of the impacting particles. For the 500 particle diameters generated via the Inversion method, the temperature of these particles on impact with the target were calculated using the lumped capacity method described previously. These temperatures for the different particles were used in the viscosity model, alongside compositional data for Soda Lime Glass from [106]. Any resulting particle viscosity calculated from the model that was $\mu > 10^{12}$ Pas was not considered in the calculations of the dimensionless numbers, this is because at these viscosities the glass

particles are not behaving as a viscoelastic fluid.

The kinetic energy of the impacting particles was calculated for each particle diameter using the mean velocity calculated for each test. A constant density was assumed of $\rho = 2550 \text{ kgm}^{-3}$, allowing the kinetic energy $E_{p,\text{Kin}}$ to be found as:

$$E_{p,\text{Kin}} = \frac{\pi}{12} \rho D^3 v^2. \quad (6.16)$$

Here the symbols have the same meaning as before and v is the impact velocity.

Calculation of Weissenberg and Weber numbers

Having found the velocity, size and corresponding viscosities it was possible to calculate the Weissenberg and Weber numbers for the particle impacts for each test, where the Weissenberg and Weber numbers are given by:

$$Wi = \frac{v \mu}{D G}, \quad (6.17)$$

and

$$We = \frac{\rho v^2 L}{\sigma}, \quad (6.18)$$

respectively. Here all the symbols have the same meaning as previously and μ corresponds to the viscosity, G the relaxation modulus which was taken to be $G = 10^{10} \text{ Pa}$ for the glass particles, and σ the surface tension which was taken to be $\sigma = 0.25 \text{ Nm}^{-1}$ [79, 80].

6.3 Results

The results of these experiments are presented here via the kinetic energy, the viscosity, the Weber and Weissenberg numbers of the impacting glass particles. It is important to understand the interplay between these quantities. In Fig [6.9] below can be seen the results taken from a single test. The results are plotted as the particle diameter against particle viscosity, kinetic energy against viscosity and Weissenberg number against Weber number. Each individual point corresponds to a single particle. The particle diameters were found via the Inversion method as described previously.

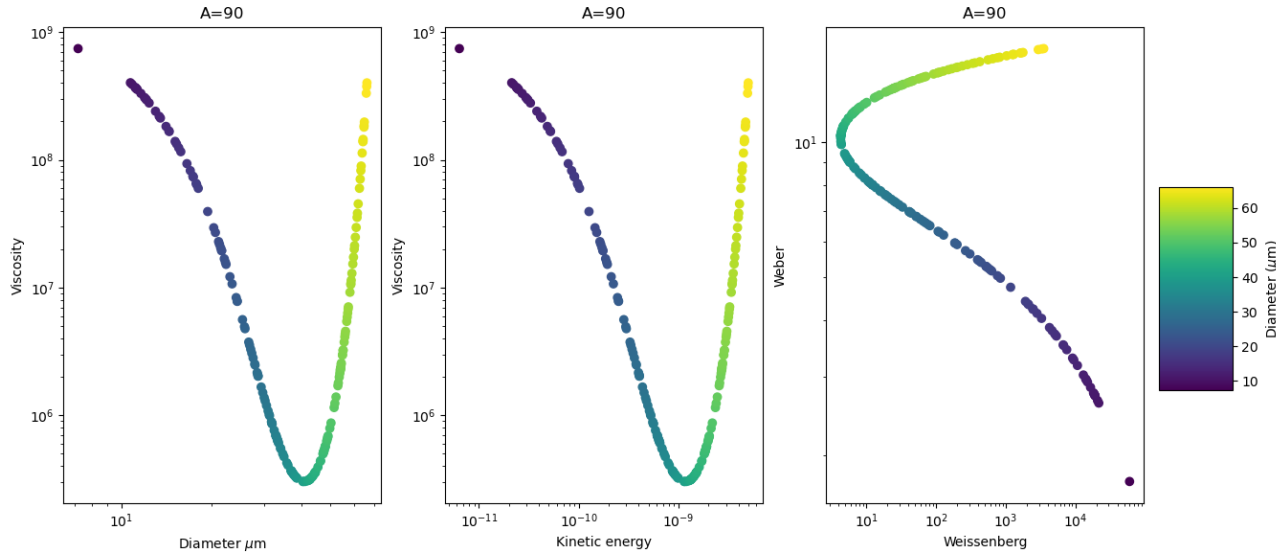


Figure 6.9: Plots of particle diameter versus particle viscosity, kinetic energy versus viscosity, and Weissenberg number versus Weber number for a single test of particles dropped into a flame and impacted on a metal target. Each point is coloured according to its diameter in microns.

It can be seen in Fig [6.9], that initially the viscosity of the glass particles decreases with diameter before increasing. This is because the smaller particles were well coupled to the flame and so heated up quickly and cooled quickly with the flame. The largest particles heated up very slowly and never got close to the temperature of the flame, but the ‘Goldilocks’ particles heated slowly up to the temperature of the flame and cooled slowly meaning on impact with the target they were the hottest particles and the least viscous. As kinetic energy is proportional to the cube of the particle diameter, the viscosity initially decreases with increasing kinetic energy and then increases. As the Weissenberg number is indirectly proportional to the particle diameter but also directly proportional to the viscosity, these Goldilocks particles corresponded to the smallest Weissenberg numbers. This causes the characteristic curves in the Weber-Weissenberg number plots in Fig [6.9]. The range of diameters that form the Goldilocks range vary with flame profile and the target distance from the nozzle.

Fig [6.10] shows where the Weissenberg and Weber numbers from the experiments sat in the Weber-Weissenberg number space occupied by the impacts of volcanic ash on the NGV.

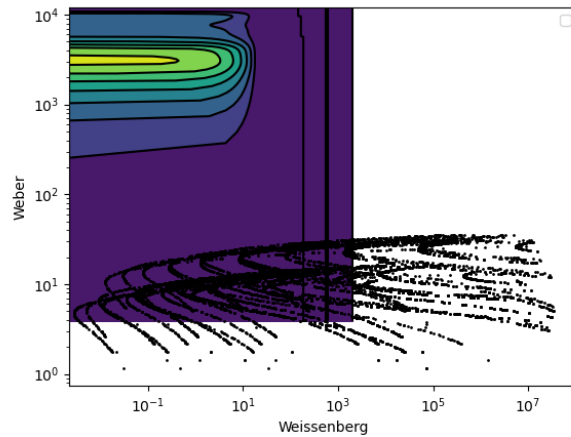


Figure 6.10: Gaussian kernel density plot of the Weber numbers against the Weissenberg numbers associated with the impacts of volcanic ash on the NGV surface, with each point weighted to the individual particles non-dimensional mass. The Weber and Weissenberg numbers from the experiments are plotted as black points.

It can be seen that while the experiments are well scaled to the Weissenberg number, they are not quite as well scaled to the Weber number. This is because the glass particles are impacting at lower velocities than the volcanic ash particles impact the NGV surfaces.

Fig [6.11] shows photographs of the targets after demonstrating the different behaviours identified earlier, namely: firm deposition, no deposition, and light deposition which blew off.

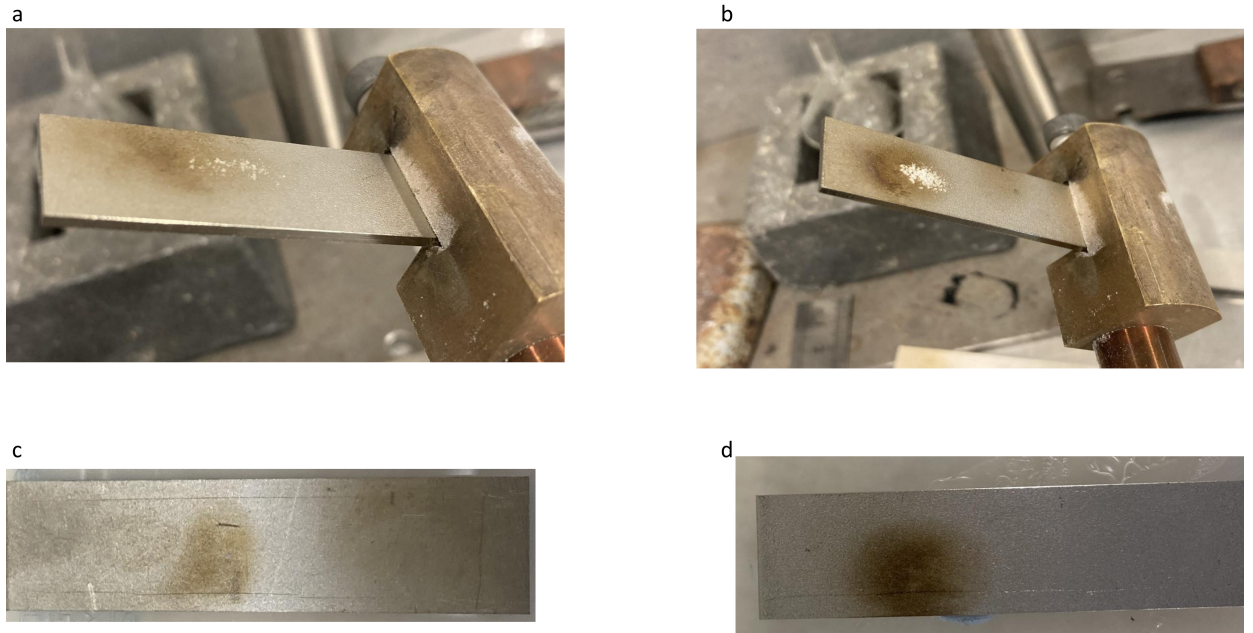


Figure 6.11: a: The deposition of molten soda lime glass beads on a target that was angled at 30° . b: The deposition of molten soda lime glass beads on a target that was angled at 50° . c: A target that was angled at 50° and had glass deposit on the surface but that was easily blown off. d: A target that was angled at 30° , and to which no glass stuck.

The calculated values for the Weissenberg and Weber numbers are shown plotted against each other in Fig [6.12] for the glass particle impacts. Each point is coloured according to the sticking/bouncing behaviour observed overall in the test. The position of the hypothesised critical Weissenberg number $Wi_c = 0.01$ is also shown.

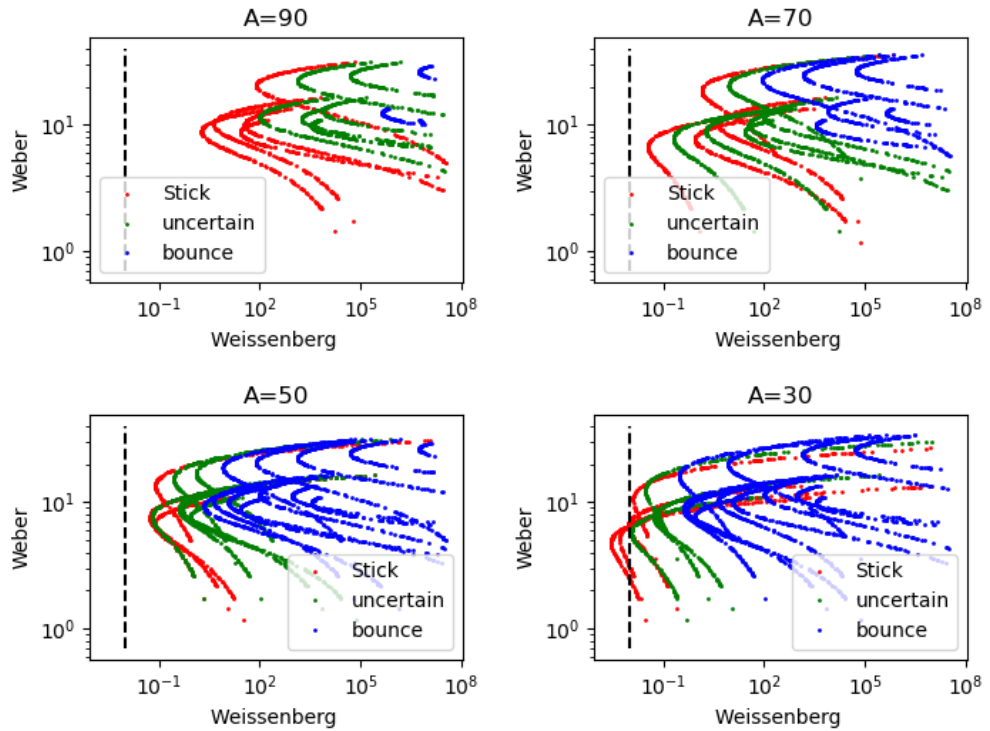


Figure 6.12: The calculated Weissenberg and Weber numbers for the experiments conducted on the targets. The red points correspond to firm sticking of glass to the surface, the green points to when glass deposits could be blown off the surface, and blue points to when no deposition was observed. The position of $Wi_c = 0.01$ is indicated by a black dashed line.

The Weissenberg number is indirectly proportional to the diameter of the particle, therefore as the diameter increases (and the Weber number increases also) the Weissenberg number decreases for a constant viscosity and velocity. However as can be seen in Fig [6.12], above a certain particle size (which varies from test to test) the Weissenberg number of the glass particles increases with diameter. This is because, as was described earlier, the smaller particles were closely coupled with the flame, causing them to heat up and cool down quickly. In contrast, the largest particles heated up very slowly, never reaching the flame's temperature. The intermediate particles, referred to as 'Goldilocks' particles, heated gradually to the flame's temperature and cooled slowly. Consequently, upon impact with the target, they were the hottest and least viscous. As the Weissenberg number is directly proportional to the viscosity, this means the Weissenberg numbers were smaller for these Goldilocks particles.

It can be seen in Fig [6.12] that as the inclination angle increases from $30^\circ - 90^\circ$ the

Weissenberg number at which the onset of sticking occurs increases. Fig [6.12] shows that sticking occurs at $Wi \gg 0.01$ for impact angles of $\theta = 90^\circ$, and for all the other impact angles sticking was observed for $Wi > 0.01$.

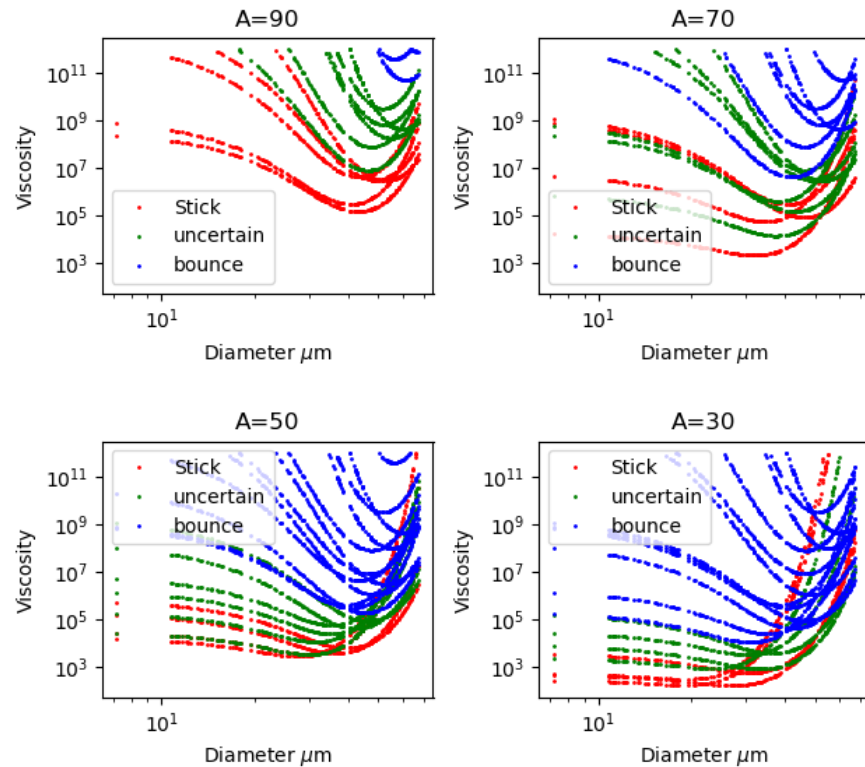


Figure 6.13: This figure shows a plot of how the viscosity of the impacting glass beads changes with diameter for the results corresponding to Fig [6.12]. The red points correspond to firm sticking of glass to the surface, the green points to when glass deposits could be blown off the surface, and blue points to when no deposition was observed.

Fig [6.13] shows the calculated values for the particle diameters and viscosities upon impact with the targets. It is observed that the viscosity of the glass particles initially decreases with diameter before increasing. As was described previously this is because the smaller particles were well-coupled to the flame, heating up quickly and cooling quickly with the flame. The largest particles heated up very slowly and never reached the temperature of the flame. However, the ‘Goldilocks’ particles heated slowly, eventually reaching the flame’s temperature, and cooled slowly, and consequently were the hottest particles on impact. Note that in a given test, it is impossible to determine the exact diameter at which particles begin to bounce. Therefore, in tests where deposition occurred, all particle impacts are logged as

sticking events. This explains why, in Fig [6.12] and Fig [6.13], the red curves representing deposition observations intersect the blue curves of tests where no glass droplet deposition was seen.

The results for the viscosity and corresponding particle kinetic energies are shown in Fig [6.14] below. The thresholds for particle bouncing versus sticking from Kleinhans et al [70] are also displayed as a solid blue line. When considering the plots for the viscosity of the particles against their kinetic energy, the viscosity decreases with kinetic energy before increasing. This is not surprising as the kinetic energy is proportional to the cube of the particle diameter.

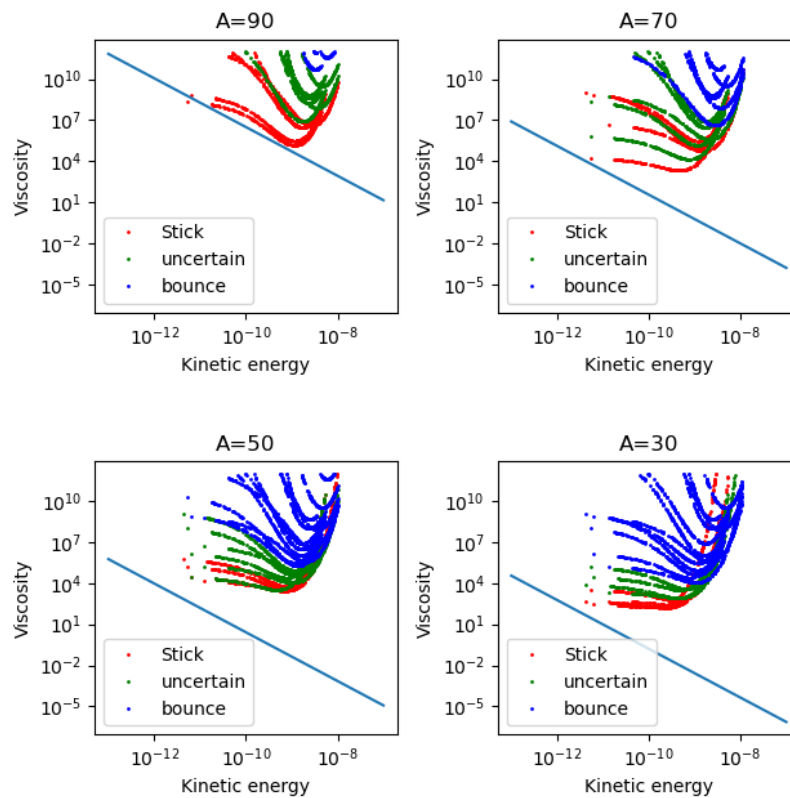


Figure 6.14: The calculated particle viscosities and particle kinetic energies for the experiments conducted on the targets. The red points correspond to firm sticking of glass to the surface, the green points to when glass deposits could be blown off the surface, and blue points to when no deposition was observed. The bouncing/sticking threshold of Kleinhans et al [70], where below the line sticking is predicted and above bouncing, is shown as a blue solid line.

Fig [6.14] also shows that as the inclination angle increases from $30^\circ - 90^\circ$, the viscosity

at which the onset of sticking occurs increases.

Error analysis was conducted on the data shown in the previously presented graphs. Only the error in the temperature of the impacting particles was considered, as it is the dominant error in the subsequent calculations of the glass particle viscosity. The error in the temperature of the particles was taken to be the larger of either $\pm 30^\circ\text{C}$ (i.e., the error in each measurement of the flame temperature taken with the thermocouple) or the mean residual of the flame temperature measurements with respect to the linear regression fitted to these measurements. The error bars are not shown in the graphs above to enhance readability; however, in Fig. [9.1] in the appendix, the data for tests where the three different outcomes (firm deposition, no deposition, and light deposition which blew off) were observed for a target inclination angle of 50° are plotted with error bars. It can be seen that for the tests that occurred at higher temperatures, the error bars are smaller. This is due to the exponential relationship between glass temperature and viscosity.

6.4 Discussion

It was first hypothesised that when the molten glass particles impacted on the metal target, despite molten glass having a Newtonian rheology, the particles could experience such high-strain rates that the particles would exhibit a solid-like response and bounce off the target rather than sticking. The onset of solid-like behaviour of magmatic liquids under deformation has been shown in the literature to be controlled by the Weissenberg number, with [72, 73, 102] showing the onset of this solid-like behaviour for $Wi < 0.01$. It was thought that this critical Weissenberg number, $Wi_c = 0.01$, could be used to predict the bouncing or sticking behaviour of molten glass droplets impacting the target, with droplets bouncing if their associated Weissenberg number was $Wi > 0.01$.

However these experiments, presented here, do not support this hypothesis of the critical Weissenberg number. Fig [6.12] shows that for all impact angles, glass droplets would stick to the target for Weissenberg numbers $Wi > 0.01$. In the case where the impact angle was 90° , one would expect the strain rates to be greater as the droplets impact the target head on, as opposed to for more glancing impacts. However the onset of sticking occurs for droplet impacts for angles at 90° , at higher Weissenberg numbers compared to droplet impacts at more glancing impact angles. These results and the analysis of previous work presented in

the introduction to this chapter, leads to the conclusion that the Weissenberg number does not control the bouncing/sticking behaviour. However it is important to note that though these experiments have been designed to be well scaled to the jet engine in terms of the Weissenberg number, they are not as well scaled in terms of the Weber number. It could be that at the larger velocities corresponding to these larger Weber numbers, the Weissenberg number does influence the sticking/bouncing threshold.

Empirical models for the bouncing/sticking behaviour of molten ash and glass droplets in terms of their kinetic energies and viscosities, reported in the literature, define a critical viscosity μ_{crit} as a function of a particle's kinetic energy. If the viscosity of a given particle, μ_p is less than its associated critical viscosity, $\mu_p < \mu_{\text{crit}}$, then the particle will stick on impact and if $\mu_p > \mu_{\text{crit}}$ the particle will bounce. I chose to compare my experimental data to the critical viscosity model of Kleinhans et al [70]. This was chosen as they used a broad range of data from the literature to determine their model. Though they also considered the effect of droplet angle, it is important to note again that Kleinhans et al [70] do not compare this model against any experimental data.

It can be seen in Fig [6.14] that the model of Kleinhans et al [70] does not well describe the data presented in this chapter, with sticking observed at viscosities far greater than the critical viscosities predicted. However the constants in the model were fitted empirically, and therefore could vary with the material properties of the impacting droplets, the surface properties of the target, and other experimental conditions. There is no reason to reject, based on the experimental data presented here, the relation between a particle's kinetic energy and its associated critical viscosity presented by Kleinhans et al [70], $\mu_{\text{crit}} \propto E_{\text{p,Kin}}^{-1.78}$. For this reason it was decided to use the experimental data presented here, to find an expression for the critical viscosity of the form:

$$\mu_{\text{crit}} = A \times E_{\text{p,Kin}}^{-1.78}, \quad (6.19)$$

where A is an empirical constant that is a function of the impact angle.

The main challenge in identifying the onset of sticking from the results in Fig [6.14] comes from the range of sizes of droplets that impact the target. For tests where sticking was observed, larger particles with higher viscosities will have bounced, whereas smaller particles with lower viscosities will have stuck. Recall there is no way to distinguish, for a

given test, at what diameter the particles start to bounce. Consequently, all particle impacts for a test where deposition was observed are recorded as sticking. This is why, in Fig [6.13], at larger kinetic energies (and hence particle diameters), the red curves associated with deposition observations intersect the blue curves associated with tests where no deposition of glass droplets was observed.

To determine an expression for A , distinct values of A were selected for each test in Fig [6.14]. These values were chosen so that the resulting curve for the critical viscosity evenly divided the associated data points, with half lying above and the other half below the critical viscosity curve. The decision for this 50-50 split stems from the recognition that, for a given sticking event, not all particles may deposit on the target, however, enough particles needed to stick for any deposit to be visible. An algorithm was written by myself in Python that selected for each test a value of the constant A , such that $50\% \pm 1\%$ of the data points lay above or below the resultant critical viscosity curve. The resulting curves are shown in Fig [6.15].

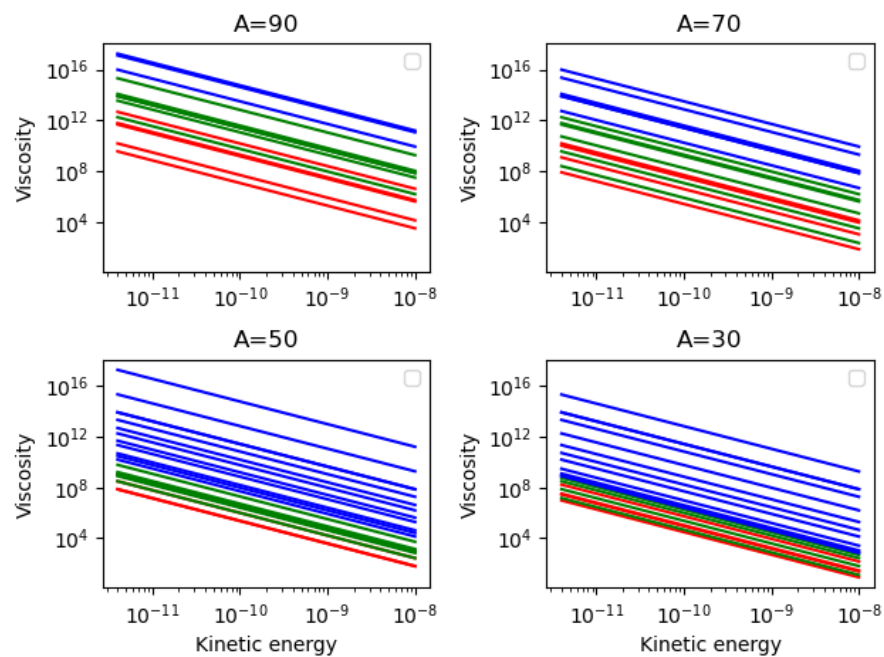


Figure 6.15: The critical viscosity curves that bisect the data presented in Fig [6.14]. Note that as the graph is on a log-scale, the curves appear as straight lines. As before the red lines correspond to observed deposition, the blue lines to no deposition, and the green lines to where deposition was observed but the deposit was easily blown off.

It is evident from Fig [6.15] that the fitted critical viscosity curves partition the viscosity-kinetic energy space into regions where sticking and bouncing behaviour can be expected, respectively.

For each impact angle the largest value of A corresponding to a sticking event, and the smallest value of A corresponding to a bouncing event were selected. The base 10 logarithm of these bouncing and sticking coefficients was then plotted against the cosine of the impact angle. This is shown in Fig [6.16].

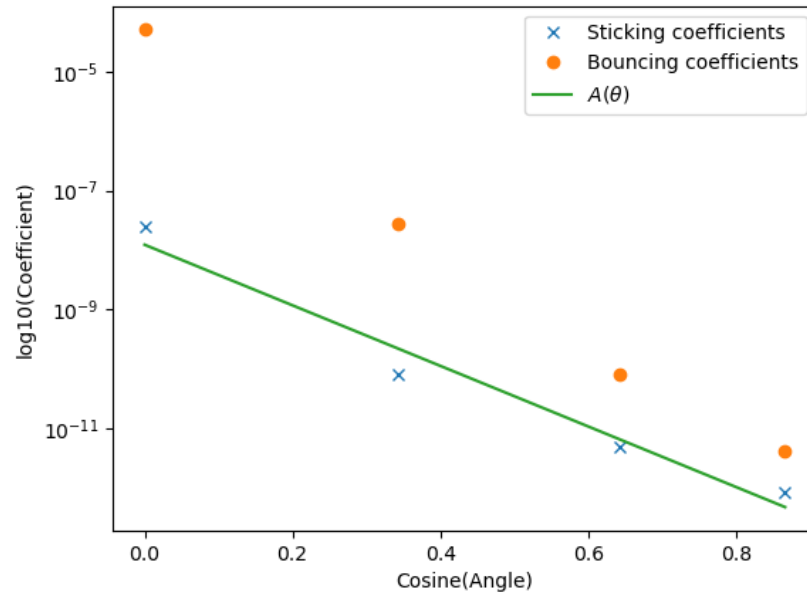


Figure 6.16: The standard logarithm of the minimum and maximum bouncing and sticking coefficients against the cosine of the impact angle. $A(\theta)$ is the function in Eqn [6.20].

In Fig [6.16], the plot shows a decrease in both sticking and bouncing coefficients as the cosine of the impact angle increases. Linear regression was performed on the sticking coefficients, which allowed an expression for the coefficient A as a function of the impact angle θ to be written as:

$$A(\theta) = 10^{-(7.9+5.1 \cos(\theta))}. \quad (6.20)$$

This expression can be seen in Fig [6.16]. Combining Eqn [6.20] with the original expression for the critical viscosity in Eqn [6.19], allows us to write a new expression for the critical viscosity as a function of particle kinetic energy and impact angle as:

$$\mu_{\text{crit}}(\theta, E_{\text{p,Kin}}) = 10^{-(7.9+5.1 \cos(\theta))} \times E_{\text{p,Kin}}^{-1.78}. \quad (6.21)$$

In determining an expression for $A(\theta)$ recall values of A were selected for each test in Fig[6.14] such that the resulting curves for the critical viscosity divided the corresponding data points 50-50. To test the sensitivity of the resulting expression $A(\theta)$ to this choice, the algorithm was rerun to find values of A where 55% of the data points lay above the critical viscosity curves, and then rerun a third time to find values of A where 45% of the data points lay above the curves. Linear regression was applied again to these new values of A to find two new expressions for $A(\theta)$:

$$A(\theta)_{55\%} = 10^{-(7.6+4.8 \cos(\theta))}, \quad (6.22)$$

and

$$A(\theta)_{45\%} = 10^{-(7.9+5.5 \cos(\theta))}. \quad (6.23)$$

Eqns[6.22-6.23] were plotted alongside Eqn[6.20]. This plot can be seen in Fig[9.2] in the appendix.

6.4.1 Limitations

The primary challenge in this work was the inability to further constrain the range of particle diameters delivered into the flame. In the analysis presented earlier, where coefficients for Eqn [6.19] were determined, these coefficients were found so as to bisect the data on the curves associated with observed deposition. It is improbable that, for every sticking event, exactly half of the droplets bounced while the other half stuck. Hence, the expression for the critical viscosity in Eqn [6.21] could be refined further. In future experiments, particles could be sieved into narrower size fractions, for example, 2 – 30 μm and then 30 – 60 μm . Under a given flame setting and target distance from the funnel, the two different samples of glass beads could be fed into the flame. For a given set of conditions, it would likely be found that the finer particle size fraction would stick to the plate, while particles from the larger size fraction would bounce. This approach would allow the location of the sticking-bouncing threshold to be constrained further.

This investigation did not study in detail any surface property effects on the bouncing/sticking behaviour of impacting droplets. Surface roughness was briefly investigated on the last day available in the laboratory. Several targets were polished until the surface resembled a mirror. The same methodology was then repeated, but now using these polished

targets. The data from these experiments are not presented here due to the small amount of data collected. The initial results were mixed, showing that for most impact angles, the polished surfaces promoted sticking compared to the rough surfaces. However, for impact angles of 30° , the opposite was observed, with particles more likely to bounce off the surface.

Finally though the experiments presented here were well scaled to the Weissenberg numbers associated with the volcanic ash droplet impacts on the NGVs, they were not as well scaled to the associated Weber numbers. For this the glass particles would need to have been impacting on the target with greater velocities, this would have required a larger torch than was available.

6.5 Conclusions

In this chapter, I have presented an experimental investigation to explore the bouncing and sticking behaviour of molten glass droplets impacting a metal surface at different inclination angles. This was accomplished by delivering glass particles into the flame of an oxy-acetylene torch, directed at a Nimonic 75 plate, and observing whether any glass adhered to the target surface.

The experiments were initially scaled to explore the range of Weissenberg numbers associated with the impacts of volcanic ash on the Nozzle Guide Vanes (NGVs). Contrary to the initial hypothesis, it was found that a particle impact with a Weissenberg number less than the critical Weissenberg number of $Wi_c = 0.01$ did not accurately predict the onset of sticking. Experimental data showed sticking occurring at values of $Wi \gg 0.01$. The data also revealed a strong dependence on the angle at which the target was held, with more glancing angles promoting bouncing.

I then compared the experimental data against the empirical critical viscosity model from Kleinhans et al [70], which uses an impacting particle's kinetic energy, viscosity, and impact angle to determine whether it will stick or bounce. This model was found to not effectively describe the data from my experiments. Therefore, this model was adapted to fit the experimental data found here, incorporating a novel dependence on impact angle based on the experimental data.

In the final chapter of this thesis, I will describe how this new critical viscosity model

was employed to predict the distribution of volcanic ash deposits, varying in chemical compositions, along the NGV.

Chapter 7

Predicting Ash Deposition on the NGVs.

7.1 Introduction

As described in Chapter 3, volcanic ash deposition on the Nozzle Guide Vanes (NGVs) causes significant problems for jet engine operability when an aircraft encounters airborne volcanic ash during flight. When molten ash particles deposit on the NGVs, the ash deposits can cause the throat gap (the minimum flow area in the passage between two neighbouring NGVs) to narrow [7, 17]. As described before, even if the ash deposits form upstream of the throat, the throat gap can narrow due to complex fluid dynamics effects, such as a thickening boundary layer or a local separation bubble [110, 111].

When the throat gap narrows, the airflow through the engine is restricted, increasing the likelihood of an engine surge. Therefore, it is important to understand how much volcanic ash is likely to stick to the NGVs in an engine-volcanic ash encounter, and where the ash deposits are most likely to build up on the NGV surfaces. It is also important to understand how the nature of the distributions of the depositions along the surface varies for different volcanic ash compositions, and how the total amount of ash that sticks to the NGV varies with different ash compositions.

I conducted computational fluid dynamics (CFD) simulations for volcanic ash particles impacting on the NGVs as described in Chapter 3. Using the results from these simulations, I calculated the impact velocity, impact angle, and impact temperature of the various impacting particles. Additionally, I determined the location of particle impacts on the NGV and demonstrated how the impact properties associated with the impacting particles varied along

the NGV surface.

I performed experiments using glass particles dropped into a flame and made to impact on angled metal targets, described in Chapter 6. Observations were made as to whether the molten glass particles stuck to the surface or not. The results from these experiments were used to construct a critical viscosity model for molten particle sticking/bouncing, which was based on the model reported in Kleinhans et al [70]. This model defines a critical viscosity as a function of the particle's kinetic energy and impact angle. If the particle viscosity is less than the critical viscosity then the particle will stick to the surface, otherwise the particle will bounce. The form of the critical viscosity as defined by my new model (and first presented in Chapter 6) is given in Eqn [7.1]:

$$\mu_{\text{crit}}(\theta, E_{\text{p,Kin}}) = 10^{-(7.91+5.1 \cos(\theta))} \times E_{\text{p,Kin}}^{-1.78}. \quad (7.1)$$

Here μ_{crit} is the critical viscosity, θ the impact angle, and $E_{\text{p,Kin}}$ the particle kinetic energy.

In this final chapter of the thesis, I integrate the findings from Chapter 3 with the model presented in Chapter 6 to investigate the behaviour of four different volcanic ash compositions (Basalt, Andesite, Dacite, and Rhyolite) upon impacting the NGV surface. I calculate, for each composition, the proportion of impacting mass that adheres to the vane and analyse how this mass is distributed along the NGV surface. The results of this analysis demonstrate qualitative agreement with evidence from aircraft jet engines exposed to volcanic ash.

7.2 Method

7.2.1 Computational Fluid Dynamics simulations.

As described in detail in Chapter 3 Computational Fluid Dynamics (CFD) simulations were performed, using the software Ansys Fluent, for an air-flow through an NGV array. After a converged solution had been found for the airflow, particles were injected into the simulation domain at randomly selected points along the inlet. The diameters of the particles were drawn from a uniform distribution between 0 – 25 μm , and were each given a density, within the CFD software, of 2000 kg m^{-3} . All particles were assumed to be perfect spheres. The particles' trajectories through the NGV array were then tracked using the Lagrangian discrete phase within Ansys Fluent.

The impact velocity, impact position on the NGV, impact angle and particle diameter of any particle that impacted the NGV was extracted using code written in Python. The Ansys Fluent CFD software computes particle temperatures with an in-built inert particle heating model [78] so that the temperatures of the particles on impact with the NGV surfaces could be extracted.

As described in Chapter 3, five separate simulations were performed for different inlet temperature fields. In the first simulation a uniform inlet temperature of 1728 K was used. In subsequent simulations, after consultation with Rolls-Royce, the inlet temperature field was instead modelled as a sinusoidal function with a mid-point temperature of 1700 K, amplitudes of 100 K and 300 K respectively, and a wavelength equal to twice the distance between the stagnation points of two neighbouring NGVs.

The location of the peak sinusoidal temperatures, known as ‘hot-spots’, with respect to the position of the NGVs can vary between engine designs. Two hot-spot locations were considered here.

In the first case considered, called Case A in Chapter 3, the hot-spots are aligned with the stagnation point on alternate NGVs. In the second case, called Case B in Chapter 3, the hot-spots are aligned with the centre of the flow passage between alternate pairs of NGVs. For both Case A and Case B two simulations were done, 4 in total, with an amplitude in the temperature field of 150 K and 100 K respectively. In Fig [7.1] can be seen simulations of Case A and Case B for a temperature amplitude of 150 K.

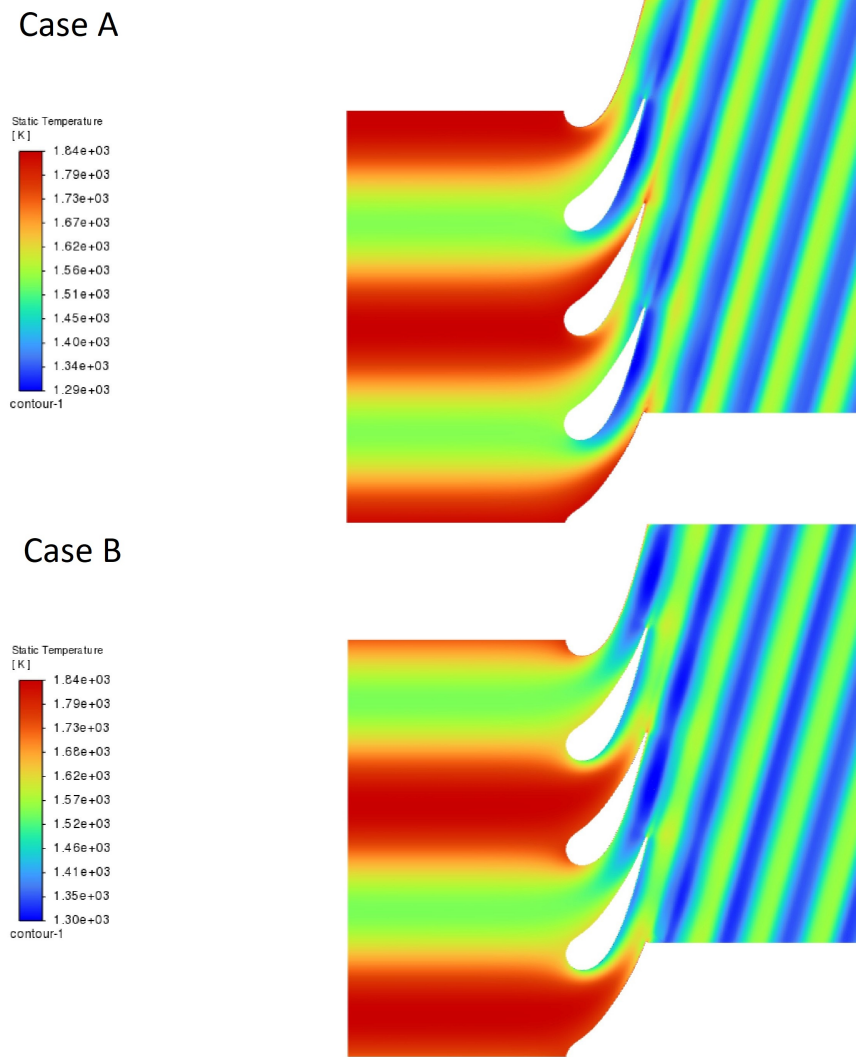


Figure 7.1: Temperature fields for the inlet temperature fields for Case A and Case B with an amplitude of 150 K, reproduced from Chapter 3.

It can be seen in Fig [7.1] that for both inlet temperature fields, Case A and Case B, neighbouring NGVs are exposed to different local temperatures. For each simulation particle temperatures were taken for particle impacts on both the ‘hot’ and ‘cold’ NGVs.

A more detailed description of these Computational Fluid Dynamics simulations can be found in Chapter 3.

7.2.2 Calculation of particle viscosities and critical particle viscosities.

The viscosity model of [14] was used to calculate the viscosities of the droplets on impact. This model takes the elemental composition of the volcanic ash and its temperature as arguments to return a viscosity. A similar density model of [55] was also used to calculate

the particle densities. The input temperatures used were those particle impact temperatures extracted from the various CFD simulations as described in section 7.2.1.

Four different rock types were considered, Basalt, Rhyolite, Dacite, and Andesite, and the corresponding chemical compositions were taken from [16]. The impact temperatures of the particles were determined for the ‘hot’ and ‘cold’ NGVs within the 4 different sinusoidal temperature fields. These temperatures were used in conjunction with the different chemical composition data to calculate impact viscosities and densities. This means that for each composition, eight combinations of particle viscosities and densities were calculated.

It can be seen in Eqn [7.1] that a particle’s critical viscosity is dependent on both its kinetic energy and the angle with which it impacts the surface. Therefore in evaluating a given impacting particle’s critical viscosity, $\mu_{p,crit}$, it is necessary to know both its impact angle and its kinetic energy. The impact angles of the particles were extracted from the CFD simulations as described previously in Chapter 3. The kinetic energy for any given impacting particle was calculated as:

$$E_{p,Kin} = \frac{\pi}{12} \rho D^3 v^2, \quad (7.2)$$

where D is the particle diameter, ρ is the particle density, and v is the particle impact velocity. Using the extracted impact angles and the calculated particle kinetic energies, the critical viscosities were calculated for the impacting particles for the 5 different CFD simulations and 4 compositions.

7.2.3 Calculating the proportion of ash that sticks or bounces.

For each of the particles that impacts the NGVs in the simulations for the different inlet temperature fields, and for each of the 4 different ash compositions, the particle viscosity, μ_p was compared with its calculated critical viscosity, $\mu_{p,crit}$. If for an individual particle $\mu_p < \mu_{p,crit}$ then the particle was recorded as sticking to the NGV surface and assigned a stick/bounce value of $\alpha_{SB} = 1$. If, however, $\mu_p > \mu_{p,crit}$ then the particle was recorded as bouncing off the NGV surface and assigned a stick/bounce value of $\alpha_{SB} = 0$.

To demonstrate how the ash particles that stuck to the vane distributed themselves along the NGV surface, Gaussian kernels were used (as described in Chapter 3) to create estimated probability densities (EPDs) that were displayed graphically. The variables that were used

in these EDPs were the particle's mass normalised by the total mass that impacted the vane, and the particle distance along the NGV. As before, a dimensionless distance was used. This distance was established relative to the y-coordinates of both the trailing edge and the stagnation point. The highest point on the trailing edge is designated as a distance of 1, with the stagnation point serving as the 'origin'. Subsequently any impacts on the suction surface are denoted by a 'negative' distance from the stagnation point.

Each particle data point in the EDP was weighted by the associated value of the Particle Size Distribution for volcanic ash found in the combustor [19], detailed in Chapter 3. This accounts for the size distribution of particles that enter the turbine. Every particle data point was also weighted with the stick/ bounce value, α_{SB} , previously identified. That meant that any particle that bounced would be neglected in the EDP, with only the particles that stuck being considered. This allowed the EDPs to show how the particles that stuck to the NGV distributed themselves along the vane surface.

In separate EDPs, the particle data points were also weighted by the normalised particle mass. This allowed the EDPs to show how the bulk of the mass that stuck to the NGV distributed itself along the vane surface.

One result of interest was the difference in the proportion of mass that stuck to the vane, between the different ash compositions for a given NGV in a given inlet temperature field. The percentage of the mass that impacted the vane that stuck, M_{stuck} was calculated as:

$$M_{stuck} = \frac{\sum_{i=1}^{N_T} m_i \times PSD(D_i) \times \alpha_{SB,i}}{\sum_{i=1}^{N_T} m_i \times PSD(D_i)} \times 100. \quad (7.3)$$

Here m_i , is the individual particle mass, D_i , the particle diameter, N_T the total number of particles that impact the vane, and $PSD()$ is the particle size distribution function, and:

$$\alpha_{SB,i} = \begin{cases} 0, & \text{If particle bounced.} \\ 1, & \text{If particle stuck.} \end{cases} \quad (7.4)$$

7.3 Results.

7.3.1 Overall levels of sticking.

In section 7.2.3 it is described how the percentage of mass that stuck to the vane out of the total mass that impacts the vane is calculated, via Eqn [7.3]. Using this equation, the per-

centage of mass that stuck to the NGVs associated with Case A hot, Case A cold, Case B hot and Case B cold was calculated, for the four different volcanic ash compositions considered here, namely: Basalt, Andesite, Dacite, and Rhyolite. The results from these calculations are shown in Fig [7.2] and Fig [7.3], corresponding to the different sinusoidal temperature amplitudes of 150 K and 100 K respectively.

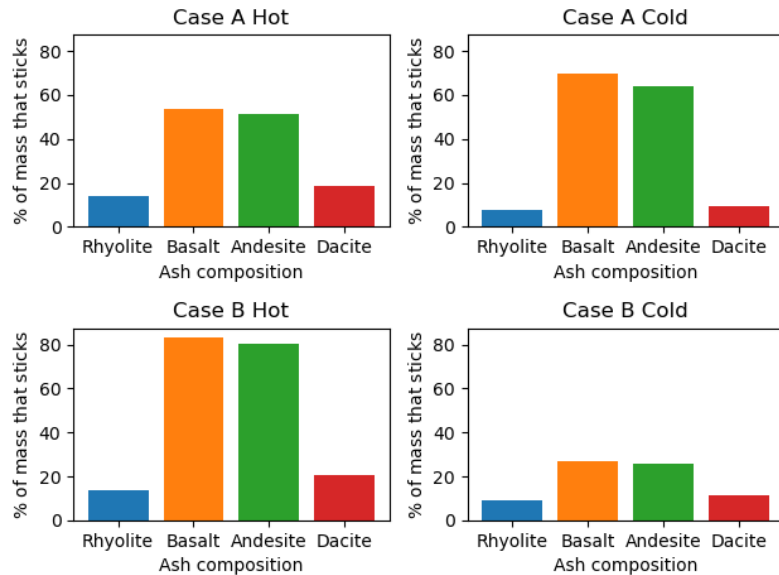


Figure 7.2: Histograms showing the percentage of mass that sticks to the NGV on impact, for Case A and Case B ‘hot’ and ‘cold’ NGVs. This figure corresponds to a sinusoidal temperature amplitude of 150 K.

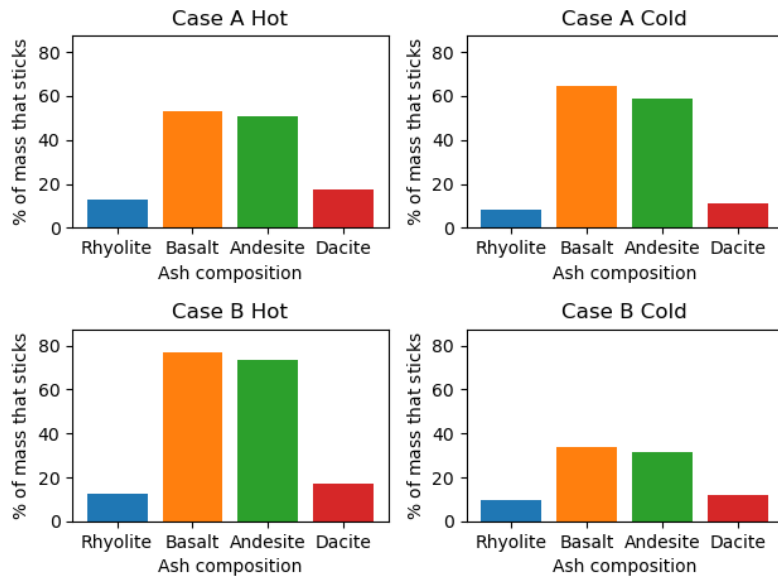


Figure 7.3: Histograms showing the percentage of mass that sticks to the NGV on impact, for Case A and Case B ‘hot’ and ‘cold’ NGVs. This figure corresponds to a sinusoidal temperature amplitude of 100 K.

It can be seen in Fig [7.2] and Fig [7.3] whatever the inlet temperature field, or NGV the highest proportion of ash mass that sticks to the NGV is Basalt, followed by Andesite, Dacite and then finally Rhyolite. This is not surprising, as Basalt is the least viscous ash of all the types considered here, and Rhyolite the most viscous. It can be seen for both temperature amplitudes, that for all compositions Case B hot has the highest proportion of the mass sticking to the NGV surface, and Case B cold has the least.

There is not any change in this behaviour between the different temperature amplitudes, with only a slight change in the percentage values of the mass that sticks.

In this next section I present the results of the Gaussian kernel EDPs weighted for the particle size distribution (PSD) and the sticking/bouncing outcome. These EDPs show the most probable location for particle sticking along the NGV.

I also present the EDPs where the particle mass was included as a weight, these show the most probable location for the deposition of the bulk of the mass impacting the vane. This section is broken up into the results for the 4 different volcanic ash compositions considered in this work: Basalt, Andesite, Dacite and Rhyolite.

7.3.2 Basalt

In Fig [7.4] and Fig [7.5] can be seen the results of the Gaussian kernel EDPs weighted for the particle size distribution (PSD) and the sticking/bouncing outcome, for a Basaltic ash composition, corresponding to the different inlet sinusoidal temperature fields, with amplitudes of 150 K and 100 K respectively.

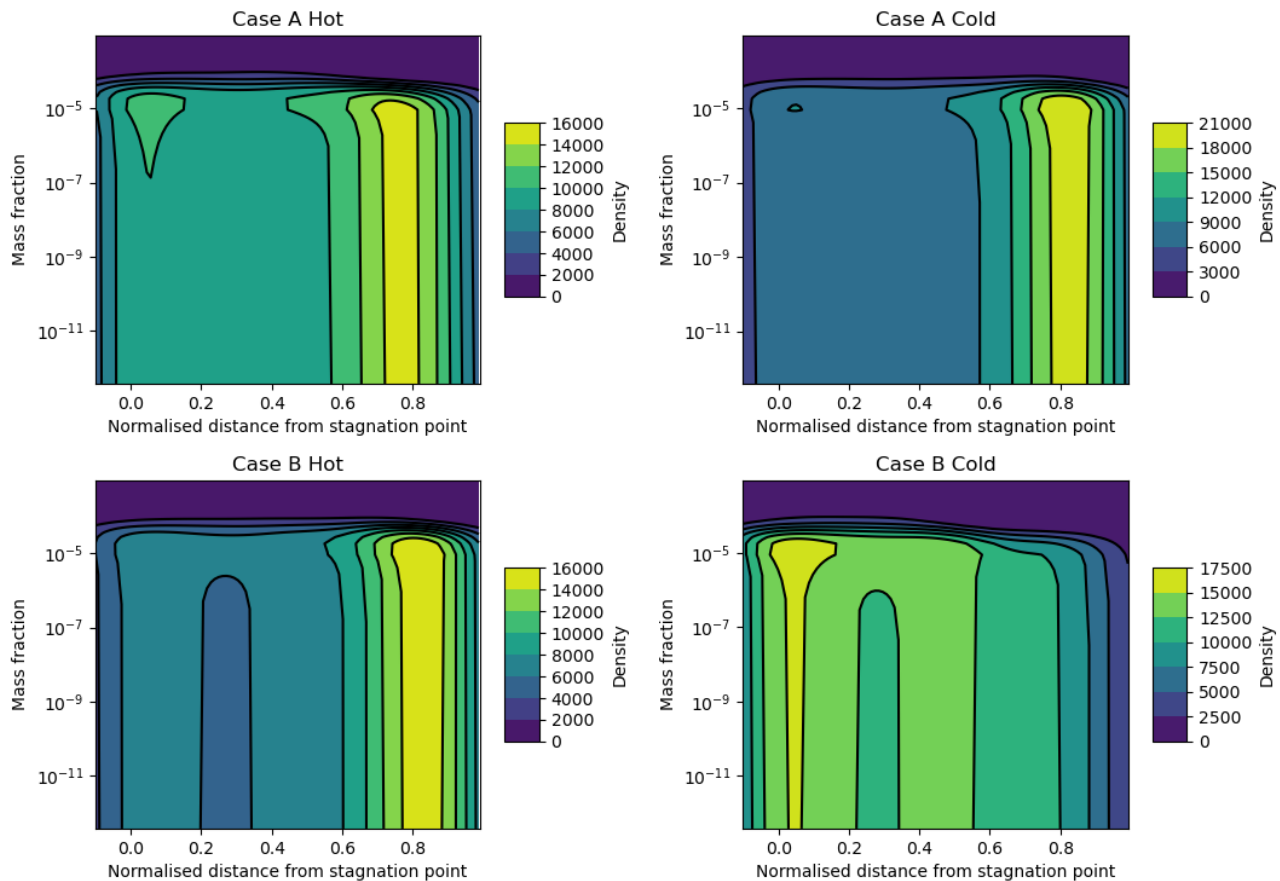


Figure 7.4: Gaussian kernel density plots of the normalised mass of particles against the dimensionless NGV distance, but with each data point weighted for the associated PSD value, and the stick/bounce result. This corresponds to a temperature amplitude of 150 K.

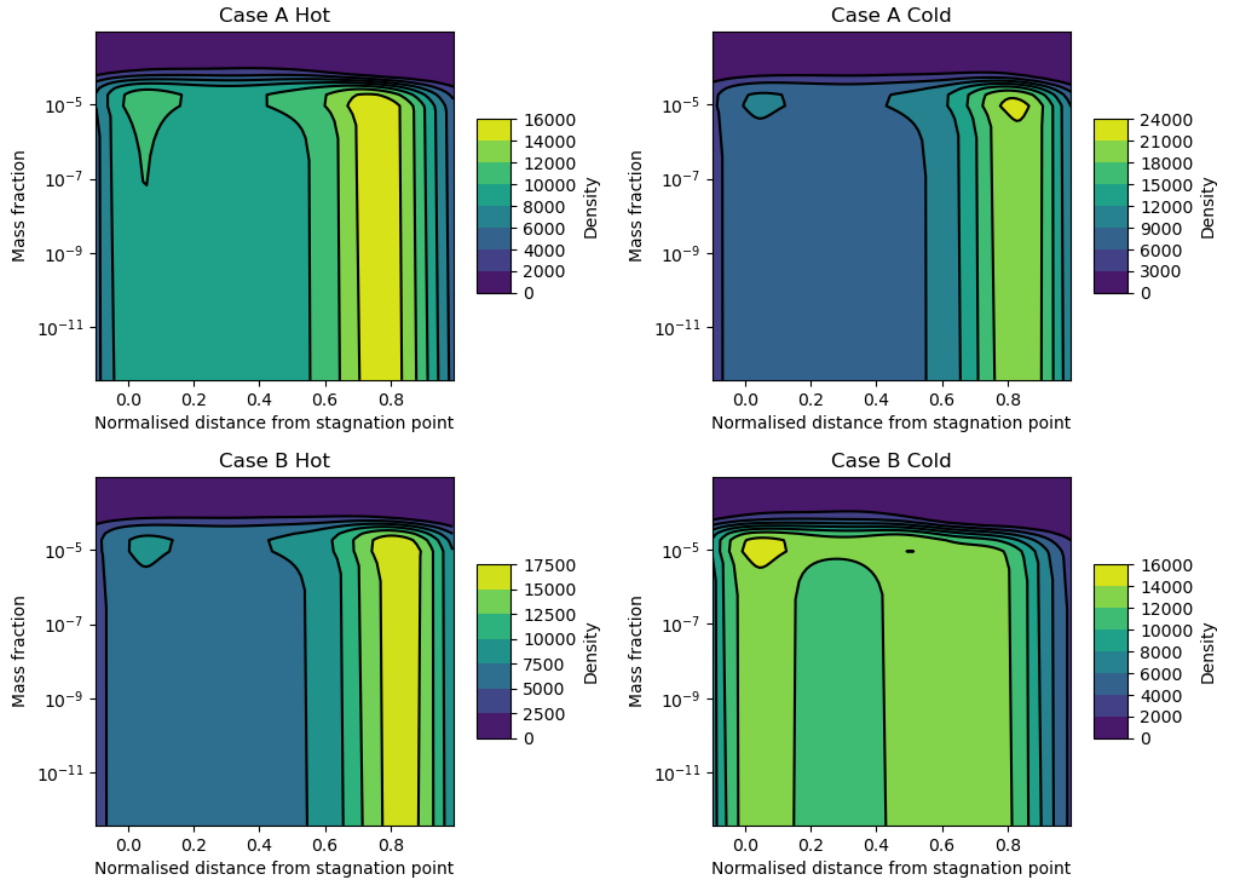


Figure 7.5: Gaussian kernel density plots of the normalised mass of particles against the dimensionless NGV distance, but with each data point weighted for the associated PSD value, and the stick/bounce result. This corresponds to a temperature amplitude of 100 K.

It can be seen in Fig [7.4] that for all the particles on the NGVs associated with Case A hot and cold, and Case B hot, the largest proportion of the particle sticking occurs on the trailing edge of the NGV, with both the massive and less massive particles sticking on the trailing edge. However for Case B cold, the highest proportion of the sticking occurs on the leading edge of the NGV towards the stagnation point. This disparity is not surprising. If one looks at Fig [7.1] it can be seen that in the case of the cold NGV in temperature field Case B, the gases at the trailing edge are cooler, and the particles impacting the trailing edge have not travelled through hotter gases compared to both NGVs in Case A and the ‘hot’ NGV in Case B.

For the lower temperature amplitude of 100 K, as can be seen in Fig [7.5], there was very similar distributive behaviour of sticking along the NGV surface compared to the results for

the higher temperature amplitude of 150 K.

In Fig [7.6] and Fig [7.7] can be seen the results of the Gaussian kernel EDPs weighted for the particle size distribution (PSD), the sticking/bouncing outcome, and the individual particle mass for a Basaltic ash composition, corresponding to the different inlet sinusoidal temperature fields, with amplitudes of 150 K and 100 K respectively.

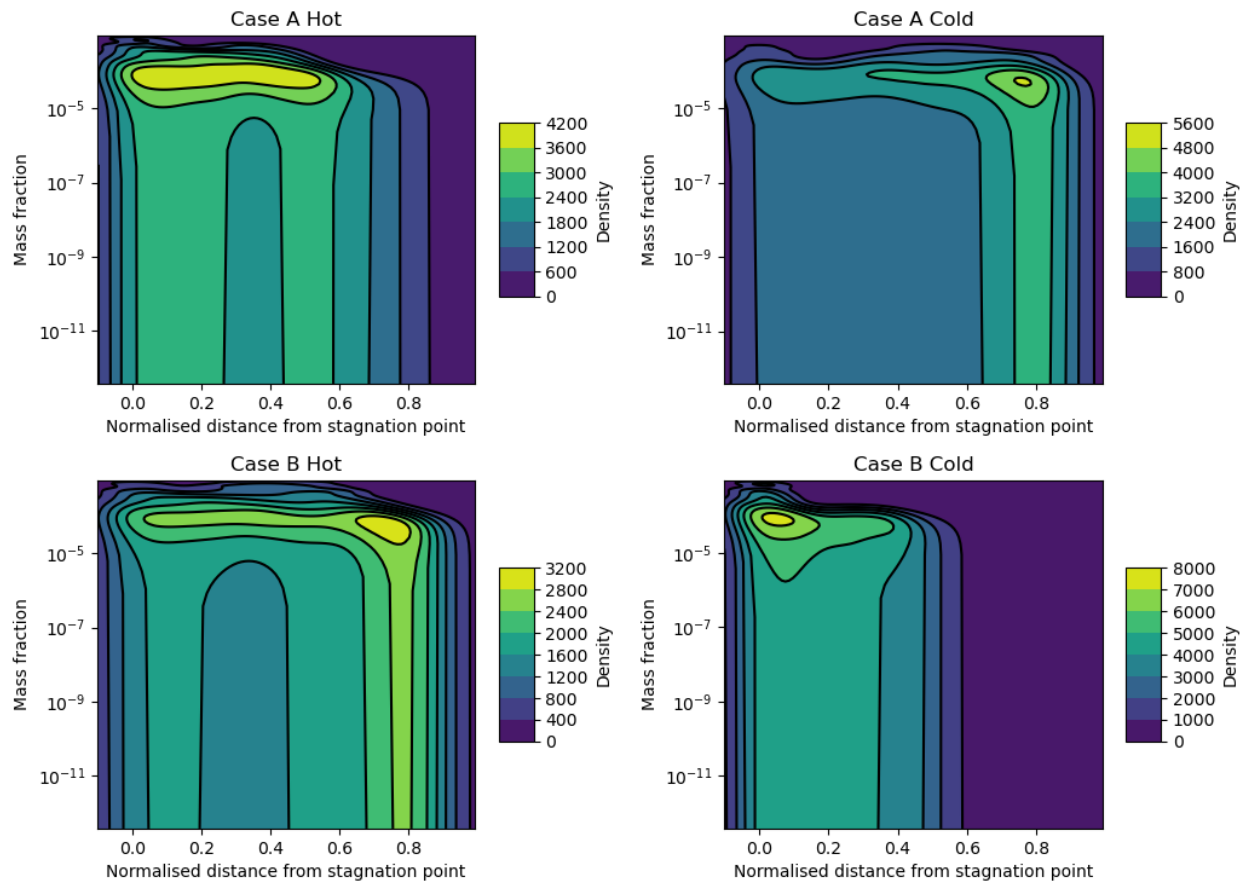


Figure 7.6: Gaussian kernel density plots of the normalised mass of particles against the dimensionless NGV distance, but with each data point weighted for the associated PSD value, the stick/bounce result and the normalised mass of the particle. This corresponds to a temperature amplitude of 150 K.

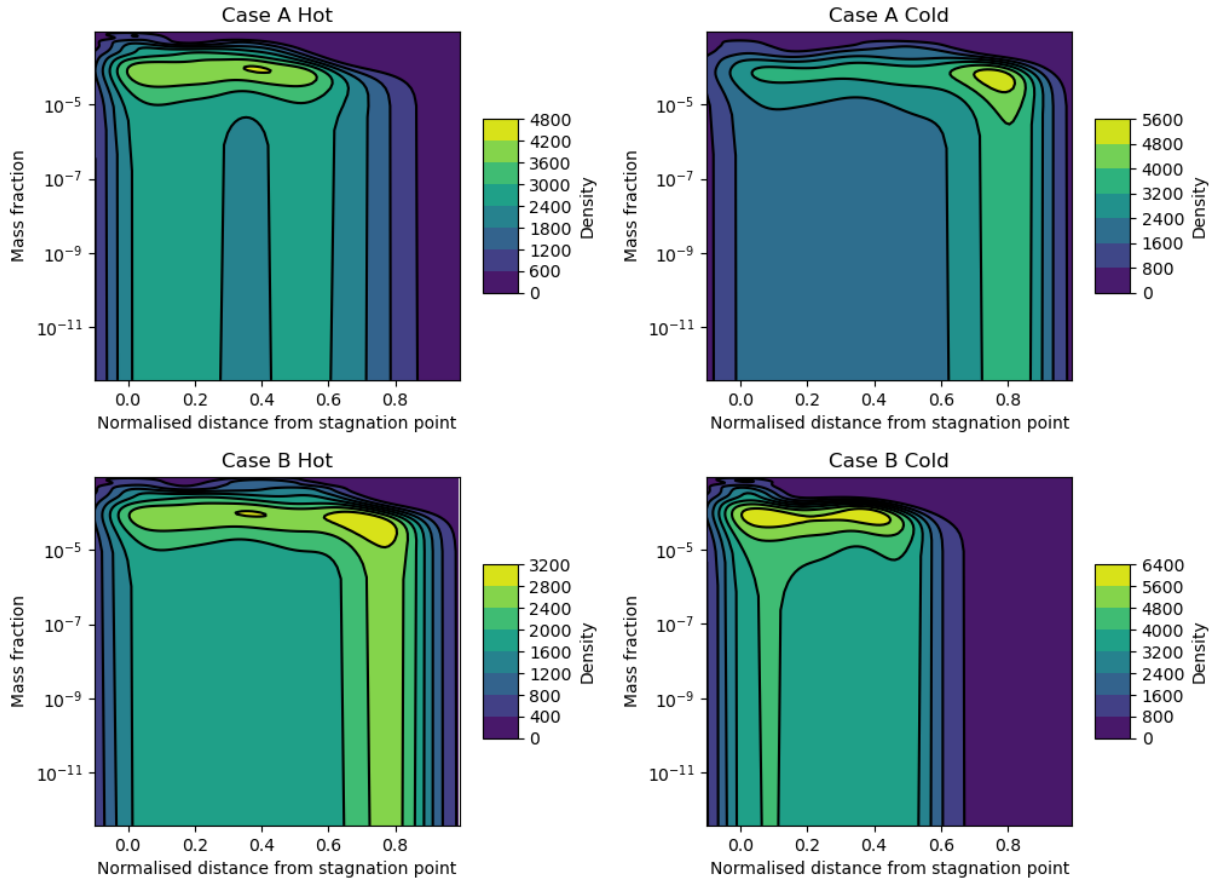


Figure 7.7: Gaussian kernel density plots of the normalised mass of particles against the dimensionless NGV distance, but with each data point weighted for the associated PSD value, the stick/bounce result and the normalised mass of the particle. This corresponds to a temperature amplitude of 100 K.

It can be seen in Fig [7.6] that in Case A hot, the bulk of the mass is distributed from the stagnation point up to just over half-way along the NGV. It can be seen that not much mass is deposited on the trailing edge, where most of the sticking was shown to occur in Fig [7.4]. For Case A cold, and Case B hot, the mass deposit is most dense at the trailing edge of the NGV, but there is still a wide distribution of mass down along the vane to the stagnation point. For Case B cold, it can be seen that the mass deposit is most dense at around the stagnation point, with a wide distribution of mass up to just over half-way along the vane. The results in Fig [7.7] corresponding to a temperature amplitude of 100 K, show a similar distributive behaviour as the results in Fig [7.6]. However it should be noted that in Fig [7.7], there is a wider distribution of mass along the vane for Case B cold than in Fig [7.6].

7.3.3 Andesite

In Fig [7.8] and Fig [7.9] can be seen the results of the Gaussian kernel EDPs weighted for the particle size distribution (PSD) and the sticking/bouncing outcome, for an Andesitic ash composition, corresponding to the different inlet sinusoidal temperature fields, with amplitudes of 150 K and 100 K respectively.

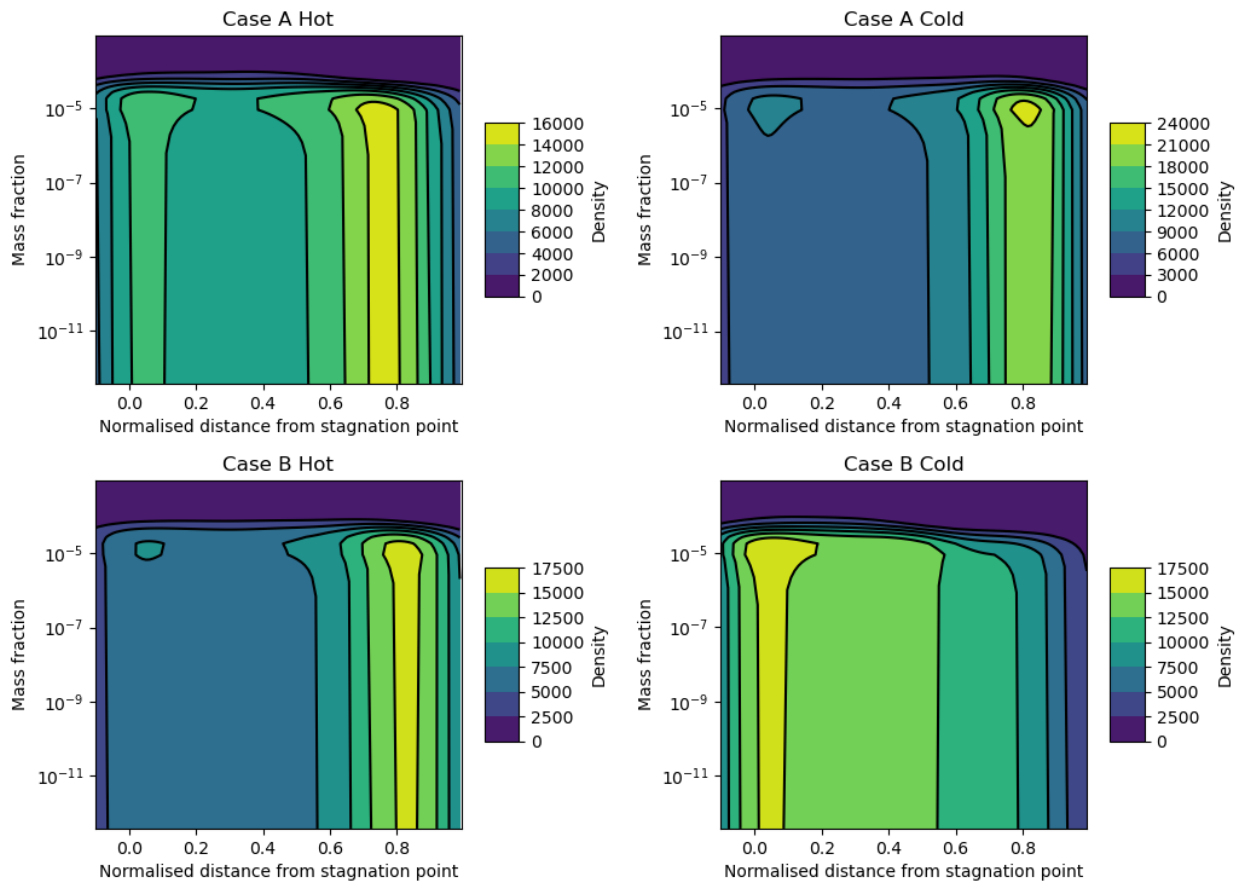


Figure 7.8: Gaussian kernel density plots of the normalised mass of particles against the dimensionless NGV distance, but with each data point weighted for the associated PSD value, and the stick/bounce result. This corresponds to a temperature amplitude of 150 K.

It can be seen in these results for Andesite ash, the results follow a similar pattern for the Basaltic results, with a wide distribution of sticking along the NGV surface which is most dense at the trailing edge. Again the only exception to this appears to be for Case B cold, where the sticking is most dense at the stagnation point. Similar behaviour can be seen in Fig [7.9] for a lower temperature amplitude, though note again the lower amplitude causes a wider distribution on the NGV surface for Case B cold.

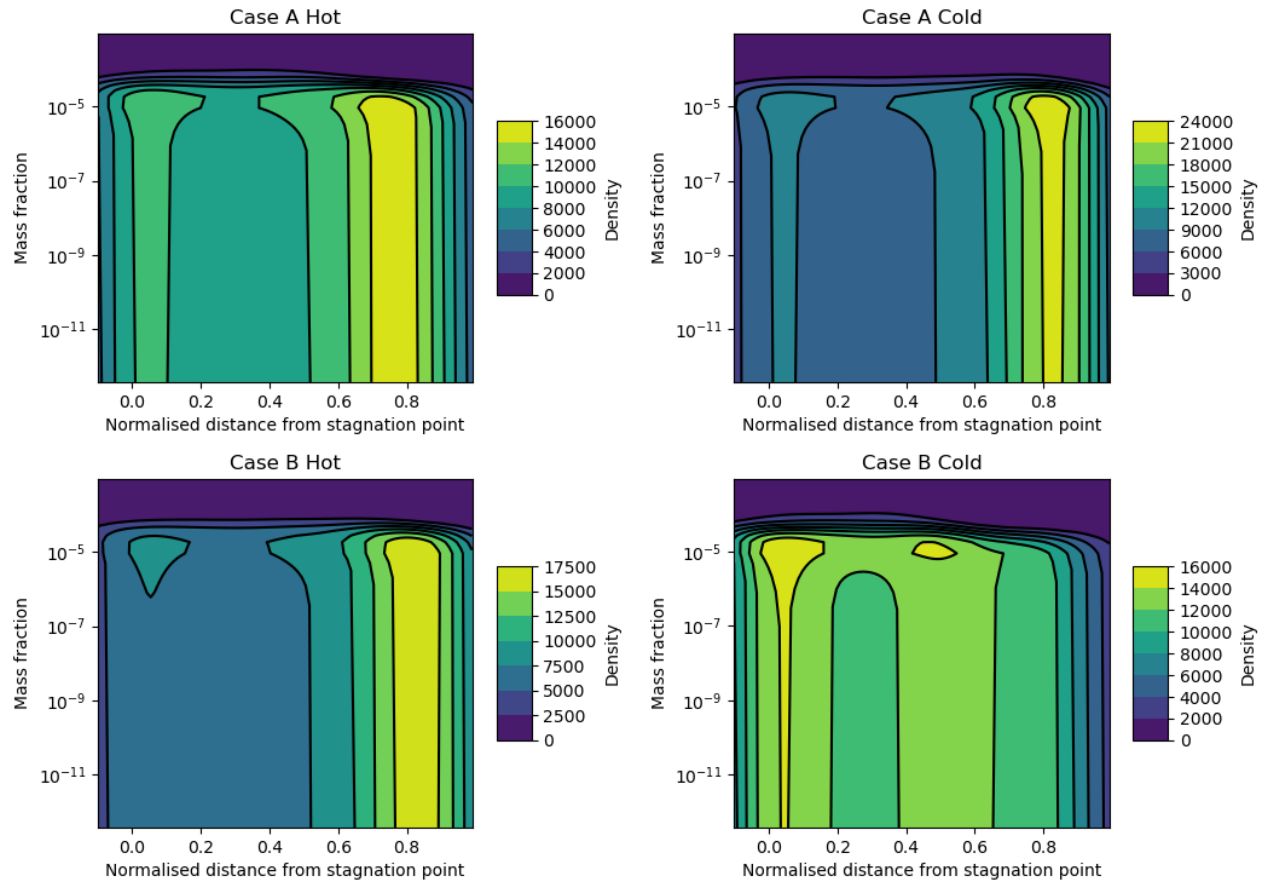


Figure 7.9: Gaussian kernel density plots of the normalised mass of particles against the dimensionless NGV distance, but with each data point weighted for the associated PSD value, and the stick/bounce result. This corresponds to a temperature amplitude of 100 K.

In Fig [7.10] and Fig [7.11] can be seen the results of the Gaussian kernel EDPs weighted for the particle size distribution (PSD), the sticking/bouncing outcome, and the individual particle mass for an Andesitic ash composition, corresponding to the different inlet sinusoidal temperature fields, with amplitudes of 150 K and 100 K respectively.

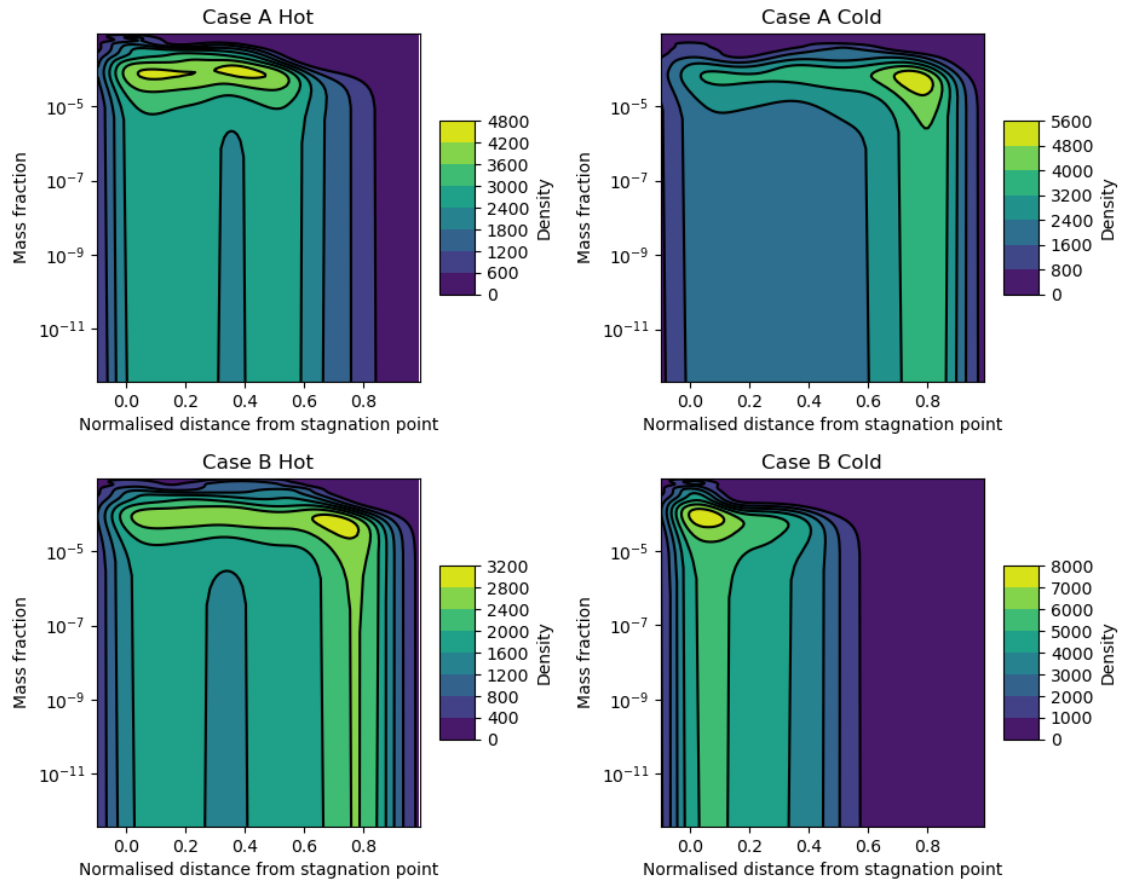


Figure 7.10: Gaussian kernel density plots of the normalised mass of particles against the dimensionless NGV distance, but with each data point weighted for the associated PSD value, the stick/bounce result and the normalised mass of the particle. This corresponds to a temperature amplitude of 150 K.

When looking at the results for the distribution of mass on the NGV in Fig [7.10] and Fig [7.11], a similar distributive behaviour to Basalt can be seen. In Fig [7.10] for Case A hot, there is a wide distribution of mass from the stagnation point towards the trailing edge. In Case A cold, and Case B hot, the mass deposition is most dense at the trailing edge, with a wide distribution towards the stagnation point. In Case B cold there is a wide distribution of mass along the NGV from the stagnation point, note the distribution is tighter compared to Case A hot and cold, and Case B hot.

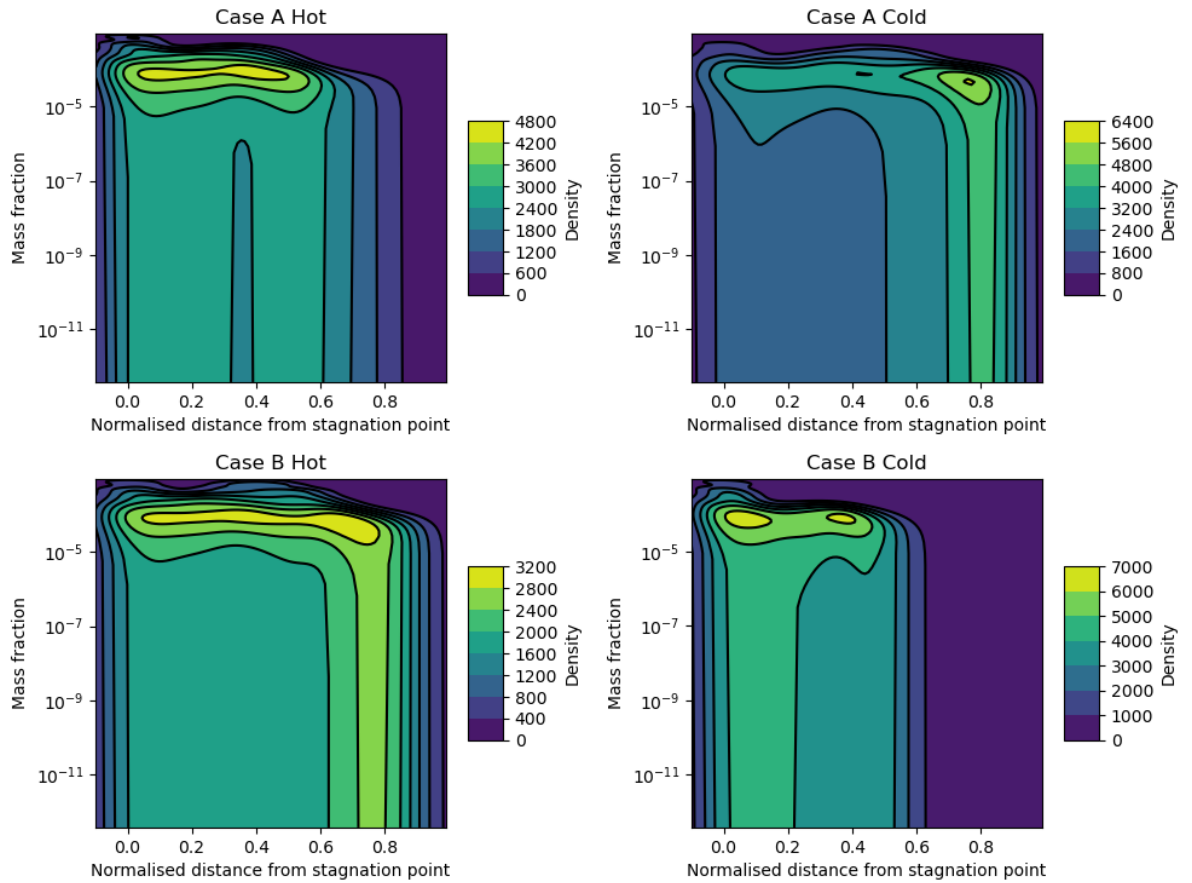


Figure 7.11: Gaussian kernel density plots of the normalised mass of particles against the dimensionless NGV distance, but with each data point weighted for the associated PSD value, the stick/bounce result and the normalised mass of the particle. This corresponds to a temperature amplitude of 100 K.

Looking at Fig [7.11] for the results corresponding to a lower temperature amplitude, again similar distributive behaviour can be seen.

7.3.4 Dacite

In Fig [7.12] and Fig [7.13] can be seen the results of the Gaussian kernel EDPs weighted for the particle size distribution (PSD) and the sticking/bouncing outcome, for a Dacitic ash composition, corresponding to the different inlet sinusoidal temperature fields, with amplitudes of 150 K and 100 K respectively.

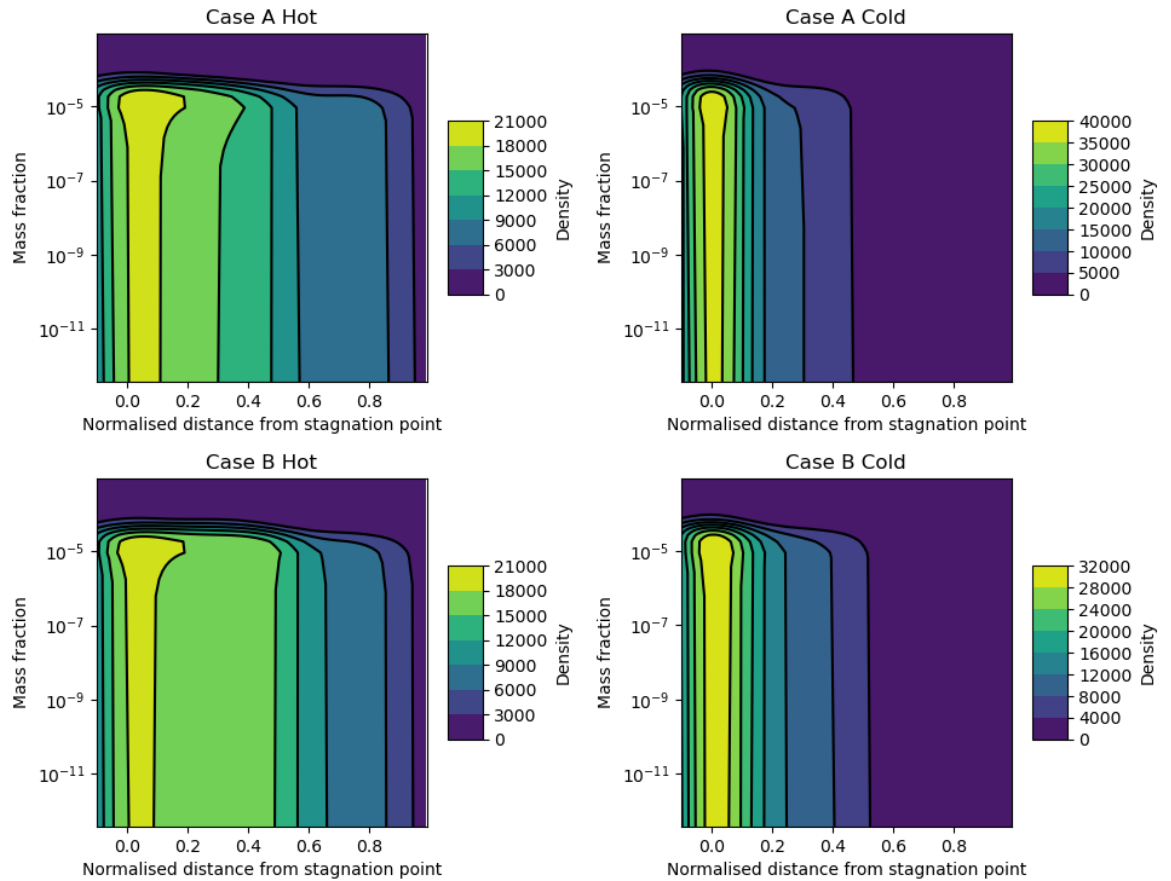


Figure 7.12: Gaussian kernel density plots of the normalised mass of particles against the dimensionless NGV distance, but with each data point weighted for the associated PSD value, and the stick/bounce result. This corresponds to a temperature amplitude of 150 K.

The results shown in Fig [7.12] and Fig [7.13] for a Dacitic ash are very different to those presented earlier for a Basaltic, and Andesitic ash. Looking at Fig [7.12] it can be seen that the sticking events are most densely distributed close to the stagnation point of the NGV, independent of the temperature field, or indeed the ‘hot’ or ‘cold’ NGV in either temperature field. It can be seen that there is a wide distribution of sticking along the NGV surface with not much difference observed between the ‘hot’ NGVs in Case A and Case B, nor between the ‘cold’ NGVs in Case A and Case B. The cold NGVs have a narrower distribution of sticking along the NGV surface, compared to the ‘hot’ NGVs.

Looking at Fig [7.13] corresponding to a lower temperature amplitude of 100 K, there is no real difference in the distributive behaviour compared to Fig [7.12] corresponding to a higher temperature amplitude.

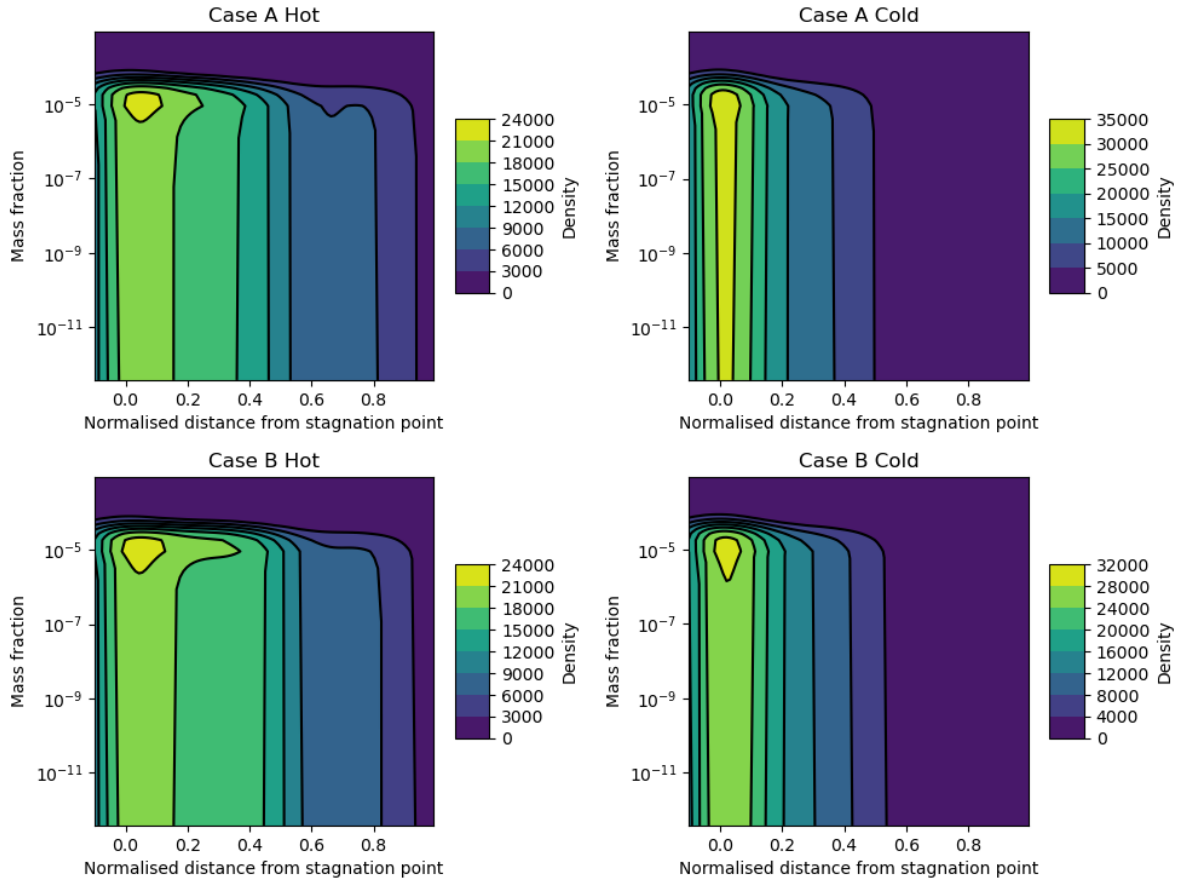


Figure 7.13: Gaussian kernel density plots of the normalised mass of particles against the dimensionless NGV distance, but with each data point weighted for the associated PSD value, and the stick/bounce result. This corresponds to a temperature amplitude of 100 K.

In Fig [7.14] and Fig [7.15] can be seen the results of the Gaussian kernel EDPs weighted for the particle size distribution (PSD), the sticking/bouncing outcome, and the individual particle mass for a Dacitic ash composition, corresponding to the different inlet sinusoidal temperature fields, with amplitudes of 150 K and 100 K respectively.

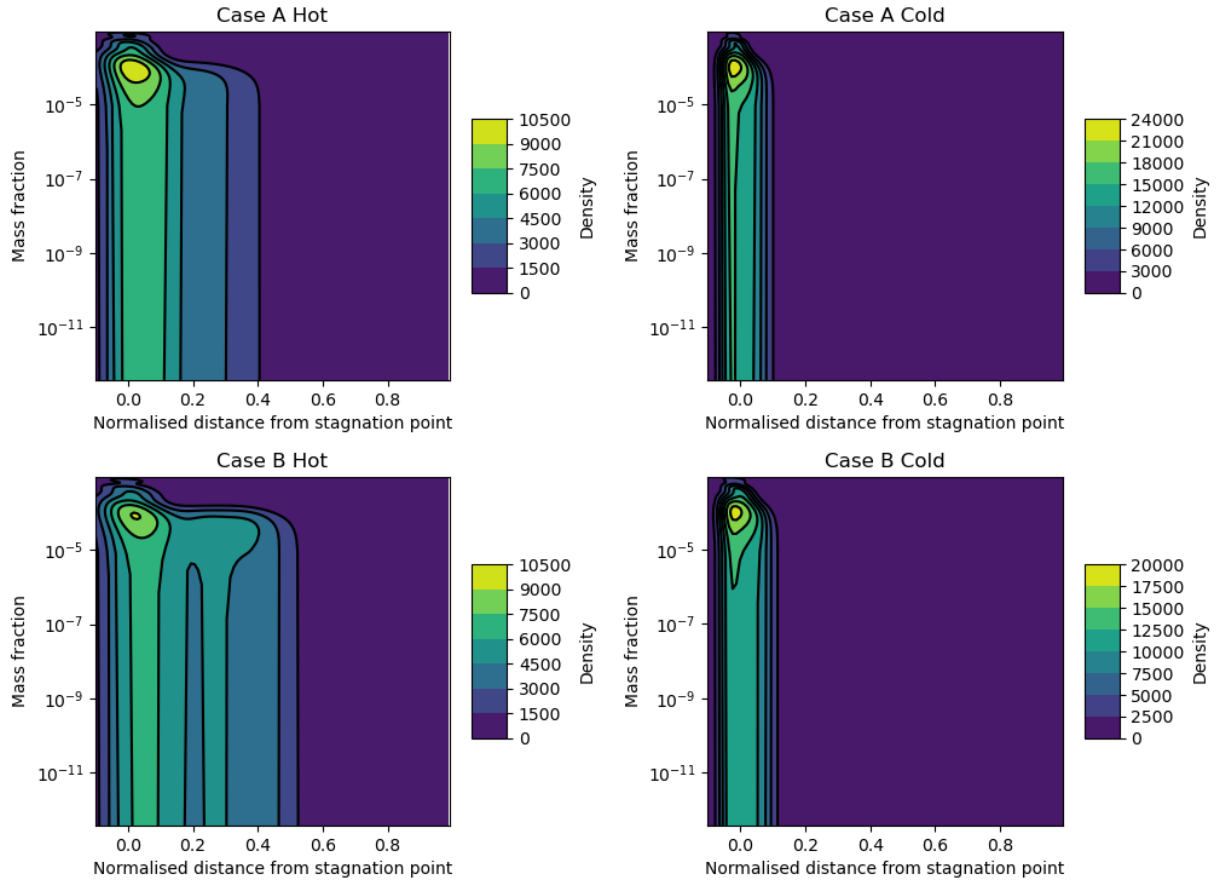


Figure 7.14: Gaussian kernel density plots of the normalised mass of particles against the dimensionless NGV distance, but with each data point weighted for the associated PSD value, the stick/bounce result and the normalised mass of the particle. This corresponds to a temperature amplitude of 150 K.

It can be seen comparing Fig [7.12] to Fig [7.14] that the distribution of the deposited mass is much tighter than the distribution of sticking events along the NGV surface. It can be seen that all of the mass that sticks to the vane is deposited on the lower half of the NGV and is concentrated close to the stagnation point. The distribution of the mass is tighter for the ‘cold’ NGVs. The widest distribution of mass corresponds to Case B hot, and the tightest distribution corresponds to Case A cold. Again there is no significant change in distributive behaviour with a change in temperature amplitude, as can be seen by comparing Fig [7.14] to Fig [7.15].

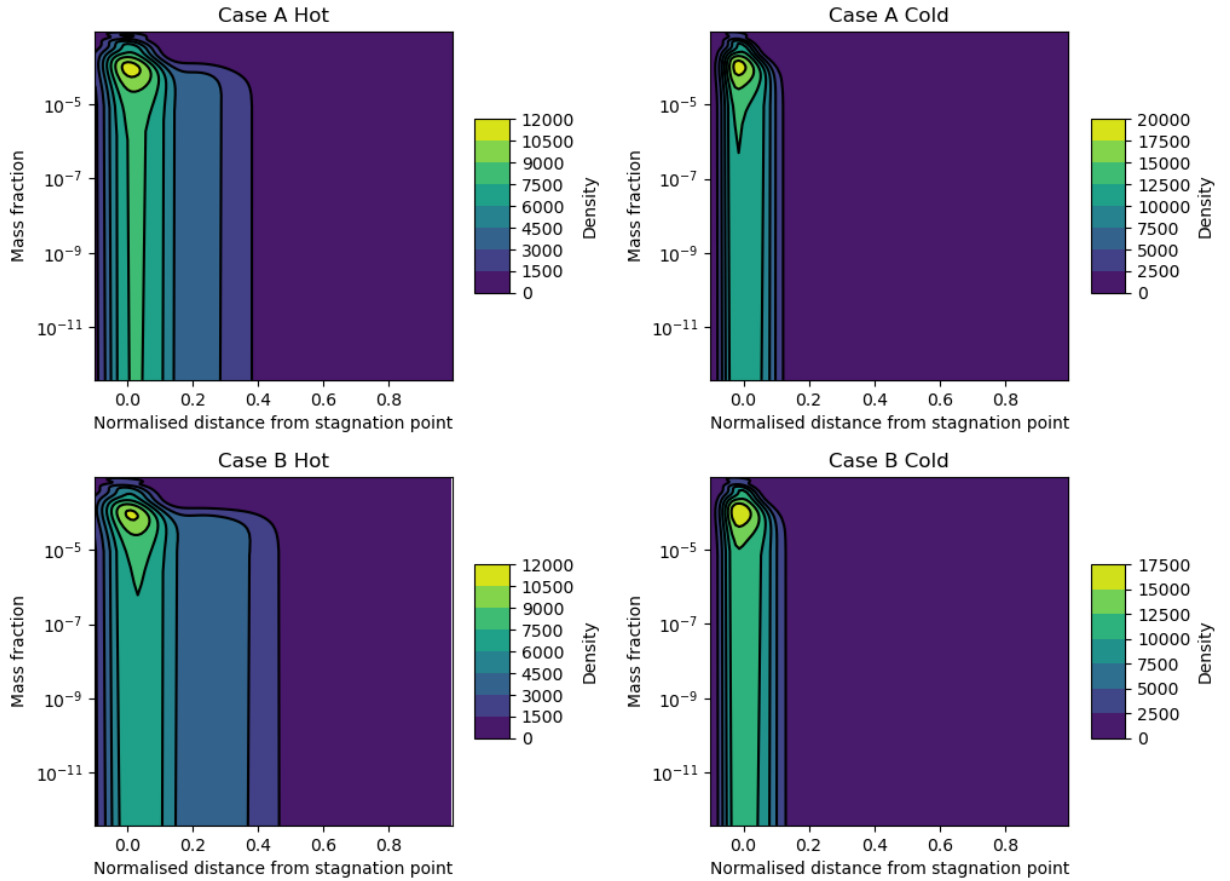


Figure 7.15: Gaussian kernel density plots of the normalised mass of particles against the dimensionless NGV distance, but with each data point weighted for the associated PSD value, the stick/bounce result and the normalised mass of the particle. This corresponds to a temperature amplitude of 100 K.

7.3.5 Rhyolite

In Fig [7.16] and Fig [7.17] can be seen the results of the Gaussian kernel EDPs weighted for the particle size distribution (PSD) and the sticking/bouncing outcome, for a Rhyolitic ash composition, corresponding to the different inlet sinusoidal temperature fields, with amplitudes of 150 K and 100 K respectively.

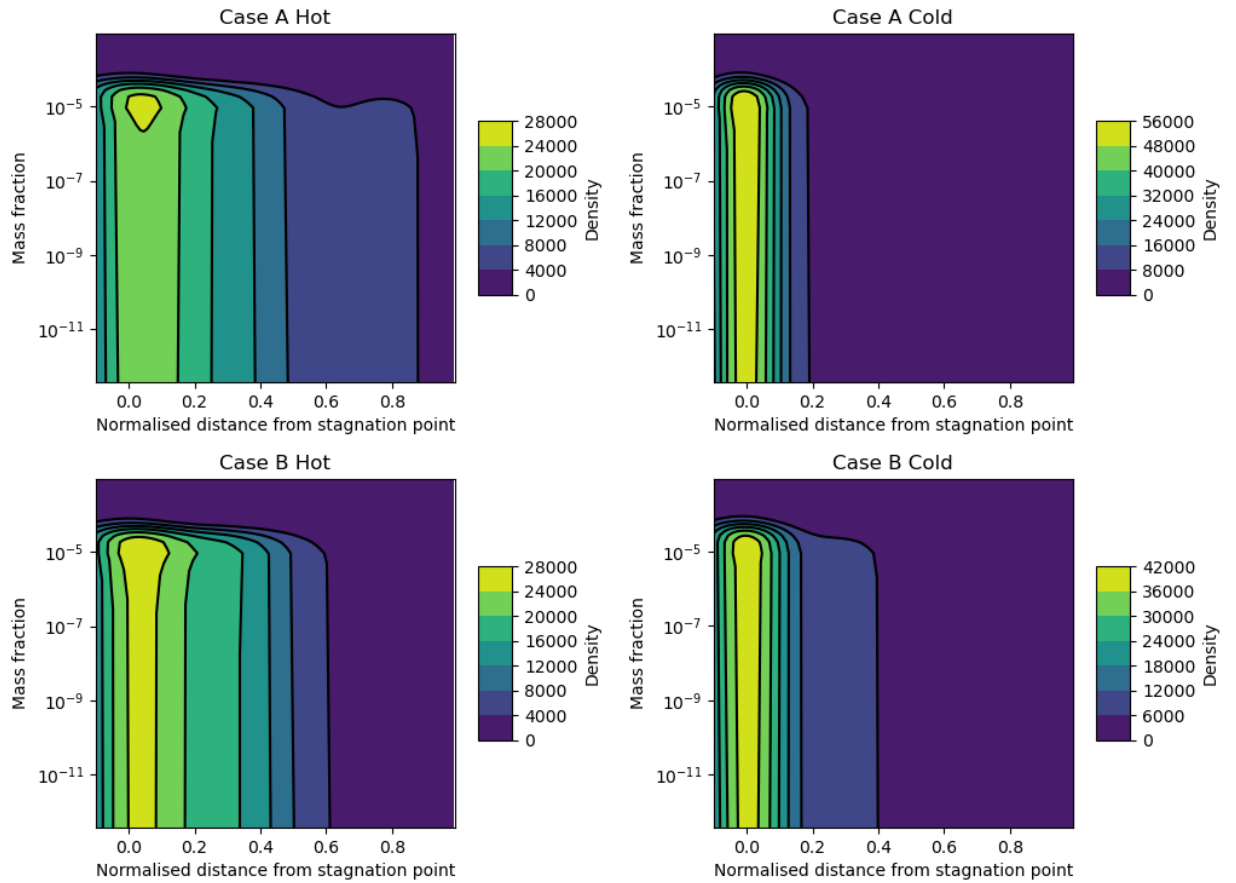


Figure 7.16: Gaussian kernel density plots of the normalised mass of particles against the dimensionless NGV distance, but with each data point weighted for the associated PSD value, and the stick/bounce result. This corresponds to a temperature amplitude of 150 K.

Comparing Fig [7.16] to Fig [7.12] it can be seen that the sticking of Rhyolitic ash to the NGV shows the same distributive behaviour as Dacitic ash, with sticking clustered towards the stagnation point of the NGV. However the distributions corresponding to the Rhyolite ash are tighter than those of the Dacite ash. Again as can be seen by comparing Fig [7.16] to Fig [7.17], there is no significant variation in distributive behaviour for the different temperature amplitudes.

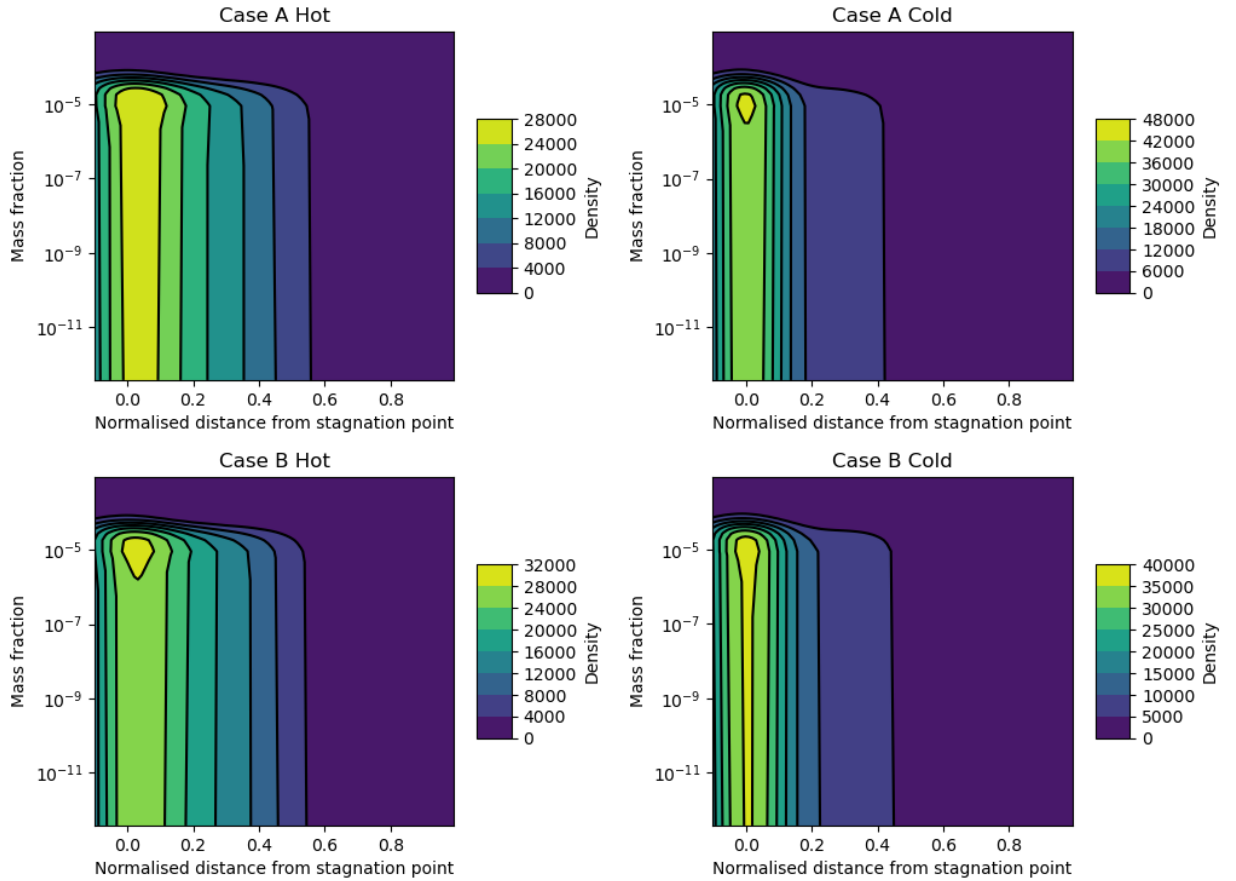


Figure 7.17: Gaussian kernel density plots of the normalised mass of particles against the dimensionless NGV distance, but with each data point weighted for the associated PSD value, and the stick/bounce result. This corresponds to a temperature amplitude of 100 K.

In Fig [7.18] and Fig [7.19] can be seen the results of the Gaussian kernel EDPs weighted for the particle size distribution (PSD), the sticking/bouncing outcome, and the individual particle mass for a Rhyolitic ash composition, corresponding to the different inlet sinusoidal temperature fields, with amplitudes of 150 K and 100 K respectively.

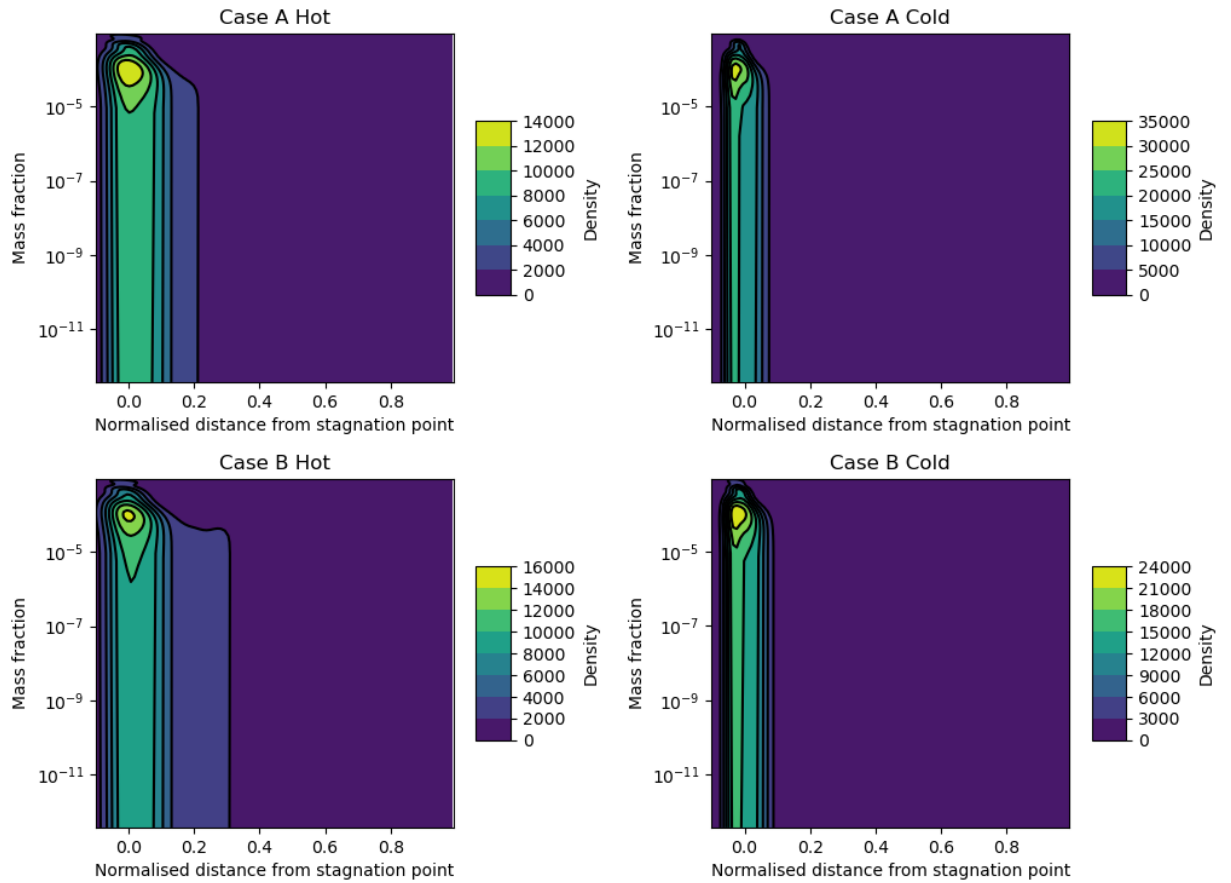


Figure 7.18: Gaussian kernel density plots of the normalised mass of particles against the dimensionless NGV distance, but with each data point weighted for the associated PSD value, the stick/bounce result and the normalised mass of the particle. This corresponds to a temperature amplitude of 150 K.

It can be seen in Fig [7.18] and Fig [7.19] for both temperature amplitudes that the distributions of the mass on the NGV are very tight and are concentrated around the stagnation point. The ‘cold’ NGVs have a slightly tighter distribution, with Case A cold having the tightest distribution, and Case B hot having the widest distribution for a temperature amplitude of 150 K.

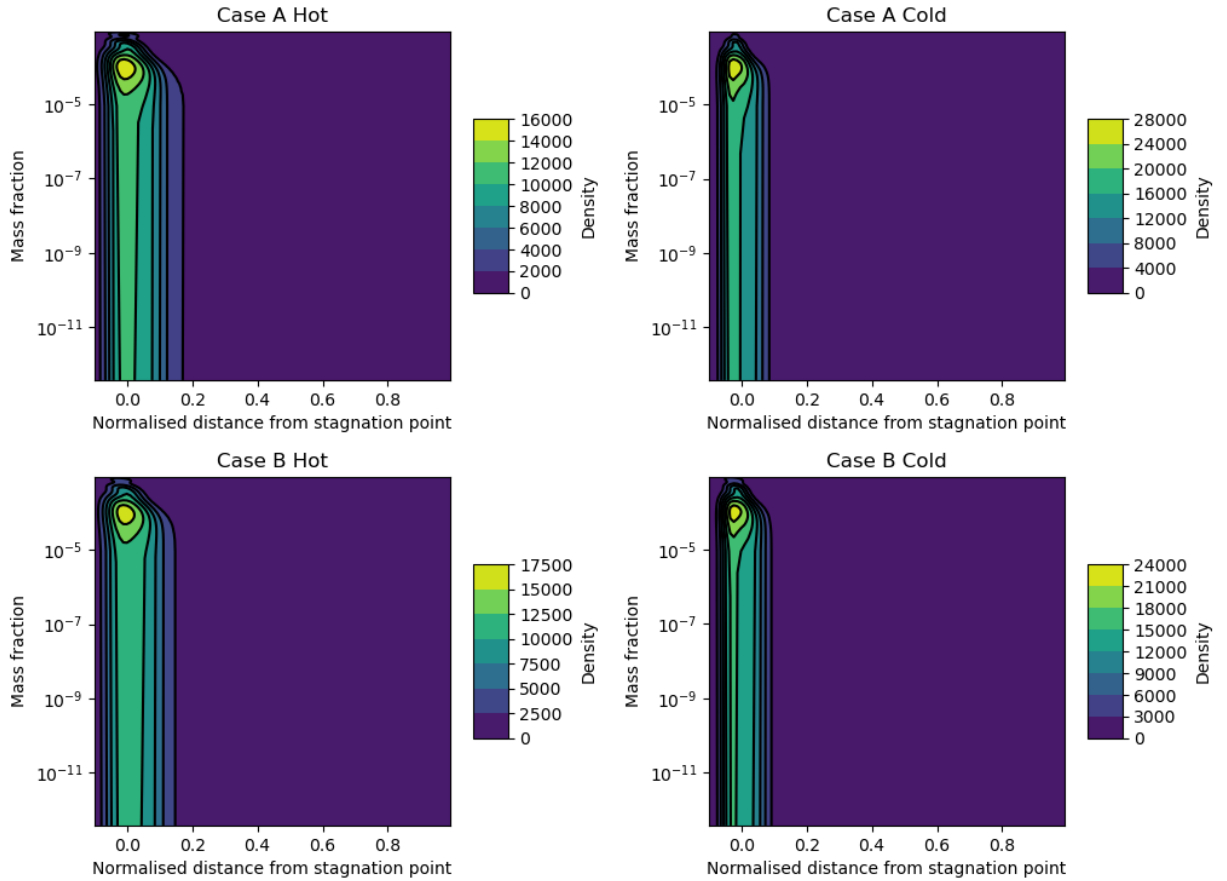


Figure 7.19: Gaussian kernel density plots of the normalised mass of particles against the dimensionless NGV distance, but with each data point weighted for the associated PSD value, the stick/bounce result and the normalised mass of the particle. This corresponds to a temperature amplitude of 100 K.

7.4 Discussion

The graphs shown in the previous section show that for the less viscous ash compositions, namely Basalt and Andesite, there was generally a wide deposition of mass across the majority of the vane surface, independent of the inlet temperature field or whether the NGV was ‘hot’ or ‘cold’. For the more viscous compositions, Dacite and Rhyolite, distributions of mass were tighter and concentrated towards the leading edge off the NGV.

The results presented in Fig [7.2] and Fig [7.3] also show that impacts of Rhyolitic ash are less likely to stick to the NGV than Basaltic ash, whatever the inlet temperature field or whether the NGV was ‘hot’ or ‘cold’. These results suggest that the chemical composition of the ash is the most important factor in determining whether or not an ash particle will stick

to the NGV surface.

These results are readily interpretable. Consider the expression for the critical viscosity $\mu_{p,crit}$, in Eqn [7.1]. The critical viscosity is inversely proportional to a particle's kinetic energy and impact angle. For a particle to adhere, its viscosity μ_p must be lower than the critical viscosity, i.e., $\mu_p < \mu_{p,crit}$. Therefore in the model proposed in Chapter 6 a particle is more likely to stick to the surface on impact, if it impacts with low kinetic energy, at a normal impact angle, and if the particle itself has a very low viscosity. In the results presented in Chapter 3, it is demonstrated that the impact velocity of the ash increases along the NGV surface from the stagnation point towards the trailing edge, with the impact angle also generally increasing relative to the surface normal. This implies that, for a given ash particle, adherence is more probable at the leading edge than at the trailing edge. This is because the kinetic energy of the particle and the impact angle increase towards the trailing edge, leading to a decrease in the critical viscosity. The particle impact conditions used to generate the results in sections 3.1-3.4 were consistent across all compositions and inlet temperature fields. Consequently, how the critical viscosity varies across the vane for the different compositions is identical. Fig [7.20] below illustrates how the average critical viscosity (for the impacting ash particles) varies with distance along the NGV.

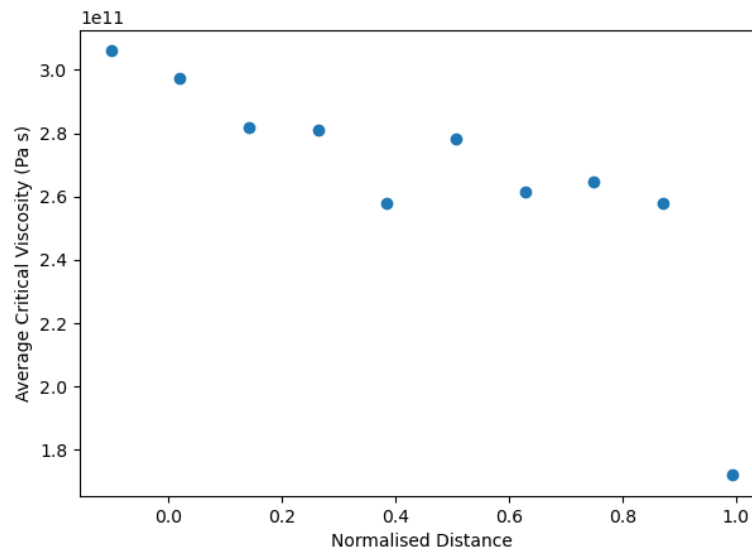


Figure 7.20: How the average critical viscosity varied across the NGV for volcanic ash impacts. After calculating the critical viscosities associated with particle impacts on the NGV, using the particle size distribution from Chapter 3, the NGV surface was split up into 10 ‘bins’ and the average critical viscosity of each bin was calculated.

In Fig [7.20], the average critical viscosity is highest at the trailing edge and generally decreases towards the leading edge, with a dramatic drop at the end of the vane. This implies that the maximum particle viscosity for which adhesion may occur, decreases from the leading edge to the trailing edge. This explains why, under identical impact conditions, Rhyolite and Dacite depositions were clustered towards the leading edge, while the less viscous Basalt and Andesite depositions were clustered towards the trailing edge.

Aeroengineers are interested in how volcanic ash depositions on the NGV surfaces narrow the throat gap and restrict airflow through the engine. It is therefore necessary to know for a given amount of mass that an engine is exposed to, how this mass is distributed along the vane surfaces for the two neighbouring NGVs. Recall that for each temperature field considered, the neighbouring NGVs correspond to one ‘hot’ NGV and one ‘cold’. The results in sections 7.3.2-7.3.5 demonstrate the distribution of mass on each individual NGV. To determine, for instance, the relative amount of ash buildup at the stagnation point between the hot NGV in Case A and the cold NGV in Case A, further processing of the results from sections 7.3.2-7.3.5 was required.

A resample function was employed in Python to randomly generate a dataset from the estimated probability densities (EDPs) depicted in Figures [7.4, 7.5, 7.8, 7.9, 7.12, 7.13, 7.16, 7.17], which illustrate the distribution of sticking events along the NGV surface (noting that this does not represent the mass distribution). Each EDP yielded a dataset of 40,000 points, with each data point corresponding to a position along the NGV and a normalized mass. Any data point that fell outside the range of the raw numbers obtained from the original CFD simulations in terms of NGV position and/or normalized mass was discarded.

Recall that each of the EDPs corresponds to a particular NGV within a given inlet sinusoidal temperature field, for different ash compositions. For each sampled EDP, the total mass along the corresponding NGVs was computed. Subsequently, each NGV surface was segmented into 20 equal sections, and the respective proportion of the total mass adhering to the vane was determined for each section.

Figures [7.2] and [7.3] depict the percentage of mass adhering to the vane across different NGVs, temperature fields, and ash compositions. For each NGV and composition, the proportion of adhered mass in each section was multiplied by the percentage of mass that sticks on impact to the NGV surface for the corresponding ash composition. This facilitates visualization of mass deposition patterns on the NGV and enables easy comparison across different NGVs, temperature fields, and ash compositions, arising from the consistent total mass impacting the NGV. The results of these distributions are shown in the Fig [7.21] to Fig [7.28] below.

7.4.1 Basalt

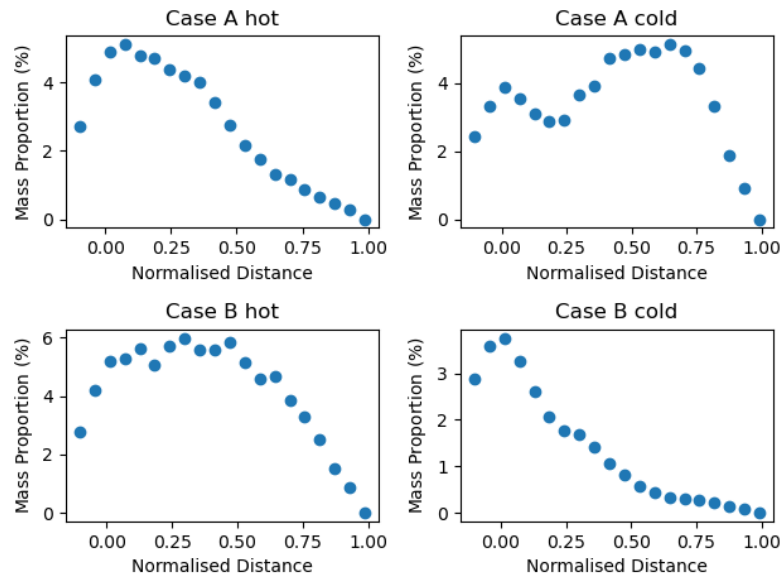


Figure 7.21: Plots illustrating the percentage of mass adhered to the NGV surface, segmented into 20 equally sized sections, for Basaltic ash and a temperature amplitude of 150 K.

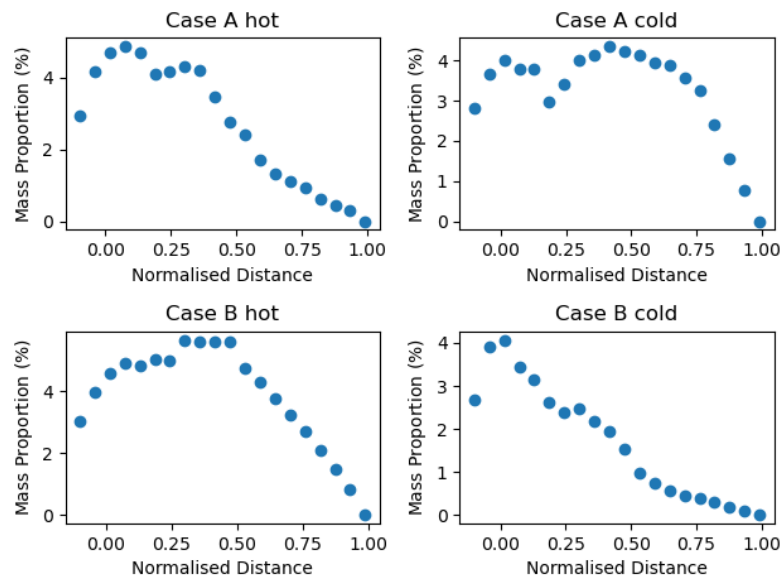


Figure 7.22: Plots illustrating the percentage of mass adhered to the NGV surface, segmented into 20 equally sized sections, for Basaltic ash and a temperature amplitude of 100 K.

Figures [7.21] and [7.22] present findings consistent with Figures [7.6] and [7.7]. It is evident that in Case A hot a greater proportion of the mass accumulates towards the leading edge,

whereas in Case A cold a larger proportion is distributed towards the trailing edge. In Case B hot the peak in mass distribution occurs midway along the NGV surface, sharply declining towards the trailing edge. Conversely, Case B cold exhibits the narrowest distribution, with the peak concentration at the leading edge, gradually decreasing towards the trailing edge. This general distribution pattern is consistent across both temperature amplitudes.

7.4.2 Andesite

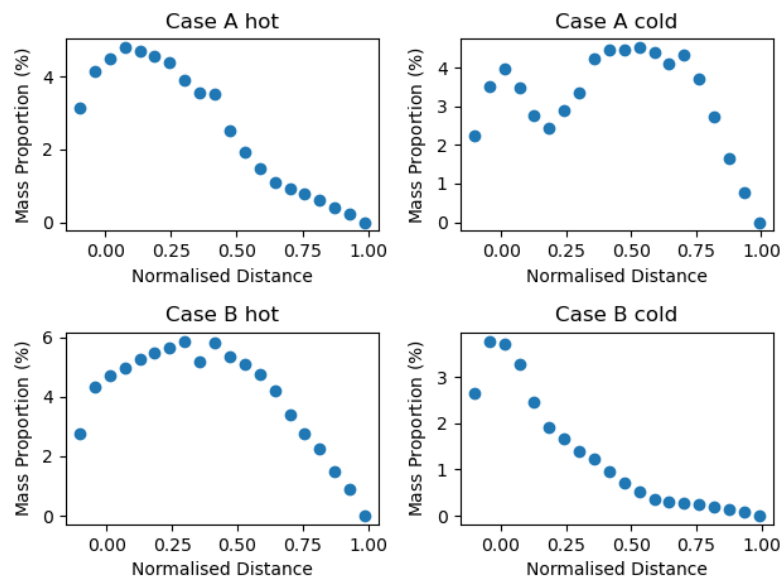


Figure 7.23: Plots illustrating the percentage of mass adhered to the NGV surface, segmented into 20 equally sized sections, for Andesitic ash and a temperature amplitude of 150 K.

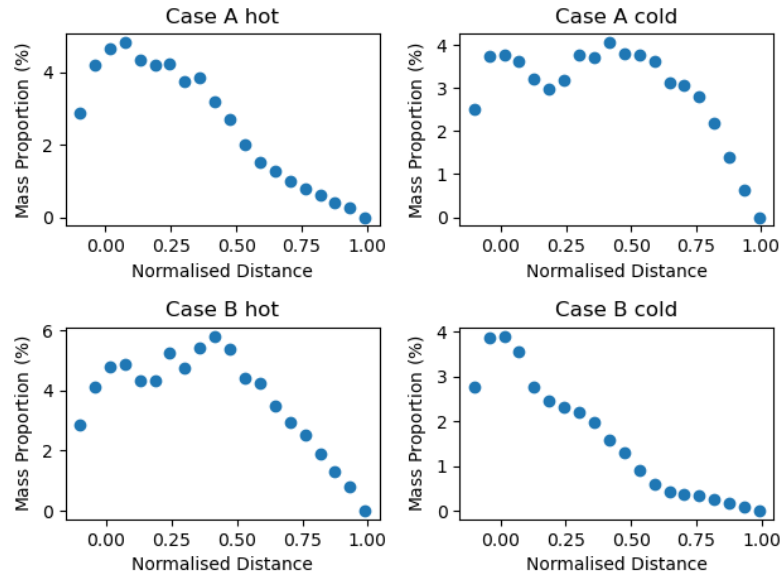


Figure 7.24: Plots illustrating the percentage of mass adhered to the NGV surface, segmented into 20 equally sized sections, for Andesitic ash and a temperature amplitude of 100 K.

For depositions of Andesitic ash very similar distributive behaviour was seen in Fig [7.23] and Fig [7.24] to the depositions of Basaltic ash seen in Fig [7.21] and Fig [7.22]. Again in Case A hot a larger proportion of the mass gathers towards the leading edge, while in Case A cold a greater proportion is spread towards the trailing edge. As before in Case B hot the peak mass distribution is centred midway along the NGV surface, sharply decreasing towards the trailing edge. Conversely, Case B cold shows the narrowest distribution, with the highest concentration at the leading edge, gradually diminishing towards the trailing edge. This general distribution pattern applies to both temperature amplitudes.

7.4.3 Dacite

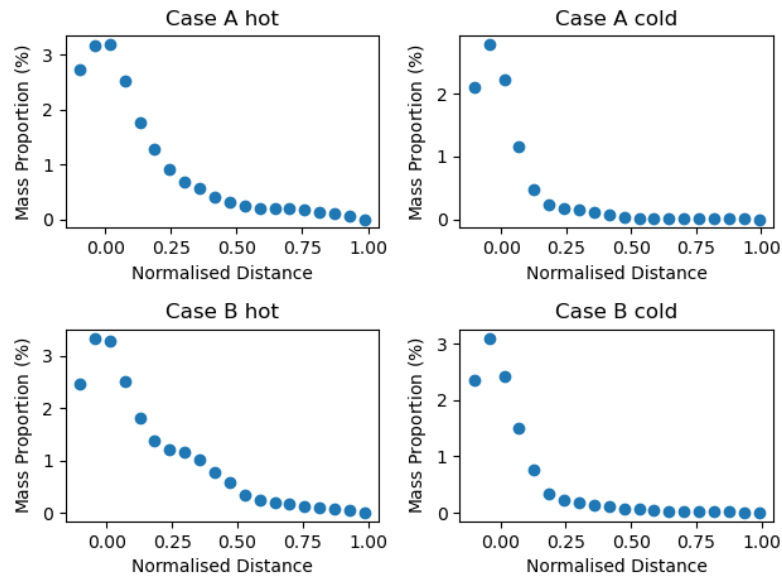


Figure 7.25: Plots illustrating the percentage of mass adhered to the NGV surface, segmented into 20 equally sized sections, for Dacitic ash and a temperature amplitude of 150 K.

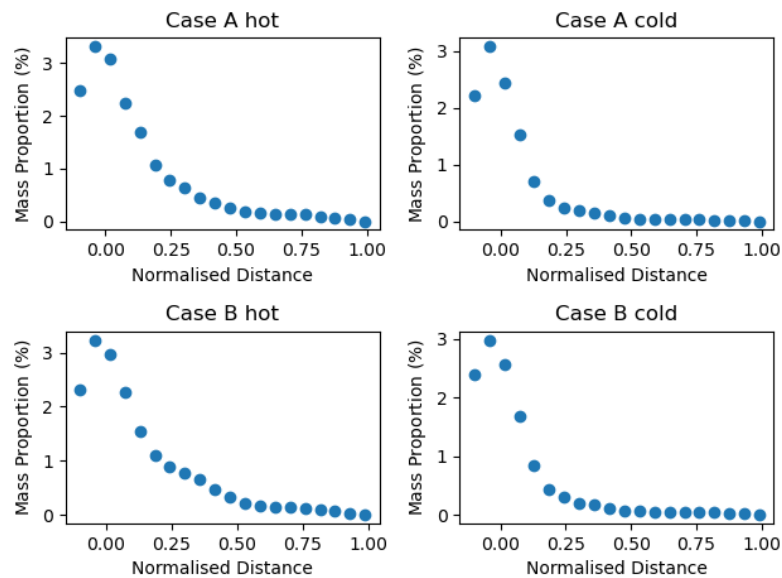


Figure 7.26: Plots illustrating the percentage of mass adhered to the NGV surface, segmented into 20 equally sized sections, for Dacitic ash and a temperature amplitude of 100 K.

Compared to the depositions of Basaltic and Andesitic ash, the depositions of Dacitic ash, shown in Figures [7.25] and [7.26], exhibit narrower distribution across the NGV surface. In

both Case A and B, hot and cold, most of the mass is deposited towards the stagnation point, with a steep decline in the amount of mass towards the trailing edge, nearly reaching zero. This pattern holds true for both temperature amplitudes considered.

7.4.4 Rhyolite

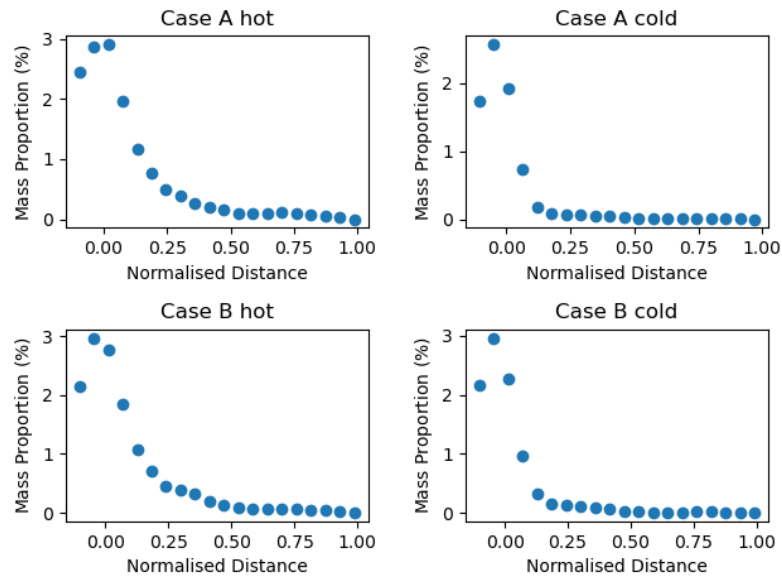


Figure 7.27: Plots illustrating the percentage of mass adhered to the NGV surface, segmented into 20 equally sized sections, for Rhyolitic ash and a temperature amplitude of 150 K.

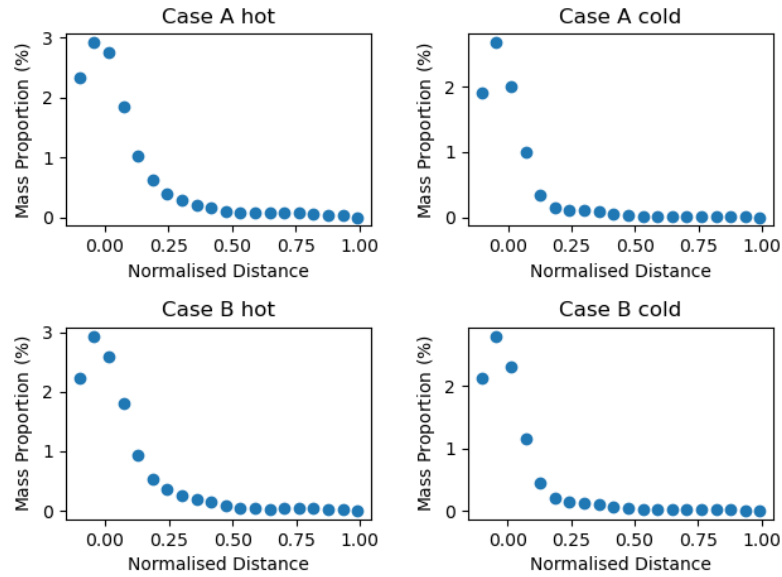


Figure 7.28: Plots illustrating the percentage of mass adhered to the NGV surface, segmented into 20 equally sized sections, for Rhyolitic ash and a temperature amplitude of 100 K.

The same distributive behaviour is seen for Rhyolitic ash distributions in Fig [7.27] and Fig [7.28], as for Dacitic ash distributions in Fig [7.25] and Fig [7.26], with the majority of the mass deposited towards the stagnation point, and a steep decline in the amount of mass towards the trailing edge. This was observed, again, for both temperature amplitudes considered.

In order to assess the sensitivity of the sticking predictions to the expression for $A(\theta)$ in Eqn[6.20], the plots in Figs[7.21-7.28] were then reproduced, using the different expressions for $A(\theta)$ given in Eqn [6.22] and Eqn [6.23] to calculate the critical viscosity. These plots can be seen in Figs [9.3-9.10] in the Appendix. It was found that the overall distributive behaviour of the sticking was not overly sensitive to the form of $A(\theta)$ used.

7.4.5 Comparison of Results with Engine Evidence.

In the results presented here it is established that depositions of Basalt and Andesite ash are generally more widely distributed across the NGV surface, while depositions of Dacite and Rhyolite ash tend to concentrate around the leading edge of the NGV. Validating these results is not a simple task. In this work the assumption has been made that all ash droplets impact a clean, smooth surface. However, if a layer of ash builds up on a section of the NGV

surface, it would not be unreasonable to assume that this would promote greater adhesion of subsequent ash droplets impacting the same section [12]. This could mean that over a long exposure period, even though very little Rhyolitic ash accumulates on the trailing edge of the NGV, enough would deposit on this section to encourage a significant buildup of Rhyolitic ash, especially considering the results presented in Chapter 3, which indicate that the bulk of the impacting mass hits the trailing edge. Additionally, the NGV is perforated with cooling holes that blow air over the surface, a factor which has not been accounted for in this work. This all makes comparison of the results presented here with engine evidence non-trivial.

Two examples of engine-evidence of ash depositions on the NGV have been found from the broader literature. On June 24, 1982, British Airways Flight 9, a Boeing 747-200, encountered a cloud of volcanic ash from the eruption of Mount Galunggung in Indonesia, the ash of which was primarily composed of Andesite [112]. The ash caused all four engines to fail, leading to a complete loss of power. However, the pilots managed to successfully glide the aircraft to a lower altitude, where they were able to restart the engines and make an emergency landing in Jakarta, Indonesia. The engines were disassembled and inspected for damage [7]. During this inspection deposits of ash on the NGVs were observed and photographed. A photograph of the deposits on the NGVs can be seen below in Fig [7.29].



Figure 7.29: Two neighbouring NGVs taken from an engine on the 1982 British Airways Flight 9, showing the depositions of volcanic ash from Mount Galunggung. Image taken from [7].

It can be observed that the depositions of this Andesitic ash are uniform across the NGV surface, with particularly heavy deposits evident on the right-hand side (RHS) NGV at the trailing edge, and on the left-hand side (LHS) NGV particularly heavy deposits are present on both the leading and trailing edges. This image seems consistent with the results presented for the deposition of Andesitic ash in Fig [7.23] and Fig [7.24].

In 2015 a Vehicle Integrated Propulsion Research (VIPR III) experiment was performed on a jet engine [19]. In this experiment the engine was exposed to volcanic ash from Mount Mazama, the ash of which is primarily composed of Rhyolite [113]. After the engine had been exposed to the ash, it was disassembled and inspected for damage. As part of this inspection, deposits of ash on the NGVs were photographed. A photo of the depositions on two neighbouring NGVs from this VIPR III experiment are shown in Fig [7.30] below.

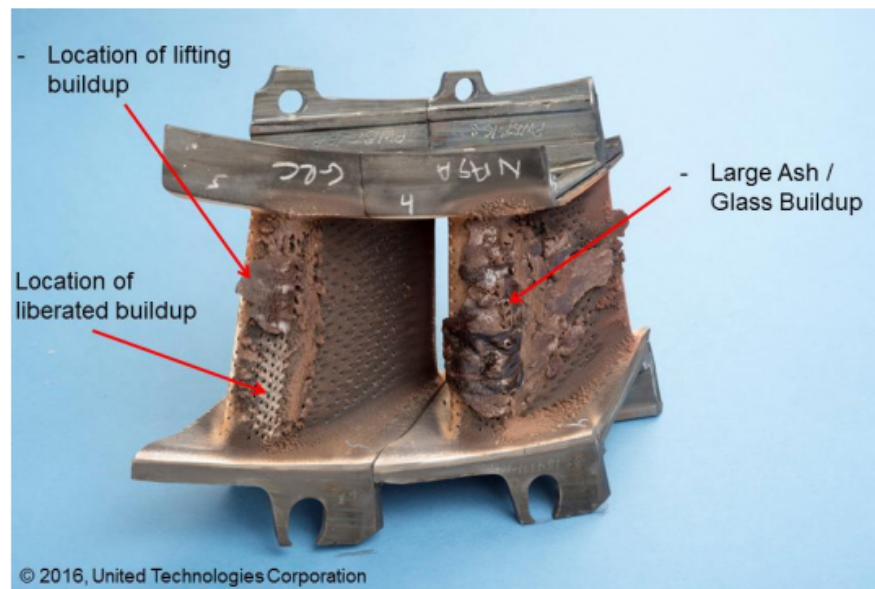


Figure 7.30: Two neighbouring NGVs taken from the VIPR III engine, showing the depositions of Rhyolitic Mazama volcanic ash. This image was taken from [19].

In Fig [7.30] it can be seen that the ash deposits are most heavily built up on the leading edge of the NGV. This is consistent with the results for Rhyolite depositions on the NGV surface shown in Fig [7.27] and Fig [7.28].

It can be seen that the results we find for the deposition of Andesitic and Rhyolitic ash on NGVs, shows good qualitative agreement with evidence from engine-encounters. For a

more quantitative comparison, the Phi value for the distributions of ash deposits on the NGV can be used. This is a method developed by aero-engineers at Rolls-Royce, which is used to characterise the distributions of ash deposits on the NGV, with a wider distribution leading to a larger Phi value. The Phi value is defined as:

$$\Phi = \frac{\delta A_{th}}{l_{th} \bar{h}}. \quad (7.5)$$

Here l_{th} is the throat gap, defined in Chapter 3, and δA_{th} is the effective throat area with the deposition present. Finally \bar{h} is defined as:

$$\bar{h} = \frac{V_{dep,TE} + V_{dep,LE}}{A_{NGV}}. \quad (7.6)$$

Here, $V_{dep,TE}$ represents the volume of the deposit on the trailing edge, $V_{dep,LE}$ denotes the volume of the deposit on the leading edge, and A_{NGV} refers to the surface area of the NGV. Calculating the effective throat area is not a straightforward task. This is because it is not solely determined by the volume of the deposit on the NGV, but also by complex fluid dynamic effects, such as the formation of separation bubbles on the NGV surface, which further reduce the effective throat area. During engine exposures to ash, this reduction in throat area can be estimated using in-flight data on airflow through the engine. Solely from the results presented in this chapter, it is not possible to estimate the effective throat area.

However, the results in Fig [7.21]-Fig [7.28] could be used in conjunction with new CFD simulations to provide an estimate of the effective throat area. The curves in Fig [7.21]-Fig [7.28] could be used to construct new NGV geometries with volcanic ash deposits on them. These new geometries could then be incorporated into CFD simulations similar to those presented in Chapter 3. The results from these simulations would allow an estimation of the reduction in the throat area.

This work suggests that the tolerance of a given aircraft engine to exposure to volcanic ash is highly dependent on the ash composition, and consequently the ash viscosity. Less viscous ash (such as Basalt and Andesite) has higher overall levels of sticking to the NGV compared to more viscous ashes (such as Dacite and Rhyolite). The primary implication of this is that the level of airborne ash that an aircraft with gas turbine engines can safely operate in is also dependent on the airborne ash composition. Recall that Clarkson et al. [10] defined the safe dose of airborne volcanic ash that an aircraft can withstand as equivalent to an aircraft operating in a concentration of ash of 4 mg m^{-3} for one hour [10]. In defining

this dose, Clarkson et al. [10] estimated the rate of accumulation of ash on the NGV and the rate of shedding. The work presented here suggests that more viscous volcanic ash would accumulate on the NGV at a much slower rate than less viscous ashes, and therefore, the resulting safe dose that an aircraft can be exposed to would be greater for more viscous ashes and lesser for less viscous ashes. This would mean that an aircraft would be able to be exposed to a greater amount of Rhyolitic or Dacitic ash, than it would Basaltic or Andesitic ash.

However, as aircraft engines are designed to run more efficiently, the operating temperatures will increase. Therefore, it is possible that in the aircraft engines of the future, Rhyolitic and Dacitic ash could behave more like Basaltic or Andesitic ash does in today's engines.

7.4.6 Limitations

The main limitation in this work arises from the formation of the critical viscosity model, as detailed in Chapter 6. As mentioned in that chapter, the data used to establish the empirical model were well-scaled to the Weissenberg numbers associated with ash droplet impacts on the NGV, but not as well-scaled to the Weber numbers. This means that in applying the model to the case of ash droplets impacting the NGV, the model is being extrapolated and applied to particle kinetic energies greater than those used to construct it. It would be necessary to conduct further experiments at greater velocities to investigate whether the model still accurately predicts bouncing and sticking events at greater kinetic energies.

Another limitation of this work is that the effect of deposited ash on further deposition was not studied. It would be reasonable to assume that if an ash droplet impacts a puddle of ash deposited on the vane, it is more likely to stick than if it were to impact on a totally clean vane. This behaviour could potentially lead to different deposition patterns than predicted here. In the case of Rhyolite and Dacite, although most droplets impact towards the trailing edge of the NGV, most of the impacts bounce off at the trailing edge, and the mass deposits towards the leading edge. However, if a small deposit formed at the trailing edge, this could prompt more sticking here, which due to the many impacts at the trailing edge, could lead to a chain reaction-style process, by which the bulk of the mass deposited ends up being concentrated at the trailing edge.

Another limitation in this work was the lack of quantitative validation. However, how this could be done has been detailed in the previous section. This work was not undertaken by myself due to time constraints. At the time of writing, a new PhD project is being initiated to conduct CFD simulations of an NGV array with ash deposits on the NGV surfaces.

7.5 Conclusions

In this chapter, I have presented an application of the empirical stick/bounce model developed and presented in Chapter 6 to the results of the computational fluid dynamics simulations of volcanic ash droplets impacting the NGV. Using the results from these two chapters, I have mapped and shown the region of the Nozzle Guide Vane where ash sticking to the surface is most prominent and have also shown where the bulk of the mass of the impacting ash is deposited on the NGV.

This mapping was done for two neighbouring NGVs (exposed to different temperatures), within a total of four different inlet temperature fields and for four different volcanic ash compositions. The inlet temperature field and the different temperatures that the neighbouring NGVs were exposed to were found to have some effect on the propensity of ash to stick to the NGV surface. However, the most important parameter in determining the sticking of ash was found to be the ash composition. For any given NGV or temperature field, Basalt was the ash composition for which most mass stuck to the surface, followed by Andesite, Dacite, and then Rhyolite. The depositions of the Basaltic and Andesitic ash were found to be generally broadly distributed along the NGV surface, whereas for the Rhyolitic and Dacitic ash, the depositions were tightly distributed around the stagnation point.

These results were shown to have good qualitative agreement with observations of ash depositions on NGVs from two different engines exposed to Andesitic ash and Rhyolitic ash respectively. A method for how a more quantitative comparison between the results presented here and engine evidence was described. The results here suggest that Rhyolitic ash poses the least threat to aircraft engines, and Basaltic ash poses the greater risk.

Chapter 8

Conclusions

8.1 Summary

Gas turbine engines on aircraft exposed to airborne volcanic ash risk performance degradation, potentially leading to in-flight engine failure. The primary mechanism of engine damage from volcanic ash is the deposition of ash droplets on the surfaces of the Nozzle Guide Vanes (NGVs), causing airflow restriction and subsequent engine failure. To determine the safe exposure level of volcanic ash that jet engines can withstand, we must understand the rate of ash accumulation on the NGV. This depends on the propensity for ash droplets to stick, splash, or bounce upon impact with the NGV surface. It is necessary to understand how the various impact properties of the volcanic ash droplets control these outcomes.

In this research I aimed to understand the physics that governs the potential impact outcomes (stick, splash, or bounce) of volcanic ash droplets on the NGV, and to identify the impact properties and physics governing these outcomes through the design and execution of scaled droplet impact experiments using analogue materials. The experiments were designed by calculating relevant dimensionless numbers and other impact properties associated with volcanic ash droplet impacts on the NGV. These factors are crucial in determining whether the outcome is sticking, splashing, or bouncing behaviour. I then performed droplet impact experiments within the same dimensionless number space. The framework for this work was built around three questions as defined in the introduction:

- 1.) What dimensionless numbers are important in controlling the stick/splash/bounce

outcome of the ash droplet - NGV interaction?

2.) What are the values of the dimensional impact properties and the dimensionless numbers associated with the ash droplet - NGV interaction?

3.) Under what conditions do ash droplets stick, splash or bounce on impact with the NGV surfaces?

I will now address these questions individually, summarising the answers found, and assessing the extent to which the questions were answered in this thesis.

8.2 What dimensionless numbers are important in controlling the stick/splash/bounce outcome of the ash droplet - NGV interaction?

In Chapter 2, a combined statistical analysis was conducted on published datasets to identify the most important dimensional and dimensionless properties influencing droplet splashing on impact with a dry surface. It was found that impact velocity was the most significant dimensional property, with higher velocities increasing the propensity for splashing. Droplet viscosity was found to be the least influential variable. Surface roughness of the impact surface and droplet impact angle were also found to be important factors which affect splashing outcomes. However, the analysis showed that a complete understanding of all conditions controlling droplet splashing has yet to be achieved.

Among the dimensionless numbers considered, the Weber number emerged as the most important in determining splashing outcomes, while the Ohnesorge number had the least influence. The analysis also highlighted the significance of the Reynolds and Capillary numbers in determining splashing outcomes. However, for the scaled experiments, only the Weber and Ohnesorge numbers were considered based on the work of Schiaffino and Sonin [48], which suggests variations in the mathematical formulations of the Reynolds and Capillary numbers depending on the corresponding location of the droplet impact in Weber-Ohnesorge number space.

In Chapters 3 and 6, it was hypothesized that the Weissenberg number could control ash droplet bouncing on impact with the NGV surface, with a critical Weissenberg number ($Wi_c = 0.01$) delineating between sticking and bouncing outcomes, such that when $Wi < Wi_c$ sticking would occur. The literature review reported in Chapter 6 regarding the role of Wi_c was inconclusive. However, experimental results presented in Chapter 6 suggested that $Wi_c = 0.01$ could not accurately discriminate between sticking and bouncing outcomes. Instead, a bouncing/sticking threshold was found as a function of the droplet viscosity, kinetic energy, and impact angle.

8.3 What are the values of the dimensional impact properties and the dimensionless numbers associated with the ash droplet - NGV interaction?

This question was comprehensively addressed in Chapter 3. In this chapter, computational fluid dynamics (CFD) simulations were conducted to analyse airflow, laden with ash particles around an array of NGVs. Simulations were performed for four different temperature fields around the NGVs, corresponding to different engine designs. These temperature variations resulted in neighbouring NGVs being exposed to gases of different temperatures. The dimensional impact properties of volcanic ash particles on the neighbouring NGVs for each simulation were extracted, including impact velocity, impact angle, particle diameter, and impact temperature. The analysis revealed variations in these properties with respect to each other and with impact position on the NGV. Smaller particles were observed to impact the NGV at more glancing angles, more frequently than larger particles. Additionally, impacts at higher velocities and more glancing angles occurred towards the trailing edge of the NGV, while impacts were generally slower and more ‘head-on’ towards the leading edge.

These dimensional properties were then used to calculate the Weber, Ohnesorge, and Weissenberg numbers associated with the ash droplet impacts. These numbers indicated the predominant regions of dimensionless number space occupied by the ash impacts and how their values varied along the NGV surface. It was observed that most ash impacts fell within region 4 of Weber-Ohnesorge number space, as defined by Schiaffino and Sonin [48], with the remainder in region 1. Furthermore, a critical Weissenberg number of $Wi_c = 0.01$

bisected the region of Weber-Weissenberg number space occupied by volcanic ash droplet impacts. Additionally, it was demonstrated that there was only slight variation in the values of the Weber, Ohnesorge, and Weissenberg numbers for impacts across neighbouring NGVs within a given temperature field and across different temperature fields as well.

8.4 Under what conditions do ash droplets stick, splash or bounce on impact with the NGV surfaces?

8.4.1 The sticking/splashing threshold.

Chapters 4 and 5 describe the work to determine whether ash droplets splash on impact with NGV surfaces. In Chapter 4 it is described how droplet impact experiments were conducted using various analogue fluids. Droplets of the fluids were generated using a micro dispenser and then impacted onto a glass slide held at a range of angles. The vast majority of impacts fell within region 1 and region 4 of Weber-Ohnesorge number space, as defined by Schiaffino and Sonin [48]. No splashing was observed for any of the droplet impacts. However, due to limitations of the micro dispenser, only 8 droplet impacts were performed within the precise same area of Weber-Ohnesorge number space as the ash droplet impacts on the NGV. The micro dispenser was incapable of producing droplets with sufficient viscosity and initial velocity to scale the impacts to the Weber and Ohnesorge numbers associated with volcanic ash impacts. Consequently, limited conclusions regarding the propensity for ash droplets to splash on impact with the NGV can be drawn from these results. Nevertheless, the results suggest that at the very least some of the ash impacting the NGV would not splash.

Chapter 5 describes how the CFD software Flow 3D was used to conduct simulations of droplets onto a smooth, dry surface held at various angles. The simulations were scaled to the area of Weber-Ohnesorge number space occupied by the impacts of volcanic ash on the NGV. It was observed that with an increasing Ohnesorge number, the Weber number at which splashing starts to occur also increases. No significant effect due to varying the impact angle was found. Additionally, no splashing was observed in the area of Weber and Ohnesorge number space occupied by the ash impacts. The results from the simulations suggested that the volcanic ash impacts occur at Ohnesorge numbers which are too large, and Weber numbers which are too small for splashing to occur. However, these results must

be interpreted with caution, as there were no corresponding experimental data in the same region of Weber-Ohnesorge number space that these CFD simulations could be compared with and validated against.

In conclusion the results presented in Chapter 4 and Chapter 5 would suggest that volcanic ash does not splash when it impacts on the NGV surfaces.

8.4.2 The sticking/bouncing threshold.

In Chapter 6 I present the results from an experimental investigation to study the bouncing and sticking behaviour of molten glass droplets impacting a metal surface at various inclination angles. Glass particles were introduced into the flame of an oxy-acetylene torch directed at a metal Nimonic 75 plate, and observations were made to determine if any glass adhered to the target surface.

Initially, the experiments were scaled to explore the range of Weissenberg numbers associated with the impacts of volcanic ash on the Nozzle Guide Vanes (NGVs). Contrary to the initial hypothesis, it was discovered that a critical Weissenberg number of ($Wi_c = 0.01$) did not accurately delineate the sticking/bouncing threshold. Sticking was observed at values of $Wi \gg 0.01$, with a notable dependence on the angle of the target surface, favouring bouncing at more glancing angles. It was also found that a particle was less likely to stick if it had a large viscosity.

Subsequently, I compared the experimental data with the empirical critical viscosity model proposed by Kleinhans et al. [70], which considers impacting particle kinetic energy, viscosity, and impact angle to determine sticking or bouncing behaviour. However, this model was inadequate to describe my experimental data. Therefore, I adapted the model to better fit the experimental results, incorporating a novel dependence on impact angle based on the observed experimental data.

8.5 Synthesis and application of results.

In Chapter 7, I used the new critical viscosity model presented in Chapter 6 in conjunction with the CFD modelling results from Chapter 3 to predict the level of ash deposition and deposition patterns on the NGV surfaces for four different ash compositions. Results were

presented for the deposition of Basaltic, Andesitic, Dacitic and Rhyolitic ash, on neighbouring NGVs for the 4 different temperature fields that were considered in Chapter 3.

It was found, that for any given NGV in any given temperature field, Basaltic ash had the greatest propensity for sticking, followed by Andesite, Dacite and then Rhyolite. The deposits of Basaltic and Andesitic ash on the vane were shown to be broadly distributed across the length of the vane, while the deposits of Rhyolite and Dacite were more tightly distributed on the leading edge. These results had good qualitative agreement with observations on NGVs taken from two gas turbine engines after exposure to Andesite ash and Rhyolite ash respectively. These results suggest that it is the composition of the volcanic ash that is most important in determining the level of deposition and the pattern of deposition upon the NGV surface. These results also suggest that Rhyolitic ash poses is least hazardous to aircraft, whereas Basaltic ash poses the greatest hazard.

8.6 Further Work

This section briefly summarises recommendations for further work, which are set out in detail at the end of each chapter.

8.6.1 Further Droplet Impact Experiments, Better Scaled to the Weber Number.

In all the experimental work conducted in Chapter 4 and Chapter 6, achieving droplet impacts within the most populated range of the Weber number space proved challenging and unsuccessful. Consequently, the critical viscosity model developed in Chapter 6 was extrapolated in Chapter 7 to predict ash deposition on the NGVs. The inability to achieve higher Weber numbers in Chapter 4 experiments also precluded observation of splashing, and validation of the results from the Chapter 5 CFD simulations against real experimental data. Therefore, a logical next step would be to repeat the experiments in Chapter 4 and Chapter 6 at higher velocities.

8.6.2 Examine Behaviour of Deposition on ‘Dirty’ Surfaces.

Throughout this study, ash deposition was only considered on clean metal surfaces without existing ash deposits. However, it is known from Dean et al. [12] that existing ash deposits on a metal surface can facilitate further deposition. Therefore, investigating this effect in further experiments would be a logical progression and could enhance the understanding of ash deposition presented in Chapter 7.

8.6.3 Examine the Role of Other Properties Affecting Droplet Impact Outcomes.

This study focused on investigating the influence of the Weber number, Ohnesorge number, Weissenberg number, and impact angle on ash droplet impact outcomes. However, as demonstrated in Chapter 2, surface roughness also affects droplet splashing outcomes. Scaled experiments on surfaces with varying roughness would further refine the predictions and conclusions drawn in this study.

Chapter 9

Appendix

9.1 Chapter 2

Table 9.1: The dimensional properties considered in section 2.1.4 and their S.I units..

Property	S.I units.
Viscosity (μ)	$\text{kgm}^{-1}\text{s}^{-1}$
Density (ρ)	kgm^{-3}
Velocity (v)	ms^{-1}
Diameter (D)	m
Surface tension (σ)	kgs^{-2}
Elastic Modulus (G)	$\text{kgm}^{-1}\text{s}^{-2}$
Gravitational acceleration (g)	ms^{-2}
Temperature of particle (T_p)	K
Temperature of particle (T_∞)	K

9.2 Chapter 3

The realisable k-epsilon form of the compressible Reynolds-Averaged Navier-Stokes (RANS) equations:

Continuity Equation (Mass Conservation):

$$\frac{\partial \rho}{\partial t} + \frac{\partial(\rho \bar{u}_i)}{\partial x_i} = 0 \quad (9.1)$$

Where:

- ρ : Fluid density.
- \bar{u}_i : Mean velocity in the i -direction.

Momentum Conservation (RANS Equations):

$$\frac{\partial(\rho\bar{u}_i)}{\partial t} + \frac{\partial(\rho\bar{u}_i\bar{u}_j)}{\partial x_j} = -\frac{\partial\bar{p}}{\partial x_i} + \frac{\partial\tau_{ij}}{\partial x_j} - \frac{\partial\overline{\rho u'_i u'_j}}{\partial x_j} \quad (9.2)$$

Where:

- \bar{p} : Mean pressure.
- τ_{ij} : Viscous stress tensor (accounting for molecular viscosity).
- $\overline{\rho u'_i u'_j}$: Reynolds stress tensor for compressible flows, representing the effects of turbulence on the momentum field.

Reynolds Stress Closure for Compressible Flow:

In the realizable $k - \epsilon$ model, the Reynolds stress tensor $\overline{\rho u'_i u'_j}$ for compressible flow is approximated as:

$$\overline{\rho u'_i u'_j} = -\rho\nu_t \left(\frac{\partial\bar{u}_i}{\partial x_j} + \frac{\partial\bar{u}_j}{\partial x_i} \right) + \frac{2}{3}\rho k\delta_{ij} \quad (9.3)$$

Where:

- $\nu_t = C_\mu \frac{k^2}{\epsilon}$: Turbulent viscosity.
- k : Turbulent kinetic energy.
- ϵ : Turbulent dissipation rate.
- δ_{ij} : Kronecker delta (1 if $i = j$, 0 otherwise).
- C_μ : Empirical constant.

Turbulent Kinetic Energy Equation (k) for Compressible Flow:

$$\frac{\partial(\rho k)}{\partial t} + \frac{\partial(\rho k\bar{u}_j)}{\partial x_j} = \frac{\partial}{\partial x_j} \left[\left(\mu + \frac{\mu_t}{\sigma_k} \right) \frac{\partial k}{\partial x_j} \right] + P_k - \rho\epsilon + P_{\text{compress}} \quad (9.4)$$

Where:

- $P_k = \mu_t \left(\frac{\partial\bar{u}_i}{\partial x_j} + \frac{\partial\bar{u}_j}{\partial x_i} \right) \frac{\partial\bar{u}_i}{\partial x_j}$.

- $P_{\text{compress}} = 2\mu_t \left(\frac{\partial \bar{u}_k}{\partial x_k} \right)^2$.

- σ_k : Turbulent Prandtl number for k .

Turbulent Dissipation Rate Equation (ϵ) for Compressible Flow:

$$\frac{\partial(\rho\epsilon)}{\partial t} + \frac{\partial(\rho\epsilon\bar{u}_j)}{\partial x_j} = \frac{\partial}{\partial x_j} \left[\left(\mu + \frac{\mu_t}{\sigma_\epsilon} \right) \frac{\partial \epsilon}{\partial x_j} \right] + C_1 \frac{\epsilon}{k} P_k - C_2 \frac{\rho\epsilon^2}{k + \sqrt{\nu}\epsilon} + C_\epsilon P_{\text{compress}} \quad (9.5)$$

Where:

- C_1 and C_2 : Empirical constants.
- C_ϵ : Compressibility correction coefficient.
- σ_ϵ : Turbulent Prandtl number for ϵ .

Sinusoidal Temperature field Equation:

$$T(x) = 1700 + A \sin \frac{2\pi}{\lambda} x. \quad (9.6)$$

Here $T(x)$ is the temperature (in Kelvin) along the inlet, A is the temperature amplitude (which took values of 100K or 150K), and λ is the wavelength, which assumed distinct values for Case A and Case B, respectively.

9.3 Chapter 4

Code written to extract droplet velocities and diameters from videos of droplet impacts:

```
from __future__ import division
from PIL import Image
import numpy as np
from numpy import array
import matplotlib.pyplot as plt #Image.open(r'C:\Users\thoma\Desktop/test.png')
from matplotlib import gridspec
#Run VideConverterFirst
Frames=10#number of frames we want.
FPS=10000#37500
pressure=88
StartingFrame=0

Pixel=5.2e-6
VelFactor=Pixel*FPS
B='None'#other things to note
Vid=5
```

```

Conc='GlycerolGlass'
Angle='Angle60'

YBottom=np.zeros(1)
XDiam=np.zeros(1)
for k in range(Frames):
    j=k+StartingFrame #j=k+startingFrame
    print k
    z=r'C:\Users\thoma\Desktop\Code\data\frame%d.tif'%j
    img2 = Image.open(z)
    img2=img2.convert('L')
    #img2=img2.convert('1', dither=Image.NONE)
    I2=array(img2)#[:,0:150]
    Zim=r'C:\Users\thoma\Desktop\Code\data\frame0.tif'
    I1=Image.open(Zim).convert('L')
    Initialarr=array(I1)
    plt.figure()
    plt.title('no crop')
    plt.imshow(Initialarr)
    plt.show()
    #arr=arr[0:int(np.min(Counts2)),:]
    arr=I2[0:100,130:]
    plt.figure()
    plt.imshow(arr)
    plt.title('%d'%k)
    plt.show()
    y_coords=np.zeros(1)
    x_coords=np.zeros(1)
    plt.figure()
    for i in range(len(arr[:,0])):
        for j in range(len(arr[0,:])):
            if arr[i,j]<7:#150 #Dark image settings
                x=j;y=i
                y_coords=np.vstack([y_coords,y])
                x_coords=np.vstack([x_coords,x])
            else:
                continue
    x_coords=x_coords[1,:];
    y_coords=y_coords[1,:];
    plt.imshow((arr))
    plt.plot(x_coords,y_coords,'x')
    XARRAY=np.arange(np.min(x_coords),np.max(x_coords),1)
    plt.plot(XARRAY,np.zeros(len(XARRAY))+np.mean(y_coords),'x',label='%dmm'%(np.max(x_coords)-np.min(x_coords))*Pixel*1000)
    plt.plot(np.median(XARRAY),np.max(y_coords),'o',label='%dm/s'%(np.max(y_coords)-YBottom[k])*VelFactor))
    plt.savefig(r'C:\Users\thoma\Desktop\Code\Images\%d.jpg'%k)
    plt.text(200,100,'%dmm'%(np.max(x_coords)-np.min(x_coords))*Pixel*1000)
    plt.text(200,300,'%dm/s'%(np.max(y_coords)-YBottom[k])*VelFactor))
    plt.legend()
    YBottom=np.vstack([YBottom,np.max(y_coords)])
    XDiam=np.vstack([XDiam,np.max(x_coords)-np.min(x_coords)])
    YBottom=YBottom[1,:];
    XDiam=XDiam[1,:];
    # MAKES GIF
    frames = []
    for i in range(Frames):
        P=r'C:\Users\thoma\Desktop\Code\GIFs'
        C=r'%dVid'%Vid
        Pr=r'%dKpa'%pressure
        T=r'.gif'%FPS
        Zambia=P+C+T#+Pr+B+T
        F=r'C:\Users\thoma\Desktop\Code>ContactAngle'
        Zimbabwe=F+Conc+Angle+'%dImpact'%Vid+T
        new_frame = Image.open(r'C:\Users\thoma\Desktop\Code\Images\%d.jpg'%i)
        frames.append(new_frame)
    # Save into a GIF file that loops forever
    #frames[0].save(r'C:\Users\thoma\Desktop\Code\data\GIFs\png_to_gif.gif', format='GIF',

```

```

frames[0].save(Zimbabwe, format='GIF',
append_images=frames[1:],
save_all=True,
duration=300, loop=0)
FramesArray=np.arange(1,Frames+1,1)
T=r'.jpg' #%FPS
plt.figure()
plt.plot(FramesArray,YBottom,'x-')
plt.xlabel('frame')
plt.ylabel('YBottom')
plt.savefig(P+C+'displacement'+T)

plt.figure()
plt.plot(FramesArray,XDiam*Pixel,'x-')
plt.xlabel('frame')
plt.ylabel('XDiam')
plt.savefig(P+C+'diameter')
Vel=np.zeros(len(YBottom)-1)
for i in range(len(YBottom)-1):
Vel[i]=YBottom[i+1]-YBottom[i]
plt.figure()
plt.plot(Vel*VelFactor,'x-')
plt.savefig(P+C+'velocity')

for i in range(len(Vel)):
TV=Vel[i]
if TV==0:
Index=i-2
break
else:
continue
Index=i#len(Vel)-10

#np.hstack([Vel[:]*VelFactor, XDiam[:-1]*Pixel])
F=r'C:\Users\thoma\Desktop\Code>ContactAngle'

Array=Vel*VelFactor
T=r'%dfps.txt' %FPS
np.savetxt(F+Conc+Angle+'%dVelData.txt'%Vid,Array)

Array2=XDiam*Pixel
np.savetxt(F+Conc+Angle+'%dDiamData.txt'%Vid,Array2)
plt.close()

print ('velocity')
print (Array)

print ('Diameter')
print (Array2)

```

9.4 Chapter 5

Table 9.2: Droplet impact conditions from [40] used for verification, alongside recorded experimental and simulated outcomes. Note Outcome= 1 indicates no splash, Outcome= 2 indicates a splash.

Simulation	Fluid	ρ (kg/m ³)	σ (N/m)	μ (Pa·s)	D (m)	v (m/s)	We	Oh	Experimental Outcome	Simulation Outcome
1	Water	1000	7.30E-02	1.00E-03	2.41	2.34	1.81E+02	2.38E-03	2	1
2	Water	1000	7.30E-02	1.00E-03	2.60	4.40	6.90E+02	2.30E-03	1	2
3	Water	1000	7.30E-02	1.00E-03	2.67	4.53	7.51E+02	2.27E-03	1	2
4	Water	1000	7.30E-02	1.00E-03	2.53	3.73	4.82E+02	2.33E-03	2	2
5	Water	1000	7.30E-02	1.00E-03	2.40	3.73	4.57E+02	2.39E-03	2	2
6	Water	1000	7.30E-02	1.00E-03	2.67	3.87	5.48E+02	2.27E-03	2	2
7	Water	1000	7.30E-02	1.00E-03	2.60	3.87	5.33E+02	2.30E-03	2	2
8	Water	1000	7.30E-02	1.00E-03	2.53	4.00	5.55E+02	2.33E-03	2	2
9	Water	1000	7.30E-02	1.00E-03	2.53	3.73	4.82E+02	2.33E-03	2	2
10	Water	1000	7.30E-02	1.00E-03	2.53	2.13	1.57E+02	2.33E-03	1	1
11	Water	1000	7.30E-02	1.00E-03	2.47	3.33	3.75E+02	2.35E-03	1	2
12	Water	1000	7.30E-02	1.00E-03	2.60	3.87	5.33E+02	2.30E-03	1	2
13	Water	1000	7.30E-02	1.00E-03	2.53	3.87	5.19E+02	2.33E-03	1	2
14	Water	1000	7.30E-02	1.00E-03	2.53	3.33	3.84E+02	2.33E-03	1	1
15	Water	1000	7.30E-02	1.00E-03	2.53	2.53	2.22E+02	2.33E-03	1	1
16	Water	1000	7.30E-02	1.00E-03	2.47	3.87	5.07E+02	2.35E-03	1	2

Table 9.2: Droplet impact conditions from [40] used for verification, alongside recorded experimental and simulated outcomes. Note Outcome= 1 indicates no splash, Outcome= 2 indicates a splash.

Simulation	Fluid	ρ (kg/m ³)	σ (N/m)	μ (Pa·s)	D (m)	v (m/s)	We	Oh	Experimental Outcome	Simulation Outcome
17	Water	1000	7.30E-02	1.00E-03	2.60	2.53	2.28E+02	2.30E-03	2	1
18	Water	1000	7.30E-02	1.00E-03	2.53	3.87	5.19E+02	2.33E-03	2	2
19	Water	1000	7.30E-02	1.00E-03	2.53	3.33	3.84E+02	2.33E-03	2	1
20	Water	1000	7.30E-02	1.00E-03	2.40	4.00	5.26E+02	2.39E-03	2	2
21	Water	1000	7.30E-02	1.00E-03	2.60	2.53	2.28E+02	2.30E-03	1	1
22	Water	1000	7.30E-02	1.00E-03	2.53	4.27	6.32E+02	2.33E-03	2	2
23	Water	1000	7.30E-02	1.00E-03	2.52	3.93	5.33E+02	2.33E-03	2	2
24	Water	1000	7.30E-02	1.00E-03	2.50	4.19	6.01E+02	2.34E-03	2	2
25	Water	1000	7.30E-02	1.00E-03	2.48	2.62	2.33E+02	2.35E-03	2	1
26	Water	1000	7.30E-02	1.00E-03	2.47	2.74	2.54E+02	2.35E-03	2	1
27	Water	1000	7.30E-02	1.00E-03	2.47	4.27	6.17E+02	2.35E-03	2	2
28	Water	1000	7.30E-02	1.00E-03	2.45	3.72	4.64E+02	2.36E-03	2	2
29	Water	1000	7.30E-02	1.00E-03	2.45	2.81	2.65E+02	2.36E-03	2	1
30	Water	1000	7.30E-02	1.00E-03	2.45	2.55	2.18E+02	2.36E-03	2	1
31	Water	1000	7.30E-02	1.00E-03	2.44	3.42	3.91E+02	2.37E-03	2	1
32	Water	1000	7.30E-02	1.00E-03	2.42	3.25	3.50E+02	2.38E-03	2	2

Table 9.2: Droplet impact conditions from [40] used for verification, alongside recorded experimental and simulated outcomes. Note Outcome= 1 indicates no splash, Outcome= 2 indicates a splash.

Simulation	Fluid	ρ (kg/m ³)	σ (N/m)	μ (Pa·s)	D (m)	v (m/s)	We	Oh	Experimental Outcome	Simulation Outcome
33	Water	1000	7.30E-02	1.00E-03	2.42	2.47	2.02E+02	2.38E-03	2	1
34	Water	1000	7.30E-02	1.00E-03	2.42	0.63	1.32E+01	2.38E-03	1	1
35	Water	1000	7.30E-02	1.00E-03	2.42	0.61	1.23E+01	2.38E-03	1	1
36	Water	1000	7.30E-02	1.00E-03	2.41	3.57	4.21E+02	2.38E-03	2	2
37	Water	1000	7.30E-02	1.00E-03	2.41	3.42	3.86E+02	2.38E-03	2	2
38	Water	1000	7.30E-02	1.00E-03	2.41	3.10	3.17E+02	2.38E-03	2	2
39	Water	1000	7.30E-02	1.00E-03	2.41	2.85	2.68E+02	2.38E-03	2	1
40	Water	1000	7.30E-02	1.00E-03	2.40	4.00	5.26E+02	2.39E-03	2	2
41	Water	1000	7.30E-02	1.00E-03	2.39	4.57	6.84E+02	2.39E-03	2	2
42	Water	1000	7.30E-02	1.00E-03	2.39	4.38	6.28E+02	2.39E-03	2	2
43	Water	1000	7.30E-02	1.00E-03	2.39	3.80	4.73E+02	2.39E-03	2	2
44	Water	1000	7.30E-02	1.00E-03	2.39	1.33	5.79E+01	2.39E-03	1	1
45	Water	1000	7.30E-02	1.00E-03	2.39	1.16	4.41E+01	2.39E-03	1	1
46	Water	1000	7.30E-02	1.00E-03	2.39	0.53	9.20E+00	2.39E-03	1	1
47	Water	1000	7.30E-02	1.00E-03	2.38	2.83	2.61E+02	2.40E-03	2	1
48	Water	1000	7.30E-02	1.00E-03	2.38	2.62	2.24E+02	2.40E-03	2	1

Table 9.2: Droplet impact conditions from [40] used for verification, alongside recorded experimental and simulated outcomes. Note Outcome= 1 indicates no splash, Outcome= 2 indicates a splash.

Simulation	Fluid	ρ (kg/m ³)	σ (N/m)	μ (Pa·s)	D (m)	v (m/s)	We	Oh	Experimental Outcome	Simulation Outcome
49	Water	1000	7.30E-02	1.00E-03	2.38	2.40	1.88E+02	2.40E-03	2	1
50	Water	1000	7.30E-02	1.00E-03	2.38	2.26	1.67E+02	2.40E-03	2	1
51	Water	1000	7.30E-02	1.00E-03	2.38	1.62	8.56E+01	2.40E-03	1	1
52	Water	1000	7.30E-02	1.00E-03	2.38	0.57	1.06E+01	2.40E-03	1	1
53	Water	1000	7.30E-02	1.00E-03	2.36	2.40	1.86E+02	2.41E-03	2	1
54	Water	1000	7.30E-02	1.00E-03	2.36	2.26	1.65E+02	2.41E-03	1	1
55	Water	1000	7.30E-02	1.00E-03	2.36	0.93	2.80E+01	2.41E-03	1	1
56	Water	1000	7.30E-02	1.00E-03	2.34	2.64	2.23E+02	2.42E-03	2	1
57	Water	1000	7.30E-02	1.00E-03	2.33	3.87	4.78E+02	2.42E-03	2	2
58	Water	1000	7.30E-02	1.00E-03	2.33	0.63	1.27E+01	2.42E-03	1	1
59	Water	1000	7.30E-02	1.00E-03	2.33	0.57	1.04E+01	2.42E-03	1	1
60	Water	1000	7.30E-02	1.00E-03	2.27	3.47	3.74E+02	2.46E-03	1	1
61	Water	1000	7.30E-02	1.00E-03	2.27	3.28	3.35E+02	2.46E-03	1	1
62	Water	1000	7.30E-02	1.00E-03	2.27	2.49	1.93E+02	2.46E-03	1	1
63	Water	1000	7.30E-02	1.00E-03	2.27	2.34	1.70E+02	2.46E-03	1	1
64	Water	1000	7.30E-02	1.00E-03	2.24	4.38	5.89E+02	2.47E-03	2	2

Table 9.2: Droplet impact conditions from [40] used for verification, alongside recorded experimental and simulated outcomes. Note Outcome= 1 indicates no splash, Outcome= 2 indicates a splash.

Simulation	Fluid	ρ (kg/m ³)	σ (N/m)	μ (Pa·s)	D (m)	v (m/s)	We	Oh	Experimental Outcome	Simulation Outcome
65	Water	1000	7.30E-02	1.00E-03	2.24	3.16	3.06E+02	2.47E-03	2	1
66	Water	1000	7.30E-02	1.00E-03	2.24	2.35	1.69E+02	2.47E-03	1	1
67	Water	1000	7.30E-02	1.00E-03	2.23	3.81	4.43E+02	2.48E-03	2	2
68	Water	1000	7.30E-02	1.00E-03	2.23	3.69	4.16E+02	2.48E-03	2	2
69	Water	1000	7.30E-02	1.00E-03	2.23	3.48	3.70E+02	2.48E-03	2	1
70	Water	1000	7.30E-02	1.00E-03	2.23	2.28	1.59E+02	2.48E-03	1	1
71	Water	1000	7.30E-02	1.00E-03	2.67	4.13	6.24E+02	2.27E-03	2	2
72	Water	1000	7.30E-02	1.00E-03	2.57	2.40	2.03E+02	2.31E-03	1	1
73	Water	1000	7.30E-02	1.00E-03	2.53	3.33	3.84E+02	2.33E-03	2	1
74	Water	1000	7.30E-02	1.00E-03	2.53	4.57	7.24E+02	2.33E-03	2	2
75	Water	1000	7.30E-02	1.00E-03	2.47	3.72	4.68E+02	2.35E-03	2	2
76	Water	1000	7.30E-02	1.00E-03	2.44	4.61	7.10E+02	2.37E-03	2	2
77	Water	1000	7.30E-02	1.00E-03	2.44	3.63	4.40E+02	2.37E-03	2	2
78	Water	1000	7.30E-02	1.00E-03	2.42	0.55	1.00E+01	2.38E-03	1	1
79	Water	1000	7.30E-02	1.00E-03	2.41	1.65	8.99E+01	2.38E-03	1	1
80	Water	1000	7.30E-02	1.00E-03	2.41	0.63	1.32E+01	2.38E-03	1	1

Table 9.2: Droplet impact conditions from [40] used for verification, alongside recorded experimental and simulated outcomes. Note Outcome= 1 indicates no splash, Outcome= 2 indicates a splash.

Simulation	Fluid	ρ (kg/m ³)	σ (N/m)	μ (Pa·s)	D (m)	v (m/s)	We	Oh	Experimental Outcome	Simulation Outcome
81	Water	1000	7.30E-02	1.00E-03	2.40	3.73	4.57E+02	2.39E-03	2	2
82	Water	1000	7.30E-02	1.00E-03	2.39	4.40	6.34E+02	2.39E-03	2	2
83	Water	1000	7.30E-02	1.00E-03	2.39	4.21	5.80E+02	2.39E-03	2	2
84	Water	1000	7.30E-02	1.00E-03	2.39	3.14	3.23E+02	2.39E-03	2	1
85	Water	1000	7.30E-02	1.00E-03	2.39	2.62	2.25E+02	2.39E-03	2	1
86	Water	1000	7.30E-02	1.00E-03	2.39	0.97	3.08E+01	2.39E-03	1	1
87	Water	1000	7.30E-02	1.00E-03	2.38	2.62	2.24E+02	2.40E-03	2	1
88	Water	1000	7.30E-02	1.00E-03	2.38	2.19	1.56E+02	2.40E-03	1	1
89	Water	1000	7.30E-02	1.00E-03	2.38	1.65	8.88E+01	2.40E-03	1	1
90	Water	1000	7.30E-02	1.00E-03	2.38	0.80	2.09E+01	2.40E-03	1	1
91	Water	1000	7.30E-02	1.00E-03	2.38	0.63	1.29E+01	2.40E-03	1	1
92	Water	1000	7.30E-02	1.00E-03	2.37	3.63	4.28E+02	2.40E-03	2	2
93	Water	1000	7.30E-02	1.00E-03	2.36	4.61	6.87E+02	2.41E-03	2	2
94	Water	1000	7.30E-02	1.00E-03	2.36	3.84	4.77E+02	2.41E-03	2	2
95	Water	1000	7.30E-02	1.00E-03	2.36	2.19	1.55E+02	2.41E-03	1	1
96	Water	1000	7.30E-02	1.00E-03	2.36	0.97	3.04E+01	2.41E-03	1	1

Table 9.2: Droplet impact conditions from [40] used for verification, alongside recorded experimental and simulated outcomes. Note Outcome= 1 indicates no splash, Outcome= 2 indicates a splash.

Simulation	Fluid	ρ (kg/m ³)	σ (N/m)	μ (Pa·s)	D (m)	v (m/s)	We	Oh	Experimental Outcome	Simulation Outcome
97	Water	1000	7.30E-02	1.00E-03	2.34	2.24	1.61E+02	2.42E-03	1	1
98	Water	1000	7.30E-02	1.00E-03	2.34	0.61	1.19E+01	2.42E-03	1	1
99	Water	1000	7.30E-02	1.00E-03	2.33	3.08	3.03E+02	2.42E-03	2	1
100	Water	1000	7.30E-02	1.00E-03	2.33	3.04	2.95E+02	2.42E-03	2	1
101	Water	1000	7.30E-02	1.00E-03	2.33	2.21	1.56E+02	2.42E-03	1	1
102	Water	1000	7.30E-02	1.00E-03	2.33	0.61	1.19E+01	2.42E-03	1	1
103	Water	1000	7.30E-02	1.00E-03	2.33	0.57	1.04E+01	2.42E-03	1	1
104	Water	1000	7.30E-02	1.00E-03	2.30	0.55	9.53E+00	2.44E-03	1	1
105	Water	1000	7.30E-02	1.00E-03	2.26	4.21	5.49E+02	2.46E-03	2	2
106	Water	1000	7.30E-02	1.00E-03	2.26	3.44	3.66E+02	2.46E-03	1	1
107	Water	1000	7.30E-02	1.00E-03	2.26	2.89	2.59E+02	2.46E-03	1	1
108	Water	1000	7.30E-02	1.00E-03	2.26	2.41	1.80E+02	2.46E-03	1	1
109	Water	1000	7.30E-02	1.00E-03	2.26	2.31	1.65E+02	2.46E-03	1	1
110	Water	1000	7.30E-02	1.00E-03	2.26	2.21	1.51E+02	2.46E-03	1	1
111	Water	1000	7.30E-02	1.00E-03	2.25	4.02	4.98E+02	2.47E-03	2	2
112	Water	1000	7.30E-02	1.00E-03	2.13	3.64	3.87E+02	2.54E-03	1	1

Table 9.2: Droplet impact conditions from [40] used for verification, alongside recorded experimental and simulated outcomes. Note Outcome= 1 indicates no splash, Outcome= 2 indicates a splash.

Simulation	Fluid	ρ (kg/m ³)	σ (N/m)	μ (Pa·s)	D (m)	v (m/s)	We	Oh	Experimental Outcome	Simulation Outcome
113	Water	1000	7.30E-02	1.00E-03	2.13	3.59	3.76E+02	2.54E-03	1	1
114	Water	1000	7.30E-02	1.00E-03	2.13	3.43	3.43E+02	2.54E-03	2	1
115	Water	1000	7.30E-02	1.00E-03	2.13	2.36	1.63E+02	2.54E-03	1	1
116	Water	1000	7.30E-02	1.00E-03	2.57	3.60	4.56E+02	2.31E-03	2	2
117	Water	1000	7.30E-02	1.00E-03	2.57	3.47	4.24E+02	2.31E-03	2	2
118	Water	1000	7.30E-02	1.00E-03	2.53	2.40	2.00E+02	2.33E-03	1	1
119	Water	1000	7.30E-02	1.00E-03	2.47	3.20	3.46E+02	2.35E-03	2	2
120	Water	1000	7.30E-02	1.00E-03	2.40	4.00	5.26E+02	2.39E-03	2	2
121	Water	1000	7.30E-02	1.00E-03	2.53	2.53	2.22E+02	2.33E-03	2	1
122	Water	1000	7.30E-02	1.00E-03	2.40	3.87	4.92E+02	2.39E-03	2	2
123	Water	1000	7.30E-02	1.00E-03	2.47	3.73	4.71E+02	2.35E-03	2	2
124	Water	1000	7.30E-02	1.00E-03	2.40	3.60	4.26E+02	2.39E-03	2	2
125	Glycerol	1260	6.34E-02	1.41E+00	1.48	2.38	1.67E+02	4.11E+00	1	1
126	Glycerol	1260	6.34E-02	1.41E+00	1.80	2.93	3.07E+02	3.72E+00	1	1
127	Glycerol	1260	6.34E-02	1.41E+00	1.40	2.61	1.90E+02	4.22E+00	1	1
128	Glycerol	1260	6.34E-02	1.41E+00	1.85	2.32	1.98E+02	3.67E+00	1	1

Table 9.2: Droplet impact conditions from [40] used for verification, alongside recorded experimental and simulated outcomes. Note Outcome= 1 indicates no splash, Outcome= 2 indicates a splash.

Simulation	Fluid	ρ (kg/m ³)	σ (N/m)	μ (Pa·s)	D (m)	v (m/s)	We	Oh	Experimental Outcome	Simulation Outcome
129	Glycerol	1260	6.34E-02	1.41E+00	1.48	3.57	3.75E+02	4.11E+00	1	1
130	Glycerol	1260	6.34E-02	1.41E+00	1.28	3.29	2.75E+02	4.42E+00	1	1
131	Isopropanol	786	2.30E-02	1.96E-03	1.69	2.21	2.83E+02	1.12E-02	1	1
132	Isopropanol	786	2.30E-02	1.96E-03	1.72	2.33	3.18E+02	1.11E-02	2	1
133	Isopropanol	786	2.30E-02	1.96E-03	1.69	2.33	3.13E+02	1.12E-02	2	2
134	Isopropanol	786	2.30E-02	1.96E-03	1.69	2.34	3.16E+02	1.12E-02	2	1
135	Isopropanol	786	2.30E-02	1.96E-03	1.67	2.48	3.49E+02	1.13E-02	2	2
136	Isopropanol	786	2.30E-02	1.96E-03	1.67	2.06	2.42E+02	1.13E-02	1	1
137	Isopropanol	786	2.30E-02	1.96E-03	1.67	2.02	2.34E+02	1.13E-02	2	1
138	Isopropanol	786	2.30E-02	1.96E-03	1.65	2.23	2.80E+02	1.13E-02	2	2
139	Isopropanol	786	2.30E-02	1.96E-03	1.67	1.46	1.22E+02	1.13E-02	1	1
140	Isopropanol	786	2.30E-02	1.96E-03	1.67	1.84	1.92E+02	1.13E-02	1	1
141	Isopropanol	786	2.30E-02	1.96E-03	1.67	2.33	3.08E+02	1.13E-02	2	2
142	Isopropanol	786	2.30E-02	1.96E-03	1.69	2.59	3.87E+02	1.12E-02	2	2
143	Isopropanol	786	2.30E-02	1.96E-03	1.69	1.39	1.11E+02	1.12E-02	1	1
144	Isopropanol	786	2.30E-02	1.96E-03	1.75	2.25	3.03E+02	1.10E-02	2	2

Table 9.2: Droplet impact conditions from [40] used for verification, alongside recorded experimental and simulated outcomes. Note Outcome= 1 indicates no splash, Outcome= 2 indicates a splash.

Simulation	Fluid	ρ (kg/m ³)	σ (N/m)	μ (Pa·s)	D (m)	v (m/s)	We	Oh	Experimental Outcome	Simulation Outcome
145	Isopropanol	786	2.30E-02	1.96E-03	1.75	2.33	3.23E+02	1.10E-02	2	2
146	Isopropanol	786	2.30E-02	1.96E-03	1.79	4.27	1.12E+03	1.09E-02	2	2

Table 9.3: Droplet impact conditions from the scaled simulations. Note Outcome= 1 indicates no splash, Outcome= 2 indicates a splash.

Simulation	D (m)	σ (N/m)	μ (Pa·s)	v (m/s)	θ_I (°)	ρ (kg/m ³)	We	Re	Oh	Splash Outcome (1 or 2)
1	0.0024	0.0073	0.001	1	20	100	32.88	240.00	0.02	1
2	0.0024	0.0073	0.001	10	20	100	3287.67	2400.00	0.02	1
3	0.0024	0.0073	0.001	20	20	100	13150.68	4800.00	0.02	2
4	0.0024	0.0073	0.001	100	20	100	328767.12	24000.00	0.02	2
5	0.0024	0.0073	0.001	150	20	100	739726.03	36000.00	0.02	2
6	0.0024	0.0073	0.01	1	20	100	32.88	24.00	0.24	1
7	0.0024	0.0073	0.01	10	20	100	3287.67	240.00	0.24	1
8	0.0024	0.0073	0.01	20	20	100	13150.68	480.00	0.24	1
9	0.0024	0.0073	0.01	100	20	100	328767.12	2400.00	0.24	2
10	0.0024	0.0073	0.01	150	20	100	739726.03	3600.00	0.24	2
11	0.0024	0.0073	0.1	1	20	100	32.88	2.40	2.39	1
12	0.0024	0.0073	0.1	10	20	100	3287.67	24.00	2.39	1
13	0.0024	0.0073	0.1	20	20	100	13150.68	48.00	2.39	1
14	0.0024	0.0073	0.1	100	20	100	328767.12	240.00	2.39	1
15	0.0024	0.0073	0.1	150	20	100	739726.03	360.00	2.39	1
16	0.0024	0.0073	1	1	20	100	32.88	0.24	23.89	1
17	0.0024	0.0073	1	10	20	100	3287.67	2.40	23.89	1

Table 9.3: Droplet impact conditions from the scaled simulations. Note Outcome= 1 indicates no splash, Outcome= 2 indicates a splash.

Simulation	D (m)	σ (N/m)	μ (Pa·s)	v (m/s)	θ_I (°)	ρ (kg/m ³)	We	Re	Oh	Splash Outcome (1 or 2)
18	0.0024	0.0073	1	20	20	100	13150.68	4.80	23.89	1
19	0.0024	0.0073	1	100	20	100	328767.12	24.00	23.89	1
20	0.0024	0.0073	1	150	20	100	739726.03	36.00	23.89	1
21	0.0024	0.0073	10	1	20	100	32.88	0.02	238.91	1
22	0.0024	0.0073	10	10	20	100	3287.67	0.24	238.91	1
23	0.0024	0.0073	10	20	20	100	13150.68	0.48	238.91	1
24	0.0024	0.0073	10	100	20	100	328767.12	2.40	238.91	1
25	0.0024	0.0073	10	150	20	100	739726.03	3.60	238.91	1
26	0.0024	0.0073	0.001	1	40	100	32.88	240.00	0.02	1
27	0.0024	0.0073	0.001	10	40	100	3287.67	2400.00	0.02	2
28	0.0024	0.0073	0.001	20	40	100	13150.68	4800.00	0.02	2
29	0.0024	0.0073	0.001	100	40	100	328767.12	24000.00	0.02	2
30	0.0024	0.0073	0.001	150	40	100	739726.03	36000.00	0.02	2
31	0.0024	0.0073	0.01	1	40	100	32.88	24.00	0.24	1
32	0.0024	0.0073	0.01	10	40	100	3287.67	240.00	0.24	1
33	0.0024	0.0073	0.01	20	40	100	13150.68	480.00	0.24	1
34	0.0024	0.0073	0.01	100	40	100	328767.12	2400.00	0.24	1

Table 9.3: Droplet impact conditions from the scaled simulations. Note Outcome= 1 indicates no splash, Outcome= 2 indicates a splash.

Simulation	D (m)	σ (N/m)	μ (Pa·s)	v (m/s)	θ_I (°)	ρ (kg/m ³)	We	Re	Oh	Splash Outcome (1 or 2)
35	0.0024	0.0073	0.01	150	40	100	739726.03	3600.00	0.24	2
36	0.0024	0.0073	0.1	1	40	100	32.88	2.40	2.39	1
37	0.0024	0.0073	0.1	10	40	100	3287.67	24.00	2.39	1
38	0.0024	0.0073	0.1	20	40	100	13150.68	48.00	2.39	1
39	0.0024	0.0073	0.1	100	40	100	328767.12	240.00	2.39	1
40	0.0024	0.0073	0.1	150	40	100	739726.03	360.00	2.39	1
41	0.0024	0.0073	1	1	40	100	32.88	0.24	23.89	1
42	0.0024	0.0073	1	10	40	100	3287.67	2.40	23.89	1
43	0.0024	0.0073	1	20	40	100	13150.68	4.80	23.89	1
44	0.0024	0.0073	1	100	40	100	328767.12	24.00	23.89	1
45	0.0024	0.0073	1	150	40	100	739726.03	36.00	23.89	1
46	0.0024	0.0073	10	1	40	100	32.88	0.02	238.91	1
47	0.0024	0.0073	10	10	40	100	3287.67	0.24	238.91	1
48	0.0024	0.0073	10	20	40	100	13150.68	0.48	238.91	1
49	0.0024	0.0073	10	100	40	100	328767.12	2.40	238.91	1
50	0.0024	0.0073	10	150	40	100	739726.03	3.60	238.91	1
51	0.0024	0.0073	0.001	1	60	100	32.88	240.00	0.02	1

Table 9.3: Droplet impact conditions from the scaled simulations. Note Outcome= 1 indicates no splash, Outcome= 2 indicates a splash.

Simulation	D (m)	σ (N/m)	μ (Pa·s)	v (m/s)	θ_I (°)	ρ (kg/m ³)	We	Re	Oh	Splash Outcome (1 or 2)
52	0.0024	0.0073	0.001	10	60	100	3287.67	2400.00	0.02	2
53	0.0024	0.0073	0.001	20	60	100	13150.68	4800.00	0.02	2
54	0.0024	0.0073	0.001	100	60	100	328767.12	24000.00	0.02	2
55	0.0024	0.0073	0.001	150	60	100	739726.03	36000.00	0.02	2
56	0.0024	0.0073	0.01	1	60	100	32.88	24.00	0.24	1
57	0.0024	0.0073	0.01	10	60	100	3287.67	240.00	0.24	1
58	0.0024	0.0073	0.01	20	60	100	13150.68	480.00	0.24	1
59	0.0024	0.0073	0.01	100	60	100	328767.12	2400.00	0.24	1
60	0.0024	0.0073	0.01	150	60	100	739726.03	3600.00	0.24	2
61	0.0024	0.0073	0.1	1	60	100	32.88	2.40	2.39	1
62	0.0024	0.0073	0.1	10	60	100	3287.67	24.00	2.39	1
63	0.0024	0.0073	0.1	20	60	100	13150.68	48.00	2.39	1
64	0.0024	0.0073	0.1	100	60	100	328767.12	240.00	2.39	1
65	0.0024	0.0073	0.1	150	60	100	739726.03	360.00	2.39	1
66	0.0024	0.0073	1	1	60	100	32.88	0.24	23.89	1
67	0.0024	0.0073	1	10	60	100	3287.67	2.40	23.89	1
68	0.0024	0.0073	1	20	60	100	13150.68	4.80	23.89	1

Table 9.3: Droplet impact conditions from the scaled simulations. Note Outcome= 1 indicates no splash, Outcome= 2 indicates a splash.

Simulation	D (m)	σ (N/m)	μ (Pa·s)	v (m/s)	θ_I (°)	ρ (kg/m ³)	We	Re	Oh	Splash Outcome (1 or 2)
69	0.0024	0.0073	1	100	60	100	328767.12	24.00	23.89	1
70	0.0024	0.0073	1	150	60	100	739726.03	36.00	23.89	1
71	0.0024	0.0073	10	1	60	100	32.88	0.02	238.91	1
72	0.0024	0.0073	10	10	60	100	3287.67	0.24	238.91	1
73	0.0024	0.0073	10	20	60	100	13150.68	0.48	238.91	1
74	0.0024	0.0073	10	100	60	100	328767.12	2.40	238.91	1
75	0.0024	0.0073	10	150	60	100	739726.03	3.60	238.91	1
76	0.0024	0.0073	0.001	1	80	100	32.88	240.00	0.02	1
77	0.0024	0.0073	0.001	10	80	100	3287.67	2400.00	0.02	2
78	0.0024	0.0073	0.001	20	80	100	13150.68	4800.00	0.02	2
79	0.0024	0.0073	0.001	100	80	100	328767.12	24000.00	0.02	2
80	0.0024	0.0073	0.001	150	80	100	739726.03	36000.00	0.02	2
81	0.0024	0.0073	0.01	1	80	100	32.88	24.00	0.24	1
82	0.0024	0.0073	0.01	10	80	100	3287.67	240.00	0.24	1
83	0.0024	0.0073	0.01	20	80	100	13150.68	480.00	0.24	1
84	0.0024	0.0073	0.01	100	80	100	328767.12	2400.00	0.24	1
85	0.0024	0.0073	0.01	150	80	100	739726.03	3600.00	0.24	2

Table 9.3: Droplet impact conditions from the scaled simulations. Note Outcome= 1 indicates no splash, Outcome= 2 indicates a splash.

Simulation	D (m)	σ (N/m)	μ (Pa·s)	v (m/s)	θ_I (°)	ρ (kg/m ³)	We	Re	Oh	Splash Outcome (1 or 2)
86	0.0024	0.0073	0.1	1	80	100	32.88	2.40	2.39	1
87	0.0024	0.0073	0.1	10	80	100	3287.67	24.00	2.39	1
88	0.0024	0.0073	0.1	20	80	100	13150.68	48.00	2.39	1
89	0.0024	0.0073	0.1	100	80	100	328767.12	240.00	2.39	1
90	0.0024	0.0073	0.1	150	80	100	739726.03	360.00	2.39	1
91	0.0024	0.0073	1	1	80	100	32.88	0.24	23.89	1
92	0.0024	0.0073	1	10	80	100	3287.67	2.40	23.89	1
93	0.0024	0.0073	1	20	80	100	13150.68	4.80	23.89	1
94	0.0024	0.0073	1	100	80	100	328767.12	24.00	23.89	1
95	0.0024	0.0073	1	150	80	100	739726.03	36.00	23.89	1
96	0.0024	0.0073	10	1	80	100	32.88	0.02	238.91	1
97	0.0024	0.0073	10	10	80	100	3287.67	0.24	238.91	1
98	0.0024	0.0073	10	20	80	100	13150.68	0.48	238.91	1
99	0.0024	0.0073	10	100	80	100	328767.12	2.40	238.91	1
100	0.0024	0.0073	10	150	80	100	739726.03	3.60	238.91	1
101	0.0024	0.0073	0.001	1	30	100	32.88	240.00	0.02	1
102	0.0024	0.0073	0.001	10	30	100	3287.67	2400.00	0.02	1

Table 9.3: Droplet impact conditions from the scaled simulations. Note Outcome= 1 indicates no splash, Outcome= 2 indicates a splash.

Simulation	D (m)	σ (N/m)	μ (Pa·s)	v (m/s)	θ_I (°)	ρ (kg/m ³)	We	Re	Oh	Splash Outcome (1 or 2)
103	0.0024	0.0073	0.001	20	30	100	13150.68	4800.00	0.02	2
104	0.0024	0.0073	0.001	100	30	100	328767.12	24000.00	0.02	2
105	0.0024	0.0073	0.001	150	30	100	739726.03	36000.00	0.02	2
106	0.0024	0.0073	0.01	1	30	100	32.88	24.00	0.24	1
107	0.0024	0.0073	0.01	10	30	100	3287.67	240.00	0.24	1
108	0.0024	0.0073	0.01	20	30	100	13150.68	480.00	0.24	1
109	0.0024	0.0073	0.01	100	30	100	328767.12	2400.00	0.24	2
110	0.0024	0.0073	0.01	150	30	100	739726.03	3600.00	0.24	2
111	0.0024	0.0073	0.1	100	30	100	328767.12	240.00	2.39	1
112	0.0024	0.0073	0.1	150	30	100	739726.03	360.00	2.39	1
113	0.0024	0.0073	1	100	30	100	328767.12	24.00	23.89	1
114	0.0024	0.0073	1	150	30	100	739726.03	36.00	23.89	1
115	0.0024	0.0073	10	100	30	100	328767.12	2.40	238.91	1
116	0.0024	0.0073	10	150	30	100	739726.03	3.60	238.91	1
117	0.0024	0.0073	0.001	1	50	100	32.88	240.00	0.02	1
118	0.0024	0.0073	0.001	10	50	100	3287.67	2400.00	0.02	2
119	0.0024	0.0073	0.001	20	50	100	13150.68	4800.00	0.02	2

Table 9.3: Droplet impact conditions from the scaled simulations. Note Outcome= 1 indicates no splash, Outcome= 2 indicates a splash.

Simulation	D (m)	σ (N/m)	μ (Pa·s)	v (m/s)	θ_I (°)	ρ (kg/m ³)	We	Re	Oh	Splash Outcome (1 or 2)
120	0.0024	0.0073	0.001	100	50	100	328767.12	24000.00	0.02	2
121	0.0024	0.0073	0.001	150	50	100	739726.03	36000.00	0.02	2
122	0.0024	0.0073	0.01	1	50	100	32.88	24.00	0.24	1
123	0.0024	0.0073	0.01	10	50	100	3287.67	240.00	0.24	1
124	0.0024	0.0073	0.01	20	50	100	13150.68	480.00	0.24	1
125	0.0024	0.0073	0.01	100	50	100	328767.12	2400.00	0.24	2
126	0.0024	0.0073	0.01	150	50	100	739726.03	3600.00	0.24	2
127	0.0024	0.0073	0.1	100	50	100	328767.12	240.00	2.39	1
128	0.0024	0.0073	0.1	150	50	100	739726.03	360.00	2.39	1
129	0.0024	0.0073	1	100	50	100	328767.12	24.00	23.89	1
130	0.0024	0.0073	1	150	50	100	739726.03	36.00	23.89	1
131	0.0024	0.0073	10	100	50	100	328767.12	2.40	238.91	1
132	0.0024	0.0073	10	150	50	100	739726.03	3.60	238.91	1
133	0.0024	0.0073	0.001	1	70	100	32.88	240.00	0.02	1
134	0.0024	0.0073	0.001	10	70	100	3287.67	2400.00	0.02	2
135	0.0024	0.0073	0.001	20	70	100	13150.68	4800.00	0.02	2
136	0.0024	0.0073	0.001	100	70	100	328767.12	24000.00	0.02	2

Table 9.3: Droplet impact conditions from the scaled simulations. Note Outcome= 1 indicates no splash, Outcome= 2 indicates a splash.

Simulation	D (m)	σ (N/m)	μ (Pa·s)	v (m/s)	θ_I (°)	ρ (kg/m ³)	We	Re	Oh	Splash Outcome (1 or 2)
137	0.0024	0.0073	0.001	150	70	100	739726.03	36000.00	0.02	2
138	0.0024	0.0073	0.01	1	70	100	32.88	24.00	0.24	1
139	0.0024	0.0073	0.01	10	70	100	3287.67	240.00	0.24	1
140	0.0024	0.0073	0.01	20	70	100	13150.68	480.00	0.24	1
141	0.0024	0.0073	0.01	100	70	100	328767.12	2400.00	0.24	1
142	0.0024	0.0073	0.01	150	70	100	739726.03	3600.00	0.24	2
143	0.0024	0.0073	0.1	100	70	100	328767.12	240.00	2.39	1
144	0.0024	0.0073	0.1	150	70	100	739726.03	360.00	2.39	1
145	0.0024	0.0073	1	100	70	100	328767.12	24.00	23.89	1
146	0.0024	0.0073	1	150	70	100	739726.03	36.00	23.89	1
147	0.0024	0.0073	10	100	70	100	328767.12	2.40	238.91	1
148	0.0024	0.0073	10	150	70	100	739726.03	3.60	238.91	1
149	0.0024	0.0073	0.001	1	90	100	32.88	240.00	0.02	1
150	0.0024	0.0073	0.001	10	90	100	3287.67	2400.00	0.02	2
151	0.0024	0.0073	0.001	20	90	100	13150.68	4800.00	0.02	2
152	0.0024	0.0073	0.001	100	90	100	328767.12	24000.00	0.02	2
153	0.0024	0.0073	0.001	150	90	100	739726.03	36000.00	0.02	2

Table 9.3: Droplet impact conditions from the scaled simulations. Note Outcome= 1 indicates no splash, Outcome= 2 indicates a splash.

Simulation	D (m)	σ (N/m)	μ (Pa·s)	v (m/s)	θ_I (°)	ρ (kg/m ³)	We	Re	Oh	Splash Outcome (1 or 2)
154	0.0024	0.0073	0.01	1	90	100	32.88	24.00	0.24	1
155	0.0024	0.0073	0.01	10	90	100	3287.67	240.00	0.24	1
156	0.0024	0.0073	0.01	20	90	100	13150.68	480.00	0.24	1
157	0.0024	0.0073	0.01	100	90	100	328767.12	2400.00	0.24	1
158	0.0024	0.0073	0.01	150	90	100	739726.03	3600.00	0.24	2
159	0.0024	0.0073	0.1	100	90	100	328767.12	240.00	2.39	1
160	0.0024	0.0073	0.1	150	90	100	739726.03	360.00	2.39	1
161	0.0024	0.0073	1	100	90	100	328767.12	24.00	23.89	1
162	0.0024	0.0073	1	150	90	100	739726.03	36.00	23.89	1
163	0.0024	0.0073	10	100	90	100	328767.12	2.40	238.91	1
164	0.0024	0.0073	10	150	90	100	739726.03	3.60	238.91	1
165	0.0024	0.0073	0.1	300	50	100	2958904.11	720.00	2.39	2
166	0.0024	0.0073	0.1	400	50	100	5260273.97	960.00	2.39	2
167	0.0024	0.0073	0.1	500	50	100	8219178.08	1200.00	2.39	2
168	0.0024	0.0073	1	300	50	100	2958904.11	72.00	23.89	1
169	0.0024	0.0073	1	400	50	100	5260273.97	96.00	23.89	1
170	0.0024	0.0073	1	500	50	100	8219178.08	120.00	23.89	1

Table 9.3: Droplet impact conditions from the scaled simulations. Note Outcome= 1 indicates no splash, Outcome= 2 indicates a splash.

Simulation	D (m)	σ (N/m)	μ (Pa·s)	v (m/s)	θ_I (°)	ρ (kg/m ³)	We	Re	Oh	Splash Outcome (1 or 2)
171	0.0024	0.0073	10	300	50	100	2958904.11	7.20	238.91	1
172	0.0024	0.0073	10	400	50	100	5260273.97	9.60	238.91	1
173	0.0024	0.0073	10	500	50	100	8219178.08	12.00	238.91	1
174	0.0024	0.0073	0.1	300	30	100	2958904.11	720.00	2.39	1
175	0.0024	0.0073	0.1	400	30	100	5260273.97	960.00	2.39	1
176	0.0024	0.0073	0.1	500	30	100	8219178.08	1200.00	2.39	2
177	0.0024	0.0073	1	300	30	100	2958904.11	72.00	23.89	1
178	0.0024	0.0073	1	400	30	100	5260273.97	96.00	23.89	1
179	0.0024	0.0073	1	500	30	100	8219178.08	120.00	23.89	1
180	0.0024	0.0073	10	300	30	100	2958904.11	7.20	238.91	1
181	0.0024	0.0073	10	400	30	100	5260273.97	9.60	238.91	1
182	0.0024	0.0073	10	500	30	100	8219178.08	12.00	238.91	1
183	0.0024	0.0073	0.1	300	20	100	2958904.11	720.00	2.39	1
184	0.0024	0.0073	0.1	400	20	100	5260273.97	960.00	2.39	1
185	0.0024	0.0073	0.1	500	20	100	8219178.08	1200.00	2.39	1
186	0.0024	0.0073	1	300	20	100	2958904.11	72.00	23.89	1
187	0.0024	0.0073	1	400	20	100	5260273.97	96.00	23.89	1

Table 9.3: Droplet impact conditions from the scaled simulations. Note Outcome= 1 indicates no splash, Outcome= 2 indicates a splash.

Simulation	D (m)	σ (N/m)	μ (Pa·s)	v (m/s)	θ_I (°)	ρ (kg/m ³)	We	Re	Oh	Splash Outcome (1 or 2)
188	0.0024	0.0073	1	500	20	100	8219178.08	120.00	23.89	1
189	0.0024	0.0073	10	300	20	100	2958904.11	7.20	238.91	1
190	0.0024	0.0073	10	400	20	100	5260273.97	9.60	238.91	1
191	0.0024	0.0073	10	500	20	100	8219178.08	12.00	238.91	1
192	0.0024	0.0073	0.001	1	10	100	32.88	240.00	0.02	1
193	0.0024	0.0073	0.001	10	10	100	3287.67	2400.00	0.02	2
194	0.0024	0.0073	0.001	20	10	100	13150.68	4800.00	0.02	2
195	0.0024	0.0073	0.001	100	10	100	328767.12	24000.00	0.02	2
196	0.0024	0.0073	0.001	150	10	100	739726.03	36000.00	0.02	2
197	0.0024	0.0073	0.01	1	10	100	32.88	24.00	0.24	1
198	0.0024	0.0073	0.01	10	10	100	3287.67	240.00	0.24	1
199	0.0024	0.0073	0.01	20	10	100	13150.68	480.00	0.24	1
200	0.0024	0.0073	0.01	100	10	100	328767.12	2400.00	0.24	1
201	0.0024	0.0073	0.01	150	10	100	739726.03	3600.00	0.24	2
202	0.0024	0.0073	0.1	100	10	100	328767.12	240.00	2.39	1
203	0.0024	0.0073	0.1	150	10	100	739726.03	360.00	2.39	1
204	0.0024	0.0073	1	100	10	100	328767.12	24.00	23.89	1

Table 9.3: Droplet impact conditions from the scaled simulations. Note Outcome= 1 indicates no splash, Outcome= 2 indicates a splash.

Simulation	D (m)	σ (N/m)	μ (Pa·s)	v (m/s)	θ_I (°)	ρ (kg/m ³)	We	Re	Oh	Splash Outcome (1 or 2)
205	0.0024	0.0073	1	150	10	100	739726.03	36.00	23.89	1
206	0.0024	0.0073	10	100	10	100	328767.12	2.40	238.91	1
207	0.0024	0.0073	10	150	10	100	739726.03	3.60	238.91	1

9.5 Chapter 6

Table 9.4: Average Particle velocities that impacted the Nimonic 75 metal targets.

Average Velocity (ms^{-1})	Standard error (ms^{-1})
2.0	± 0.1
2.6	± 0.1
4.2	± 0.1
4.5	± 0.1
5.0	± 0.1
5.5	± 0.1
7.6	± 0.1
7.9	± 0.1
8.1	± 0.1
15.0	± 0.2

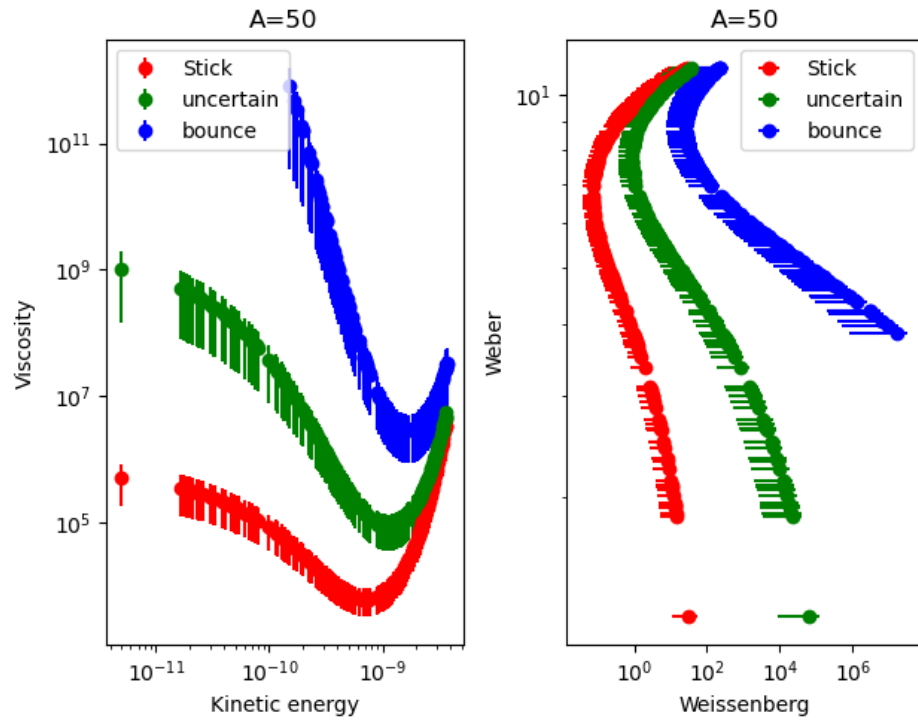


Figure 9.1: A reproduction of the results of tests for glass particle impacts at an impact angle of 50° , showing the three different outcomes: firm deposition, no deposition, and light deposition (which blew off). Error bars for the individual data points are included.

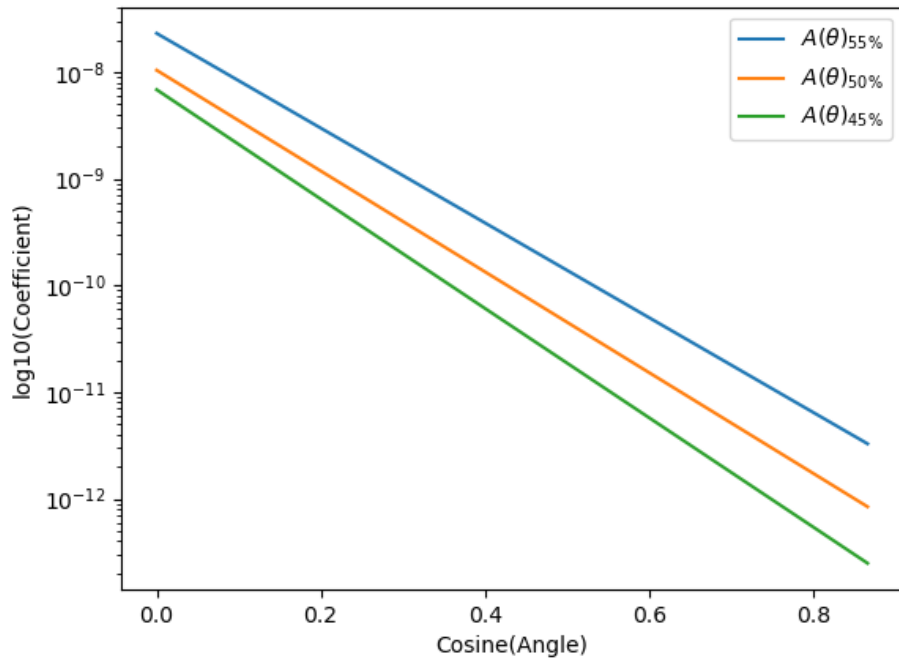


Figure 9.2: A reproduction of Fig[6.16] alongside the expressions for $A(\theta)_{45\%}$ and $A(\theta)_{55\%}$.

9.6 Chapter 7

9.6.1 Basalt

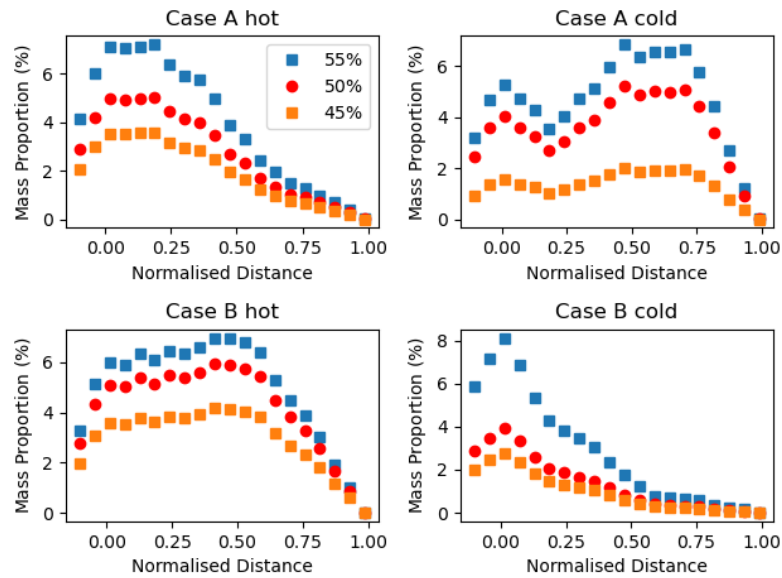


Figure 9.3: Reproduction of Fig[7.21] illustrating the results for the percentage of mass adhered to the NGV surface, segmented into 20 equally sized sections, for Basaltic ash and a temperature amplitude of 150 K, where the critical viscosity was calculated using the expressions for $A(\theta)$ in Eqn[6.22] and Eqn[6.23], alongside the original expression for the critical viscosity in Eqn[6.21].

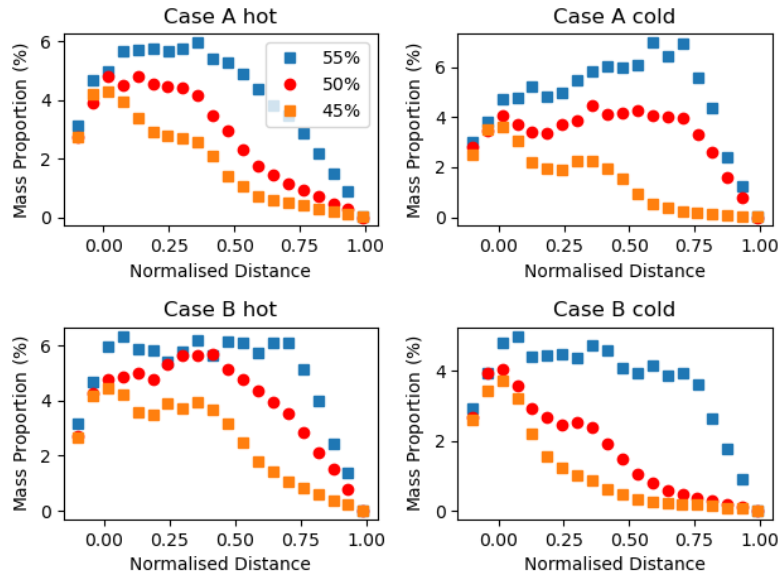


Figure 9.4: Reproduction of Fig[7.22] illustrating the results for the percentage of mass adhered to the NGV surface, segmented into 20 equally sized sections, for Basaltic ash and a temperature amplitude of 100 K, where the critical viscosity was calculated using the expressions for $A(\theta)$ in Eqn[6.22] and Eqn[6.23], alongside the original expression for the critical viscosity in Eqn[6.21].

9.6.2 Andesite

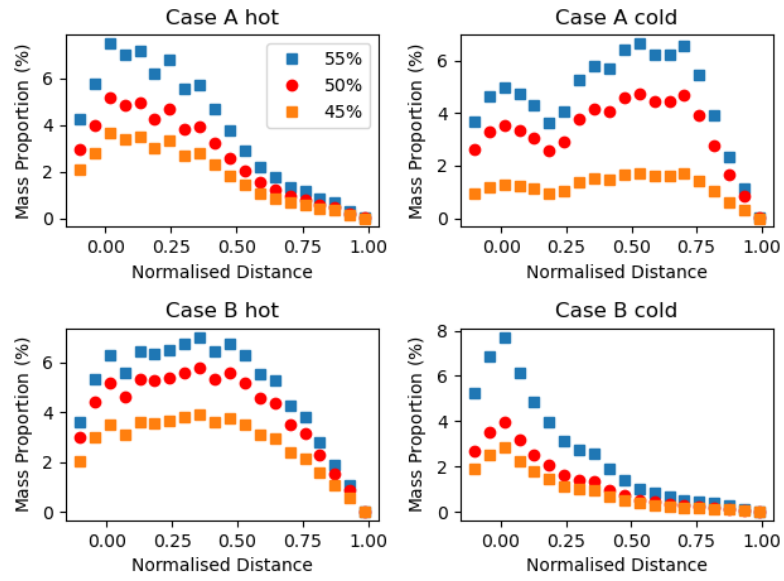


Figure 9.5: Reproduction of Fig[7.23] illustrating the results for the percentage of mass adhered to the NGV surface, segmented into 20 equally sized sections, for Andesitic ash and a temperature amplitude of 150 K, where the critical viscosity was calculated using the expressions for $A(\theta)$ in Eqn[6.22] and Eqn[6.23], alongside the original expression for the critical viscosity in Eqn[6.21].

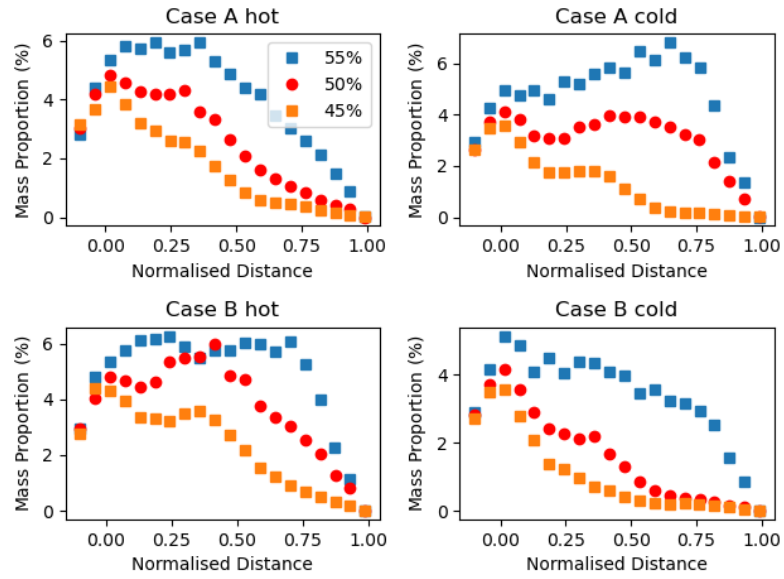


Figure 9.6: Reproduction of Fig[7.24] illustrating the results for the percentage of mass adhered to the NGV surface, segmented into 20 equally sized sections, for Andesitic ash and a temperature amplitude of 100 K, where the critical viscosity was calculated using the expressions for $A(\theta)$ in Eqn[6.22] and Eqn[6.23], alongside the original expression for the critical viscosity in Eqn[6.21].

9.6.3 Dacite

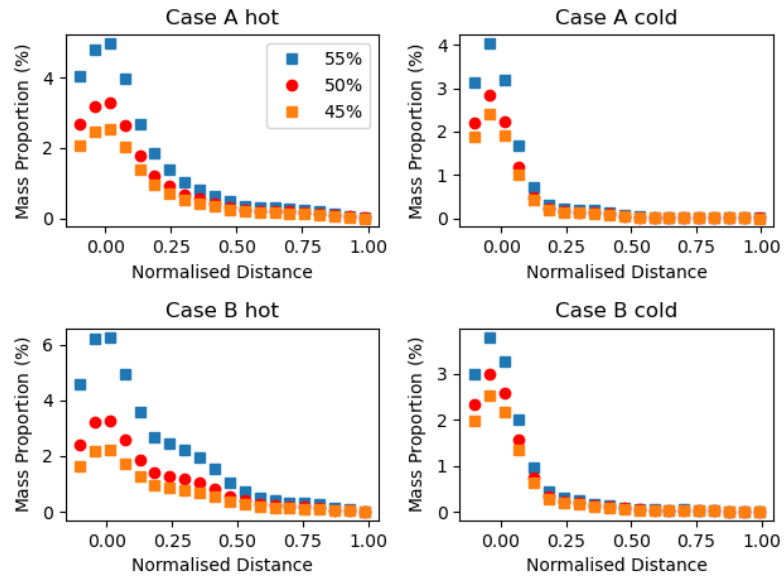


Figure 9.7: Reproduction of Fig[7.25] illustrating the results for the percentage of mass adhered to the NGV surface, segmented into 20 equally sized sections, for Dacitic ash and a temperature amplitude of 150 K, where the critical viscosity was calculated using the expressions for $A(\theta)$ in Eqn[6.22] and Eqn[6.23], alongside the original expression for the critical viscosity in Eqn[6.21].

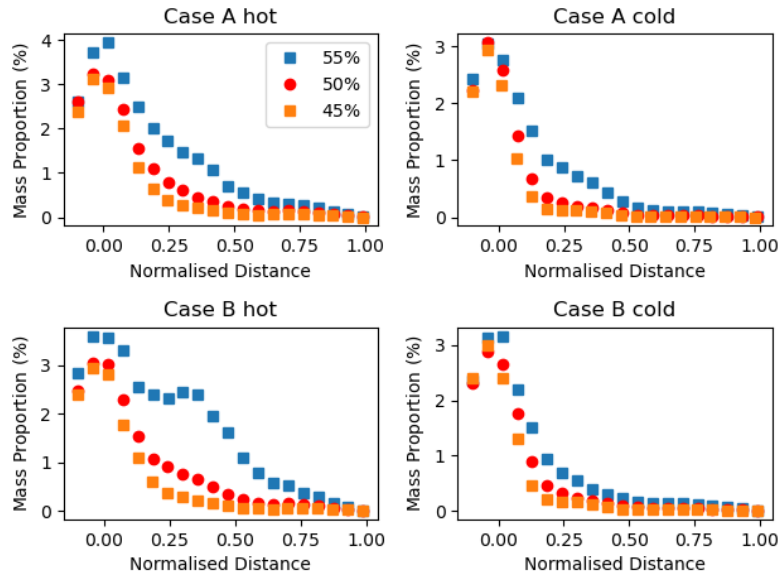


Figure 9.8: Reproduction of Fig[7.26] illustrating the results for the percentage of mass adhered to the NGV surface, segmented into 20 equally sized sections, for Dacitic ash and a temperature amplitude of 100 K, where the critical viscosity was calculated using the expressions for $A(\theta)$ in Eqn[6.22] and Eqn[6.23], alongside the original expression for the critical viscosity in Eqn[6.21].

9.6.4 Rhyolite

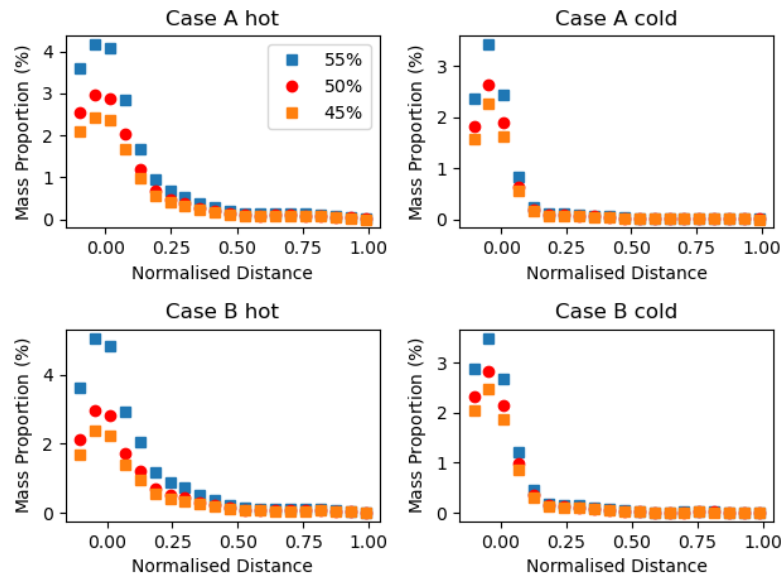


Figure 9.9: Reproduction of Fig[7.27] illustrating the results for the percentage of mass adhered to the NGV surface, segmented into 20 equally sized sections, for Rhyolitic ash and a temperature amplitude of 150 K, where the critical viscosity was calculated using the expressions for $A(\theta)$ in Eqn[6.22] and Eqn[6.23], alongside the original expression for the critical viscosity in Eqn[6.21].

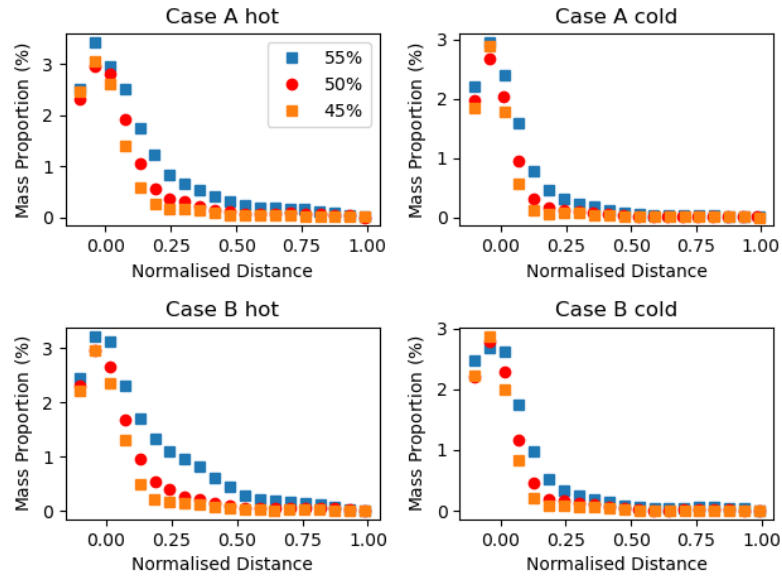


Figure 9.10: Reproduction of Fig[7.28] illustrating the results for the percentage of mass adhered to the NGV surface, segmented into 20 equally sized sections, for Rhyolitic ash and a temperature amplitude of 100 K, where the critical viscosity was calculated using the expressions for $A(\theta)$ in Eqn[6.22] and Eqn[6.23], alongside the original expression for the critical viscosity in Eqn[6.21].

Bibliography

- [1] Marianne Guffanti, Thomas J Casadevall, and Karin E Budding. Encounters of aircraft with volcanic ash clouds: A compilation of known incidents, 1953-2009. US Department of Interior, US Geological Survey, 2010.
- [2] A Gourgaud, G Camus, M-C Gerbe, J-M Morel, A Sudradjat, and PM Vincent. The 1982–83 eruption of galunggung (indonesia): a case study of volcanic hazards with particular relevance to air navigation. In Volcanic Hazards: Assessment and Monitoring, pages 151–162. Springer, 1989.
- [3] Samuel E Swanson and James E Beget. Volcanic ash and aviation safety. In Volcanic Ash and Aviation Safety: Proceedings of the First International Symposium on Volcanic Ash and Aviation Safety, number 2047, page 87. US Government Printing Office, 1994.
- [4] Michael G Dunn and Douglas P Wade. Volcanic ash and aviation safety. In Volcanic Ash and Aviation Safety: Proceedings of the First International Symposium on Volcanic Ash and Aviation Safety, number 2047, page 107. US Government Printing Office, 1994.
- [5] ZJ Przedpelski and TJ Casadevall. Impact of volcanic ash from 15 december 1989 re-doubt volcano eruption on ge cf6-80c2 turbofan engines. In Volcanic ash and aviation safety: Proc. of the First International Symposium on Volcanic Ash and Aviation Safety, pages 129–135, 1994.
- [6] Jet engine design and optimisation. <https://aerospaceengineeringblog.com/jet-engine-design/>. Accessed: 2023-09-14.
- [7] M. Grayburn. British airways boeing 747-236 volcanic cloud encounter on the 24 june 1982—investigation report; technical report spa 60332. Rolls Royce, 1983.

- [8] Helen F Dacre, Alan LM Grant, and BT Johnson. Aircraft observations and model simulations of concentration and particle size distribution in the eyjafjallajökull volcanic ash cloud. Atmospheric Chemistry and Physics, 13(3):1277–1291, 2013.
- [9] Rory J Clarkson, Elizabeth JE Majewicz, and Peter Mack. A re-evaluation of the 2010 quantitative understanding of the effects volcanic ash has on gas turbine engines. Proceedings of the Institution of Mechanical Engineers, Part G: Journal of Aerospace Engineering, 230(12):2274–2291, 2016.
- [10] Rory Clarkson and Harry Simpson. Maximising airspace use during volcanic eruptions: matching engine durability against ash cloud occurrence. In Proceedings of the NATO STO AVT-272 Specialists Meeting on: Impact of Volcanic Ash Clouds on Military Operations, Vilnius, Lithuania, pages 15–17, 2017.
- [11] Catalina Taltavull, James Dean, and Trevor William Clyne. Adhesion of volcanic ash particles under controlled conditions and implications for their deposition in gas turbines. Advanced Engineering Materials, 18(5):803–813, 2016.
- [12] J Dean, C Taltavull, and TW Clyne. Influence of the composition and viscosity of volcanic ashes on their adhesion within gas turbine aeroengines. Acta Materialia, 109:8–16, 2016.
- [13] Daniele Giordano and D Dingwell. Viscosity of hydrous etna basalt: implications for plinian-style basaltic eruptions. Bulletin of Volcanology, 65:8–14, 2003.
- [14] Daniele Giordano, James K Russell, and Donald B Dingwell. Viscosity of magmatic liquids: a model. Earth and Planetary Science Letters, 271(1-4):123–134, 2008.
- [15] KU Hess and Donald B Dingwell. Viscosities of hydrous leucogranitic melts: A non-arrhenian model. American Mineralogist: Journal of Earth and Planetary Materials, 81(9-10):1297–1300, 1996.
- [16] Christopher Giehl, Richard A Brooker, Holger Marxer, and Marcus Nowak. An experimental simulation of volcanic ash deposition in gas turbines and implications for jet engine safety. Chemical Geology, 461:160–170, 2017.

- [17] David Pearson and Richard Brooker. The accumulation of molten volcanic ash in jet engines; simulating the role of magma composition, ash particle size and thermal barrier coatings. Journal of Volcanology and Geothermal Research, 389:106707, 2020.
- [18] Wenjia Song, Shanjie Yang, Masahiro Fukumoto, Yan Lavallée, Siddharth Lokachari, Hongbo Guo, Yancheng You, and Donald B Dingwell. Impact interaction of in-flight high-energy molten volcanic ash droplets with jet engines. Acta Materialia, 171:119–131, 2019.
- [19] North Atlantic Treaty Organisation Science Organisation. Vopr engine tear-down observations for nasa vopr partner report. 2011.
- [20] Adel Ghenaiet. Prediction of erosion in an axial turbine with initial position of blade. In Proceedings of the 13th European Turbomachinery Conference, ETC2019-111, Lausanne, Switzerland, pages 8–12, 2019.
- [21] Arthur Mason Worthington and Reginald Sorrè Cole. V. impact with a liquid surface, studied by the aid of instantaneous photography. Philosophical Transactions of the Royal Society of London. Series A, Containing Papers of a Mathematical or Physical Character, (189):137–148, 1897.
- [22] Romain Rioboo, Cameron Tropea, and Marco Marengo. Outcomes from a drop impact on solid surfaces. Atomization and sprays, 11(2), 2001.
- [23] Gianpietro E Cossali, ALDO Coghe, and Marco Marengo. The impact of a single drop on a wetted solid surface. Experiments in fluids, 22(6):463–472, 1997.
- [24] CHR Mundo, M Sommerfeld, and Cameron Tropea. Droplet-wall collisions: experimental studies of the deformation and breakup process. International journal of multiphase flow, 21(2):151–173, 1995.
- [25] C David Stow and Mark G Hadfield. An experimental investigation of fluid flow resulting from the impact of a water drop with an unyielding dry surface. Proceedings of the Royal Society of London. A. Mathematical and Physical Sciences, 373(1755):419–441, 1981.
- [26] Chengxin Bai and AD Gosman. Development of methodology for spray impingement simulation. SAE transactions, pages 550–568, 1995.

- [27] M Gavaises, A Theodorakakos, and G Bergeles. Modeling wall impaction of diesel sprays. International journal of heat and fluid flow, 17(2):130–138, 1996.
- [28] Randy L Vander Wal, Gordon M Berger, and Steven D Mozes. The combined influence of a rough surface and thin fluid film upon the splashing threshold and splash dynamics of a droplet impacting onto them. Experiments in fluids, 40(1):23–32, 2006.
- [29] H Almohammadi and A Amirfazli. Droplet impact: Viscosity and wettability effects on splashing. Journal of colloid and interface science, 553:22–30, 2019.
- [30] Kai Range and François Feuillebois. Influence of surface roughness on liquid drop impact. Journal of colloid and interface science, 203(1):16–30, 1998.
- [31] Lei Xu, Wendy W Zhang, and Sidney R Nagel. Drop splashing on a dry smooth surface. Physical review letters, 94(18):184505, 2005.
- [32] Jiguang Hao, Jie Lu, Liaonan Lee, Zhihu Wu, Gengkai Hu, and JM Floryan. Droplet splashing on an inclined surface. Physical review letters, 122(5):054501, 2019.
- [33] David A Burzynski and Stephan E Bansmer. Role of surrounding gas in the outcome of droplet splashing. Physical Review Fluids, 4(7):073601, 2019.
- [34] Benoit-Paul Emile Clapeyron. Memoir sur la puissance motrice de la chaleur. Journal de l'École royale polytechnique, pages 153–190, 1834.
- [35] Yisen Guo, Yongsheng Lian, and Mark Sussman. Investigation of drop impact on dry and wet surfaces with consideration of surrounding air. Physics of Fluids, 28(7), 2016.
- [36] Haixiang Zhang, Xiwen Zhang, Xian Yi, Yanxia Du, Feng He, Finglei Niu, and Pengfei Hao. How surface roughness promotes or suppresses drop splash. Physics of Fluids, 34(2), 2022.
- [37] Thijs de Goede, Karla de Bruin, Noushine Shahidzadeh, and Daniel Bonn. Droplet splashing on rough surfaces. Physical Review Fluids, 6(4):043604, 2021.
- [38] Sigurdur T Thoroddsen, Kohsei Takehara, and TG Etoh. Micro-splashing by drop impacts. Journal of Fluid Mechanics, 706:560–570, 2012.

- [39] Zi Niu Wu. Modélisation et calcul implicite multidomaine d'écoulements diphasiques gaz-gouttelettes. PhD thesis, Paris 6, 1992.
- [40] Ilya V Roisman, Andreas Lembach, and Cameron Tropea. Drop splashing induced by target roughness and porosity: The size plays no role. Advances in colloid and interface science, 222:615–621, 2015.
- [41] James C Bird, Scott SH Tsai, and Howard A Stone. Inclined to splash: triggering and inhibiting a splash with tangential velocity. New Journal of Physics, 11(6):063017, 2009.
- [42] Kock-Yee Law. Definitions for hydrophilicity, hydrophobicity, and superhydrophobicity: getting the basics right, 2014.
- [43] Andrzej Latka, Arnout MP Boelens, Sidney R Nagel, and Juan J de Pablo. Drop splashing is independent of substrate wetting. Physics of Fluids, 30(2), 2018.
- [44] Damon GK Aboud and Anne-Marie Kietzig. Splashing threshold of oblique droplet impacts on surfaces of various wettability. Langmuir, 31(36):10100–10111, 2015.
- [45] Haixiang Zhang, Xiwen Zhang, Xian Yi, Feng He, Fenglei Niu, and Pengfei Hao. Effect of wettability on droplet impact: Spreading and splashing. Experimental Thermal and Fluid Science, 124:110369, 2021.
- [46] Guichao Wang, Ya Gao, Subhasish Mitra, Yanfeng Li, Shenjie Zhou, and Geoffrey Evans. Instantaneous bond number for a particle detaching from a bubble. International Journal of Mineral Processing, 142:22–29, 2015.
- [47] Jh Bertrand. Sur l'homogénéité dans les formules de physique. Cahiers de recherche de l'Academie de Sciences, 86:916–920, 1878.
- [48] Stefano Schiaffino and Ain A Sonin. Molten droplet deposition and solidification at low weber numbers. Physics of fluids, 9(11):3172–3187, 1997.
- [49] Annette J Dobson and Adrian G Barnett. An introduction to generalized linear models. CRC press, 2018.
- [50] Julián Palacios, Julio Hernández, Pablo Gómez, Claudio Zanzi, and Joaquín López. Experimental study of splashing patterns and the splashing/deposition threshold in

- drop impacts onto dry smooth solid surfaces. Experimental Thermal and Fluid Science, 44:571–582, 2013.
- [51] RM Lark. Controlling the marginal false discovery rate in inferences from a soil dataset with α -investment. European Journal of Soil Science, 68(2):221–234, 2017.
- [52] Dean P Foster and Robert A Stine. α -investing: a procedure for sequential control of expected false discoveries. Journal of the Royal Statistical Society Series B: Statistical Methodology, 70(2):429–444, 2008.
- [53] Lei Yang, Zhonghong Li, Tao Yang, Yicheng Chi, and Peng Zhang. Experimental study on droplet splash and receding breakup on a smooth surface at atmospheric pressure. Langmuir, 37(36):10838–10848, 2021.
- [54] Kuo-Long Pan, Kun-Cheng Tseng, and Ching-Hua Wang. Breakup of a droplet at high velocity impacting a solid surface. Experiments in fluids, 48:143–156, 2010.
- [55] Kayla Iacovino and Christy B Till. Densityx: A program for calculating the densities of magmatic liquids up to 1,627 c and 30 kbar. Volcanica, 2(1):1–10, 2019.
- [56] Jozef KRAXNeR, M Liška, Robert Klement, and M Chromčíková. Surface tension of borosilicate melts with the composition close to the e-glass. Ceramics-silikaty, 53(2):141–143, 2009.
- [57] NM Parikh. Effect of atmosphere on surface tension of glass. Journal of the American Ceramic Society, 41(1):18–22, 1958.
- [58] Thomas J Casadevall. Volcanic ash and aviation safety: proceedings of the first international symposium on volcanic ash and aviation safety. Number 2047. US Government Printing Office, 1994.
- [59] Volcanic ash fall—a ”hard rain” of abrasive particles. <https://pubs.usgs.gov/fs/fs027-00/>. Accessed: 2023-06-26.
- [60] Sharon Webb. Silicate melts: Relaxation, rheology, and the glass transition. Reviews of Geophysics, 35(2):191–218, 1997.
- [61] J Taddeucci, P Scarlato, C Montanaro, C Cimarelli, E Del Bello, C Freda, D Andronico, MT Gudmundsson, and DB Dingwell. Aggregation-dominated ash settling

- from the eyjafjallajökull volcanic cloud illuminated by field and laboratory high-speed imaging. Geology, 39(9):891–894, 2011.
- [62] Noel Djobo. Synthesis factors, characteristics and durability of volcanic ash-based geopolymer cement. PhD thesis, 11 2017.
- [63] Nicholas Bojdo, Matthew Ellis, Antonio Filippone, Merren Jones, and Alison Pawley. Particle-vane interaction probability in gas turbine engines. Journal of Turbomachinery, 141(9):091010, 2019.
- [64] R Israel and Daniel E Rosner. Use of a generalized stokes number to determine the aerodynamic capture efficiency of non-stokesian particles from a compressible gas flow. Aerosol Science and Technology, 2(1):45–51, 1982.
- [65] Matthew Ellis, Nicholas Bojdo, Stephen Covey-Crump, Merren Jones, Antonio Filippone, and Alison Pawley. Generalized predictions of particle-vane retention probability in gas turbine engines. Journal of Turbomachinery, 143(11):111008, 2021.
- [66] Nicola Casari, Michele Pinelli, Alessio Suman, Luca di Mare, and Francesco Montomoli. An energy-based fouling model for gas turbines: Ebfog. Journal of Turbomachinery, 139(2):021002, 2017.
- [67] Srivats Srinivasachar, Joseph J Helble, and Arthur A Boni. An experimental study of the inertial deposition of ash under coal combustion conditions. In Symposium (International) on Combustion, volume 23, pages 1305–1312. Elsevier, 1991.
- [68] Stefan Richter. Numerische Simulation der Flugaschedeposition in kohlestaubgefeuerten Dampferzeugern. VDI-Verlag, 2003.
- [69] Robert Scharler, Ingwald Obernberger, and Mariusz K Cieplik. Development and evaluation of a flexible model for cfd simulation of ash deposit formation in biomass fired boilers. 2007.
- [70] Ulrich Kleinhans, Christoph Wieland, Flemming J Frandsen, and Hartmut Spliethoff. Ash formation and deposition in coal and biomass fired combustion systems: Progress and challenges in the field of ash particle sticking and rebound behavior. Progress in energy and combustion science, 68:65–168, 2018.

- [71] Donald B Dingwell and Sharon L Webb. Structural relaxation in silicate melts and non-newtonian melt rheology in geologic processes. Physics and Chemistry of Minerals, 16:508–516, 1989.
- [72] B Cordonnier, L Caricchi, M Pistone, J Castro, K-U Hess, S Gottschaller, M Manga, DB Dingwell, and L Burlini. The viscous-brittle transition of crystal-bearing silicic melt: direct observation of magma rupture and healing. Geology, 40(7):611–614, 2012.
- [73] Fabian B Wadsworth, Taylor Witcher, Caron EJ Vossen, Kai-Uwe Hess, Holly E Unwin, Bettina Scheu, Jonathan M Castro, and Donald B Dingwell. Combined effusive-explosive silicic volcanism straddles the multiphase viscous-to-brittle transition. Nature communications, 9(1):4696, 2018.
- [74] Steven M Whitaker, Robin Prenter, and Jeffrey P Bons. The effect of freestream turbulence on deposition for nozzle guide vanes. Journal of Turbomachinery, 137(12):121001, 2015.
- [75] Margaritis Kostoglou and Athanasios G Konstandopoulos. Particulate deposit shape evolution on cylinders in cross-flow at high stokes numbers. Journal of aerosol science, 31(4):427–436, 2000.
- [76] Caleb bell and contributors (2016-2023). fluids: Fluid dynamics component of chemical engineering design library (chedl). <https://github.com/CalebBell/fluids>. Accessed: 2023-02-15.
- [77] scipy.stats.gaussiankde. https://docs.scipy.org/doc/scipy/reference/generated/scipy.stats.gaussian_kde.html. Accessed: 2022-09-30.
- [78] Inert heating or cooling (law 1/law 6). <https://www.afs.enea.it/project/neptunius/docs/fluent/html/th/node252.htm>. Accessed: 2023-06-26.
- [79] Jozef KRAXNeR, M Liška, Robert Klement, and M Chromčíková. Surface tension of borosilicate melts with the composition close to the e-glass. Ceramics-silikaty, 53(2):141–143, 2009.

- [80] N. PARIKH. Effect of atmosphere on surface tension of glass. Journal of the American Ceramic Society, 41:18 – 22, 06 2006.
- [81] THOMAS JONES et al. Fissures and fountains: magma dynamics in basaltic conduits. PhD thesis, Durham University, 2018.
- [82] EW Llewelin, HM Mader, and SDR Wilson. The rheology of a bubbly liquid. Proceedings of the Royal Society of London. Series A: Mathematical, Physical and Engineering Sciences, 458(2020):987–1016, 2002.
- [83] Stephen Peacock. Predicting physical properties of factory juices and syrups. International Sugar Journal, 97(1162):571–2, 1995.
- [84] Glycerine Producers' Association et al. Physical properties of glycerine and its solutions. Glycerine Producers' Association, 1963.
- [85] SR Gregory. Physical properties of glycerine. In Glycerine, pages 113–156. CRC Press, 2018.
- [86] Martin Laun, Dietmar Auhl, Rüdiger Brummer, Dirk J Dijkstra, Claus Gabriel, Marc A Mangnus, Maximilian Rüllmann, Wim Zoetelief, and Ulrich A Handge. Guidelines for checking performance and verifying accuracy of rotational rheometers: viscosity measurements in steady and oscillatory shear (iupac technical report). Pure and Applied Chemistry, 86(12):1945–1968, 2014.
- [87] Vermes faq. <https://www.vermes.com/faq#:~:text=The%20medium%20is%20supplied%20at,not%20deviated%20in%20different%20directions..>
Accessed: 2023-11-22.
- [88] Droppy. <https://michaelorella.github.io/droppy/build/html/index.html>.. Accessed: 2023-02-14.
- [89] Cyril W Hirt and Billy D Nichols. Volume of fluid (vof) method for the dynamics of free boundaries. Journal of computational physics, 39(1):201–225, 1981.
- [90] J Eddie Welch, Francis Harvey Harlow, John P Shannon, and Bart J Daly. The mac method-a computing technique for solving viscous, incompressible, transient

- fluid-flow problems involving free surfaces. Technical report, Los Alamos National Lab.(LANL), Los Alamos, NM (United States), 1965.
- [91] LTM van der Linden, JGM Kuerten, and HMA Wijshoff. Numerical simulations of the impact, absorption and evaporation of a small drop.
- [92] Gerardo Trapaga and Julian Szekely. Mathematical modeling of the isothermal impingement of liquid droplets in spraying processes. Metallurgical and Materials Transactions B, 22:901–914, 1991.
- [93] Chan-Seong Park, Chun-Hwa Ihm, Nam-Soo Cho, and Nak-Eun Chung. Application of volume-of-fluid method to analyze the viscosity effect on the spine formation of bloodstains. Journal of Forensic Sciences, 59(6):1552–1558, 2014.
- [94] Wen-Jaur Chang and David J Hills. Sprinkler droplet effects on infiltration. i: Impact simulation. Journal of irrigation and drainage engineering, 119(1):142–156, 1993.
- [95] Markus Bussmann. A three-dimensional model of an impacting droplet. PhD thesis, 2000.
- [96] JM Sumner, S Blake, RJ Matela, and JA Wolff. Spatter. Journal of Volcanology and Geothermal Research, 142(1-2):49–65, 2005.
- [97] Abdulrahman Barakat Aljedaani. Drop impacts under extreme conditions on thin liquid films or solid walls. PhD thesis, 2019.
- [98] Srivats Srinivasachar, Joseph J Helble, and Arthur A Boni. An experimental study of the inertial deposition of ash under coal combustion conditions. In Symposium (International) on Combustion, volume 23, pages 1305–1312. Elsevier, 1991.
- [99] Robert Scharler, Ingwald Obernberger, and Mariusz K Cieplik. Development and evaluation of a flexible model for cfd simulation of ash deposit formation in biomass fired boilers. 2007.
- [100] Stefan Richter. Numerische Simulation der Flugaschedeposition in kohlestaubgefeuerten Dampferzeugern. VDI-Verlag, 2003.
- [101] Ted Mao, David CS Kuhn, and Honghi Tran. Spread and rebound of liquid droplets upon impact on flat surfaces. AIChE Journal, 43(9):2169–2179, 1997.

- [102] Sharon L Webb and Donald B Dingwell. The onset of non-newtonian rheology of silicate melts: A fiber elongation study. Physics and Chemistry of Minerals, 17:125–132, 1990.
- [103] James Clerk Maxwell. Iv. on the dynamical theory of gases. Philosophical transactions of the Royal Society of London, (157):49–88, 1867.
- [104] Joseph H Simmons, Robert K Mohr, and CJ Montrose. Non-newtonian viscous flow in glass. Journal of Applied Physics, 53(6):4075–4080, 1982.
- [105] Donald B Dingwell and Sharon L Webb. Relaxation in silicate melts. European Journal of Mineralogy, (4):427–449, 1990.
- [106] Thomas P Seward and Terese Vascott. High temperature glass melt property database for process modeling. (No Title), 2005.
- [107] Alexander Fluegel. Glass viscosity calculation based on a global statistical modelling approach. Glass Technology-European Journal of Glass Science and Technology Part A, 48(1):13–30, 2007.
- [108] Frank P Incropera, David P DeWitt, Theodore L Bergman, Adrienne S Lavine, et al. Fundamentals of heat and mass transfer, volume 6. Wiley New York, 1996.
- [109] Fabian B Wadsworth, Jérémie Vasseur, Edward W Llewelin, Kimberly Genareau, Corrado Cimarelli, and Donald B Dingwell. Size limits for rounding of volcanic ash particles heated by lightning. Journal of Geophysical Research: Solid Earth, 122(3):1977–1989, 2017.
- [110] Anna Petersen, Michael Hilfer, and Robin Brakmann. Influence of thermal barrier coating roughness on the boundary layer state of a high-pressure turbine vane with high acceleration close to relaminarization. Transition, 2021.
- [111] Christopher Stephen Smith. Experimental Validation of a Hot Gas Turbine Particle Deposition Facility. PhD thesis, The Ohio State University, 2010.
- [112] A Gourgaud, G Camus, M-C Gerbe, J-M Morel, A Sudradjat, and PM Vincent. The 1982–83 eruption of galunggung (indonesia): a case study of volcanic hazards

with particular relevance to air navigation. In Volcanic Hazards: Assessment and Monitoring, pages 151–162. Springer, 1989.

- [113] Glen A Izett. Volcanic ash beds: Recorders of upper cenozoic silicic pyroclastic volcanism in the western united states. Journal of Geophysical Research: Solid Earth, 86(B11):10200–10222, 1981.